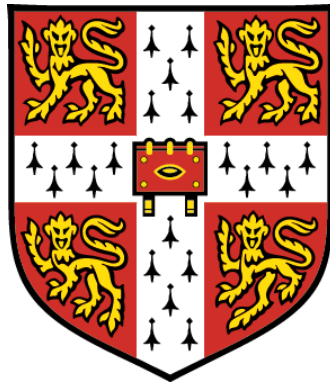# Nitride semiconductors studied by atom probe tomography and correlative techniques

Samantha E. Bennett
Pembroke College

A dissertation submitted for the degree of Doctor of Philosophy at the University of Cambridge

September 2010

Nitride semiconductors studied by atom probe tomography and correlative techniques
Samantha E. Bennett

Optoelectronic devices fabricated from nitride semiconductors include blue and green light emitting diodes (LEDs) and laser diodes (LDs). To design efficient devices, the structure and composition of the constituent materials must be well-characterised. Traditional microscopy techniques used to examine nitride semiconductors include transmission electron microscopy (TEM), and atomic force microscopy (AFM). This thesis describes the study of nitride semiconductor materials using these traditional methods, as well as atom probe tomography (APT), a technique more usually applied to metals that provides three-dimensional (3D) compositional information at the atomic scale. By using both APT and correlative microscopy techniques, a more complete understanding of the material can be gained, which can potentially lead to higher-efficiency, longer-lasting devices.

Defects, such as threading dislocations (TDs), can harm device performance. An AFM-based technique was used to show that TDs affect the local electrical properties of nitride materials. To investigate any compositional changes around the TD, APT studies of TDs were attempted, and evidence for oxygen enrichment near the TD was observed. The dopant level in nitride devices also affects their optoelectronic properties, and the combination of APT and TEM was used to show that Mg dopants were preferentially incorporated into pyramidal inversion domains, with a Mg content two orders of magnitude above the background level.

Much debate has been focused on the microstructural origin of charge carrier localisation in InGaN. Alloy inhomogeneities have often been suggested to provide this localisation, yet APT has revealed InGaN quantum wells to be a statistically random alloy. Electron beam irradiation in the TEM caused damage to the InGaN, however, and a statistically significant deviation from a random alloy distribution was then observed by APT. The alloy homogeneity of InAlN was also studied, and this alloy system provided a unique opportunity to study gallium implantation damage to the APT sample caused during sample preparation by the focused ion beam (FIB).

The combination of APT with traditional microscopy techniques made it possible to achieve a thorough understanding of a wide variety of nitride semiconductor materials.

This thesis is submitted to the University of Cambridge for the degree of Doctor of Philosophy. It is an account of the research that I have undertaken under the supervision of Prof. Sir C. J. Humphreys in the Department of Materials Science and Metallurgy at the University of Cambridge between October 2007 and September 2010. It is my own work and contains nothing which is the outcome of work done in collaboration with others, except as specified in the text and Acknowledgements. This thesis is less than 60,000 words in length and has not been submitted to any other institution for a degree.

Samantha E. Bennett
September 2010

For my mother, Kitty Bennett, and my step-father, David Knoll.

'No longer forward nor behind
I look in hope or fear;
But, grateful, take the good I find,
The best of now and here.'
-- John Greenleaf Whittier

I am grateful to the many people who have helped and supported me during my three years in the Cambridge Centre for gallium nitride. Firstly, I would like to thank my supervisor, Prof. Sir Colin Humphreys, for the opportunity to undertake this exciting research project. I am especially indebted to Dr. Rachel Oliver for all of her efforts as my mentor, including guidance on experimental work throughout my project, help with paper writing, and revision of this thesis. In addition, I would like to thank Dr. Menno Kappers and Dr. Shelly Moram for help with editing my review article and other valuable assistance. For basic TEM training, I am grateful to Mr. Graham Sharp, and for extensive assistance with more advanced TEM techniques, I would like to thank Dr. Jonathan Barnard. For FIB/SEM training and assistance, I am grateful to Dr. Richard Beanland and Dr. Martin Ritter. I am also grateful to everyone in the department for making it such an enjoyable place to work.

I was fortunate to receive training in the technique of atom probe tomography from Mr. Robert Ulfig and Dr. Peter Clifton at Imago Scientific Instruments, and I am grateful to them, and to everyone at Imago for their help. In addition to my work in Cambridge, I have had the pleasure of collaborating with the FIM group in the University of Oxford Materials Department on APT experiments. I would like to thank everyone in their group, especially Dr. David Saxey, with whom I worked closely on my many experimental visits.

This project has been funded by the EPSRC, Pembroke College (Cambridge), and Sharp Laboratories of Europe. I would like to thank Dr. Tim Smeeton from Sharp Laboratories, for providing exciting samples for study, and for his interest in my project.

My family and friends have been both supportive and enthusiastic during my PhD. I would especially like to thank my boyfriend, William Deacon, for his support throughout. Finally, I am tremendously grateful to my parents for allowing me to come home and write my thesis *en la casa rustica.*

CONTENTS

PUBLICATIONS RELATED TO THIS WORK

Bennett, S. E., Dislocations and their reduction in GaN. *Materials Science and Technology* **2010,** 26 (9), 1017-1028.

Bennett, S. E.; Clifton, P. H.; Ulfig, R. M.; Kappers, M. J.; Barnard, J. S.; Humphreys, C. J.; Oliver, R. A., Atom probe extended to AlGaN: three-dimensional imaging of a Mg-doped AlGaN/GaN superlattice. *Physica Status Solidi C* **2010,** *7,* 1781-1783.

Bennett, S. E.; Holec, D.; Kappers, M. J.; Humphreys, C. J.; Oliver, R. A., Imaging dislocations in gallium nitride across broad areas using atomic force microscopy. *Review of Scientific Instruments* **2010,** 81, 063701-1 – 063701-7.

Bennett, S. E.; Clifton, P. H.; Ulfig, R. M.; Kappers, M. J.; Barnard, J. S.; Humphreys, C. J.; Oliver, R. A., Mg dopant distribution in an AlGaN/GaN p-type superlattice assessed using atom probe tomography, TEM and SIMS. *Journal of Physics: Conference Series* **2010,** 209, 012014-1 – 012014-4.

Barnard, J. S.; **Bennett, S. E.**; Oliver, R. A.; Kappers, M. J.; Humphreys, C. J., The role of rough surfaces in quantitative ADF imaging of gallium nitride-based materials. *Journal of Physics: Conference Series* **2010,** 209, 012019-1 – 012019-4.

Oliver, R. A.; **Bennett, S. E.**; Sumner, J.; Kappers, M. J.; Humphreys, C. J., Scanning capacitance microscopy studies of GaN grown by epitaxial layer overgrowth. *Journal of Physics: Conference Series* **2010,** 209, 012049-1 – 012049-4.

Oliver, R. A.; **Bennett, S. E.**; Zhu, T.; Beesley, D. J.; Kappers, M. J.; Saxey, D. W.; Cerezo, A.; Humphreys, C. J., Microstructural origins of localization in InGaN quantum wells. *Journal of Physics D: Applied Physics* **2010,** 43, 354003-1 – 354003-8.

Bennett, S. E.; Ulfig, R. M.; Clifton, P. H.; Kappers, M. J.; Barnard, J. S.; Humphreys, C. J.; Oliver, R. A., Atom probe tomography and transmission electron microscopy of a Mg-doped AlGaN/GaN superlattice. *Ultramicroscopy* **2011,** 111, 207-211.

LIST OF COMMONLY USED ABBREVIATIONS

a, c	lattice parameters of wurtzite III-nitride alloys
b	Burgers vector
AFM	atomic force microscopy
APT	atom probe tomography
ARM	Axial Rotational Manipulator
BF	bright field
CB	conduction band
CCD	charge-coupled device
CL	cathodoluminescence
DBR	distributed Bragg reflector
DF	dark field
DLD	delay line detector
DOF	degrees of freedom
EDX	energy-dispersive X-ray spectroscopy
EELS	electron energy-loss spectroscopy
EFTEM	energy filtered transmission electron microscopy
EL	electroluminescence
ELOG	epitaxial lateral overgrowth
FEG	field emission gun
FIB	focused ion beam
GIS	gas injection system
HAADF	high angle annular dark field
HRTEM	high resolution transmission electron microscopy
ICF	image compression factor
IQE	internal quantum efficiency
IVAS	Imago Visualization and Analysis Software
KPFM	Kelvin probe force microscopy
LD	laser diode
LEAP	local electrode atom probe
LED	light emitting diode
MBE	molecular beam epitaxy
MCP	micro-channel plate
MOVPE	metal organic vapour phase epitaxy

MQW	multiple quantum well
PAMBE	plasma-assisted molecular beam epitaxy
PID	pyramidal inversion domain
PIPS™	precision ion polishing system
QCSE	quantum confined Stark effect
QW	quantum well
RF-PAMBE	radio-frequency plasma-assisted molecular beam epitaxy
ROI	region of interest
SCH	separate confinement heterostructure
SE	secondary electron
SEM	scanning electron microscopy
SIMS	secondary ion mass spectrometry
slm	standard litres per minute
SL	superlattice
SRIM	Stopping and Range of Ions in Matter
STEM	scanning transmission electron microscopy
TD	threading dislocation
TEM	transmission electron microscopy
TMA	trimethylaluminium
TMG	trimethylgallium
TMI	trimethylindium
UV	ultraviolet
VB	valence band
WBDF	weak beam dark field
WZ	wurtzite
XRD	X-ray diffraction
ZB	zinc blende

1

INTRODUCTION

Since the mid-1990s, group III-nitride materials (GaN, AlN, InN and their alloys) have been the subject of intense research, with these efforts leading to the development of optoelectronic devices such as light emitting diodes (LEDs) and laser diodes (LDs)[1]. These III-nitride based devices can emit light over a wide range of wavelengths, from visible to ultraviolet (UV), and have been successfully commercialised for mass-market applications. High brightness LEDs emitting brilliant blue, green, or white light are manufactured in great quantities, for uses ranging from bicycle lights to full colour displays. Furthermore, the realisation of III-nitride based LDs has ushered in the newest generation of high density optical data storage systems, such as the Blu-ray Disc™ technology currently employed in home entertainment and computing systems.

Although the applications of LEDs are ever-broadening, their widespread use as energy efficient home and office lighting has yet to be achieved, and still requires advances in material and device performance[2]. Yet the performance of III-nitride based devices may be limited by underlying material properties that are not completely understood, even after nearly two decades of research. For instance, there is significant controversy over the role of crystalline defects known as threading dislocations (TDs), very high densities

of which are found in III-nitride based devices. Such high TD densities (around 10^9 cm^{-2}) would destroy the light-emission from LEDs and LDs made from other semiconductors[3], yet III-nitride materials seem to possess a unique feature, or set of features, rendering the material largely immune to the harmful effects of TDs. To unravel this apparent anomaly, and to overcome other challenges currently inhibiting III-nitride based device performance, an understanding of the material's structure at the nanoscale is crucial.

In this thesis, a novel characterisation technique known as atom probe tomography (APT) has been used alongside more conventional microscopy techniques, such as atomic force microscopy (AFM) and transmission electron microscopy (TEM), to study the nanostructure of III-nitride materials. The investigations reported in this work can be divided into three main areas:

> ➢ studies of defects,
>
> ➢ studies of alloy homogeneity,
>
> ➢ and studies of a full device structure.

During the course of these investigations, various materials questions were explored. Throughout this work, however, the overarching aim was to evaluate the capabilities of the APT technique, as applied to III-nitride research.

In Chapter 2, the characterisation techniques employed in the remainder of this work are described, focusing specifically on how best to apply them to the study of III-nitride materials. The next six chapters report experimental results obtained in the three areas listed above. Each experimental chapter is self-contained, and begins with a literature survey on specific areas of relevance. Chapters 3 to 5 focus on defects. Chapter 3 describes AFM and TEM studies of TDs, after which, in Chapter 4, APT characterisation of TDs is attempted. In Chapter 5, small Mg-rich defects found in p-type GaN are investigated using both APT and TEM, enabling a comparison of the information gained about the defects by both techniques. Chapters 6 and 7 then focus on alloy homogeneity. Chapter 6 returns to the question of light emission from III-nitride devices, by using APT to investigate the structural origins of charge carrier localisation in InGaN, with particular attention paid to the possibility of localisation at non-random fluctuations in indium content. In Chapter 7, the first APT studies of the alloy InAlN

are reported, again with a focus on possible indium clustering. Chapter 8 then presents an APT study of a full LD structure, with data collected from n-type layers, the InGaN active region, and p-type layers in the structure. Finally, concluding remarks and future directions for research are presented in Chapter 9.

The remainder of this chapter will present the basic properties of III-nitrides, followed by a discussion of heteroepitaxial growth, and an introduction to optoelectronic devices based on III-nitrides. Finally, the technique of atom probe tomography will be introduced, as it is still a niche technique, and therefore unfamiliar to many scientists.

1.1. MATERIAL PROPERTIES OF III-NITRIDES

1.1.1. CRYSTAL STRUCTURE

Although the III-nitrides crystallise in both the wurtzite (WZ) and zinc blende (ZB) structures, the WZ structure is thermodynamically more stable, and has therefore been the subject of most research[4]. As the samples used in this work are all of the WZ structure, the ZB structure will not be discussed, although further information can be found in the review by Orton and Foxon[4]. The WZ structure consists of alternating biatomic close-packed (0001) planes of group III atoms (Ga, In, or Al) and N atoms, stacked in an ABABABAB sequence. Figure 1.1 shows a schematic diagram of a unit cell of WZ GaN, viewed in projection along the [0001] direction, indicating the atomic positions and principal crystallographic directions[5]. The lattice parameter, a, is labeled, and the plane spacing in the [0001] direction is defined by the lattice parameter, c. The parameter u describes the displacement of the anion along the [0001] axis, or 'c-axis', and has been found to be 0.377 for GaN[6], deviating from the ideal value of 3/8, or 0.375.
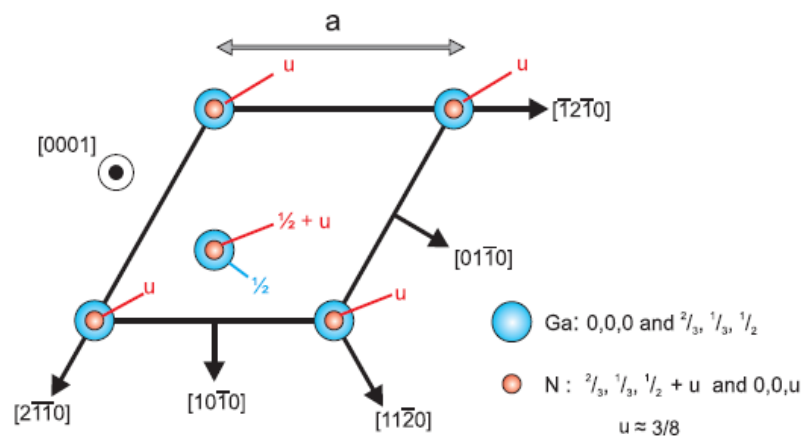
Figure 1.1. From Cherns[5], a schematic diagram of one unit cell of WZ GaN, viewed along the [0001] direction. The lattice parameter, a, is labeled.

Figure 1.2 shows a schematic diagram of the GaN WZ structure, viewed along the $[\overline{11}20]$ direction, with the c lattice parameter labeled[5]. The diagram illustrates GaN grown along the [0001] direction. Layers grown in this orientation are described as 'Ga-polar'. Most GaN grown by metal-organic vapour phase epitaxy (MOVPE) is Ga-polar, with the alternative structure being N-face polarity, in which the growth proceeds along the $[000\overline{1}]$ direction.
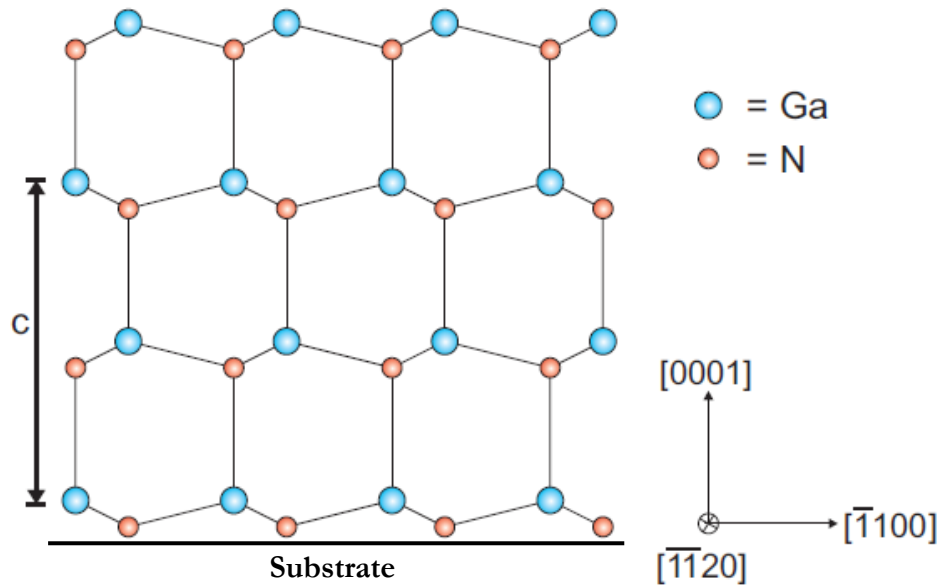
Figure 1.2. From Cherns[5], a schematic diagram of the WZ GaN structure, viewed along the $[\overline{11}20]$ direction, with the lattice parameter, c, labeled. This structure depicts Ga-polar GaN.

The room temperature lattice parameters for the III-nitride materials, according to a recent review by Vurgaftman and Meyer[7], are summarised in table 1.1. There is some debate regarding these values, and this controversy has recently been discussed by Moram and Vickers[8].

Table 1.1. Lattice parameters for the III-nitride materials[7].

Material	a (Å)	c (Å)
GaN	3.189	5.185
AlN	3.112	4.982
InN	3.545	5.703

By mixing two III-nitride materials, a binary nitride alloy can be formed. For instance, InGaN is an alloy commonly used in the active region of LED and LD devices. To

specify the amount of In present in the alloy, the notation $In_xGa_{1-x}N$ is used, where x denotes the fraction of In atoms that substitute for Ga atoms on group III lattice sites. The lattice parameters for $In_xGa_{1-x}N$ and the other binary nitrides can be approximated using a linear interpolation between the two components, according to Vegard's law:

$$a = (1-x)\, a_{GaN} + x\, a_{InN}$$

and

$$c = (1-x)\, c_{GaN} + x\, c_{InN}$$

It should be noted that some theoretical work has suggested that for InGaN layers with compositions close to 50 %, there is a significant deviation from Vegard's law[9], yet in this work the In content of the samples studied does not exceed 30 %, so the preceding equations should suffice to estimate the lattice parameters. Consensus as to a possible deviation from Vegard's law for InAlN has yet to be reached in the scientific community, although theoretical studies have predicted a slight deviation[9,10].

1.1.2. POLARISATION

Due to the partially ionic nature of the bonding in III-nitrides, and the absence of inversion symmetry in the WZ structure (the [0001] and [000$\bar{1}$] directions are crystallographically distinct), the materials exhibit a 'spontaneous polarisation', with a net dipole along the c-axis. In addition to this spontaneous polarisation, the III-nitrides show a large piezoelectric response to elastic strain, resulting in a 'piezoelectric polarisation' when strained. In a theoretical study, Bernardini *et al.*[11] found that the spontaneous polarisation in III-nitrides is very large, compared with other semiconductors, and that the absolute values for the piezoelectric constants are up to ten times larger than those found for other III-V and II-VI compounds. Thus, polarisation effects can have a significant impact on the optical properties of structures fabricated from the III-nitrides, such as quantum wells. This effect will be discussed further in section 1.3.1.

1.1.3. BAND STRUCTURE

The III-nitrides are direct band gap semiconductors, making them suitable materials for optoelectronic devices, as light emission can be realised via recombination of electrons and holes without the need for phonon mediation. Figure 1.3 shows the band gaps of GaN, AlN, and InN (green circles), plotted against their *a* lattice parameter. To illustrate the wavelengths of light produced at the various band gap energies, the visible colours in

the solar spectrum are shown at the right of the figure. The widely acknowledged band gap energies of GaN and AlN are 3.51 eV and 6.25 eV, respectively[7]. Recently, the accepted value for the band gap energy of InN has been revised, from near 2 eV, to 0.78 eV[7]. With band gap energies ranging from 0.78 eV to 6.25 eV, devices made from alloys of III-nitride materials can in theory be designed to emit light of any colour in the visible spectrum, and into the infra-red and UV. The band gaps of binary nitride alloys vary continuously between the values of the end members, as illustrated with black lines in figure 1.3.
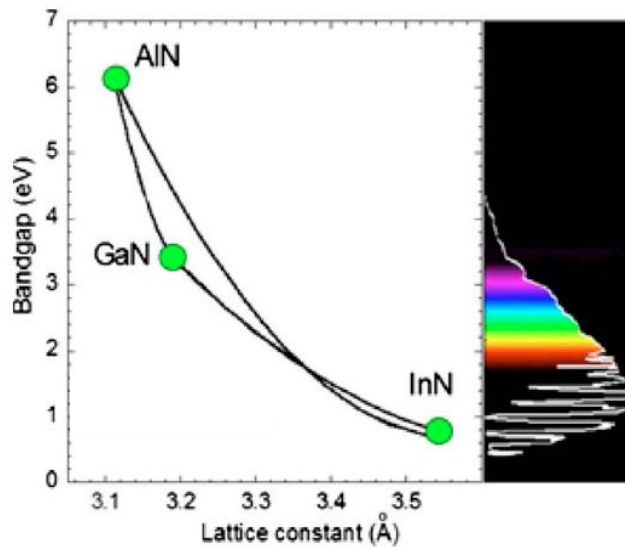
Figure 1.3. From Wu[12], a diagram showing the band gaps of AlN, GaN, and InN (green circles), as a function of their *a* lattice constant. The variations of bandgap with composition for the binary nitride alloys are indicated with black lines. For comparison, the visible colours in the solar spectrum are shown on the right of the diagram.

The composition dependences of the band gaps for the binary nitride alloys are assumed to follow a simple quadratic form, as stated by Vurgaftman and Meyer[7]:

$$E_g(A_{1-x}B_x) = (1-x)E_g(A) + xE_g(B) - x(1-x)C$$

where E_g is the band gap energy, and C is defined as the bowing parameter, which describes the deviation from a linear interpolation between the band gap values of the two end members, *A* and *B*. The non-linearity evident in the black lines in figure 1.3 illustrates this bowing. Although the bowing parameter for InGaN is accepted to be very close to 1.4 eV, there is little consensus on the value for either AlGaN or InAlN. After a review of the literature, Safta *et al.*[13] suggested the value for the AlGaN bowing parameter was likely to be near 0.7 eV for unstrained material, although they noted that reported values ranged between -0.8 and 2.6 eV. For InAlN, bowing parameters of between 2.2 and 6 eV have been stated in the literature[14]. This wide range in the reported value may be due to a lack of high quality material. Further information about InAlN can be found in a recent review by Wu[12], in which the author reported the InAlN bowing parameter to

be near 5 eV. With such uncertainty as to the bowing parameters for AlGaN and InAlN, the only reliable representation of the bowing parameter in figure 1.3 is that of InGaN.

1.2. HETEROEPITAXIAL GROWTH OF III-NITRIDES

The homoepitaxial growth of III-nitride materials is rare, due to the difficulties faced in synthesising high quality bulk single crystal substrates[15]. Efforts to produce GaN substrates are hindered by the extremely high vapour pressure of nitrogen required in most growth techniques. Although high temperature, high pressure growth has been successfully used to produce single crystal GaN substrates[15,16], these are currently very costly. In the absence of bulk substrates, nearly all III-nitride based devices realised to date have been grown on foreign substrates. This heteroepitaxial growth is most often achieved using c-plane sapphire (α-Al$_2$O$_3$) substrates, as was the case for all samples examined in this work. Alternative substrates include both single crystal SiC and Si[15], with the latter being extremely attractive due to the low cost of Si wafers, and the possibility to integrate III-nitride device fabrication with existing Si-based electronics manufacturing, to reduce the cost of such devices.

Heteroepitaxial growth has been fruitfully employed in spite of the large differences in lattice constants and thermal expansion coefficients between the substrates and the III-nitride thin films[15]. In the case of GaN on sapphire, the <11$\bar{2}$0> direction of the GaN is oriented parallel to the <1$\bar{1}$00> direction of the sapphire, which results in a lattice mismatch of approximately 16 %. This strain is accommodated by a network of misfit dislocations at the substrate/film interface. Figure 1.4 shows these misfit dislocations, marked with stars, in a Fourier filtered high resolution TEM image[17]. Extremely high densities of TDs (10^9 to 10^{11} cm^{-2}) are also thought to arise due to strain, although they do not relieve it[15]. Three types of TDs are observed: pure edge, or 'a-type' (Burgers vector, **b** = 1/3 <11$\bar{2}$0>), pure screw, or 'c-type' (**b** = <0001>), and mixed, or 'c+a type' (**b** = 1/3 <11$\bar{2}$3>). Further discussion of the origin and effect of TDs will be presented in section 3.2.
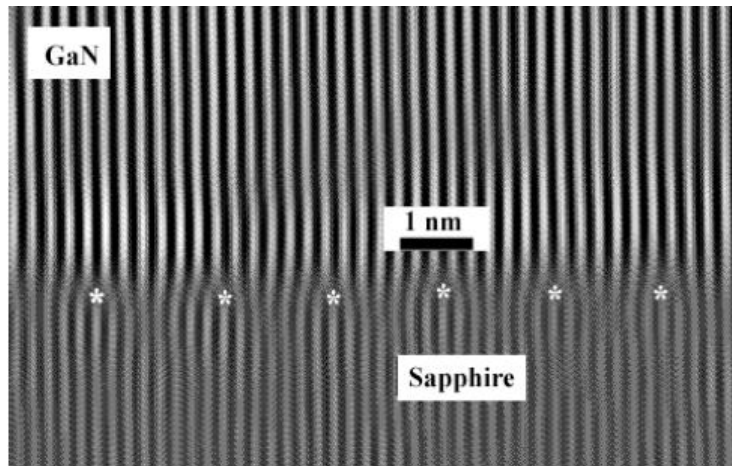
Figure 1.4. From Ruterana and Nouet[17], a Fourier filtered high resolution TEM image of misfit dislocations (marked with stars) at the GaN on sapphire interface.

Finally, it should be noted that GaN grown directly on sapphire at high growth temperatures results in isolated islands, and cannot produce material suitable for devices. To achieve reasonable quality material, a number of methods have been developed (and are reviewed by Gibart[15]), with one important step being the use of a low temperature buffer layer (or nucleation layer) of GaN at the first stage of growth. GaN material can subsequently be grown at a high temperature on the low temperature buffer layer, and the resulting material can be suitable for devices. The various growth methods used for the III-nitride samples studied in this work will be described in section 2.1.

1.3. DEVICES BASED ON III-NITRIDES

1.3.1. LIGHT EMITTING DIODES

Much of the driving force for III-nitride research has stemmed from their application in LED devices. Akasaki[18] reviewed the key breakthroughs in the history of III-nitride based LED and LD devices, highlighting the realisation of the first blue/UV LED in 1989. The first successful III-nitride based LED was a homojunction device, consisting of a junction between p-doped and n-doped regions of a single material[18]. Schematic diagrams of the band structure of a homojunction under zero bias and forward bias are shown in figures 1.5a and 1.5b, respectively[19]. Under forward bias, electrons (closed circles) in the conduction band of the n-type region diffuse towards the p-type region, and holes (open circles) in the valence band of the p-type region similarly diffuse towards the n-type region. These minority carriers can then radiatively recombine with majority carriers (electrons in the n-type region, and holes in the p-type region), resulting in the emission of a photon with energy close to that of the band gap. Alternatively,

non-radiative recombination can occur, in which energy is released as a phonon. Typically, non-radiative recombination is caused by the presence of electronic states within the band gap, due to impurities and crystal defects, such as TDs[19].

To maximise the probability that carriers will recombine radiatively, the carrier density can be increased with the use of a narrower band gap material between the p- and n-type layers. By confining the charge carriers to a limited volume, known as the 'active region', the lifetime of carriers prior to recombination (radiative lifetime) is reduced, and the efficiency of the device is thereby increased. This type of device is termed a double heterostructure, and figure 1.5c illustrates the confinement of charge carriers in the active region, when the device is under forward bias. InGaN has been used extensively as the active region in GaN-based LEDs. When the thickness of this active region falls below about 10 nm, quantum mechanical effects become significant, acting to quantise the energy levels within the layer, which can then best be described as a 'quantum well' (QW)[19]. This quantisation of energy levels can be applied to tune the emission wavelength of the device by varying the thickness of the QW.
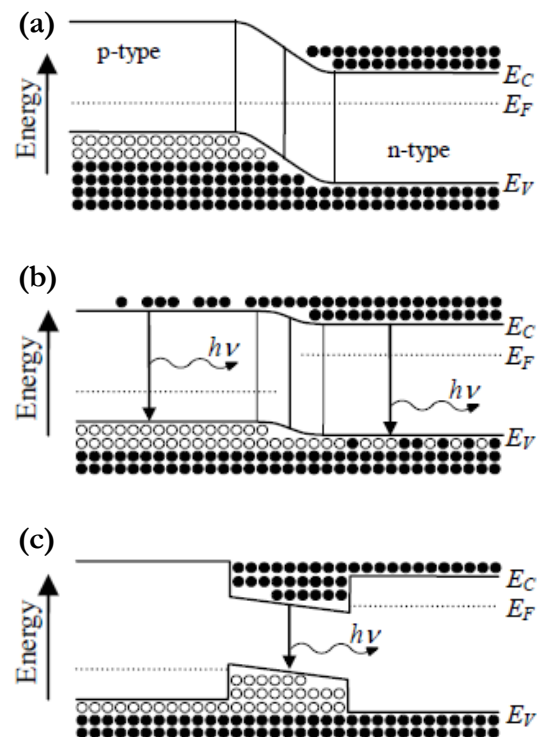
Figure 1.5. After Schubert[19], schematic diagrams of the band structure, with electrons and holes shown as closed and open circles, respectively. The conduction band energy (E_C), Fermi energy (E_F), and valence band energy (E_V) are labeled. (a) Homojunction under zero bias. (b) Homojunction under forward bias. The recombination of an electron and a hole results in emission of a photon, of energy $h\nu$. (c) Double heterostructure under forward bias. The charge carriers are confined to the central active region.

In a nitride double heterostructure device, the lattice mismatch between the QW and the surrounding material leads to strain in the QW, which gives rise to an internal electric

field. The electric field causes bending of the band structure, which lowers the transition energy, leading to a 'redshift' of the emission wavelength. This effect, known as the quantum confined Stark effect (QCSE), is illustrated in figure 1.6. Electrons and holes are shown as closed and open circles, respectively, and the conduction band (CB) and valence band (VB) are labeled for clarity. The QCSE results in a shift of the transition energy from that labeled $\Delta E_{g,QW1}$ to that labeled ΔE_{g1}, which is an amount approximately equal to the sum of the shifts of the first electron energy level (ΔE_{e1}) and the hole energy level (ΔE_{h1}), caused by band bending. As the thickness of the QW increases, the effect of the QCSE becomes more pronounced, leading to further lowering of the transition energy, labeled ΔE_{g2}. Additionally, the carriers are spatially separated, which increases the radiative lifetime, thus decreasing the device efficiency.
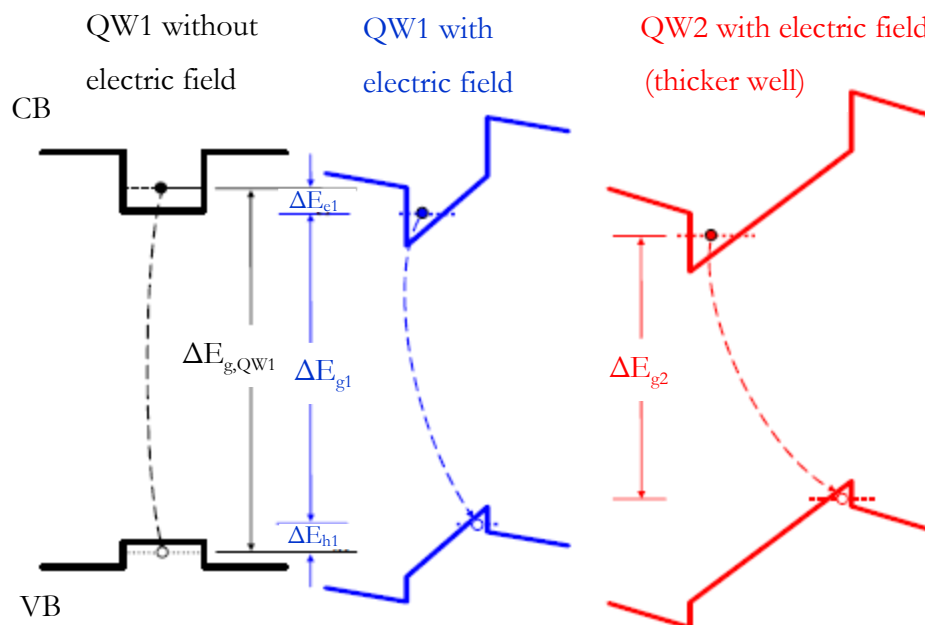
Figure 1.6. After Zhu[20], a schematic diagram, illustrating the QCSE in a thin and a thick QW. Electrons and holes are shown as closed and open circles, respectively, and the conduction band (CB) and valence band (VB) are labeled. The internal electric field leads to band bending and acts to spatially separate the charge carriers. The effect of band bending is to decrease the transition energy (from $\Delta E_{g,QW1}$ to ΔE_{g1}). The QCSE becomes more pronounced as the QW thickness is increased, resulting in a further decrease of the transition energy (labeled ΔE_{g2}).

1.3.2. LASER DIODES

The first III-nitride based injection LD was reported by Nakamura *et al.*[21] in 1996. The authors used an InGaN multiple QW (MQW) active region, into which charge carriers were injected under forward bias, just as described in the last section for LED devices. Whereas LEDs emit photons in a process known as spontaneous emission, LD devices also utilise the phenomenon of stimulated emission. In this process, the transit of a photon causes an excited electron to decay (due to the effect of the photon's electromagnetic field), producing another photon traveling in the same direction. The two photons are coherent, having the same polarisation and phase. Stimulated emission thereby leads to gain in the active region, given sufficient injection of carriers. The photons must also be confined within the active region to maintain the stimulated emission. This confinement can be realised with cladding layers (using a material with a lower refractive index) on either side of the active region. If the amplification due to stimulated emission is greater than the loss due to absorption, then the diode is said to 'lase'.

Figure 1.7 shows the structure used by Nakamura *et al.*[21] to create a violet-emitting LD. The active region consisted of 26 periods of $In_{0.2}Ga_{0.8}N/In_{0.05}Ga_{0.95}N$ MQWs. Confinement of the emitted photons was achieved with the use of $Al_{0.15}Ga_{0.85}N$ cladding layers. Under forward bias, this structure was observed to lase with an emission wavelength of 417 nm, above a threshold current of 1.7 A.
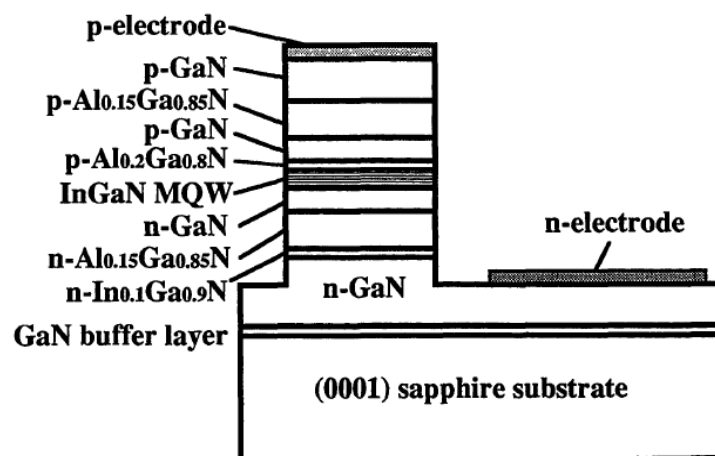
Figure 1.7. From Nakamura *et al.*[21], a schematic diagram of the structure of a violet-emitting LD with an InGaN MQW active region.

1.4. ATOM PROBE TOMOGRAPHY

Precise nanostructural characterisation is becoming ever more important, due to miniaturisation trends observed in many areas of research and commercial device design. The technique of atom probe tomography (APT) can provide three dimensional (3D) compositional information at the atomic scale with very high sensitivity, and with a field of view currently in excess of 100 nm × 100 nm × 1 μm on the latest instruments[22].

The development of the technique began with work by Müller[23], who created the field electron emission microscope in 1935. Twenty years later, atomic resolution was achieved with the field ion microscope (FIM), and the later addition of a time-of-flight mass spectrometer made it possible to chemically identify individual ions[24]. Finally, with the development of the position-sensitive atom probe (PoSAP) in 1988 by Cerezo *et al.*[25], true 3D compositional data were obtained. Recently, the advent of the local electrode atom probe (LEAP) has provided considerably increased data collection rates, making it possible to analyse much greater volumes of material[26]. Further description of the LEAP instrument and the APT technique will be provided in section 2.5.

2

TECHNIQUES

2.1. SAMPLE GROWTH

The samples studied in the experimental chapters of this work have either been grown by metal-organic vapour phase epitaxy (MOVPE) in Cambridge or by molecular beam epitaxy (MBE) at Sharp Laboratories of Europe. Although the specific growth conditions for each sample will be given at the start of each chapter, the following sections provide an overview of these growth techniques.

2.1.1. MOVPE GROWTH

In MOVPE growth, gaseous precursor molecules are transported using a carrier gas to a heated substrate where they react to form a crystalline film with an epitaxial relationship to the substrate[27]. For the growth of III-nitrides, the most commonly used group-III metal-organic precursors are trimethylgallium (TMG, $Ga(CH_3)_3$), trimethylindium (TMI, $In(CH_3)_3$), and trimethylaluminium (TMA, $Al(CH_3)_3$). Liquid TMG and TMA, and a solution containing TMI are stored in bubblers, where the temperature is carefully selected to control the vapour pressure over the source material[27]. A carrier gas (usually nitrogen or hydrogen) flows through the bubbler, saturating with vapour from the group-III source and transporting this vapour to the substrate. At the substrate, the

group-III precursor reacts with a nitrogen source, most commonly[15] ammonia (NH_3). Although intermediate reactions at the substrate may not be completely understood, the net reaction to produce crystalline GaN is as follows[27]:

$$Ga(CH_3)_3 \, (g) + NH_3 \, (g) \rightarrow GaN \, (s) + 3CH_4 \, (g)$$
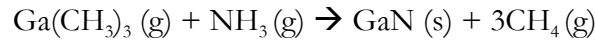
The MOVPE samples studied in this work were grown in Cambridge by Dr. Rachel Oliver and Dr. Menno Kappers, using a 6×2 inch Thomas Swan close-coupled showerhead reactor. A schematic[28] of this type of reactor can be seen in figure 2.1. The showerhead design has a large number of tiny outlet tubes through which the gases flow to the substrate. By using half of these tubes for metal-organics and half for ammonia, the two precursors are physically separated until they are close to the substrate, thus minimising unwanted gas-phase reactions.
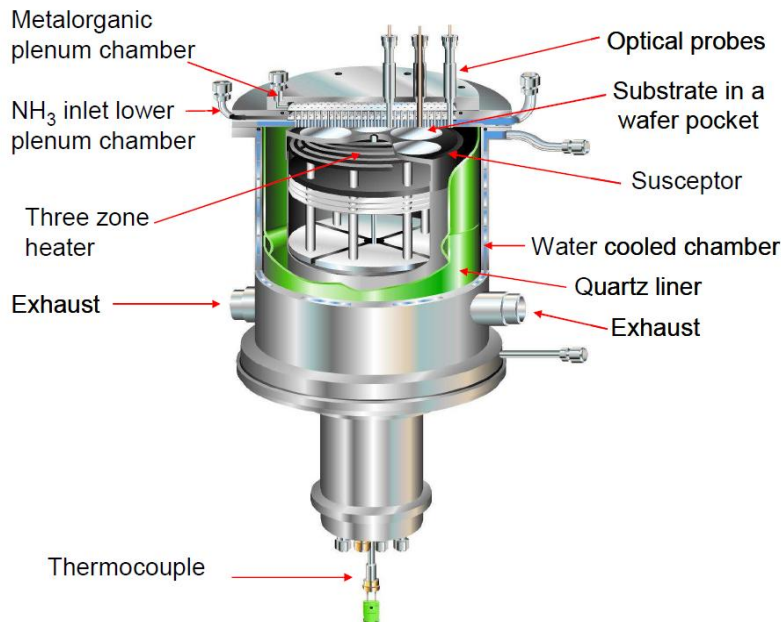
Figure 2.1. From Thrush[28], schematic of a 6×2 inch Thomas Swan close-coupled showerhead MOVPE reactor. The metal-organic precursors and the NH_3 are stored in separate chambers before they are combined and react at the substrate.

Parameters that can be tuned to alter the MOVPE growth include the substrate temperature, reactor pressure, flow rate of the gases into the reactor, and the ratio of partial pressures of group-V to group-III precursors, known as the V/III ratio. Typically, high temperatures are required for GaN growth (1000 ºC – 1100 ºC), which increases the cracking efficiency of the ammonia precursor, as well as allowing higher surface mobilities to be obtained, so that the film surface roughness can be minimised and the point defect density kept low. At these high temperatures, a high V/III ratio ($10^4 - 10^5$) prevents loss of the volatile nitrogen species, and stabilises the (0001) surface.

By altering the growth conditions in the reactor, changes can be induced in a growing GaN film: for instance, in the '3D to 2D' growth transition, altering the temperature, pressure and V/III ratio induces 3D GaN islands on sapphire to coalesce and growth to then continue as a 2D film[29]. This transition has been found to decrease the TD density[30], and illustrates the power that the MOVPE grower has to influence the resultant film quality.

High quality InGaN is much harder to grow than GaN due to the fact that InN dissociates at temperatures lower than the standard GaN growth temperature. InGaN growth must be performed below 850 °C, resulting in slow surface diffusion that can lead to increased point defect and impurity incorporation. The incorporation of In strongly increases with decreasing growth temperature[31,32], which indicates that In incorporation is limited by evaporation of the indium species from the surface. It has been shown that high growth rates can 'trap' the In within the growing layer[27], leading to an increased In content of the film. The In content is also sensitive to the choice of carrier gas: using hydrogen substantially decreases the In incorporation, possibly by slowing the reaction between TMI and ammonia[33]. Thus, nitrogen is used throughout this work as the carrier gas for InGaN growth.

In MOVPE growth, n-type doping is straightforward, with silicon being the typical dopant. Silane (SiH_4) is used as the precursor, and dopant densities of 1×10^{17} to 2×10^{19} cm^{-3} can be achieved without difficulty[27]. In this work, p-type GaN is realised using Mg dopants provided by a bis-cyclopentadienyl magnesium (Cp_2Mg) source. The Cp_2Mg used is a solid, which makes it difficult to control the amount of Mg precursor supplied, as compared with the liquid metal-organics. An additional difficulty arises during MOVPE growth, as Mg-H acceptor complexes form, which passivate the acceptor. To break this bond, a high temperature hydrogen-free annealing step is used[34]. Typically p-type carrier densities are much lower than in n-type GaN. P-type doping of GaN will be discussed further in section 5.2.1.

2.1.2. MBE GROWTH

MBE is an ultra-high vacuum technique (with base pressures from 10^{-7} to 10^{-10} Torr) that results in high purity epitaxial films with precise control of composition[4]. Unlike MOVPE, which uses precursors, MBE uses molecular beams of atoms that are directed

onto a heated substrate. These beams can be switched on and off nearly instantaneously with mechanical shutters, enabling control of composition down to a single monolayer. This precise growth can be monitored with the use of reflection high-energy electron diffraction (RHEED)[35], giving real-time feedback on film growth. Although MBE is usually considered to be a more precise, yet slower technique, in the growth of nitride materials, the low pressures used in MBE can lead to low surface mobilities. This low mobility can cause poor surface roughness, making the controlled growth of layers with precise thickness difficult.

In MBE, beams of group III atoms are introduced using high purity metallic effusion cells[35]. For the supply of atomic nitrogen, a variety of methods have been used, with the two most popular being nitrogen plasmas and ammonia. In what is known as plasma-assisted MBE, or PAMBE, the strong bond of the N_2 molecule can be dissociated in a plasma environment. The most successful PAMBE techniques are electron cyclotron resonance[36,37] and radio-frequency[38] (RF-PAMBE) plasma sources. As in MOVPE, thermal dissociation of ammonia can be used to supply nitrogen in MBE systems, although the cracking efficiency can be low at typical MBE growth temperatures of between 650 °C and 800 °C. This method is sometimes known as 'reactive MBE'.

The MBE samples studied in this work were grown at Sharp Laboratories of Europe using a combination of RF-PAMBE and reactive MBE in a Veeco V80 MBE system. The Ga, In and Al were supplied using effusion cells. For RF-PAMBE, the N_2 was dissociated using a Veeco UNI-Bulb RF Plasma Source, and for the reactive MBE, the NH_3 was thermally cracked at the substrate surface. All MBE samples were grown on ultra-low dislocation density (ULD) GaN templates supplied by Lumilog. These templates are comprised of 10 μm of MOVPE-grown GaN on a sapphire substrate. The TD density was specified by the supplier to be below 8×10^7 cm^{-2}.

2.2. AFM

Atomic force microscopy (AFM) methods offer a wide variety of characterisation tools for the study of mechanical, electrical and magnetic properties of surfaces. These different methods can be described broadly as microscopy techniques in which a small, sharp physical probe, known as a tip, is rastered across a specimen surface to acquire an

image. The tip is located on the end of a cantilever, which is deflected by interactions with the surface as it is scanned. Tip-sample interactions include attraction due to Van der Waals forces and repulsion due to overlap of the electron clouds of the surface and the tip. The deflection is measured with a laser reflected off the cantilever surface, and a feedback loop is often used to maintain a constant tip-surface interaction. In this work, two types of AFM, intermittent-contact mode topographic imaging and Kelvin probe force microscopy (KPFM), were used to image the topography and surface potential of our samples, respectively.

2.2.1. TOPOGRAPHIC IMAGING

AFM is a non-destructive technique with which to study semiconductor surfaces. In this work, a Veeco Dimension 3100 AFM with RTESP tips (with a nominal apex radius of 8 nm) was used to acquire surface topography images, information that is especially useful in the study of TDs, which terminate at surface pits. The AFM can be operated in several modes, including contact mode, intermittent-contact mode (or TappingMode™) and non-contact mode[39]. All images taken in this work used TappingMode™, in which the tip at the end of a cantilever is driven by a piezo-oscillator near its resonant frequency. As the tip is brought close to the sample, the interaction between the tip and the sample leads to a force gradient that changes the cantilever's resonant frequency, and therefore alters the vibration amplitude (for a constant drive frequency)[40]. In addition, the tip is positioned so that it makes contact with, or 'taps', the surface at the bottom of each oscillation. This contact results in damping of the oscillation amplitude. As the tip is scanned across the surface (using voltages applied to a piezoelectric crystal), the tip-sample distance will change. A feedback loop is used to respond to the resulting changes in the vibration amplitude by moving the tip vertically so that the amplitude, and therefore the tip-sample distance, is kept constant as far as is possible. In this way, a map of the surface topography can be obtained[39]. Figure 2.2 shows a schematic of an AFM setup.

Vertical resolution in AFM is excellent, limited only by the vertical scanner movement precision, which is usually sub-Ångstrom, and noise from the surrounding environment. The lateral resolution depends upon the radius of the tip apex, with smaller tips being able to achieve better lateral resolution. In practice, tips with radii less than 10 – 20 nm

are used, and these can detect the existence of features smaller than this radius, although the relative error in the feature width will be large. It should be noted that the images collected must contain sufficient pixel densities to achieve this resolution, and that the tip can blunt or pick up debris during the scan, which will reduce the lateral resolution. Additionally, the tip shape can affect the vertical resolution, if gaps between structures are so narrow that the tip cannot penetrate to the bottom of the gap[39].
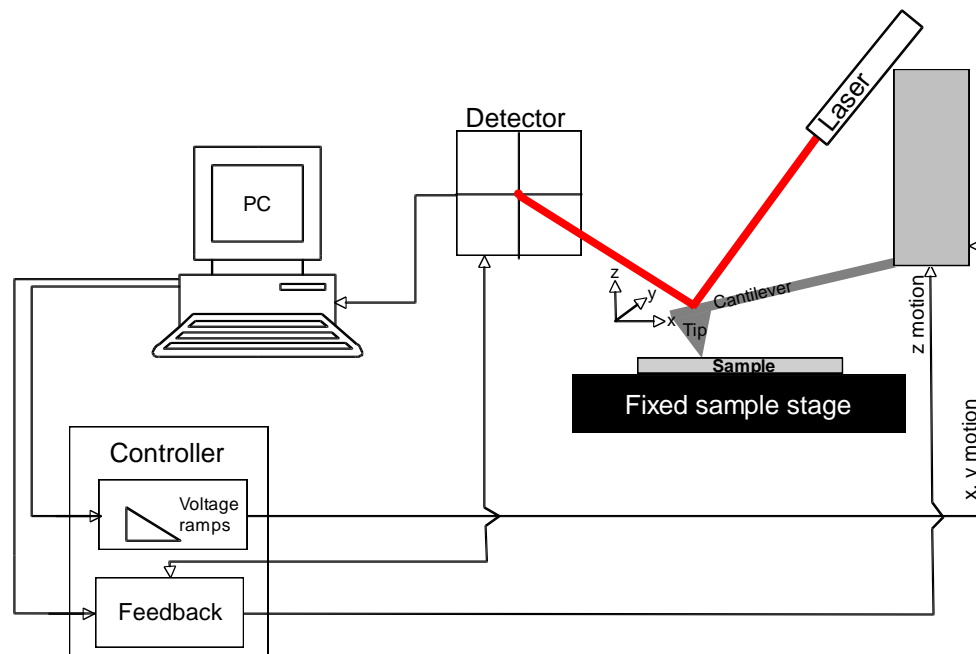
Figure 2.2. From Oliver[41], schematic of an AFM setup. The tip (at the end of a cantilever) is scanned across a sample. The cantilever deflection is measured with a laser, and a feedback system runs between the computer (PC) and the piezoelectric motor (x,y and z motion) to continuously adjust the height of the tip so that the amplitude of oscillation of the cantilever remains constant. The controller is used to manage the data.

2.2.2. KPFM

KPFM uses metal-coated tips to investigate the surface potential of a material. In KPFM, the tip initially scans the surface in TappingMode™ to record the changes in surface topography. The tip is then re-scanned along the same line, but at a small distance away from the surface (this is known as a lift scan), following the topographic contour from the first scan. During the lift scan, no mechanical vibration is applied to

the cantilever. Instead, a voltage of magnitude V_{ac} is applied, giving rise to an oscillating force as follows:

$$F = dC/dz \ (\Delta V_{dc} \ V_{ac})$$

where dC/dz is the tip-sample capacitance gradient and ΔV_{dc} is the difference in potential between the tip and the sample. The applied AC bias will vibrate the cantilever unless ΔV_{dc} is zero, in which case the surface potential and applied potential are the same. Therefore, by using a feedback circuit to adjust the potential applied to the tip so that the cantilever remains still, a map of the surface potential can be obtained[39]. In this work, KPFM scans were taken using Pt/Ir coated tips on the Veeco Dimension 3100 AFM.

As KPFM is based on a lift scan, it is important that the topographic scan has accurately tracked the surface, and that the sample or scanner has not drifted significantly between the two scans. Additionally, artefacts in KPFM measurements can be related to the topography of the sample surface. During the lift-scan, the tip-sample distance is assumed to be constant; however, the tip-sample capacitance gradient may depend on the topography. For instance, above a surface depression, the proportion of tip-surface area close to the surface may be increased[39]. In this work, attempts were made to evaluate KPFM data to assess the effect of topography-related artefacts.

2.3. TEM

The family of transmission electron microscopy (TEM) techniques is based on the elastic and inelastic interaction between high energy electrons (typically 100 – 400 keV, produced by either thermionic or field emission) and a sample that has been thinned to the point of electron transparency. A wide range of information can be obtained, including structural, compositional, and electronic properties of the sample. The following sections describe the method of TEM sample preparation used in this work, followed by the specific TEM-based methods employed to characterise our semiconductor samples.

2.3.1. TEM SAMPLE PREPARATION

TEM samples must be thin, first and foremost, to permit electron transparency, but also to minimise the problems arising from projection of the volume of the sample into a 2D image[42]. For the techniques used in this work, suitable thicknesses were in the range of 50 to 100 nm. Such thinning of the semiconductor wafers was realised using a complex and delicate process, which is not suitable for large areas. Cross-sectional TEM samples, therefore, can only assess about one part in 10^9 of the surface area of a typical 2 inch GaN wafer[43]. Although these images are often highly informative, properties deduced about the entire GaN film from such small sample areas can prove inaccurate if the film displays inhomogeneities. It can therefore be important to verify conclusions based on cross-sectional TEM using complementary characterisation techniques, where possible.

TEM samples of nitride epitaxial layers can fall into one of two categories, depending on their orientation: those made thin perpendicular to the growth direction are known as cross-sectional samples, and those thinned parallel to the growth direction are known as plan-view samples. All of the TEM samples prepared in this work were cross-sectional samples. These were prepared using a succession of steps, very similar to those used by Cherns[5]. The method can be described as follows: an area near the centre of a wafer was selected, avoiding the regions nearest the edge that are more likely to suffer from growth inhomogeneities. The wafers were cleaved into 3 mm × 3mm pieces with their edges parallel to the [11$\bar{2}$0] and [1$\bar{1}$00] directions, using a diamond scribe. If the sample needed to be investigated along both the [11$\bar{2}$0] and [1$\bar{1}$00] zone axes, the halves of the sandwich were rotated 90 degrees with respect to each other. This allows a range of crystallographic directions to be accessible in the TEM with minimal tilt. After cleaning the pieces in acetone and absolute ethanol, the two GaN faces were glued together with Araldite® epoxy to make a sandwich structure. The epoxy was set by heating to about 100 °C for 30 minutes.

The sandwich structure was manually ground to create parallel sides, after which it was mounted with wax on a South Bay Technology™ Tripod Polisher and the direction to be thinned was polished using diamond impregnated mats of 30 μm, 15, 6, 3, and 1 μm grain size. Water was flowed over the mats to remove debris and provide lubricant

during polishing. The wax was then dissolved with acetone, and the sandwich structure was cleaned in ethanol. Then the polished, mirror-smooth surface was glued with epoxy to a copper TEM grid. The sandwich structure, being still 2 mm or more in thickness, was then mounted on a stub with wax and manually ground using a Gatan Disc Grinder with progressively finer SiC discs (starting with P240 and finishing with P400) until the sample was approximately 50 μm thick. A Gatan Dimpler with a rotating brass wheel and 6 μm diamond paste was then used to create a dimple at the centre of the sample. The final thickness after these mechanical polishing steps was typically about 20 μm. The sample was then carefully removed from the stub by immersion in acetone, followed by washing with ethanol.

At this point, a Gatan precision ion polishing system (PIPS™) was used to mill the sample with argon ions until a hole appeared. The samples were milled with a beam energy of 5 keV and incident angles of ± 7 degrees. Double beam modulation was used to avoid milling the Cu grid. When a tiny hole appeared in the sample, the beam energy was reduced to 2.5 keV to finish the sample with limited ion milling damage. The regions adjacent to the hole are electron transparent, and the thickness of the sample can be estimated by white light interference fringes. Figure 2.3 shows a finished cross sectional TEM sample, in which the black fringe closest to the hole indicates the region where the thickness is approximately 100 nm (marked with red arrows).
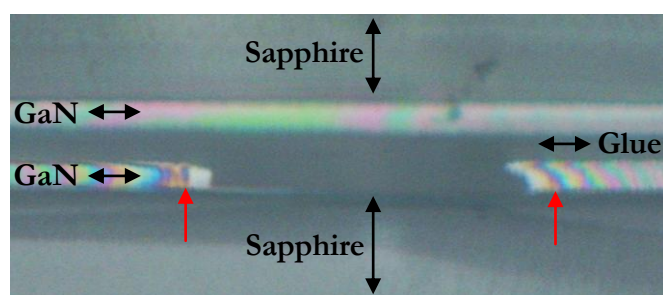
Figure 2.3. Optical micrograph of a cross-sectional TEM sample. The sapphire, glue and GaN layers are indicated, as is the black fringe closest to the hole (red arrow), at which point the thickness is approximately 100 nm.

The mechanical thinning and ion milling procedure undertaken to prepare cross-sectional TEM samples can create amorphous regions near the sample surface[44]. These regions are detrimental to TEM investigations focused on the properties of the crystalline material. To help remove this amorphous layer, some of the finished TEM samples were etched in a saturated solution of potassium hydroxide (KOH) at 60 °C for 60 s, followed by immersion in deionised water to prevent further etching, and cleaning in ethanol.

2.3.2. CONVENTIONAL TEM IMAGING

Conventional TEM makes use of electrons that are elastically scattered by Bragg diffraction as they pass through the sample. One or more of the diffracted beams can be selected in the back focal plane, by means of a suitably-sized objective aperture, to form an image[42]. If the transmitted beam is selected, by blocking the other beams with the objective aperture, then a bright field (BF) image is formed, as illustrated in figure 2.4a. In BF images, features in the sample that more strongly diffract the electron beam are darker. If the aperture is used to select a diffracted beam, then a dark field (DF) image is obtained. As illustrated in figure 2.4b, in practice the incident beam is tilted so that the diffracted beam travels down the optic axis, to avoid increasing problems with lens imperfections encountered if the image beam is far from the optic axis[42]. In DF images, strongly diffracting features such as defects are brighter than the surrounding material. Dark field images are identified by which diffraction spot, or which reciprocal lattice vector **g**, is used. In this work, BF and DF images have been used for basic imaging of sample structure and for defect analysis.
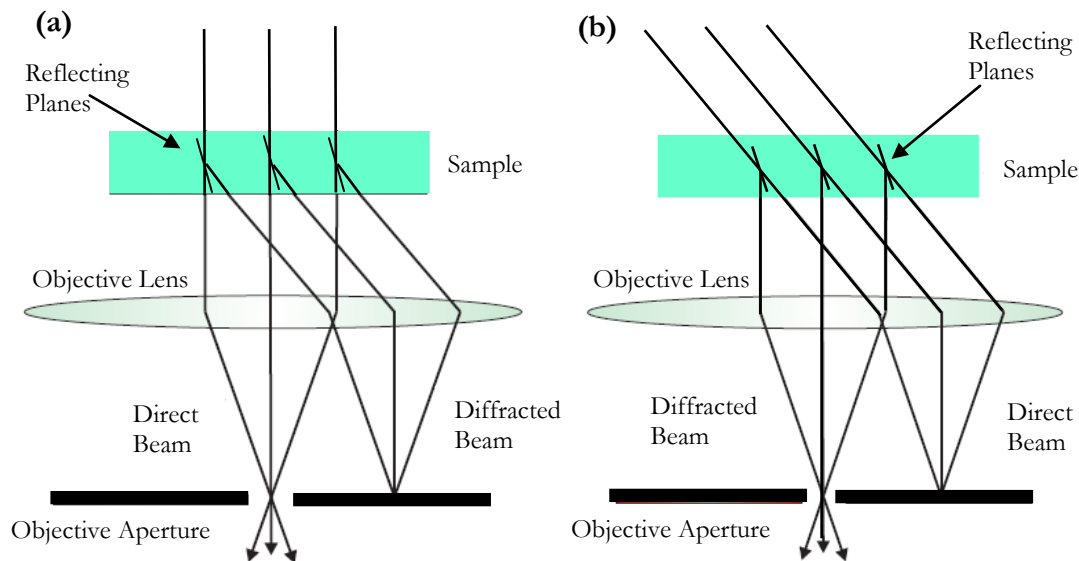
Figure 2.4. After Cherns[5], ray diagrams showing different configurations in the TEM to obtain (a) BF images, resulting from selection of the transmitted beam with the objective aperture. (b) DF images, resulting from selection of a diffracted beam. The incident beam is tilted so that the diffracted beam travels down the optic axis to minimise the effect of lens aberrations.

Although TDs can be observed in thin films using standard BF and DF imaging, an alternative technique is often used, called weak beam dark field (WBDF) imaging[45]. This technique involves the formation of a DF diffraction contrast image in which the useful information is given by the weakly excited beams[42]. Figure 2.5 illustrates the diffraction condition for the commonly used **g**-3**g** WBDF images, in which the image is formed from the diffracted beam **g**, while the 3**g** reflection is shown as at the Bragg condition. (In fact, in true WBDF images, the crystal is tilted slightly so that the 3**g** reflection is not precisely at the Bragg condition; hence no diffracted beam is strong, which avoids double peaks in the image.) As it is not at the Bragg condition, the diffracted beam **g** is weak; however, in strained regions of the specimen, such as around TD cores, the diffracting planes are bent back into the Bragg condition. This strain causes the TDs to appear as bright, narrow lines that are a few nm wide[42], much narrower than in standard DF images. Additionally, the positions of the lines are well defined with respect to the dislocation cores.
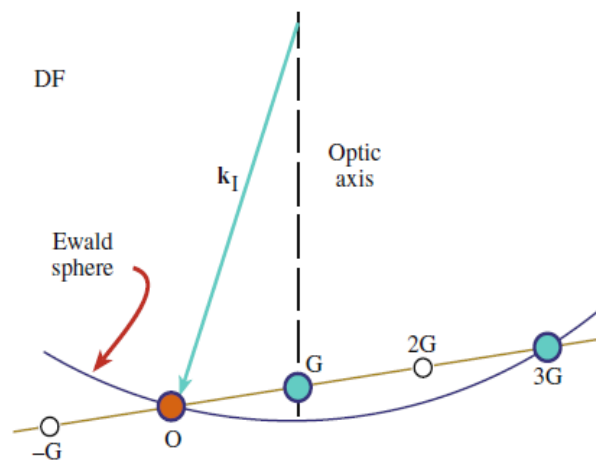
Figure 2.5. From Williams and Carter[42], representation of the g-3g WBDF condition using the Ewald sphere model, showing that g is tilted onto the optic axis to form the image, while the 3g reflection is shown as at the Bragg condition (although in true WBDF images, the crystal is tilted to ensure that the 3g reflection is slightly off axis).

As discussed in section 1.2, there are three types of perfect dislocations: edge, screw and mixed, each described by their Burgers vector, **b**. Contrast in WBDF images can be used to determine the character of these dislocations. Although the theory behind this technique is complicated[42] and will not be discussed here, its application is relatively simple: as in standard BF and DF images, pure screw dislocations are expected to be out of contrast, or invisible, when $\mathbf{g} \cdot \mathbf{b} = 0$, where **g** is the diffracted beam used to form the image. Pure edge dislocations will be invisible when $\mathbf{g} \cdot \mathbf{b} = 0$ and $\mathbf{g} \cdot \mathbf{b} \times \mathbf{u} = 0$, where **u** is the line vector of the TD. Thus, in GaN, when $\mathbf{g} = 0002$, only screw and mixed TDs will be visible, and when $\mathbf{g} = 11\bar{2}0$, only edge and mixed dislocations will show contrast[46].

The conventional TEM images taken in this work were obtained using either a Philips CM30 TEM operating at 300 keV with a LaB_6 source or an FEI Tecnai™ F20 G2 operating at 200 kV with a Schottky type field emission gun (FEG).

2.3.3. HIGH RESOLUTION IMAGING WITH ENERGY FILTERING

State of the art imaging with high resolution TEM (HRTEM) allows atomic columns to be resolved in most inorganic materials, enabling the investigation of atomic-scale microstructural defects[47]. The use of HRTEM in this work is limited to Chapter 5, where the technique is combined with energy filtering to produce lattice fringe images of pyramidal defects. Only the basic principles of both techniques will be provided in this section, with references provided to more comprehensive texts.

Lattice fringe images result from the interference between the direct beam and one or more beams diffracted within the sample[42,47]. Lattice fringes cannot be readily interpreted as a direct image of the structure due to contrast reversals that result when the defocus of the objective lens is changed, making it difficult to select the optimum objective defocus. Additionally, contrast reversals are also observed due to changes in specimen thickness. However, these images do contain useful structural information. In this work, HRTEM images were used simply to observe the contrast arising from defects in the material.

The HRTEM image contrast was enhanced using energy-filtered TEM (EFTEM), in which a filter was used to remove all of the inelastically scattered electrons (except those scattered by phonons)[48]. Energy filtering is carried out after the electrons have passed through the sample and all the lenses belonging to the TEM. The EFTEM system is comprised of an electron energy-loss (EEL) spectrometer, an energy filter and a charge-coupled device (CCD) camera, as illustrated in figure 2.6[48]. All HRTEM with energy filtering done in this work has been carried out on an FEI Tecnai™ F20 G2, which is fitted with a post-column Gatan Imaging Filter (GIF). The electron beam passes through the GIF entrance aperture and enters the spectrometer, where it is deflected through 90 degrees in a circular orbit by a magnetic field. Electrons that have lost energy, and therefore velocity, through inelastic collisions in the sample will move through a different orbit than electrons that have undergone only elastic collisions. Thus, electrons with different energies are spatially separated and focused at different positions, forming an EEL spectrum in the plane of the energy selecting slit. For

enhanced contrast, the slit is positioned to allow only electrons that have not lost energy to pass through. The transmitted electrons are refocused and the final image is recorded using the CCD camera.
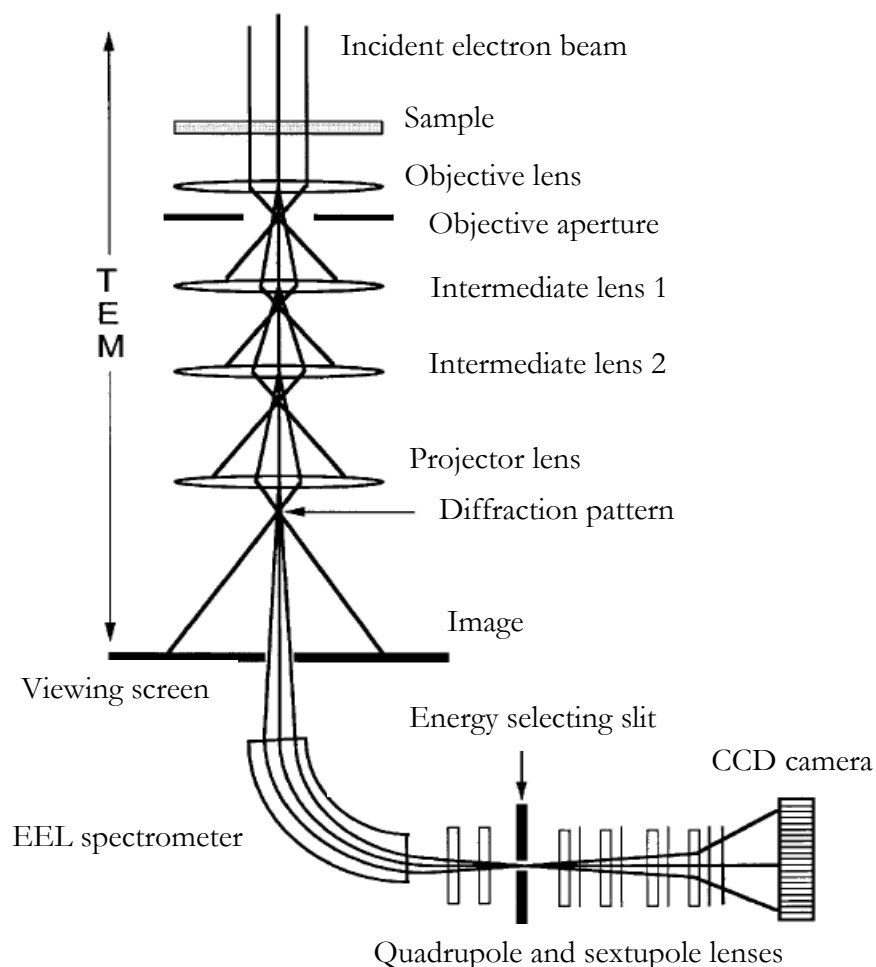
Figure 2.6. After Wang *et al.*[48], schematic of an EFTEM system. After passing through the sample and the TEM lenses, the electrons are dispersed according to their energies by a magnetic field in the EEL spectrometer. An energy selecting slit permits electrons with a certain range of energy losses to pass through, after which a set of lenses re-form the image, which is recorded with the CCD camera.

2.3.4. Z-CONTRAST IMAGING

In scanning TEM (STEM), the electron beam is focused to form an image of the source at the specimen in a tightly focused spot, or probe[49]. The probe can be rastered across the sample automatically by the microscope computer, using the scanning deflection coils, and an image can be formed by plotting the intensity as a function of probe position. Low angle scattered electrons are collected with a bright field detector or an EEL spectrometer. In 1979, Howie proposed that an annular detector with inner angle θ_i

greater than 40 mrad could be used to collect electrons scattered to higher angles, and that this scattering would be dominated by incoherent thermal diffuse scattering (TDS)[50]. The first STEM with a high angle annular dark field (HAADF) detector was built in Crewe's laboratory, and reported in 1980[51]. Figure 2.7 shows a schematic of a STEM-HAADF system.
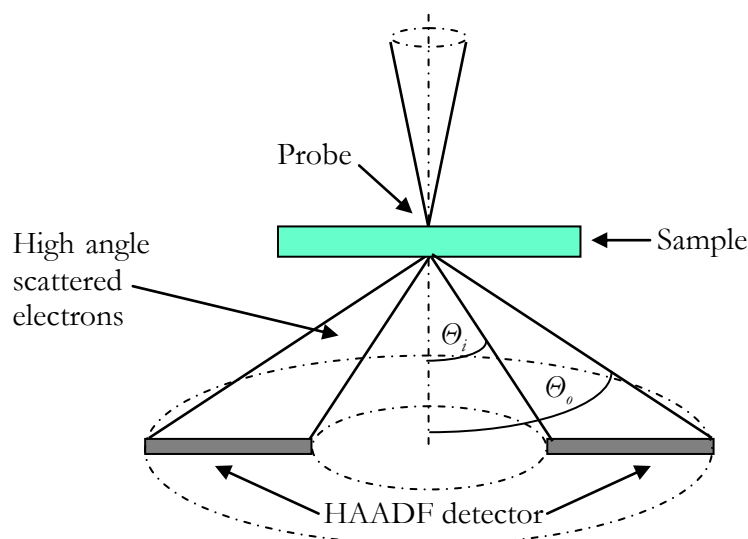
Figure 2.7. Schematic of the STEM-HAADF system configuration. The probe is rastered across the sample and high angle scattered electrons are collected by an annular detector with an inner collection angle θ_i and an outer collection angle θ_0. The intensity of the high angle elastic scattering incident on the ADF detector is approximately dependent on the square of the atomic number, Z^2, notionally providing directly interpretable chemical contrast in the resulting images (although the images do contain some strain contrast)[49]. In this work, STEM-HAADF has been used to study structures such as the InGaN QWs seen in figure 2.8, in which indium shows brighter contrast due to its higher atomic number. All STEM-HAADF was carried out using an FEI Tecnai™ F20 G2 instrument operating at 200 kV with a FEG electron source, in which the minimum probe size was approximately 2 nm.
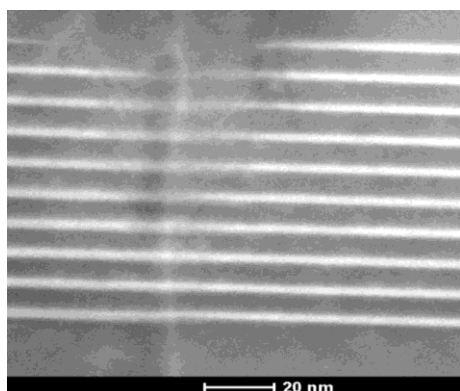
Figure 2.8. STEM-HAADF image of InGaN QWs, in which the QWs show brighter contrast due to the higher atomic number of indium.

2.3.5. COMPOSITIONAL MEASUREMENTS

In Chapter 5, pyramidal defects are observed using HRTEM with energy filtering, and two techniques are used in an attempt to observe their composition: the first makes use of EEL spectroscopy (EELS) in STEM mode, the second uses energy filtering to create a compositional map. Neither STEM-EELS nor EFTEM mapping proved successful at measuring the defects' composition, most probably because of the small defect size. These techniques will therefore only be introduced in brief.

In STEM-EELS, inelastically scattered electrons are accelerated through the EEL spectrometer, as described in section 2.3.3. For energy losses from 50 eV up to several thousand eV, the inelastic scattering events involve core electron orbitals on atom sites[49]. These inner-shell ionisations lead to core-loss edges, which can be observed in the EEL spectrum. With STEM-EELS, the probe can be positioned on a feature of interest and the spectrum that results can be analysed to obtain local compositional information.

Compositional information can also be obtained using EFTEM elemental mapping[52]. By adjusting the energy selecting slit to permit electrons of certain energy losses to pass through, elementally sensitive images can be obtained. A background subtraction is usually necessary, as the ionisation signal often sits on a strongly decreasing background signal. In this work, two methods of background subtraction were used: first, the jump ratio technique was used, in which an image recorded using electrons at the energy of the maximum of the ionisation peak is divided by an image recorded using electrons just before the peak. A ratio greater than one provides evidence of an ionisation peak at that energy. The second method used was the three-window mapping technique, in which two images are acquired using pre-peak energy windows and one image is acquired using electrons at the ionisation peak maximum. The two pre-peak images are used to obtain a fit for the background, which is extrapolated and subtracted from the intensity measured at the peak. Using either method of background subtraction, an elemental map can be obtained.

2.4. FIB/SEM

In this work, dual beam focused ion beam/scanning electron microscope (FIB/SEM) systems have been used extensively to prepare atom probe samples. The method of APT sample preparation will be described in section 2.5.2. First, the basic principles of the SEM and the FIB will be introduced.

2.4.1. SEM

The SEM uses a fine electron probe rastered across the sample, similar to that discussed in the section on STEM. In contrast to STEM, SEM imaging does not require electrons to be transmitted through the sample, but instead uses various signals generated from the beam-sample interaction, so there is no requirement for either high accelerating voltages or for the sample to be electron transparent. In fact, bulk samples can be examined with little to no sample preparation and a wide variety of materials can be examined in the SEM[53].

In an SEM, the fine electron probe is formed by an electron gun and a set of lenses, and scanned over the specimen, generating a variety of detectable signals, as illustrated in figure 2.9[54]. In modern SEM instruments, multiple imaging and analytical detectors can simultaneously collect these various signals. The electron signal used in this work was the secondary electron (SE) signal, produced when electrons from the primary beam transfer sufficient energy to an electron in the material for it to be ionised. If the SEs are generated close to the surface (within approximately 30 nm), then they can escape from the sample. The SE signal gives topographic contrast in part due to the dependence of the local SE yield on the tilt of the sample[54].
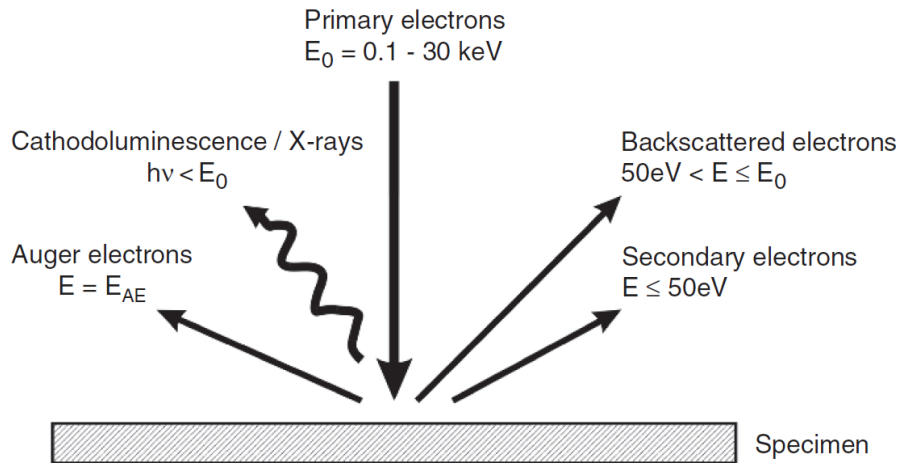
Figure 2.9. From Reichelt[54], a schematic of signals produced by the incident electron beam in the SEM.

The SE signal can be detected using an Everhart-Thornley detector[55] (ETD), which sits within the SEM chamber and consists of a Faraday cage that is positively biased to attract the SEs. Once attracted into the Faraday cage, the electrons are accelerated onto a scintillator held at a very high positive voltage, where they are converted to photons and recorded by a photomultiplier[56]. For better resolution, a Through The Lens (TTL) detector can be used, where the specimen sits very close the lower objective pole piece to minimise the effects of aberrations of the objective lens. The SEs spiral upward through the magnetic field within the bore of the objective lens and are then deflected off axis to be recorded by an ETD placed laterally above the lens[54]. Both types of SE detector have been used in this work.

The resolution of the SEM depends upon the sample volume from which the signal was generated. This volume is dependent on the type of signal used, the size of the probe, and the energy of the incident electrons. Higher energy incident electrons produce larger interaction volumes, usually resulting in lower spatial resolution due to the large volume sampled. The signal used can also affect the resolution: low energy SEs can only escape from the top few nanometers of the sample. In contrast, backscattered electrons (BSEs) (produced when an incident electron is scattered by an atom through such a high angle that it escapes the sample) have higher energies than SEs and can escape from depths of hundreds of nanometers. Figure 2.10 is a schematic[54] of the origin and escape depths of signals in the SEM. Although the BSE signal gives good compositional contrast because the high angle scattering is atomic number dependent, the BSE detector on the

FIB/SEM primarily used in this work did not function properly, and so only SEs were used for imaging.
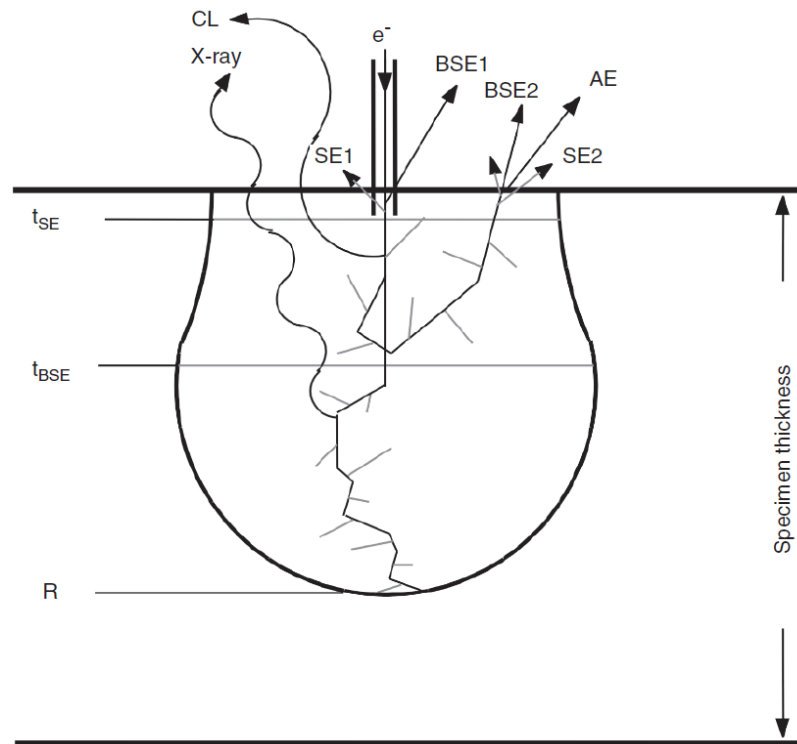
Figure 2.10. **From Reichelt[54], illustration of the origin and escape depth of the signals produced by the beam-sample interaction in the SEM: secondary electrons (SE) have an escape depth (t_{SE}) within a few nanometers of the surface, whereas back scattered electrons (BSE) can escape from depths of hundreds of nanometers (t_{BSE}). The electron range (R), and therefore the interaction volume, increases with increasing incident beam energy.**

2.4.2. FIB

The FIB is effectively a combination between a precision machining tool and a scanning ion microscope, similar to the SEM, but with a beam of Ga^+ ions[57]. The gallium ions are produced with a liquid-metal ion source, after which they are focused into a beam by an electric field, passed through apertures, and finally rastered across the surface of the sample. The accelerating voltage is typically 30 kV, although voltages down to 2 kV can often be accessed. Just as in the SEM, the ion beam-sample interaction produces a variety of signals, including SEs that can be used for imaging. In fact, FIB and SEM instruments have so many complementary features and uses that they have been

produced as a dual beam FIB/SEM, in which the techniques can be used in parallel and tasks can be achieved that are beyond the limitations of either individual system[57].

The use of gallium ions in the FIB, rather than electrons, gives the technique functionality and applicability distinct from the SEM. When the focused gallium beam hits the sample, the high momentum, relatively heavy ions collide with the atoms at the surface, causing a small amount of material to be sputtered. This milling capability can be harnessed for precise modification of the material surface, with FIB instruments allowing for control of the sputter rate, location and depth. In this work, FIB milling of samples was monitored using SEM imaging because the electron beam causes little appreciable damage to the sample, compared with imaging using the gallium beam.

The versatility of the FIB can be demonstrated by its ability to deposit material as readily as it can mill, as illustrated in figure 2.11[57]. The addition of a gas delivery system is all that is needed to realise this change in function. The gas, usually a metal-organic compound, is cracked at the sample surface using the gallium beam, resulting in the heavy metal atoms remaining on the surface as the organic material is removed by the FIB vacuum system. Metals such as Pt can be deposited in this way, although it is important to note that this ion beam deposited 'platinum' in fact contains approximately half Pt and half impurities including carbon, oxygen and gallium[57]. This 'platinum' is effectively semi-insulating, and is suitable either as 'glue' to attach one piece of material to another, or as a protective layer.
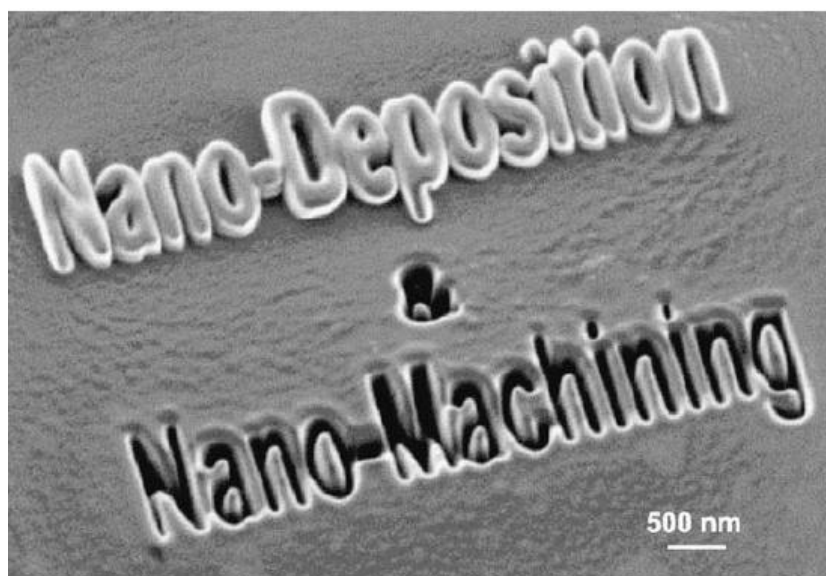
Figure 2.11. From Yao[57], an illustration of the deposition and milling capabilities of the FIB.

It would be remiss to omit the significant drawback of the FIB milling technique: the detrimental effects of beam-induced damage. Bombardment of the sample with the gallium beam results in some level of gallium implantation, and can cause the formation of an amorphous layer. Some of this damage can be removed with low energy milling[58] at 5 kV. Section 7.2.3 will discuss the topic of FIB damage in greater detail.

The dual beam FIB/SEM instruments used in this work were the FEI Company™ Nova NanoLab™ and the FEI Company™ Helios Nanolab™. Both were equipped with an Omniprobe Autoprobe™ micromanipulator to enable the movement of samples within the chamber.

2.5. APT

Chapter 1 provided a brief history of the atom probe tomography (APT) technique and an introduction to its capabilities. The local electrode atom probe (LEAP) instrument represents the state of the art in APT, and has been used throughout this work. The following sections will focus on the LEAP, first providing an overview of the technique. Next, APT samples will be discussed, including the requirements for their geometry and the method of sample preparation in the FIB. More detail will then be given regarding ion evaporation and detection in the LEAP, followed by discussion about how ions are chemically identified and spatially mapped to their original locations. The section will conclude with an overview of APT data reconstruction using the Imago Visualization and Analysis Software (IVAS).

2.5.1. LEAP OVERVIEW

The development of the LEAP instrument has transformed the field of atom probe tomography, allowing much larger volumes to be accessed in a fraction of the time, compared with previous instruments[26]. The LEAP produces 3D compositional images at the atomic scale by the controlled evaporation of atoms as ions from a tiny, needle-shaped sample held at a very high voltage in a vacuum chamber[59]. A schematic[60] of the LEAP can be seen in figure 2.12. A high voltage is applied to the sample, which creates a strong electric field that is concentrated at the sharp tip of the sample. This field should be just below the evaporation field of the material, so that the extra energy needed to field evaporate an ion can be supplied in a controlled manner. With high conductivity

samples ($>10^2$ S/cm), this extra energy can be supplied with a voltage pulse to the local electrode[61], which brings the field at the tip above the threshold for field evaporation at that temperature. Voltage pulsing cannot be used with low conductivity samples, such as semiconductors. However, such samples can be analysed using the technique of laser pulsed APT[62], in which a laser pulse hits the sample apex to induce a brief temperature spike. The evaporation field drops as the temperature is raised, enabling field evaporation.
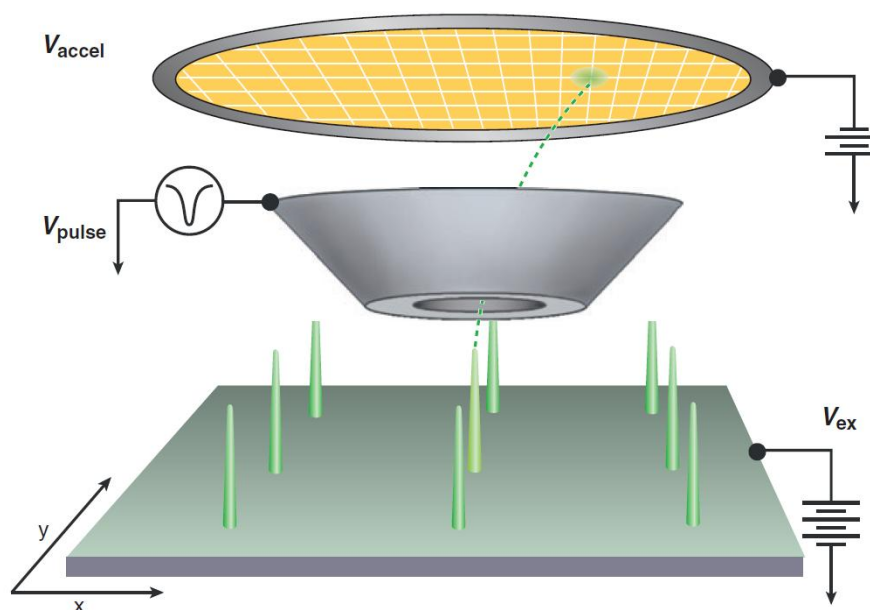
Figure 2.12. From Seidman[60], schematic of the LEAP with an array of samples. A positive potential, V_{ex}, is applied to the APT sample and controlled field evaporation is induced with either a voltage pulse to the local electrode (V_{pulse}) or a laser pulse to the sample tip. The evaporated ion is accelerated through the local electrode and to the detector.

The evaporated ion is then accelerated through an electric field to a detector, where the signal is amplified, and information about the ion's chemical identity and original position is collected. These capabilities will be discussed in later sections, but first the samples required for APT are discussed, for good quality sample preparation is the key to a successful APT experiment.

2.5.2. APT SAMPLES

With increased data collection and analysis rates possible with the LEAP, preparation of samples with the specific requirements for APT studies has become a bottleneck in the

process. The samples must be needle shaped, gradually tapering to a tip with a radius of less than 100 nm, to ensure that the field is sufficient at the tip apex for field evaporation[24]. Metal samples can be prepared by a relatively straightforward electropolishing technique. To access a wider variety of materials, including semiconductors, FIB-based techniques have been developed for bulk or site-specific APT sample preparation[63]. The FIB-based sample preparation method best suited to semiconductor wafers is known as 'liftout and annular milling', and has recently been described by Thompson *et al.*[64]. Galtrey[65] was the first to use a similar liftout technique with GaN on sapphire, making note of the peculiarities of the material system, such as the propensity for material redeposition during milling steps. The liftout and annular milling technique has been used throughout this work to prepare APT samples using a dual beam FIB/SEM.

Prior to sample preparation in the FIB/SEM, the semiconductor wafer was cleaned and sputter coated with a thin layer of platinum (less than 100 nm). The sputter coating functions to provide contrast at the location of the surface in cross-sectional SEM imaging. Once the wafer was in the FIB/SEM, the area desired for liftout was first protected by depositing approximately 100 nm of platinum with the ion beam (known as FIB-Pt), as the ion beam milling can damage the sample[24]. Next, a portion of semiconductor material was lifted out, leaving the sapphire substrate behind. It should be noted that milling into the sapphire ought to be avoided, as the sapphire redeposits extensively[65]. This liftout was achieved by milling two trenches in the wafer that meet to produce a wedge-shaped membrane of approximately 3 μm in thickness and up to 30 μm in length. In this work, the trenches were milled at a stage tilt of 22 degrees, resulting in a wedge with an equilateral triangular cross-section.

After the wedge was milled, one side was cut free and a micromanipulator needle was brought into contact and attached using FIB-Pt glue. The remaining side of the wedge was then milled to free it from the wafer, leaving the membrane attached to only the micromanipulator. Figure 2.13 shows a sample membrane being lifted out from the wafer by the micromanipulator. The wedge was then transported within the FIB/SEM chamber to a sample mount. Two different sample mounts were used in this work: first, for samples only studied by APT, etched silicon microtip sample mounts were used. These microtips were produced by Imago Scientific Instruments on silicon coupons,

each containing an array of 36 microtips. With the local electrode geometry, it is possible to analyse samples that are on adjacent microtips. Figure 2.14 shows a sample on the micromanipulator needle prior to mounting on a silicon microtip, showing the FIB-Pt gas injection system (GIS) on the left and the adjacent microtips. The sample was attached to the microtip with FIB-Pt and then cut free from the micromanipulator. This process can be repeated to allow one liftout wedge to be mounted onto multiple microtips. Figure 2.15 shows the wedge once it was attached to the micromanipulator using FIB-Pt glue.
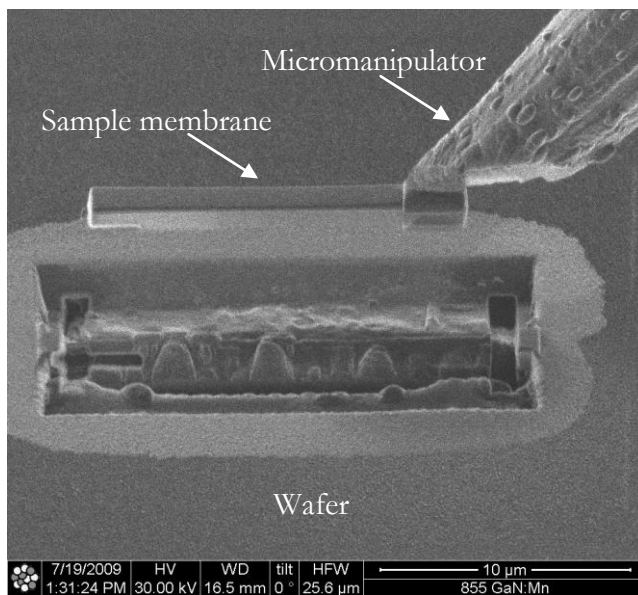
Figure 2.13. Image taken using SEs generated by the ion beam in the FIB/SEM (ion beam image), showing a sample membrane attached with FIB-Pt to a micromanipulator needle. The membrane is being lifted out, to be transported to the sample mount.
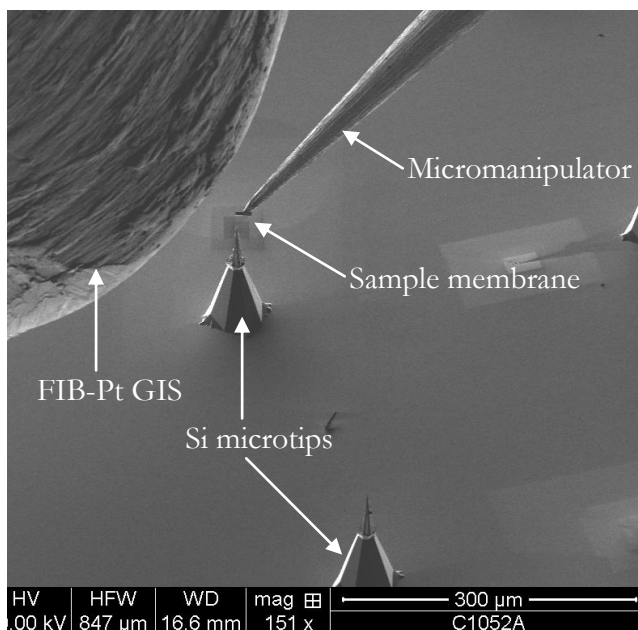
Figure 2.14. Ion beam image, showing a sample membrane mounted on a micromanipulator needle above a Si microtip array. The FIB-Pt GIS needle shown on the left supplies the metal-organic gas required for the FIB-Pt glue.
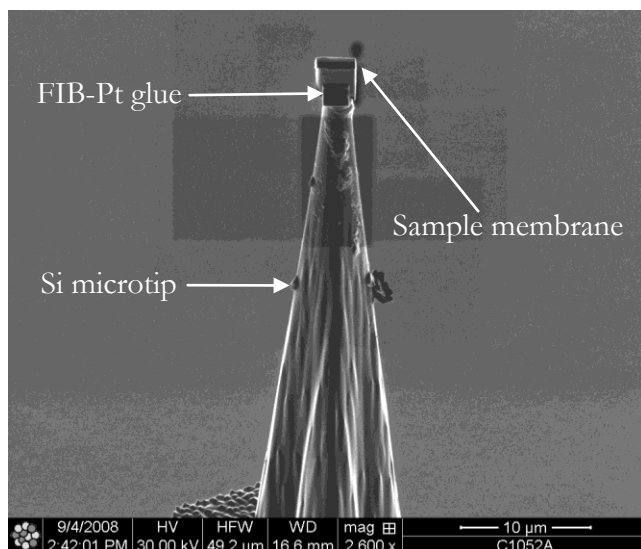
Figure 2.15. Ion beam image of the sample membrane mounted on the Si microtip with FIB-Pt glue.

For those samples that were analysed by both APT and TEM, a different sample mount was required. This was comprised of an electropolished tungsten wire in a copper tube, and designed to fit into both the LEAP and the TEM using a Fischione Model 2050 on-axis rotation tomography holder. The tungsten wire (outer diameter 0.125 mm) was electropolished in the Department of Materials at Oxford University, with the assistance of Dr. David Saxey. With the sharp end of the wire free for sample mounting, the blunt end was fitted into a copper tube (Goodfellows, outer diameter 1 mm, inner diameter 0.3 mm). The fit was tight, so crimping of the copper tube was both unnecessary and avoided, as crimping may have caused the sample to tilt off-axis - an unsatisfactory geometry for our TEM experiments. Prior to mounting the sample on the copper/tungsten (Cu/W) sample mount, the electropolished end of the tungsten needle was milled with the ion beam to create a flat platform of a similar size to those on the microtips. Figure 2.16 shows a wedge mounted onto the tungsten needle of a Cu/W sample mount.
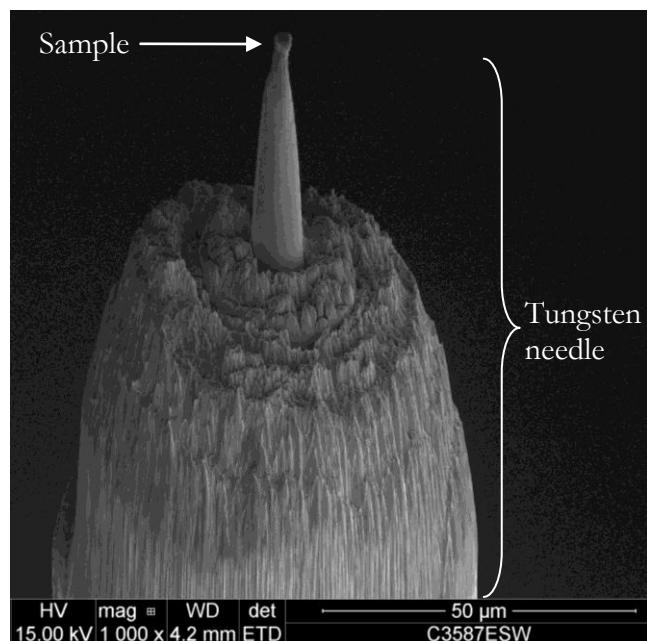
Figure 2.16. Image taken using SEs generated by the electron beam in the FIB/SEM (electron beam image), showing a sample wedge mounted onto a tungsten needle (part of the Cu/W sample mount).

Once the sample membrane was attached to a suitable mount, the sample was sharpened into a needle using annular milling: with the sample tilted so that the ion beam was parallel to the long axis of the sample, the beam was rastered in a spiral pattern that defined an annulus. Three annular milling steps were carried out, all using a 30 keV ion beam. The first used an outer radius greater than the sample width, and an inner radius of approximately 1 μm. In the second and third annular milling steps, the inner radius was made smaller, first to 400 nm and then to 250 nm, and the ion beam current was also decreased in steps, to minimise the gallium beam damage. As a final step, to both remove damaged layers and to sharpen the APT sample, a 'low keV cleanup' step was used, in which a 5 keV ion beam is used to mill the entire sample[58]. This step was continued for at least 30 s, but may be prolonged, if the region of interest is located far below the surface in the semiconductor sample. Further discussion of Ga beam damage, and low energy cleanup to remove damaged material will be presented in Chapter 7. A finished APT sample is shown in figure 2.17. It is important to mill away any 'parasitic tips', which are any sharp tips within approximately 15 μm of the end of the sample, as these could be the source of undesired evaporation in the LEAP.
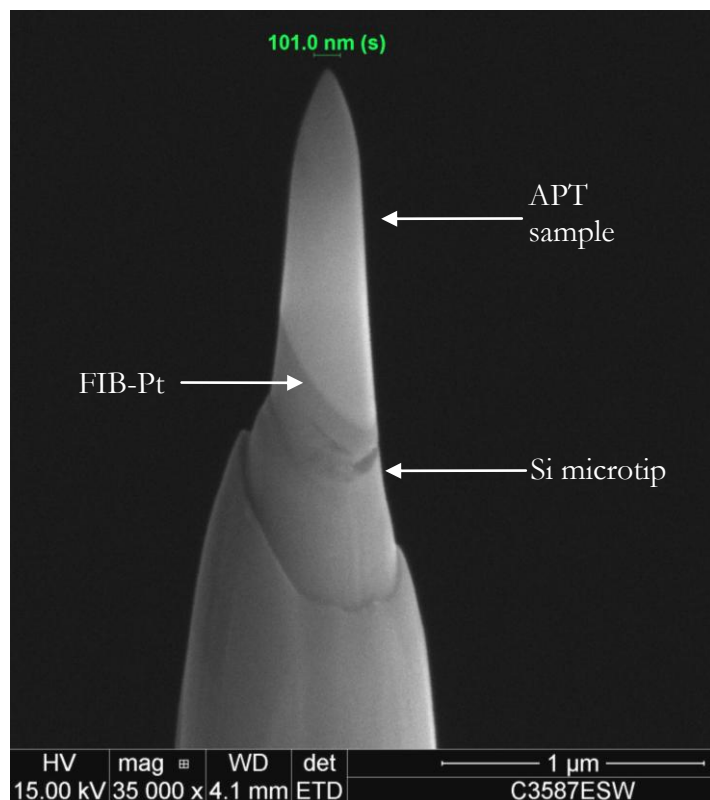
Figure 2.17. Electron beam image of a finished APT sample, after low keV cleanup. The final tip radius is significantly smaller than the 100 nm scale bar.

APT samples are notoriously delicate and many fracture in the LEAP before any useful data is collected. The fracture is often due to the attractive force between the oppositely charged tip and local electrode, causing stresses in the tip[66] of up to 10 GPa. By optimising the sample preparation to produce robust samples, however, the proportion of useful samples can be maximised. APT samples with sharp tips begin field evaporating at a lower applied DC voltage than blunt samples, which is advantageous because there is an upper limit on the DC voltage of about 15 kV (although in practice the voltage is usually limited by the local electrode, which often begins to emit at about 11 kV). The entire sample should not be sharp, however, because a wide base gives better mechanical stability. Thus, conical shaped samples with good sample/FIB-Pt/mount bonds tend to be the most successful.

2.5.3. ION EVAPORATION

In theory, field evaporation can be modeled in a straightforward way by assuming that the sample has a hemispherical end radius, and that there is a unique relationship between a point on the sample and a point on the detector. Although these models are incredibly useful, there are some problems associated with the assumptions, and some steps that can be taken to correct the errors that arise. These issues of ion evaporation will be discussed in this section.

The shape of an APT tip is modeled as roughly hemispherical. This model can be used to find the field, F, at the apex of a sample with end radius, r, resulting from an applied standing voltage, V, as follows:

$$F = V \, / \, k_f \, r$$

The geometric factor, k_f, represents the deviation from a free sphere, and depends on the sample shank angle[67]. The true tip shape may deviate from this model, being either flatter or sharper. Where the tip is locally sharper, the field will be enhanced, leading to increased evaporation. This leads to reshaping of the tip in the initial stages of evaporation (during sample 'turn-on'), in which the end shape becomes more regular. Data collected during this period is of poor quality, and is generally excluded from data analysis. As the sample runs and material is removed, the tip blunts, causing the end radius to increase. To retain the same field (monitored by the instrument as retaining a constant detection rate, defined as the fraction of pulses that result in a detected ion) the standing voltage is automatically increased, up to the limits of the instrumentation, or when the sample fractures. This limit defines the depth that can be analysed in an APT sample, which is rarely greater than 1 μm.

Trajectory aberrations can occur in multiphase materials when the evaporation fields of the two materials differ. In the case where there are precipitates with a high evaporation field in a matrix with a low evaporation field, evaporation of the matrix will occur, but the field will not be high enough to cause evaporation of the precipitate atoms. This will eventually cause the precipitates to protrude from the surface of the sample, creating a locally enhanced field. When the field builds up to the point that the precipitate is evaporated, the trajectories of the ions will result in the precipitate having a much higher magnification[67]. There is little that can be done about such trajectory aberrations in the data collection, and compensation in the reconstruction is not yet mundane. In this work, where such aberrations are likely, this will be noted, and an attempt made to elucidate their effect on the data.

Finally, it is important to note that ions can leave at very slightly different times during the laser pulse. This 'time of departure spread' will cause the ion's time of flight to deviate slightly from that expected for an ion of its type, reducing the mass resolution.

To mitigate this problem, a longer flight time can be used, which improves the mass resolution. One way of increasing the flight time is to use an electrostatic compensating lens, or a reflectron[68]. The reflectron is located between the sample and the detector and lengthens the flight path of the ions by deflecting them through an angle of approximately 156 degrees using a biased 3D metallic mesh. In this work, all but one of the APT data sets were collected on a LEAP equipped with a reflectron. More details of the LEAP specifications and run conditions will be provided in each chapter.

2.5.4. ION DETECTION

Ion detection in the LEAP is based on a micro-channel plate (MCP), which is made up of many cylindrical lead-doped glass channels, of aspect ratio near 40, sandwiched between a pair of electrodes. This design creates an electric field along each one of the channels. When an ion hits the wall of the channel, a secondary electron is produced, which leads to a cascade of up to 1,000 SEs as they ricochet and multiply down the length of the channel. This gain is independent of the ion type for all elements when the standing voltage is above 3 kV, which is below the normal standing voltage for data collection. A chevron of two MCPs is used, with plate tilts of +8 and -8 degrees, respectively. Using two MCPs prevents saturation of the electron cascade, thereby leading to higher gain. If ions strike the detector between the channels, they will not generate a SE cascade, and the ion will not be recorded. Although this happens with around 40 percent of the ions, there is no partiality as to which ions are stopped.

In the LEAP, the anode at the back of the MCP is a delay line detector (DLD)[24]. This detector features two delay lines perpendicular to each other, and a third running diagonally. When the electrons from the MCP strike the delay line at some location, they travel to each end of the line. The arrival times are measured at each end, and these times are converted into the true x and y positions on the detector, allowing the position of the ion's impact to be determined. With three delay lines, two ions can strike the detector at the same time, and they only need be separated by 5 ns in the time taken to travel to the end of the delay line for their positions to be resolved[24].

As mentioned previously, the standing voltage is optimised to ensure a constant detection rate. This rate is held low, in the vicinity of one percent, which represents one

ion detected for every 100 laser pulses. This low rate is maintained to minimise the chance of two or more ions striking the detector at once.

2.5.5. CHEMICAL IDENTIFICATION

APT uses time of flight mass spectrometry to determine the chemical identity of the ions that strike the detector. This technique measures the ion's time of flight from the tip to the detector, using the fact that ions with larger mass-to-charge ratios will be accelerated less by the same electric field than those with smaller mass-to-charge ratios. For example, singly charged gallium will have a time of flight that is more than twice as long as singly charged nitrogen. As the evaporation event is triggered by the laser pulse, which is applied with a nanosecond duration, the pulse provides a starting time for the ion flight. The ion impact at the detector is recorded as the end of the flight time.

The potential energy of an atom on the surface (neV) is converted into kinetic energy ($\frac{1}{2}mv^2$) when the ion leaves the specimen. Here, n is the charge state of the ion, e is the charge on an electron, V is the voltage difference between the sample and the detector, m is the atomic mass, and v is the velocity of the ion, which can be written as the sample-detector distance over the flight time taken, d/t. Balancing the two energies[24], it can be shown that the mass-to-charge ratio can be determined by the time of flight, given a known DC voltage and tip-detector distance:

$$m/n = 2eV\ (t^2/d^2)$$

The detected ions can be represented by a histogram of the ion counts across a spectrum of mass-to-charge state ratios, usually referred to as a mass spectrum, as shown in figure 2.18. The peaks are manually assigned ion types, as indicated by the coloured ranges. Two features of the mass spectrum are worth noting: first, the peaks can be very closely spaced, making it difficult to resolve them. As previously discussed, the LEAP system equipped with a reflectron has a longer flight path and can therefore give a mass resolution, $\Delta m/m$, of up to 1/2000 (where Δm is the full-width at half maximum value using a peak at, or close to, a mass-to-charge state ratio of 27), whereas without the reflectron the mass resolution can be 1/200. Both mass resolutions are sufficient to distinguish ions of adjacent atomic number. The second feature of note is that the peaks show tails leading to higher mass-to-charge ratios. These tails usually correspond to ions evaporating soon after the laser pulses, as the specimen temperature is still returning to

its base level. They can be minimised by changing run conditions, such as lowering the laser power (laser energy per pulse). It should be noted, however, that the mass spectrum in figure 2.18 is shown with a logarithmic scale, and the peak tails contribute little to the overall signal. Other noise in the mass spectrum will arise due to electronic noise in the instrument and evaporation of contamination ions adsorbed onto the sample, but this noise is usually observed at very low levels.
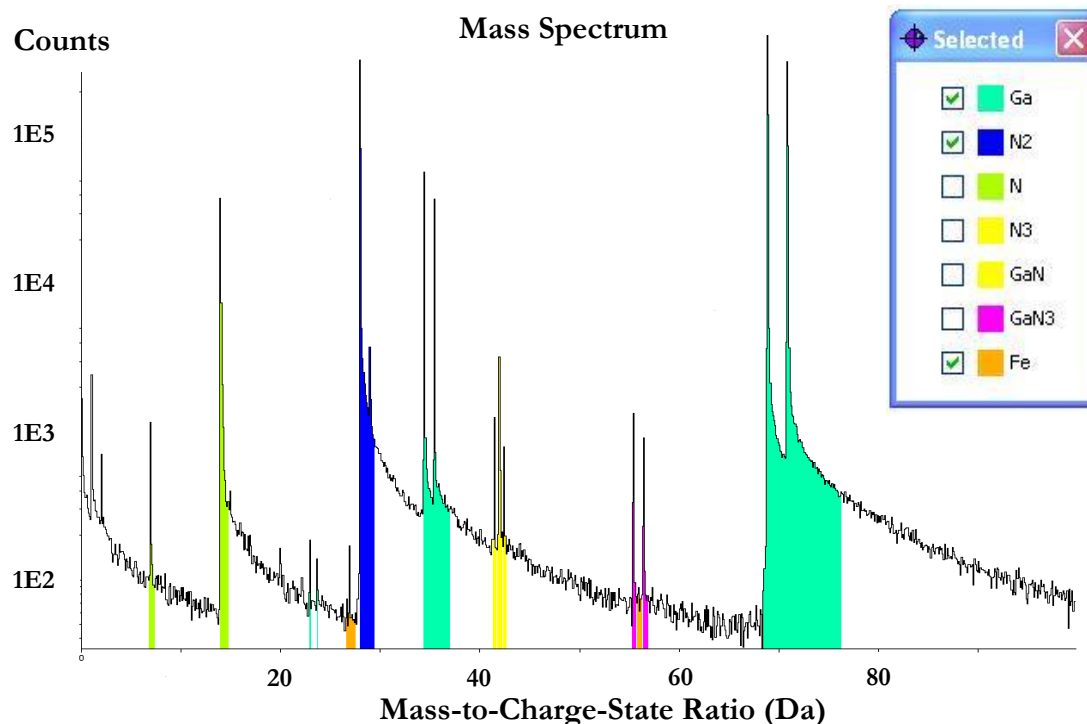
Figure 2.18. Mass spectrum of an iron-containing GaN sample studied with the LEAP. The coloured ranges have been manually applied to assign ion types to the peaks observed.

To demonstrate typical mass spectra collected in this work, Appendix 1 shows an experimentally obtained spectrum from a GaN sample and one from an InAlN sample.

2.5.6. SPATIAL INFORMATION AND RESOLUTION

Although the chemical identity of the ion is determined from its time of flight, its original location in the sample must also be found. This 3D spatial information can be determined with a combination of the x and y hit position on the detector and the hit sequence.

As previously discussed, there is ideally a one-to-one correspondence between each point on the surface of the sample and a point on the detector. The trajectory from the sample

to the detector would be a straight line if the sample were a free sphere. In reality, the ions bend inwards as they move towards the detector. This reduces the magnification, η, by a factor known as the image compression factor (ICF), ξ. The magnification can therefore be defined as follows:

$$\eta = d/r\xi$$

The sample-detector distance is d, and r is the tip radius[67]. The magnification that results is approximately one million times. Using this model, the x and y positions on the detector can be used to map the ion to its x,y position in the sample. To determine the z position, the model supposes that each evaporated ion lowers the surface by a depth defined as a shell of the tip radius that has a volume equal to the volume of the ion[69]. Scaling in the z-direction is determined using both the detection efficiency, which gives the depth of material evaporated for a given number of detected ions (and lateral field of view), and the atomic density of the material.

After supposedly determining the exact 3D position of each ion collected, any knowledgeable microscopist would ask, 'What is the resolution of this technique?'. Gault *et al.*[69] recently discussed the meaning and quantification of resolution in APT, where the idea of resolution differs from conventional techniques that are based on diffraction of radiation. In these diffraction-based techniques, the resolution is defined by the smallest distance between features that can be resolved, such as adjacent atoms. With APT, adjacent atoms will almost certainly both be detected separately, and so by this definition the resolution is sub-Ångstrom. However trajectory aberrations like those in multiphase materials discussed previously can introduce errors into the 3D position, as can any lateral movement of atoms on the sample surface. Lateral movement is minimised by holding the sample at low temperature during evaporation[69]. Temperatures as low as 20 K are used, although very low temperatures can cause the sample to fracture more easily. With low temperature evaporation, and in regions that do not suffer significant trajectory aberrations, the lateral resolution[60] of APT data can be 0.3 to 0.5 nm. The depth resolution is even better than in x and y, with z-resolution[60] down to 0.1 nm.

2.5.7. APT DATA RECONSTRUCTION

Raw APT data must be reconstructed before it can be analysed. The reconstruction process was carried out using the IVAS software produced by Imago Scientific instruments, in which raw data is converted into a 3D atom map.

To satisfactorily reconstruct the data, a number of parameters must be defined. These include parameters of the material (atomic density), of the APT sample (shank angle), and of the LEAP itself, such as the detection efficiency, ICF, and sample-detector distance. In practice, many of these parameters are difficult to determine, so standard values are used, and the reconstruction is optimised by tuning parameters such as the evaporation field of the material to reproduce known features of the sample. These features include the spacing between MQWs, as determined by X-ray diffraction, or the fact that the wells are flat, as determined by TEM.

A key user-defined step of the reconstruction process is the ranging of the mass spectrum. As shown in figure 2.18, ranges are defined which include the mass spectrum peaks, and these ranges are assigned identities, such as Ga, In or N_2 (such compound ions can often be evaporated). Correct identification and assignment of peaks must be achieved to produce accurate data. Ranging and identification can be difficult when two ions with the same mass-to-charge ratio are both present: for instance, N_2^+ and Si^+ both have peaks at 28 mass-to-charge ratio. For Si-doped GaN, this can make quantification of the dopant level impossible.

With the mass spectrum ranges and the reconstruction parameters defined, IVAS then produces a 3D atom map of the APT data. This data can then be analysed in a number of different ways, which will be explored in later chapters.

3

AFM AND TEM STUDIES OF THREADING DISLOCATIONS

3.1. AIMS

Electronic and optoelectronic devices based on heteroepitaxially-grown GaN have achieved success despite having a high density of TDs. Although the origin of these TDs is debated, they have been shown to have negative effects on devices, such as reducing the lifetime of laser diodes[70], and increasing leakage currents in blue and green LEDs[71]. Thus, many methods for TD density reduction have been developed to improve the performance of such devices. To evaluate these TD reduction techniques, a variety of methods can be used to quantify the TD density, including AFM, TEM and cathodoluminescence (CL); however these vary in time intensity of sample preparation, area measured, and ability to resolve closely spaced TDs.

Some dislocation reduction techniques introduce a further complication to measuring the TD density: the method results in a non-uniform distribution of dislocations. One such technique is epitaxial lateral overgrowth (ELOG) (described in detail in section 3.2.4), which results in areas of greatly differing TD density over typical length scales of 10 μm

or greater. To measure the dislocation density and distribution in such samples, a technique which accesses large areas must be employed.

3.1.1. BROAD AREA AFM

The first aim of this chapter was to use AFM to image an ELOG sample over broad areas with high resolution. If such images could be obtained, the next aim was to evaluate a program called PITS, written by Dr. David Holec, which automatically identifies TD pits in an AFM image, and could greatly reduce the effort needed to find the dislocation density, compared with manual counting.

3.1.2. SURFACE POTENTIAL

Our next aim was to determine what effect, if any, the TDs had on the surface potential in the ELOG sample. Motivating this study is the charged dislocations model (discussed in section 3.2.2.2), which suggests that TDs may interact with charge carriers in devices because they themselves are charged. Using KPFM, as described in section 2.2.2, we hoped to study the effect that the TDs had on the surrounding surface potential. We aimed to quantify this effect by extracting the surface potential value at each TD pit, thereby finding the change in surface potential associated with the presence of dislocations.

3.2. BACKGROUND

The characterisation of TDs in GaN-based materials forms a large part of this and other chapters of this work. Therefore, some necessary background is presented here on the origin and effect of TDs, followed by some ways in which TD densities can be measured experimentally. The key TD density reduction technique used in this chapter, ELOG, is then introduced.

3.2.1. ORIGIN OF TDS

There has been much debate surrounding the origin of TDs in GaN-based devices grown on sapphire. It has been suggested that TDs are generated where GaN islands coalesce during early stages of film growth[72]. Although the island coalescence model is often cited in the literature, and has been supported by experimental work[73,74] others have challenged its validity[75,76,77,78]. This debate will be examined in the following sections.

3.2.1.1. Island coalescence theory

The theory of TD generation at island coalescence boundaries was developed with information gleaned from TEM studies of fully coalesced GaN wafers. Using a variety of cross-sectional and plan-view TEM micrographs, Ning *et al.*[72] created a model for TD generation where slightly misoriented GaN islands grow together. Where the islands coalesce with slightly differing tilt or twist relative to the sapphire substrate, TDs are generated. Ning *et al.*[72] propose that edge dislocations are formed at the coalescence of islands of differing twist (defined as a rotation about the [0001] axis), and screw dislocations are formed at the coalescence of islands of differing tilt (defined as a rotation about an axis perpendicular to [0001]). Mixed dislocations, which show both edge and screw character, form as a result of islands both tilted and twisted with respect to each other. Figure 3.1 illustrates the model, showing an edge dislocation resulting from coalescence of twisted islands.
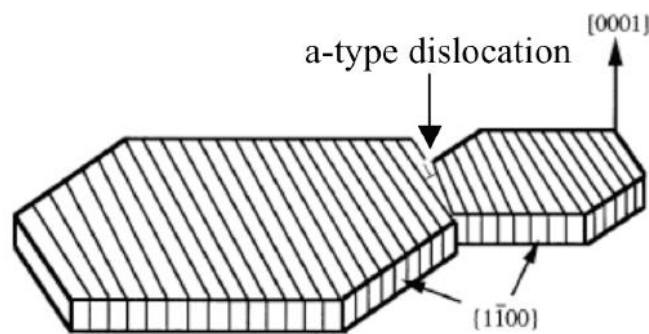
Figure 3.1. From Ning *et al.*[72], a schematic diagram illustrating the coalescence of GaN islands that are rotated around the [0001] axis with respect to each other, resulting in an edge, or 'a-type' dislocation at the boundary.

Work by Wu *et al.*[73] supported the theory of TD generation at island coalescence boundaries. WBDF TEM images were used to suggest that edge dislocations were localised at the island boundaries, as shown in figure 3.2a (with $g = 11\bar{2}0$, edge and mixed TDs visible). In this image of a fully coalesced film, Wu *et al.*[73] suggest that the two regions of high dislocation density are coalescence boundaries. These same regions were also studied with an imaging condition that highlights screw and mixed TDs ($g = 0002$), as seen in figure 3.2b. The authors attributed the presence of mixed and screw TDs away from the coalescence boundaries to an initial spiral growth mechanism, in which the island contained a central mixed or screw dislocation.
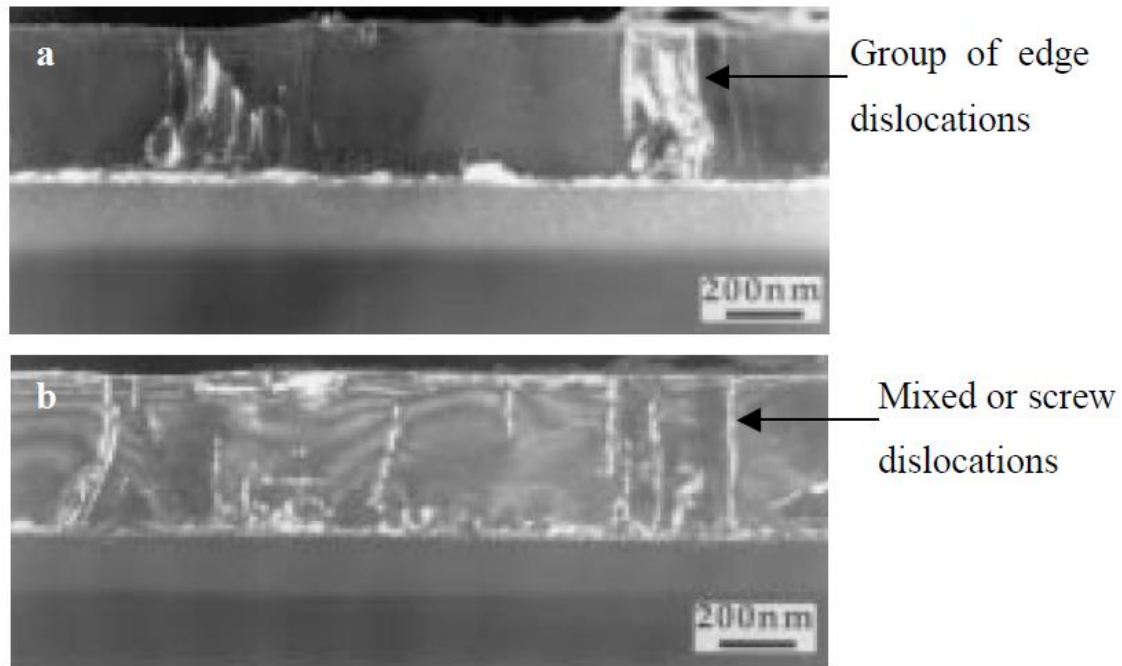
Figure 3.2. From Wu _et al._[73], WBDF TEM images of the same area of a coalesced GaN film. (a) Image with g = 11$\bar{2}$0, showing two regions with high densities of edge and mixed TDs, which are suggested to be at coalescence boundaries. (b) Image with g = 0002, showing screw and mixed TDs both at and away from the coalescence boundaries. Initial spiral growth was suggested to centre around these mixed or screw TDs.

Although there may appear to be strong TEM-based evidence for the island coalescence model, it is important to note that Wu _et al._[73] have not actually shown that the observed clusters of dislocations were formed at island coalescence boundaries, nor that these TDs do not arise through some other possible mechanism. Additionally, conclusions drawn from cross-sectional TEM images invite doubts of validity due to questions regarding the sample thickness and the statistical relevance of the images. The first difficulty is in light of the problem of projecting the full thickness of the TEM sample into a 2D image. The second simply speaks to the small area analysed per image, and the difficulty in making enough samples to collect data that can be regarded as statistically relevant. Thus, such TEM-based evidence must be examined with these difficulties in mind.

3.2.1.2. Challenges to the island coalescence theory

Other investigations into the origin of TDs in heteroepitaxial GaN have shown experimental evidence that challenges the island coalescence theory. Using

cross-sectional TEM images taken at different stages as the islands coalesced, Narayanan *et al.*[75] showed no evidence of TDs at the coalescence boundaries. Figures 3.3a and 3.3b show WBDF (g = 0002) and BF (g = 11$\overline{2}$0) TEM images, respectively, of the same area of a GaN film after 20 s of high temperature growth. With these micrographs, Narayanan *et al.*[75] demonstrated that edge and mixed TDs existed within the GaN islands before they have fully coalesced, and were not, therefore, only created upon misoriented island coalescence. The authors then examined TEM images of the GaN film upon further coalescence, after 75 s of high temperature growth. Figures 3.3c and 3.3d show WBDF TEM images of the same area with g = 0002 and g = 1$\overline{1}$00, respectively, where the 1$\overline{1}$00 reflection highlights the mixed type TDs. In these micrographs, no dislocations were found at the coalescence boundary. Again, both the projection problem and the problem of small accessible volume exist in these cross-sectional TEM images.

As an alternative mechanism for TD generation, Narayanan *et al.*[75] suggest that the TDs arise as a result of defects close to the sapphire/GaN interface. Detailed mechanisms for generation of all types of TD are proposed, and their study presents TEM-based evidence for the creation of mixed, or 'c+a type' TDs through coalescence of two Frank faults. Hypotheses for the generation of edge and screw type TDs have yet to be confirmed. In a further study, the same authors showed that, in fact, misoriented islands can grow together and cause TDs if the growth temperature and ramp rate are not carefully controlled[76]. They suggest, however, that with control over these growth parameters, well-oriented islands generate far fewer TDs at coalescence boundaries.
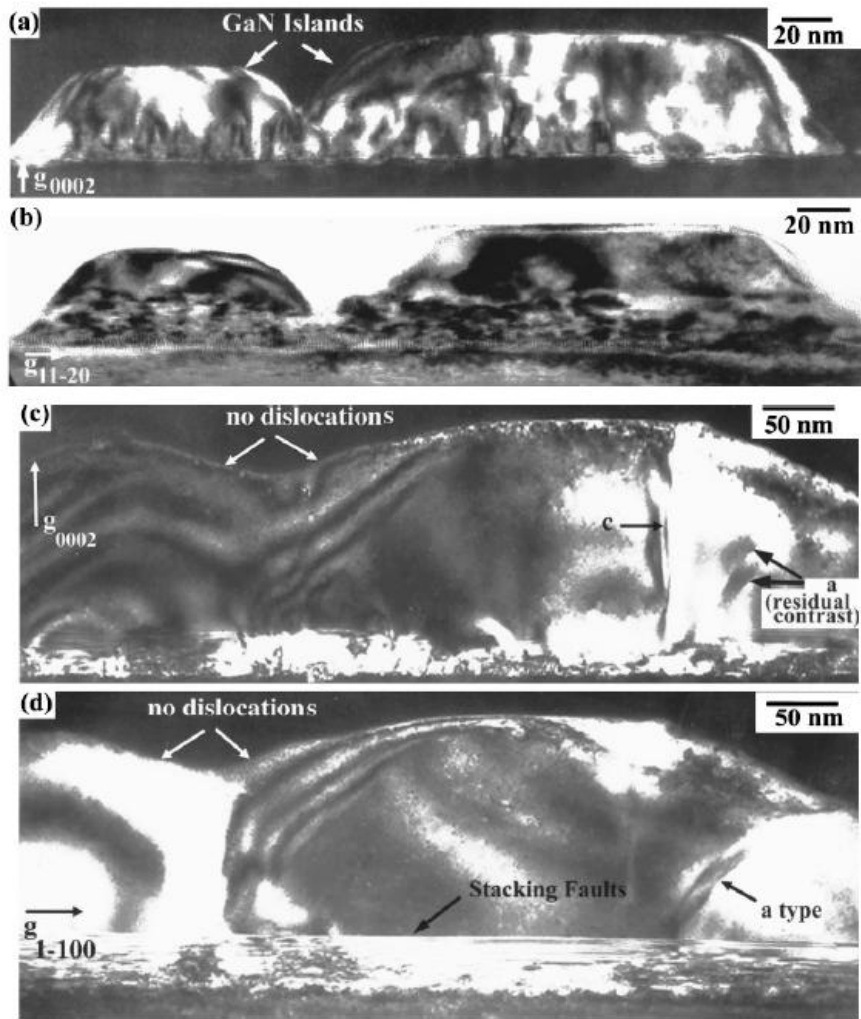
Figure 3.3. From Narayanan *et al.*[75], cross-sectional TEM images taken at different stages of GaN layer growth. (a) and (b) are the same area, after 20 s of high temperature GaN growth. (a) WBDF TEM image, g = 0002. (b) BF TEM image, g = 11$\bar{2}$0. (c) and (d) are the same area, after 75 s of high temperature GaN growth. (c) WBDF TEM image, g = 0002. (d) WBDF TEM image, g = 1$\bar{1}$00.

AFM studies have lent further statistical significance to the TEM-based conclusion that TDs do not form at coalescence boundaries by analysing far greater areas. After a silane treatment designed to reveal all types of TDs on the surface of GaN films[79], Oliver *et al.*[78] used AFM to study where TDs were present on small and large islands of a partially coalesced film. Figure 3.4 shows a typical AFM image containing a coalescence boundary between two hexagonal islands. The white box indicates the boundary region. Using this and many other similar images, the authors showed there was no increase in

TDs within the boundary: the overall TD density was $(5\pm1) \times 10^7 \, cm^{-2}$, which compared closely to the density within the coalescence boundary region of $(4\pm1) \times 10^7 \, cm^{-2}$. The study also revealed that there was no evidence of the spiral growth mechanism proposed by Wu et al.[73].
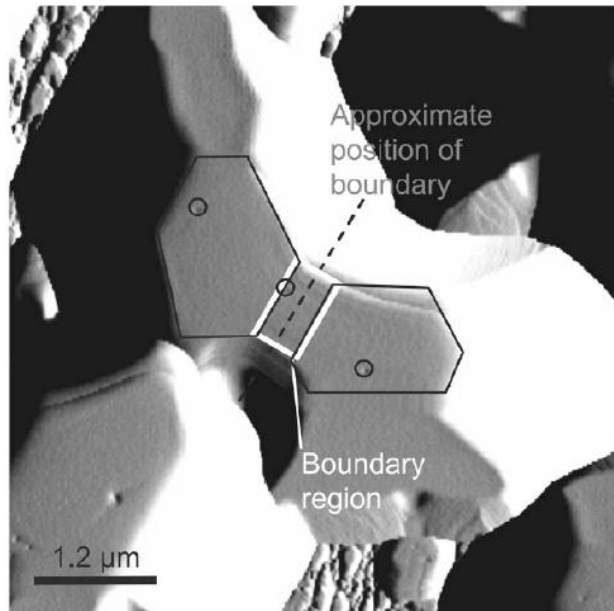
Figure 3.4. From Oliver et al.[78], AFM amplitude image of GaN islands on a partially coalesced film. The coalescence of two hexagonal islands can be seen, where the white box indicates the coalescence boundary region. Black circles indicate TDs. This and many other images show that no increase in TD density is observed at the coalescence boundary.

A fundamental barrier to the complete understanding of the origin of TDs is that it is impossible to say with certainty where the dislocations started by examining a coalesced film. To circumvent this problem, films with increasing levels of coalescence have been studied, yet the results have been widely varying: some researchers suggest that TDs are created at coalescence boundaries[72,73], whereas others find no increase in dislocation density at these boundaries[75,78]. It may be possible that the formation of TDs at coalescence boundaries depends strongly on growth conditions, as suggested by Narayanan et al.[76]. In which case, certain growth conditions might give rise to misoriented islands that coalesce to form TDs, yet other conditions do not cause such dislocations to arise.

In a recent study, Moram et al.[77] used statistically reliable spatial analysis techniques to investigate the validity of the island coalescence model. AFM was used to examine broad areas of silane-treated[79] GaN samples grown either with or without island coalescence steps to study the types and spatial distributions of the TDs. The authors investigated TD clustering on a length scale of less than one micrometer using radial distribution functions (RDFs), which show the density of other TDs as a function of distance from

the selected dislocation, averaged over all TDs in the data set. Figure 3.5 shows a typical RDF for an edge dislocation, which indicates clustering on a length scale less than 150 nm. This clustering is entirely due to linear arrays of edge TDs: the open squares show the experimental data with linear arrays removed, showing that the clustering disappears.
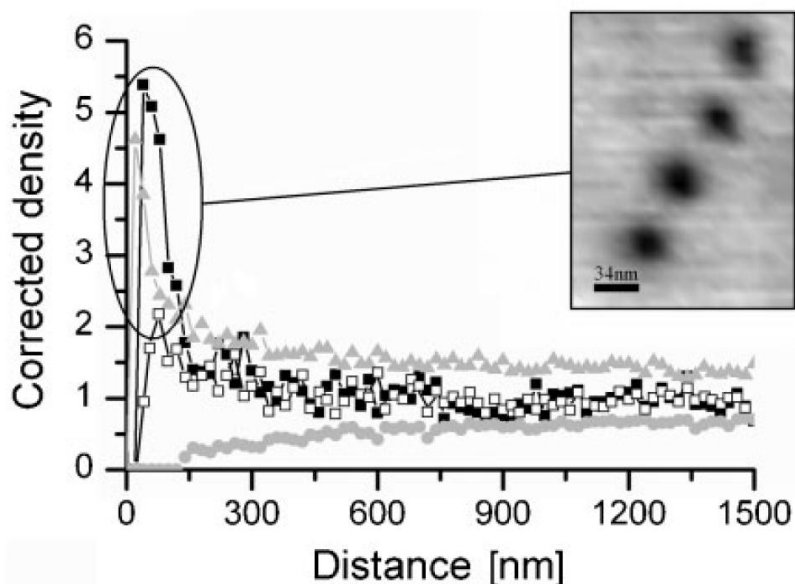
Figure 3.5. From Moram *et al.*[77], an RDF for edge TD positions for a GaN film without an island coalescence step. Gray boundaries show 99 % confidence limits for a random distribution. Filled squares indicate experimental data, and open squares show the same data with linear arrays removed. The inset shows an AFM topography image (vertical scale of 9 nm) of a linear array of edge TDs, which are the cause of the clustering that is observed below 150 nm.

These linear arrays have been attributed to island coalescence boundaries[80]; however Moram *et al.*[77] showed that the sample with the highest array density had no islands present during growth. Additionally, longer arrays would be expected in films grown with larger islands, yet this was not observed. The authors conclude that the spatial analysis is not consistent with the island coalescence model, and instead is consistent with spatially random generation of edge and mixed TDs in low TD density heteroepitaxial films. The observed arrays of edge TDs are suggested to arise from thermally activated motion of TDs (via climb), consistent with the classic metallurgical 'recovery' process, which promotes TD annihilation and creates energetically stable linear arrays of edge dislocations.

It seems that further work is needed to determine the exact origin of TDs, and to investigate the model of TD motion during growth. This work should continue the recent trend towards the use of statistically relevant characterisation techniques.

3.2.2. EFFECT OF TDS

TDs have a deleterious effect in most semiconductors, causing poorer performance in devices made from high defect density material than those fabricated from relatively defect-free material. In other III-V semiconductors, such as GaAs[81] and GaP[82], it has been shown that devices suffer a significant efficiency reduction with dislocation densities greater than approximately $4 \times 10^5 \, cm^{-2}$.

GaN-based devices exhibit a much lower sensitivity to defects than other III-V or II-VI semiconductors. Working GaN LEDs, for example, have been shown to contain dislocation densities that are extremely high $(2\text{-}10 \times 10^{10} \, cm^{-2})$, far in excess of that tolerated by other semiconductors[3]. Yet TDs do have negative effects in GaN-based devices. In addition to the shortened lifetimes of laser diodes[70], and increased leakage currents in blue and green LEDs[71] previously mentioned, high densities of TDs also reduce the efficiency of near-UV LEDs[83], lower electron mobilities in high electron mobility transistors[84] and cause a number of other problems.

These facts beg the following questions: by what mechanism do TDs affect the properties of GaN, and how is this mechanism different in GaN, compared to other III-V or II-VI materials? Two models for this mechanism will be examined in the next sections: one in which charge carriers recombine non-radiatively at TDs, and another in which charge carriers are repelled from TDs because they are electrically charged.

3.2.2.1. Non-radiative recombination model

As discussed in section 1.3.1, non-radiative recombination occurs when charge carriers recombine to generate phonons, releasing energy as heat. Non-radiative recombination is detrimental to devices because it decreases the IQE by preventing radiative recombination of carriers, and increases the heat output, which can damage the device in a variety of ways.

A number of studies have proposed that TDs act as non-radiative recombination centres in GaN[85,86]. To show the correspondence between TD location and reduced light output, TEM[85] or AFM images[86] are often used alongside CL measurements. Sugahara *et al.*[85] showed that the location of TDs (found via plan-view TEM), corresponded to dark spots in the CL map, as shown in figure 3.6. The authors claimed this correspondence provided direct evidence that TDs were non-radiative recombination centres. These studies, however, simply show a correlation between TDs and reduced luminescence. Although they cite non-radiative recombination as the cause of this reduction in light output, they do not conclusively show that the carriers are arriving at the TD at all, or that once they arrive, they are recombining non-radiatively.
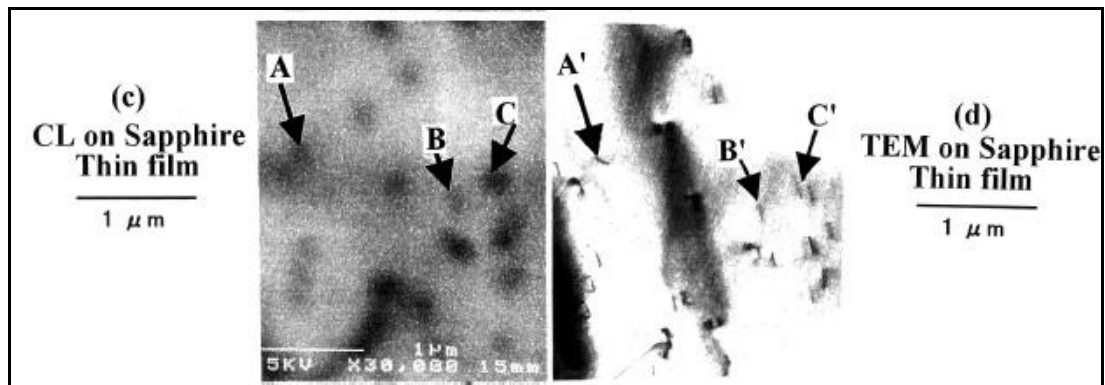
Figure 3.6. From Sugahara *et al.*[85], CL and plan-view TEM images of the same area on a GaN film, in which TDs are visible in the TEM image and corresponding dark spots are visible in the CL.

Finally, it is worth mentioning that since charge carriers in GaN are thought to exist as bound excitons, the impact of non-radiative recombination will depend on the exciton lifetime in the material and also on the timescale of the non-radiative recombination process. For instance, if radiative recombination occurs much more quickly than diffusion to defects and non-radiative recombination, then radiative recombination will be the dominant process.

3.2.2.2. Charged dislocations model

With a simple geometric model, a dangling bond would be expected at the dislocation cores, rendering the TDs charged. A schematic diagram of an edge dislocation with such a dangling bond can be seen in figure 3.7[87]. Impurity segregation to the TD cores could

neutralise such dangling bonds, yet the extent to which this occurs is unknown, which suggests that investigations into the charge state of TDs in GaN are needed.
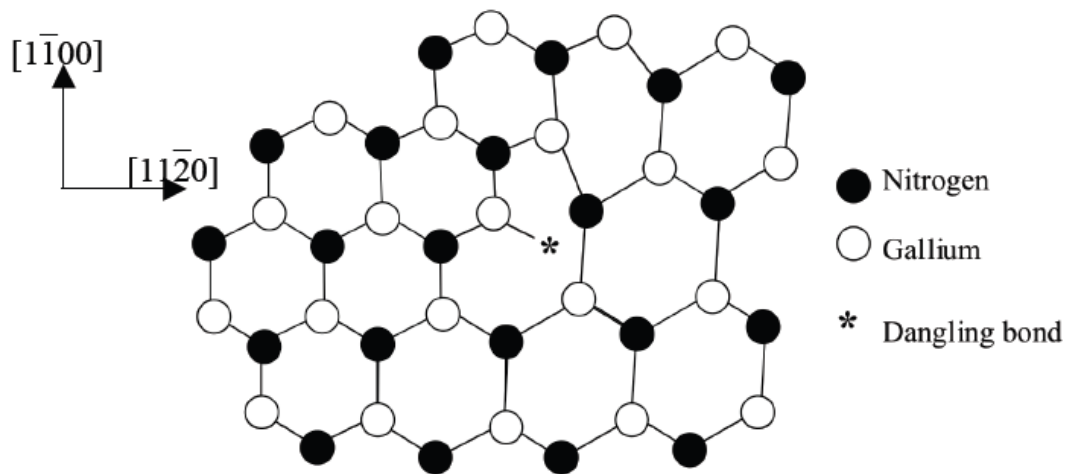
Figure 3.7. After Knott[87], A geometric model showing a dangling bond at an edge dislocation in GaN.

Electron holography has been used to study the electrical activity of TDs, informing the debate on the behaviour of charge carriers near dislocations. With this TEM-based technique, the crystal inner potential around TDs in p-type[88], n-type[89], and undoped GaN[90] was examined. Dislocations were found to be highly charged in all of these studies. In p-type GaN, edge TDs were found to be positively charged, as shown in figure 3.8, and in n-type GaN, the TDs were found to be negatively charged. This result indicates that the dislocations repel the majority carriers in both p-type and n-type GaN. If the carriers are repelled from the dislocations, then radiative recombination would be less likely to occur in the material around the TDs. Hence, it would be possible to see spots with reduced emission around TDs in CL images without the TDs being non-radiative recombination centres. Again, this interpretation would depend strongly on radiative recombination rates and carrier diffusion rates.
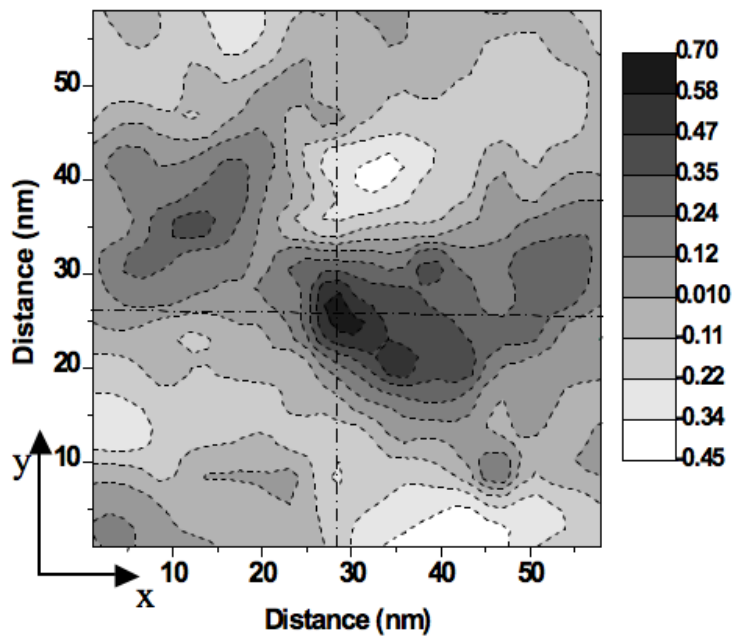
Figure 3.8. After Cherns et al.[88], map of the inner potential near an edge TD in p-type GaN. The dislocation is shown where the dashed lines cross, and the potential is highly positive in the region nearest the TD. The colour scale is given in volts.

It is worth noting that the samples made by Cherns *et al.*[89] were prepared using ion milling, which could result in preferential milling around the TDs due to their altered stress state. If the sample were thinner at the dislocations, then inaccurate results could be obtained from the holography studies. Although the authors correct for the thickness variation resulting from a wedge-shaped sample, they do not consider possible thickness changes near the TDs. Further work to ensure the validity of the analysis would lend greater weight to authors' conclusions.

Simpkins *et al.*[91] used KPFM to image the topography and surface potential of a $1.5 \times 1.5\ \mu m^2$ area of a GaN film. They were thus able to indicate the positions of the TDs on the surface potential map, as shown in figure 3.9. The TDs are seemingly associated with decreased surface potential in the area surrounding the defect. The authors present KPFM images of up to $10 \times 10\ \mu m^2$ in area, but the corresponding topography images do not have sufficient resolution to identify the TD pits.
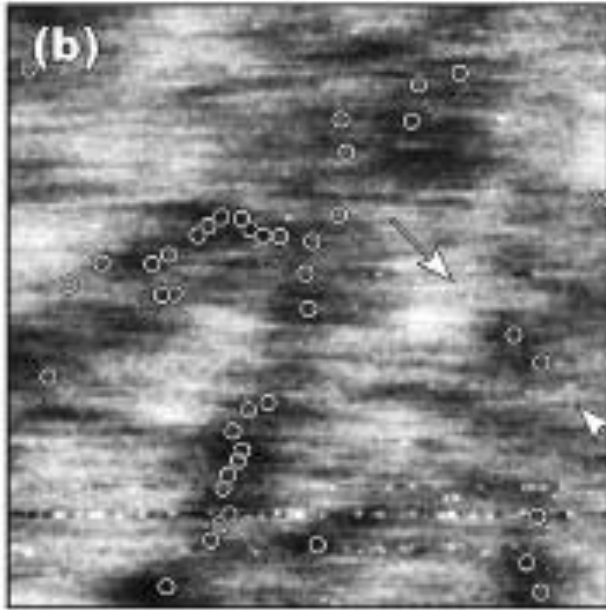
Figure 3.9. From Simpkins *et al.*[91], a 1.5 × 1.5 μm² KPFM image of GaN with the location of TDs indicated with open white circles. The TDs seem to be associated with a reduction in surface potential. The gray scale corresponds to a range of 25 mV.

The weight of evidence provided by the electron holography and KPFM studies suggests that TDs in GaN are highly electrically active. By repelling the majority carriers, charged TDs could lead to dark spots in the luminescence measurements without causing non-radiative recombination. Yet there is one question that has been largely ignored by the literature: if charge carriers in GaN exist as excitons, which are quasi-particles with no overall charge, why would they be affected by charged TDs? For the dislocation charge to affect the charge carriers, the force exerted by the dislocation must overcome the exciton binding energy. This energy is 25 meV in GaN, which is relatively high compared with 4 meV for GaAs[92]. Only by separating the exciton can the TD charge influence the individual carriers.

3.2.3. METHODS OF MEASURING TDS

A number of methods exist to study the dislocation density and types present in GaN films, including cross-sectional and plan-view TEM, CL and AFM. Three important areas in which these techniques differ are ease of sample preparation, ability to distinguish different types of TDs, and area imaged.

Using cross-sectional TEM samples, information about the TD types present, their arrangement, and behaviour, such as bending, can be observed. The dislocation density, however, is difficult to measure accurately by cross-sectional TEM, since it is problematical to determine the sample thickness, projection effects can make it difficult to resolve dislocations, and the area of the original film surface sampled is extremely

small. Plan-view TEM samples can be used, however, and an imaging technique has been developed that reveals all types of TDs in a single image over an approximately 25 μm² area, even when the sample is bent[93]. Thus, TEM-based techniques have the obvious advantage of enabling differentiation of screw, edge, and mixed TD. However, as mentioned, the area analysed in such images is often very small, leading to doubts about the statistical significance of the results. Additionally, the sample preparation is difficult and time consuming.

CL imaging in the SEM has been used to access larger areas than can be studied in the TEM. TDs are believed to be associated with dark spots in CL images, as shown in figure 3.10[94]. This method has the advantage of quick and easy sample preparation, however, at this time it is not possible to differentiate the types of TDs, and it can be impossible to resolve dark spots arising from individual dislocations in areas of high TD density.
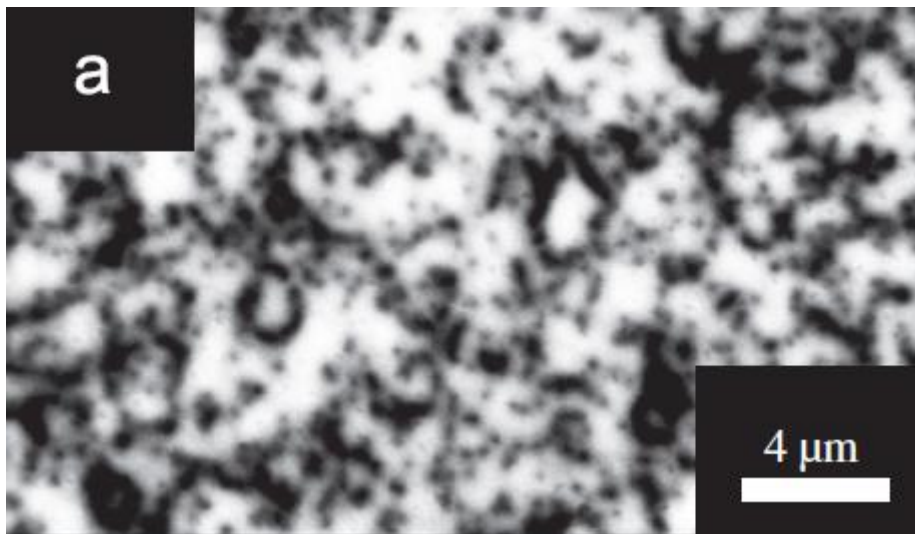
Figure 3.10. From Hemmingsson *et al.*[94], panchromatic CL image of a GaN film, showing dark spots in the luminescence believed to be associated with TDs.

The AFM can be used to study TDs over large areas in GaN films by imaging the small pits in the surface of the film that are associated with the termination of dislocations. The size of these pits in as-grown epilayers varies by type: edge TDs give rise to much smaller pits than mixed and screw TDs, making the detection of edge dislocation pits challenging[95]. A number of etching methods have been developed to increase the size of these pits for easier imaging[95,96,97]; however all of these methods require *ex-situ* treatment of the GaN film. Recently, an *in-situ* treatment has been developed using silane and

ammonia that can be performed directly in the MOVPE reactor after growth of the GaN film[79]. This treatment increases the size of the pits associated with TDs so that they can be imaged straightforwardly in the AFM, with edge TDs having a width of around 35 nm and those with a screw component having a width of around 55 nm. Thus, the pit size can be used to distinguish the edge TDs from those with a screw component (screw and mixed TDs), although it is not possible to distinguish screw from mixed TDs. Additionally, the pits remain small enough that it is possible to resolve adjacent TDs in films with dislocation densities up to $5 \times 10^9 \, \text{cm}^{-2}$. With quick and easy sample preparation, large areas analysed and the ability to distinguish edge dislocations from those with a screw character, the AFM-based method has many advantages over CL and TEM-based methods.

3.2.4. ELOG

The dislocation reduction technique used in this chapter, ELOG, is an *ex-situ* method in which a dielectric mask (SiN_x or SiO_2) is patterned onto the surface of a GaN film prior to further growth[15]. The mask filters defects by physically stopping their progress through the GaN film. Typically, the process begins with a GaN seed layer a few micrometres thick grown on a suitable substrate. The film is removed from the reactor and the dielectric mask is deposited using chemical vapour deposition (or a similar technique). Photolithography is used to etch the mask into periodic stripes, oriented along a specific crystallographic direction. The resulting masked GaN seed layer is returned to the reactor. Growth of GaN is restarted, resulting in selected area epitaxy, in which the GaN grows only where the underlying seed layer is exposed (called 'window' regions), not wetting the dielectric mask. Over the mask, in the 'wing' regions, GaN grows laterally, resulting in a very low dislocation density within these areas.

In this simple ELOG process, the window regions contain the same TD density as the seed layer. However, with a method called 2-Step ELOG, Marchand *et al.*[98] showed that the growth conditions can be tuned to induce a morphological change in the GaN layer. By tailoring the growth conditions to favour the formation of $\{11\bar{2}2\}$ facets, triangular pyramidal stripes can be formed, which induce TDs to bend over by 90 degrees into the (0001) basal plane. Coalescence is then achieved by changing the growth conditions to favour lateral growth. As the GaN growth continues, the bent TDs can meet and annihilate, reducing the dislocation density. Additionally, voids often form at the

coalescence boundaries, and TDs can be terminated at these voids. Those dislocations that are allowed to propagate to the surface can often be found in two distinct bands: one as a result of dislocations that failed to bend over, usually in the middle of the window region, and one as a result of TDs that formed at the coalescence boundary and propagated in the growth direction. A schematic of the 2-Step ELOG technique can be seen in figure 3.11. With this technique, an average TD density of 1.7×10^7 cm^{-2} has been achieved over the whole surface of the film, with an even lower TD density of 5×10^6 cm^{-2} away from the coalescence boundaries[15].
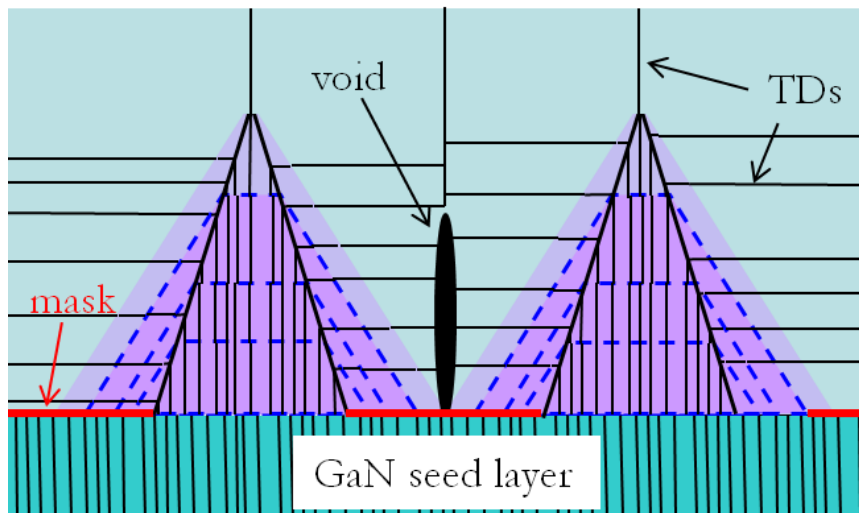
Figure 3.11. Schematic diagram of the 2-Step ELOG process. TDs are shown as solid black lines; the mask is shown in red. Dislocations propagate through the window regions of the mask and tend to bend over where they meet the {11$\bar{2}$2} facets. At the coalescence boundary voids can form, at which dislocations can be terminated. Two bands of TDs often result at the surface: one at the middle of the window region, and one at the coalescence boundary.

3.3. EXPERIMENTAL

3.3.1. SAMPLE GROWTH

The ELOG sample used in this study was grown on a c-plane sapphire substrate with a miscut of $0.25° \pm 0.10°$ toward (11$\bar{2}$0) with a 6×2 inch Thomas Swan close-coupled showerhead MOVPE reactor. A 'high TD density' template was then grown on the substrate. Growth of this template was begun with a low temperature GaN nucleation

layer, grown at 540 °C, using TMG and ammonia as precursors, with hydrogen as the carrier gas. Growth of GaN was then continued with a higher temperature, at 1,020 °C, under a flow of 10 slm ammonia and 10 slm hydrogen, and with a high V:III ratio of approximately 1,310. These conditions encouraged lateral growth, resulting in a flat, 2D layer throughout template growth. Such templates have a TD density of around 5×10^9 cm^{-2}.

On the high TD density template, a SiN$_x$ mask was then deposited *in-situ* for 1 h at 860 °C. Optical lithography was used *ex-situ* to pattern the mask, forming 5 μm stripes and 5 μm windows running parallel to the [1$\bar{1}$00] direction. After returning the wafer to the growth reactor, a 2-Step ELOG process was employed. First, epitaxial GaN growth through the window regions occurred at 980 °C, 400 Torr and a V:III ratio of 200, forming GaN stripes with a triangular cross-section bounded by {11$\bar{2}$2} facets. To induce coalescence and planarisation by favouring lateral growth, the growth conditions were changed to 1020 °C, 100 Torr, and a V:III ratio of 1300.

A surface silane treatment was employed to increase the size of the TD pits on the GaN surface[79]. The film was exposed to a SiH$_4$ flux of 200 mmol/min under a 20 slm NH$_3$/H$_2$ flow (NH$_3$/H$_2$ ratio of 1:1) at 860 °C for 240 s.

3.3.2. AFM

AFM scans were carried out in intermittent-contact mode using a Veeco Dimension 3100 with RTESP tips (with a nominal apex radius of 8 nm) and a Nanoscope V controller. With this recently improved controller, broad area images with high pixel densities could be collected, due to the increased sampling rate available. The sampling rate is important because when an AFM scan is taken, the height of the surface is sampled many times for each pixel, with the data recorded for that pixel being an average of these samples, producing an image with low noise. For a fixed time taken to scan one line (scan rate) and a fixed sampling rate, any increase in the number of pixels per line results in a reduction in the number of times the height is sampled for each pixel, leading to increased noise in the image. To achieve low noise images whilst increasing the number of pixels per line, an increased sampling rate must be used.

The Nanoscope V controller has a sampling rate of 500 kHz, a significant improvement over the Nanoscope IV, which had a sampling rate of 64 kHz. To ensure the best quality images, a low scan rate of 0.3 Hz was used and Veeco RTESP tips with a nominal apex radius of 8 nm were employed. Both topographic and amplitude error images were obtained.

3.3.3. PITS PROGRAM

A software program called PITS has been developed by Dr. David Holec for the automated detection of TD pits in JPEG images of AFM scans. According to Dr. Holec, after converting the initial image to grayscale, the program uses three filters applied to the image to enhance the pit contrast and to reduce noise. The first of these calculates the absolute values of the x and y derivatives of the image. The pit searching analysis can be performed on one of the derivatives, or on their combination, depending on image quality. As AFM images have a fast-scan direction corresponding to the x direction, analysis based on the x derivative gives better results because it avoids the common artificial contrast steps in the y direction associated with tip changes. The next filter blurs the image to reduce the noise by replacing the intensity of a given pixel by the averaged intensity of that pixel and the four adjacent pixels. Finally, an intensity threshold filter is used to remove noise, leaving only areas of sudden changes in intensity in the original image. These areas are identified as TD pits. The user is able to modify this threshold to fine tune the pit selection. Additionally, pits can be added and removed in the final stage. Once suitably identified, pit coordinates can be exported and maps of the TD density in the image can be produced.

3.3.4. TEM

TEM samples were prepared using the standard technique, as described in section 2.3.1. TEM images were obtained using a Philips CM30 300 kV analytical TEM equipped with a LaB_6 source. WBDF images were taken using a **g**-3**g** diffraction condition.

3.3.5. KPFM

Surface potential data were collected in parallel with topographic scans on the AFM. For these KPFM studies, Veeco SCM-PIT tips were used, which are coated with 20 nm of Pt/Ir and have a nominal apex radius of 20 nm. Scan sizes and pixel densities were slightly lower in our KPFM studies than in the basic topographic measurements, due to the need for two scans per line (one topographic and one surface potential), as described

in section 2.2.2. Thus, KPFM scans take twice as long to complete as images for which only topographic information is recorded.

To quantify the effect of TDs on the surface potential, the mean potential at the pit locations was found. First, the PITS program was used to find the dislocation coordinates in the topography image. Then, a routine using a Microsoft Excel Macro was used to find the potential at each of the TD pit coordinates in the corresponding KPFM data set, and the mean of these data was calculated.

3.4. RESULTS AND DISCUSSION

3.4.1. AFM

Our 2-Step ELOG sample was characterised using AFM to obtain broad area, high resolution topography images. Such images can be of great value when assessing this type of dislocation reduction technique, which results in areas of greatly differing TD density. Three distinct areas were studied to determine whether there were changes in the image attributes. A typical 30 μm × 30 μm image with 4992 × 4992 pixels can be seen in figure 3.12.

It is difficult to appreciate the level of detail present in the broad area image at the size at which it has been reproduced here. To show what can be seen at the full resolution, a small portion of the image (indicated by the white box) is displayed in figure 3.13. Both terraces and surface steps can be seen clearly, with measurement of step heights showing that both single monolayer steps (approximately 0.25 nm) and bilayer steps (approximately 0.5 nm) are present. TD pits can be identified, which have widths of 5-10 pixels in the original data set. The average dislocation density over the whole image was found by a manual counting technique to be $1.2 \times 10^8 \, \text{cm}^{-2}$. The other two images had dislocation densities of $1.3 \times 10^8 \, \text{cm}^{-2}$ and $9.2 \times 10^7 \, \text{cm}^{-2}$, similar to that of the image in figure 3.12.
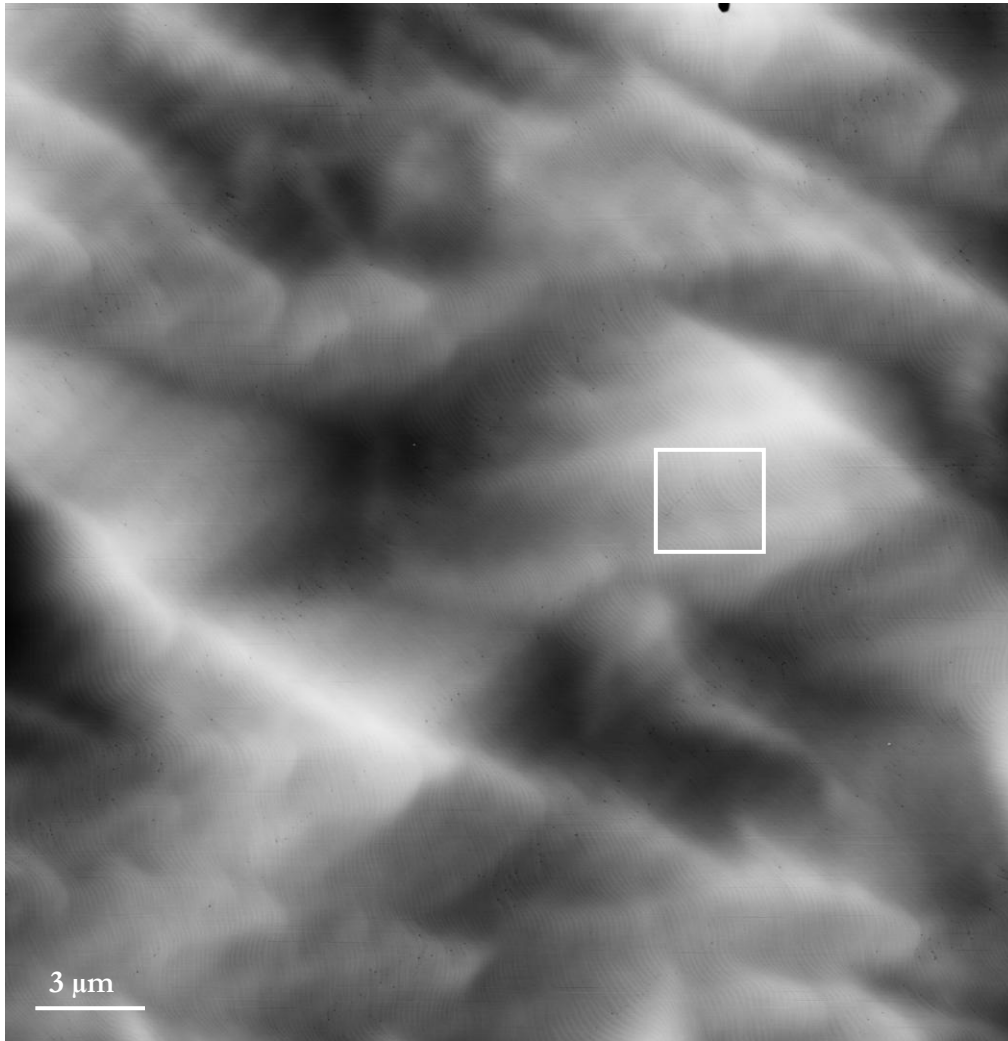
Figure 3.12. A 30 μm × 30 μm AFM topography scan of 2-Step ELOG GaN with 4992 × 4992 pixels. The vertical scale is 40 nm. The resolution is sufficient to resolve details including the TD pits within this broad area image.
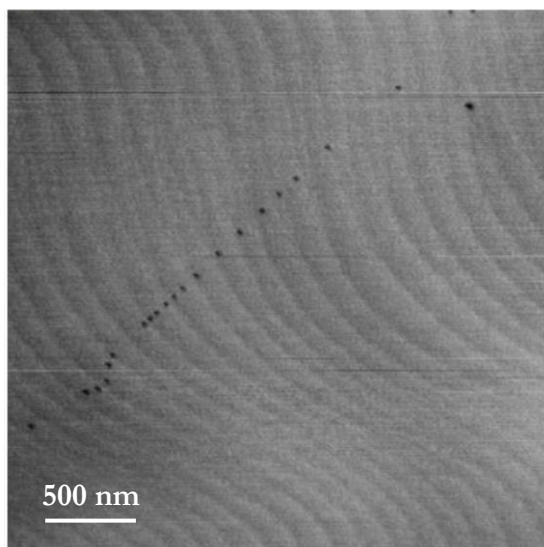
Figure 3.13. A 3 μm × 3 μm section of the AFM scan shown in figure 3.12, corresponding to the region marked by the white box. The vertical scale is 20 nm. Surface steps and TD pits can be seen clearly.

The locations of the TD pits were found by hand in all three of the 30 μm × 30 μm AFM images. TD pits were manually ringed in red to highlight the dislocations in the broad area images. Figure 3.14 shows the highlighted dislocation pits from the image in figure 3.12. Figure 3.15 is a contour plot produced by dividing up the topography image into 1 × 1 μm^2 boxes, counting the TDs, and plotting the data using Microsoft Excel. In both representations of the data, it can be seen that the dislocation density is highly non-uniform, with alternating wide and narrow bands of TD pits. The overall periodicity of the bands (defined as the distance from one wide band to the next, running perpendicular to the bands) is approximately 10 μm. This periodicity corresponds to the period spacing of the ELOG mask stripes. As discussed in section 3.2.4, the alternating broad and narrow bands suggest that one corresponds to the coalescence boundary and one to the middle of the window region, a feature that will be addressed further in section 3.4.3 on TEM.

Figure 3.14. The 30 μm × 30 μm AFM topography scan seen in figure 3.12 with TD pits ringed in red.
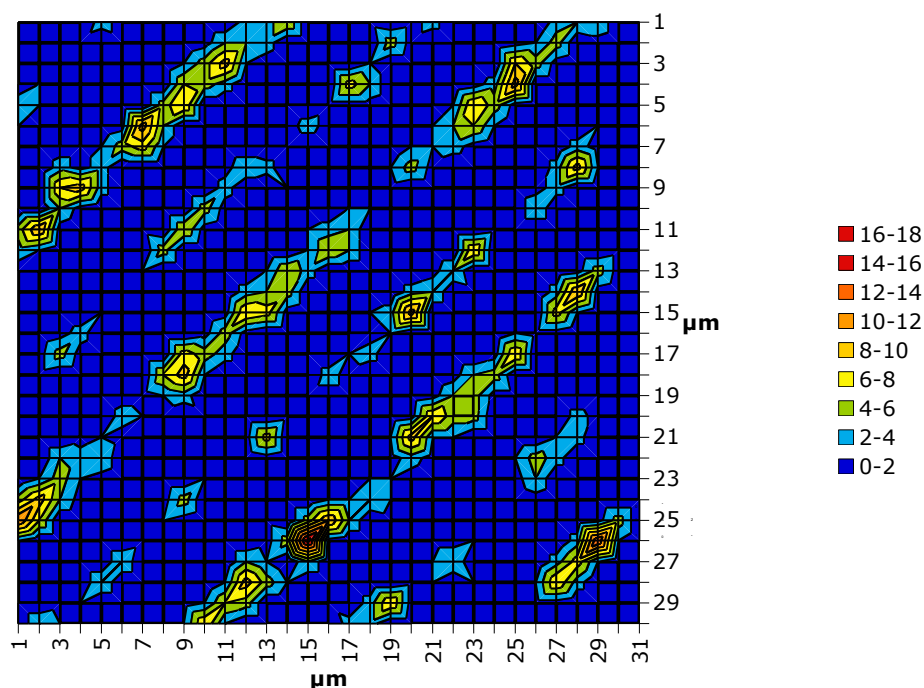
Figure 3.15. TD contour plot produced by dividing up the image seen in figure 3.12 into $1 \times 1\,\mu m^2$ boxes, counting the number of TDs per box, and plotting in Microsoft Excel as a contour plot. The key is in units of TDs / μm^2.

3.4.2. PITS

The PITS program was used to automatically identify the TD pits in the three $30\,\mu m \times 30\,\mu m$ AFM topography scans. Figure 3.16 shows a $5\,\mu m$ portion of the image in figure 3.12 after PITS has been applied to find the dislocations and ring them in red.
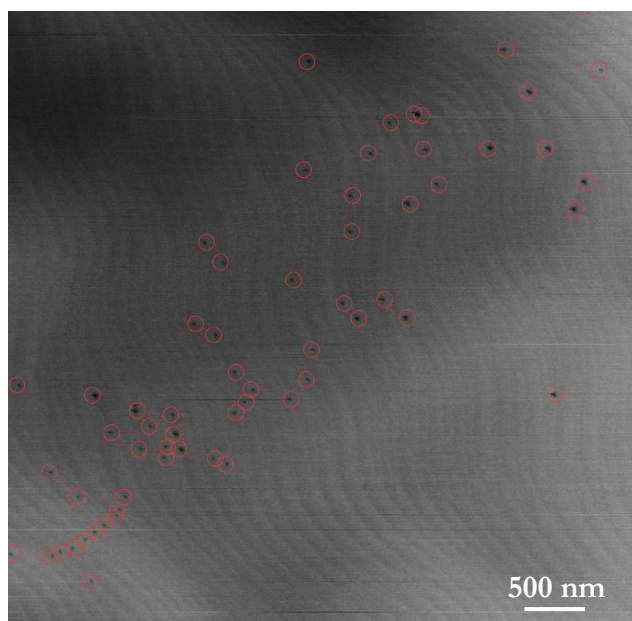
Figure 3.16. A 5 μm portion of the AFM topography image found in figure 3.12, with red rings around TD pits that have been automatically applied by the PITS program. This method greatly decreases the time needed for the analysis of TD density and distribution.

By tuning the intensity threshold filter, it is possible to use the PITS program to accurately identify most TD pits in the images studied here. To evaluate the accuracy of PITS compared with manual counting, the dislocation density was found by each method for the three images. The results can be seen in table 3.1, which shows good agreement between manual counting and the much less time-consuming PITS program.

Table 3.1. Comparison of the TD dislocation densities found by manual counting and by the PITS program for three 30 μm × 30 μm AFM topography scans of 2-Step ELOG GaN with 4992 × 4992 pixels.

Image	TD density measured by manual counting (cm^{-2})	TD density measured with the PITS program (cm^{-2})
1	1.2×10^8	1.2×10^8
2	1.3×10^8	1.4×10^8
3	9.2×10^7	9.5×10^7

3.4.3. TEM

To investigate the origin of the broad and narrow bands of TDs observed in the AFM images, WBDF TEM was used to study a cross-sectional sample of 2-Step ELOG GaN. The TEM data are shown in figure 3.17. Dislocations can be observed to propagate through the window regions of the mask, after which some are induced to bend over where they meet the $\{11\bar{2}2\}$ facets (indicated with solid white lines, as illustrated in figure 3.11). Some of the TDs which propagate laterally are annihilated at the voids present at the coalescence boundary. Interactions between TDs can lead to annihilation or to dislocations forming at the coalescence boundary and propagating in the growth direction. It can be seen that the 2-Step ELOG process is not wholly effective in inducing dislocation bending: some TDs propagate through the top of the triangular stripe, perhaps indicating that at the beginning of the lateral growth stage, (0001) facets were still present at the top of the stripes of GaN, which would allow TDs to propagate in the growth direction. Thus, it appears that the broad dislocation band is associated with the middle of the window region, and the narrow band with the coalescence boundary.
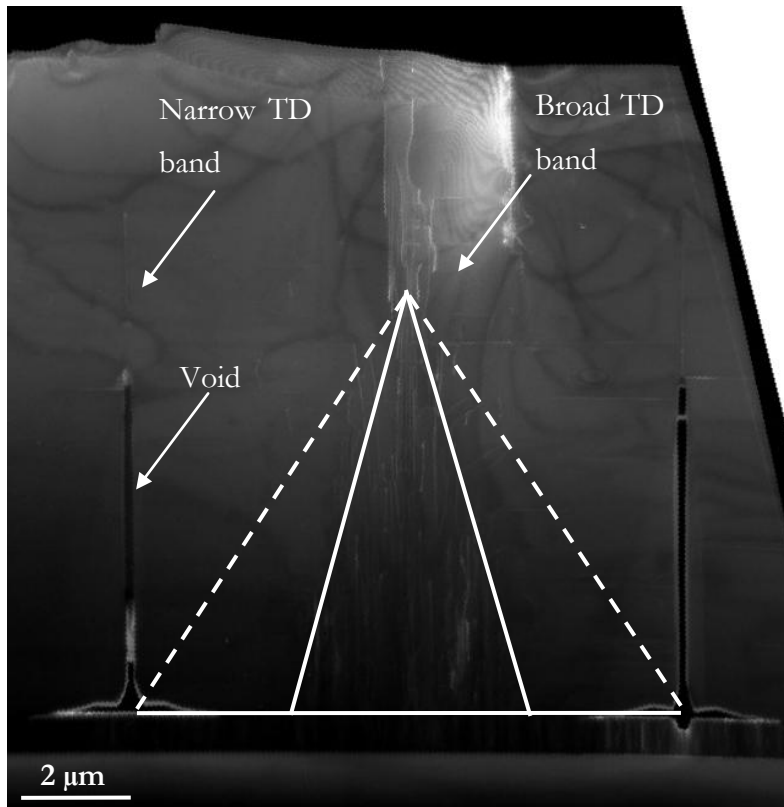
Figure 3.17. g = 0002 (g-3g) WBDF TEM image of 2-Step ELOG GaN. The solid lines indicate the {11$\bar{2}$2} facets, which induce some TD bending. The broad band of TDs results from the middle of the window region, and the narrow band from the coalescence boundary.

3.4.4. KPFM

KPFM was used to study the 2-Step ELOG sample to observe the effect of TDs on the surface potential. Two KPFM scans were taken in parallel with topography scans, and figure 3.18a shows a 20 μm × 20 μm topography image with 2048 × 2048 pixels. The resolution is sufficient to resolve the TD pits, and the same type of broad and narrow bands are observed here as highlighted in figure 3.14. The corresponding surface potential map can be seen in figure 3.18b, which shows bands of dark contrast (lower potential) in the KPFM data, which appear to run along the same direction as the TDs. Figure 3.18c shows an overlay of the TD pit positions on the surface potential map, using the inhomogeneous pattern of TDs to demonstrate that many of the areas of lower potential in the KPFM data contain a high density of TDs. The broad bands of dislocations correspond to the darkest contrast, and many of the TDs seen either in the narrow bands or in regions between the bands also show locally lower potential. That being said, not all areas around TDs show dark contrast, and not all of the areas with lowered potential contain dislocations. On the whole, however, it does appear that most TDs are associated with lowered surface potential. This result is consistent with the KPFM study by Simpkins *et al.*[91], in which they showed a lower potential associated with

the TDs in a very small area of 2.25 μm². The present work shows the same for the majority of TDs over the much larger area of 400 μm².
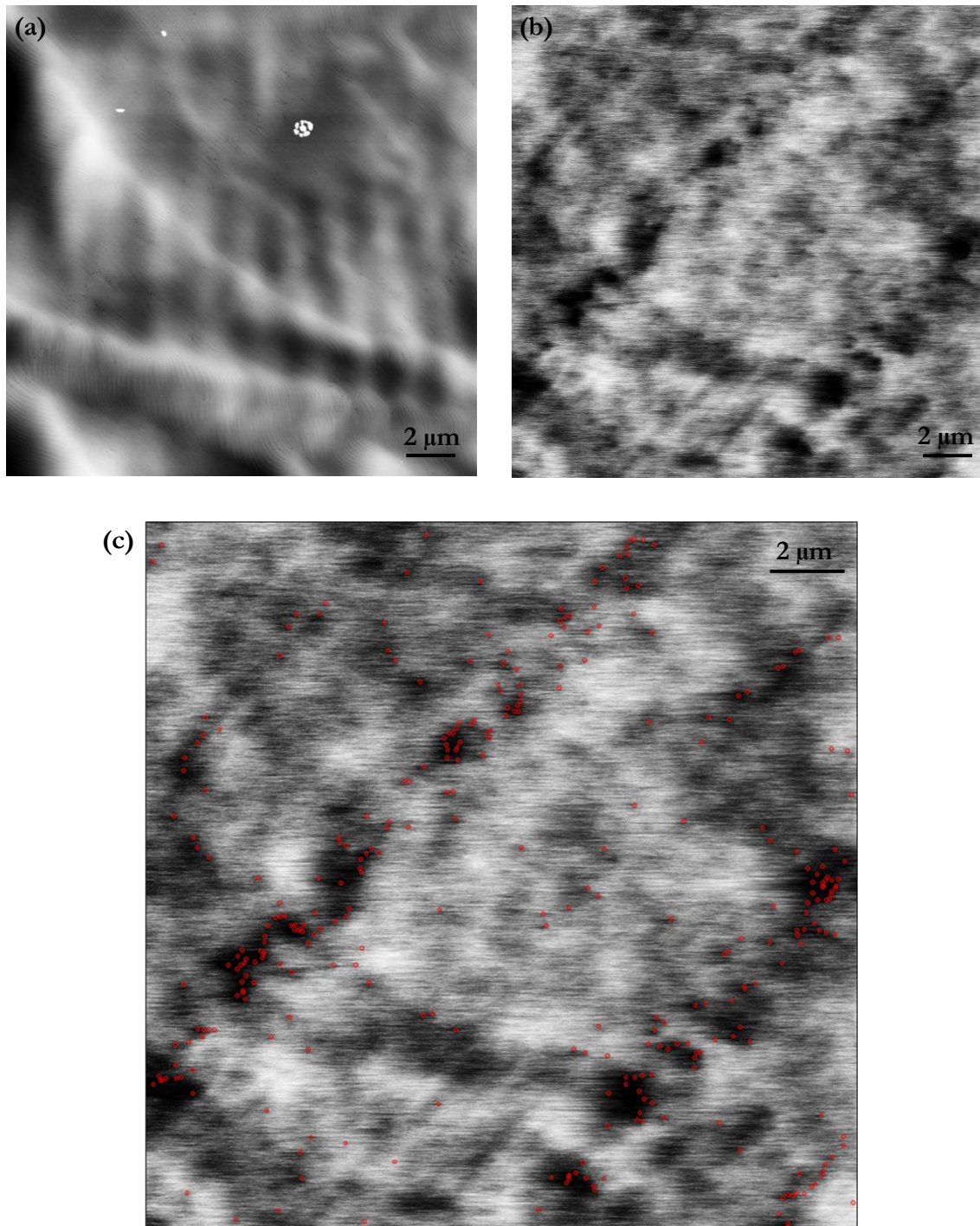
Figure 3.18. (a) 20 μm × 20 μm topographic AFM image of 2-Step ELOG GaN with 2048 × 2048 pixels and a vertical scale of 15 nm.   (b) KPFM data collected in parallel with (a), with a voltage scale of 107 mV. (c) The KPFM data from (b) overlaid with red circles indicating the positions of TD pits observed in (a).

To quantify the change in KPFM signal at the TDs, an Excel Macro was used to find the mean signal at the dislocation positions. At the dislocations, the surface potential signal was lowered by 9.5 mV compared to the mean potential found for the entire image. To assess the hypothesis that these two means were different, a student t-test was applied, and suggested a confidence level significantly greater than 99.95% that the mean potential reduction observed at the dislocation sites is genuine. This high confidence level reflects the fact that the mean values were calculated from data collected from a very large number of TD locations, made possible by imaging over such broad areas.

With the potential shown to be lowered on average by the presence of TDs, it is important to consider what might cause the dislocations to exhibit a different potential, compared to the surrounding material. Also, why might some TDs but not others show this lowered potential? As mentioned previously, a simple geometric model would suggest the presence of a dangling bond at the dislocation core, which would render the dislocation charged. Impurity segregation to the TD core could neutralise this charge, although the extent to which this occurs is unknown and difficult to study. This amount of segregation could conceivably vary over the film, causing only some TDs to show a lowered potential. With the 3D-2D growth method, as used in the ELOG sample, the V/III ratio is changed during growth, which could cause the impurity level to vary across the sample. Additionally, as GaN is a piezoelectric material, in which an electric field is caused by strain, it is also possible that the lowered potential could be caused by the strain field surrounding the dislocation. Strain fields would be expected to be present around every TD, which does not seem consistent with the fact that some dislocations do not exhibit a lowered potential. However, in an ELOG sample containing arrays of TDs, the strain around TDs might be expected to vary depending on their location. Later, in Chapter 4 of this work, an attempt is made to shed light on these questions by using atom probe to try to determine the level of impurity segregation to dislocation cores.

3.5. SUMMARY

In this chapter, an AFM with a high sampling rate controller has been used to image an ELOG sample over 30 μm × 30 μm areas with very high resolution, making it possible to see TD pits over broad areas. Manual counting of the TD pits was compared to the

PITS program by using each method to find dislocation densities in three broad area AFM images. The results compared favourably, showing that this software tool can be used to automate pit finding and greatly reduce the analysis time required. Both broad area AFM and the PITS program can be applied outside of the work described here to study samples that have very low dislocation densities, or patterns in the TD distribution, and they can also be used to provide the large amounts of data required to give statistical relevance to conclusions based on AFM data.

KPFM was used to study the surface potential of the ELOG sample. The KPFM data showed a correlation between the location of TDs and a lowering of the surface potential. Although not all TDs are associated with lowered potential, the mean lowering of the potential at the TD pits was quantified and compared with the mean potential for the entire image. The difference in the two means was found to be genuine using a student-t test, with a confidence level of over 99.95%.

4

APT STUDIES OF THREADING DISLOCATIONS

4.1. AIMS

4.1.1. APT OF A DISLOCATION

In this chapter, our first aim was to characterise a sample containing InGaN/GaN multiple QWs (MQWs) using TEM, to investigate how TDs running through the wells affected the well morphology. We then hoped to use APT to study a TD as it ran through the MQWs. We aimed to use any perturbation of the MQWs to reveal the TD position. It was hoped that, after identifying the position of the TD in the APT data, we could investigate any compositional changes at the dislocation, such as impurity or dopant segregation.

4.1.2. COMPARATIVE MICROSCOPY: APT AND TEM

The second aim of this chapter was to examine the same dislocation in both the TEM and the LEAP. We aimed to make a sample, containing a dislocation, on a mount with geometry appropriate for study in both instruments. It was hoped that the TEM could first be used to verify the presence of the dislocation, ascertain the dislocation type,

characterise its position in the sample, and determine how it perturbed the MQWs, and then the LEAP could then be used to investigate the composition at the dislocation.

4.2. OVERVIEW OF EXPERIMENTAL WORK

The aims of this chapter were very ambitious. As far as is known, APT data of a dislocation in a compound semiconductor have never been reported in the literature. Unfortunately, the aims as set out in the previous section were not achieved; however, experiments related to these aims were accomplished and have yielded interesting results. This section gives a guide to the studies that will be reported in this chapter.

A new sample preparation technique, described in section 4.5.1, was used in an attempt to capture a dislocation in an APT sample. These samples had a side-on orientation, in which the MQWs run parallel to the long axis, and the TDs run perpendicular, along the short axis of the sample. Standard orientation APT samples were also studied, and in two of these samples a V-pit defect, believed to be associated with a TD, was observed perturbing the wells.

A TD was successfully captured in an APT sample that was appropriate for study in both the TEM and the LEAP. The presence of the TD was verified with the TEM, and the TD position was estimated within the sample. Unfortunately, after running for a short time in the LEAP, the sample fractured, rendering the desired comparison impossible in this instance.

4.3. BACKGROUND

As V-pit defects are discussed in this chapter, this section will begin with some background on the structure and origin of these defects. The discussion will then focus on the study of composition at dislocations in semiconductors using TEM-based methods. Finally, APT investigations into the composition at dislocations in both metal and semiconductor materials will be described.

4.3.1. V-PITS

When TDs intersect InGaN/GaN MQWs, they have been observed to disrupt the InGaN layer, resulting in defects called 'V-pits'[99,100,101]. V-pits are initiated at a TD, and if a GaN capping layer is grown above the MQWs, the V-pit is filled in, while the TD propagates to the film surface. These defects have been characterised using STEM-HAADF[100,101], and figure 4.1a shows a Z-contrast image of a V-pit in an InGaN/GaN MQW sample, capped with GaN[101]. Within the V-pit, contrast from uninterrupted wells can be seen, as a result of projection of material in front or behind the defect in the TEM sample. Figure 4.1b is a schematic diagram of the V-pit[101].
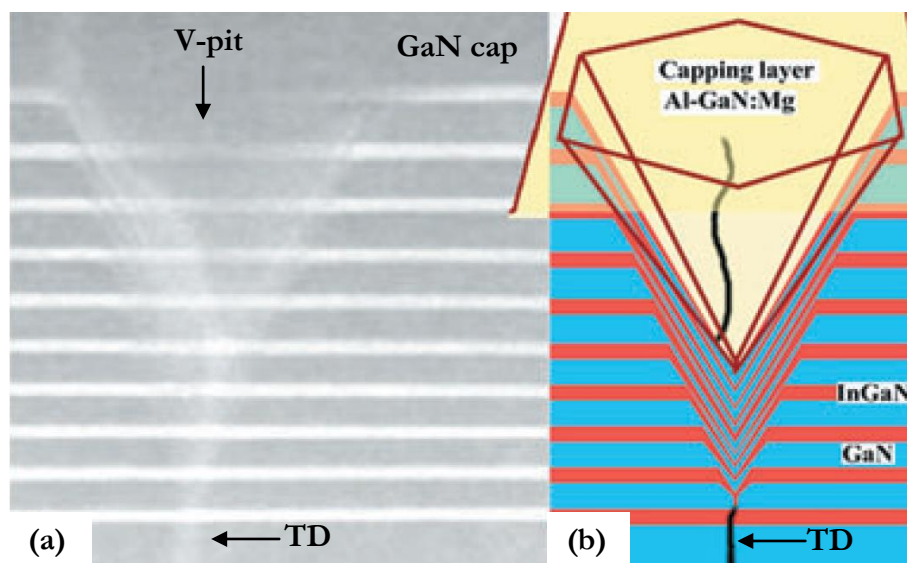
Figure 4.1. From Yang *et al.*[101], (a) STEM-HAADF image of a V-pit initiated at a TD in an InGaN/GaN MQW sample that has been capped with GaN. The V-pit shows contrast from uninterrupted MQWs due to projection of material in front or behind the defect through the TEM sample. (b) Schematic diagram of the structure of a V-pit, illustrating the inverted hexagonal pyramid shape.

Wu *et al.*[99] found the structure of these defects to be an empty inverted hexagonal pyramid shape, where the six sidewalls are $\{10\bar{1}1\}$ planes that form an open hexagon on the (0001) plane. The authors found that the sidewalls contained InGaN QWs, which are thinner than the wells on the (0001) planes. Although a number of studies have reported these thin sidewall QWs[99,100,101], recently Ding and Zeng[102] used energy-dispersive X-ray spectroscopy (EDX) analysis in the TEM to dispute the existence of such sidewall InGaN QWs: the authors claimed that In was not present in the sidewall regions, and that the contrast observed in the TEM related to interference fringes due to

lattice strain. It is possible that the samples studied by Ding and Zeng[102] were grown under conditions that did not produce sidewall QWs, but that sidewall QWs are seen in samples grown under different conditions. However, the authors make the more general assertion that their experiments show that sidewall QWs must not exist.

Kim *et al.*[103] suggested that strain caused by the lattice mismatch between InGaN and GaN is a primary cause for V-pit formation; however, the authors did not clearly state the mechanism by which the V-pits relieved this strain. Wu *et al.*[99] instead suggested that V-pit formation can be attributed to reduced Ga incorporation on the pyramidal $\{10\bar{1}1\}$ planes, in comparison with growth on the adjacent (0001) plane. The defect morphology is suggested to be kinetically governed, due to limited surface diffusion observed at the low growth temperatures required for InGaN. At higher temperatures, such as those used for GaN growth, the V-pit is quickly planarised, due to increased surface diffusion.

Yang *et al.*[101] have suggested that In atoms can be trapped and segregated in the strain field around a TD, resulting in a kind of small mask, which hinders the migration of Ga atoms on the (0001) plane. Once the mask impedes the layer-by-layer growth on the (0001) surface, growth is continued on the $\{10\bar{1}1\}$ facets, leading to the formation of a V-pit. Z-contrast images showing a bright spot at the V-pit apex have been used as evidence for this effect. Contrary to this model, however, Hangleiter *et al.*[104] observe V-pits that initiate below the InGaN wells, which suggests that V-pit formation can occur in the absence of indium.

4.3.2. TEM STUDIES OF DISLOCATION COMPOSITION

TEM has long been used to investigate the structural properties of dislocations in semiconductors, yet only recently has it been possible to resolve the core structures of dislocations at the atomic level[105]. With improving resolution, it has become possible to investigate the composition at dislocations using TEM. STEM-EELS paired with STEM-HAADF (discussed in sections 2.3.4 and 2.3.5) can be used to obtain a direct correlation between the atomic structure and the local composition, enabling the study of composition variations at TDs[106]. In this section, recent TEM studies of the local chemistry at dislocations in semiconductors will be discussed.

Xu *et al.*[105] have studied an isolated partial dislocation in beryllium-doped GaAs. A STEM-EELS probe was scanned across the associated intrinsic stacking fault (ISF), which was imaged simultaneously using STEM-HAADF. EEL spectra were obtained at the points indicated in figure 4.2, and the intensity ratios of the peaks of As/Ga and Be/C are shown in the inset (C used for calibration)[105]. The scale bar represents 0.5 nm. The EELS results reveal Ga and Be enrichment at the ISF. The authors claim that a suitable combination of imaging, local spectroscopy and theoretical modeling allows for a full characterisation of individual dislocation cores, including segregation effects; however, they do not acknowledge that TEM is limited to 2D representations of what may be interesting 3D segregation behaviours at dislocation cores.
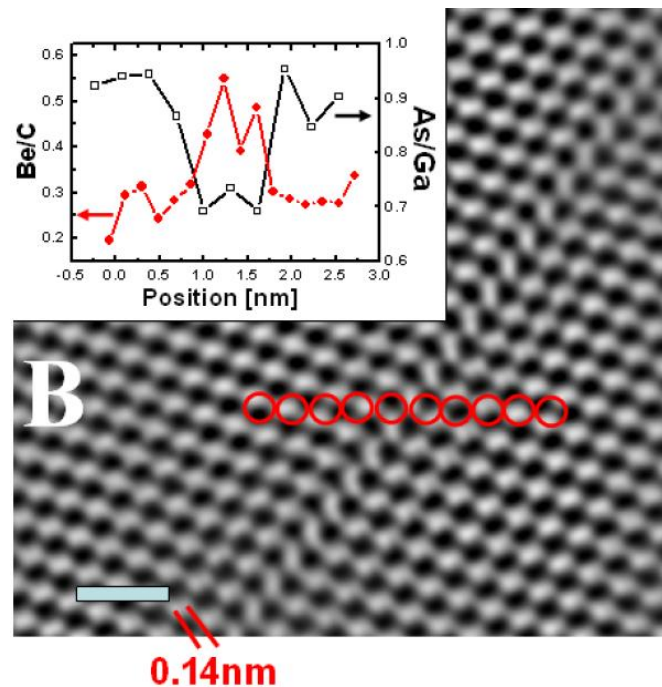
Figure 4.2. From Xu *et al.*[105], STEM-HAADF image of an ISF in GaAs, where the scale bar represents 0.5 nm. Red circles show the positions of the STEM probe at which EEL spectra were collected. The inset shows the relative concentrations of As/Ga (black squares) and Be/C (red circles) as the probe crosses the ISF. There is both Ga and Be enrichment at the ISF.

Hawkridge and Cherns[107] have studied the composition of TD cores in GaN. In a previous study, Cherns *et al.*[108] observed that some screw dislocations in undoped, MOVPE-grown GaN are of open core type, called nanopipes. The structure of these nanopipes was studied using STEM-HAADF, with accompanying compositional information obtained with EELS[107]. Figure 4.3a shows an HAADF image of an open core screw dislocation. The results of the EELS measurements, showing the compositional variation across the dislocation, are shown in figure 4.3b. The positions of the arrows in the composition profile indicate the corresponding arrows in the HAADF image. The N signal can be seen to drop as the edge of the nanopipe is approached, coinciding with a rise in the O signal, which reaches a maximum at the wall of the nanopipe. The authors assert that because the STEM-HAADF lattice structure contrast

can still be observed where there is depleted nitrogen, the oxygen is substituting on nitrogen sites. They state that such a structure would require Ga vacancies to maintain charge neutrality, which is consistent with the drop in Ga signal observed in the concentration profile in the region nearest the nanopipe.

In support of these conclusions, Arslan et al.[106] also used EELS to show a decreased N signal and an increased O signal as the edge of a nanopipe was approached. Additionally, the authors studied a normal, or full core, screw TD, at which minimal oxygen segregation was observed. These studies represent the first attempts to characterise the composition at TDs in GaN. Although substantial evidence has been presented showing oxygen segregation to nanopipes, it seems that further work is needed to characterise edge and mixed TDs, as well as to verify the absence of oxygen segregation at full core screw dislocations.
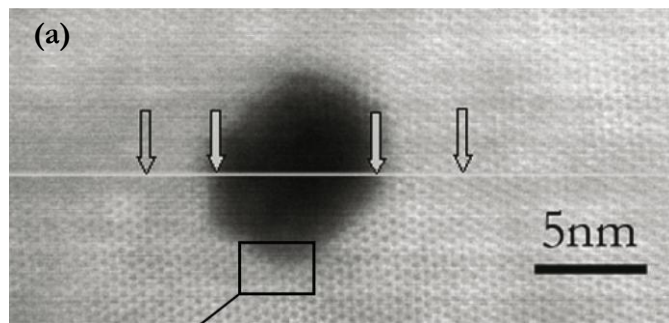
Figure 4.3. From Hawkridge et al.[107], (a) STEM-HAADF image of an open core screw dislocation in GaN.
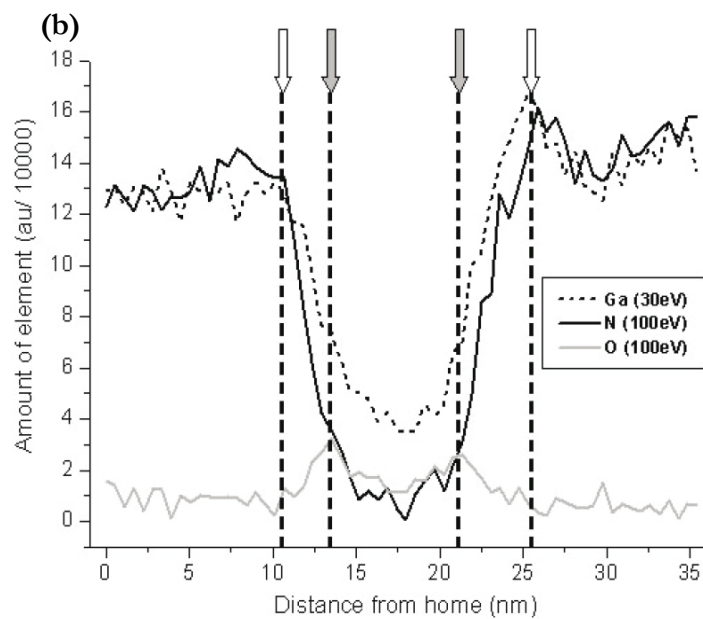
(b) EELS data showing a compositional profile across the open core TD seen in (a). As the edge of the TD is approached, the N signal drops (shown by an unfilled arrow), and the O signal rises, to a maximum at the nanopipe wall. The Ga signal also drops in this region.

4.3.3. APT STUDIES OF DISLOCATION COMPOSITION

Studying dislocations with the atom probe has proved challenging, but a small number of studies have been reported. These works are mainly restricted to metal samples using voltage pulsed APT. In this section, APT studies of TDs in metals are discussed, followed by the only known study of a dislocation in a semiconductor sample, reported in 2007 in *Science*[109].

The first atom probe studies of dislocations were carried out in Oxford, where the segregation of carbon atoms to dislocations in Fe-C alloys was observed[110]. In a later paper from the Oxford group, Wilde *et al.*[111] used non-destructive FIM imaging to pinpoint a dislocation at the surface of the electropolished tip. Atom probe analysis was then centred at the defect, and the authors showed that the TD was surrounded by a Cottrell atmosphere, which is a tiny cloud of impurity atoms around a dislocation[112]. In their seminal paper, published in 1947, Cottrell and Bilby[112] proposed that these atmospheres form due to strain relaxation that occurs when interstitial atoms migrate to regions in which the crystal structure has been expanded by a dislocation. Direct evidence for these atmospheres is difficult to obtain, due to the high spatial resolution required; however with atom probe the C-rich Cottrell atmosphere was clearly observed.

Blavette *et al.*[113] used APT to characterise boron-doped iron-aluminium alloys. The authors were able to resolve the atomic planes in the material and thereby observe an extra half-plane of Al-rich material at an edge TD. The dislocation was surrounded by a B-rich Cottrell atmosphere, and a reconstructed atom map of the decorated TD can be seen in figure 4.4, with only boron atoms shown for clarity. The APT analysis proceeded from left to right. A cylindrical envelope illustrates the rod-like morphology of the solute enriched region, in which the boron segregates parallel to the dislocation line. This example and the C-rich atmosphere described above demonstrate that APT is capable of 3D representation of the solute density along the line of the dislocation, in contrast to the 2D information that can usually be obtained using TEM.

17 x 17 x 27 nm   depth axis

B
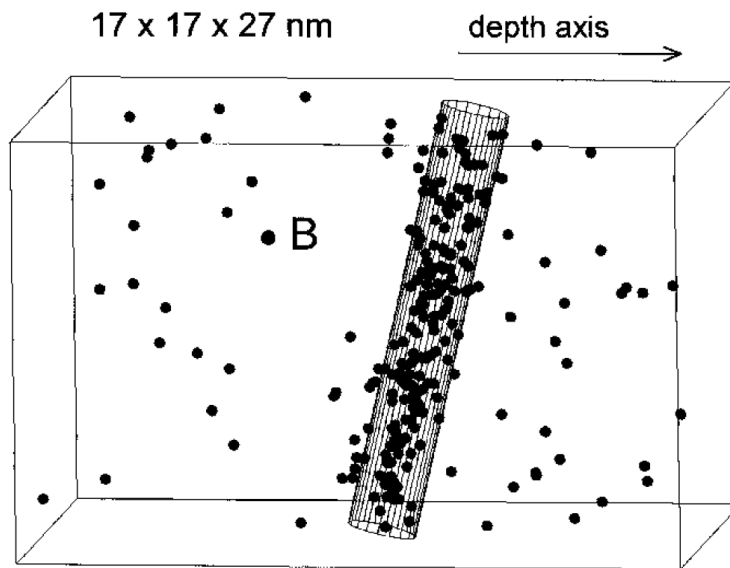
Figure 4.4. From Blavette _et al._[113], an atom map showing a B-rich Cottrell atmosphere around an edge TD in an ordered Fe/Al alloy. The Fe and Al atoms are omitted for clarity.

In another study of dislocations in metals, Miller[114] used APT to study neutron-irradiated pressure vessel steel welds. An atom map of such a weld can be seen in figure 4.5, with Cu atoms shown in green and P atoms shown in orange. Cu precipitates and P segregation can be observed along the dislocations. As Cu precipitates have a direct effect on the longevity of this material in nuclear reactors, such direct observations of their size and distribution are extremely valuable. Although the author mentions that the use of TEM can be useful to determine the character of the dislocation prior to APT analysis, this characterisation was apparently not achieved for this particular sample.

Cu P   10 nm
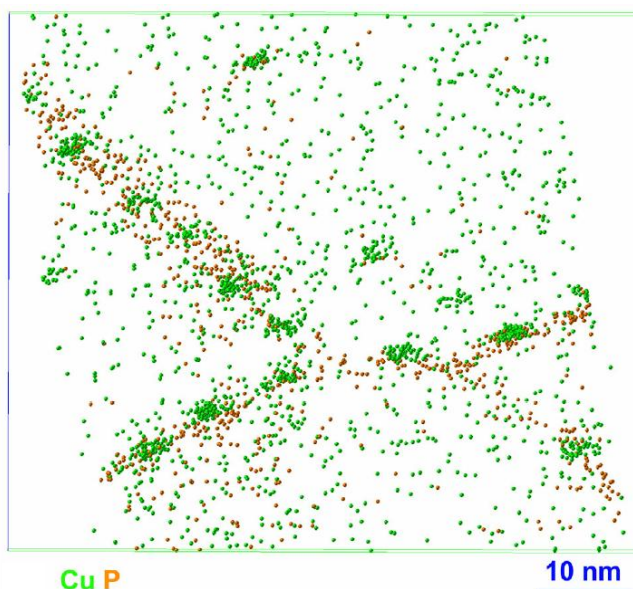
Figure 4.5. From Miller[114], an atom map of a neutron-irradiated pressure vessel steel weld. Cu precipitates and P atoms are observed to segregate to what are stated to be dislocations. Cu is shown in green, and P in orange, with all other atoms omitted for clarity.

Recently, a dislocation has been captured in a sample of As-implanted Si, which is the first reported study of a dislocation in a semiconductor material[109]. The ion implantation

of arsenic dopant atoms results in damage to the silicon, which can be partially repaired using thermal treatment. Thermally stable dislocation loops remain, however, and As-rich Cottrell atmospheres are formed at these dislocation loops. Using APT, Thompson *et al.*[109] were able to provide quantitative information about the location of individual dopant atoms relative to the dislocation loops. Figure 4.6a shows a TEM image of the As-implanted Si after annealing at 600 °C for 30 min and at 1000 °C for 30 s. A dislocation loop can be seen, which was shown to contain As using EDX.

Figure 4.6b shows an APT data set of the same material, although taken from a different area of the sample. Only 0.5 % of the Si atoms are shown (as gray dots) for clarity. The purple, ring-shaped surfaces are 2 at.% As isoconcentration surfaces, inside which the As concentration exceeds 2 at.%. These features are thought to relate to the type of dislocation loops seen in the TEM image, and the As distribution was found to be indicative of a Cottrell atmosphere. From the bulk to the Cottrell atmosphere (over 3 nm), the As concentration was found to increase by a factor of ten. Although no scale bar is provided with the atom probe data set, the authors mention that the blue oxide layer at the top of the image is roughly 2 nm in depth. The utility of this study can be understood by considering the impact that these Cottrell atmospheres might have on devices fabricated from this material. In the next generation of Si electronics, the minimal features will be on the order of 10 nm. If one As-rich dislocation loop were present within such a device, it could render it unusable[109].

The APT studies discussed in this section serve to demonstrate the remarkable potential of the technique in the 3D characterisation of dislocations, allowing details of the local chemistry of the defect to be observed.
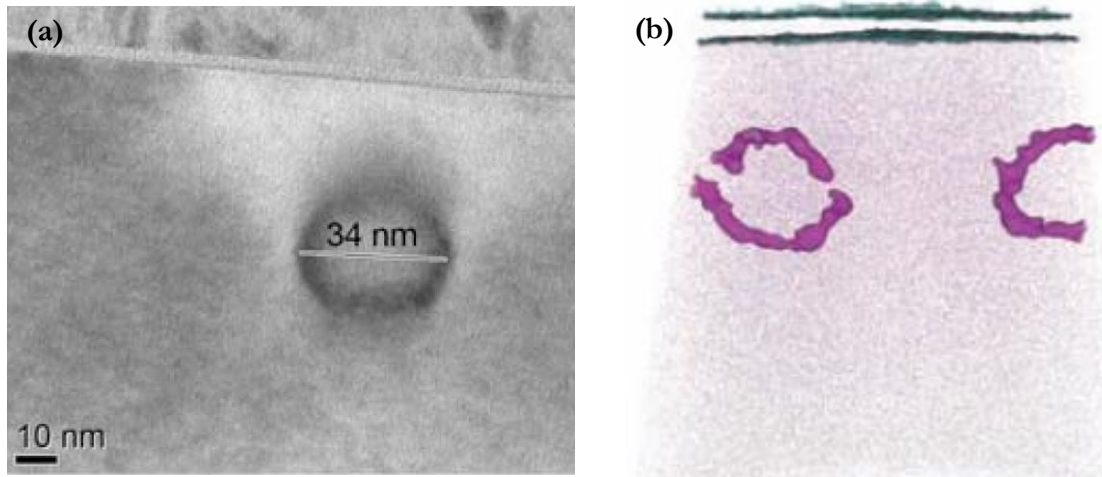
Figure 4.6. From Thompson *et al.*[109], As-implanted Si after thermal treatment (30 min at 600 ºC, 30 s at 1000 ºC), containing As-rich Cottrell atmospheres at dislocation loops. (a) TEM image of a dislocation loop. (b) APT data set, showing Si as gray dots (only 0.5 % shown). An oxide of approximately 2 nm thickness is seen on the surface of the sample, shown with blue surfaces. As-rich ring-shaped defects related to the dislocation loops seen in (a) can be observed, and are shown with purple isoconcentration surfaces at 2 at.% As.

4.4. EXPERIMENTAL

4.4.1. SAMPLE GROWTH

The samples used in this chapter were grown by Dr. Rachel Oliver on *c*-plane sapphire substrates using a 6 × 2 inch Thomas Swan close-coupled showerhead MOVPE reactor. In Sample A, a 'low TD density' template was used. This template was begun with a GaN nucleation layer, as described for the high TD density template in section 3.3.1. After the 2D nucleation layer was grown, the temperature was ramped to 1,020 ºC, and the sample was annealed under a flow of 1.5 slm ammonia and 18.5 slm hydrogen, with a V:III ratio of 715 for 300 s, to encourage growth of 3D GaN islands. Finally, lateral growth leading to coalescence of the islands was encouraged using a high V:III ratio. The final template had a flat, 2D surface with a greatly reduced TD density compared to the 2D growth used for high TD density templates. The low TD density templates used

in this work were grown by this 3D to 2D method and contain TD densities of between $3 - 5 \times 10^8$ cm^{-2}, as reported by Oliver *et al.*[79].

On top of the low TD density template, a MQW stack was grown at 740 °C, consisting of ten repeats of InGaN/GaN. The V/III ratio during InGaN growth was approximately 33,000, and the molar flows of TMI and TMG were 8 µmol/min and 5.5 µmol/min, respectively. In a separate run, a portion of the wafer was capped with a GaN layer, found to be of thickness 260 nm ± 5 nm by Dr. Clifford McAleese (using XRD). During capping, the growth temperature was approximately 1000 °C.

Sample A was previously characterised by Dr. Mark Galtrey, who found the TD density to be $(8.1 \pm 0.6) \times 10^8$ cm^{-2} (by measuring the density of pits observed in AFM), and the QW stack to be comprised of GaN layers of thickness 7.0 ± 0.1 nm and In$_x$Ga$_{1-x}$N layers of thickness 2.4 ± 0.1 nm, with indium fraction $x = 0.183 \pm 0.005$ (using XRD)[65].

Sample B was grown on a high TD density GaN template, as described in section 3.3.1. A 1 µm Si-doped GaN layer was then grown at 1020 °C, after which the MQWs were grown to the same specifications as in Sample A. A portion of the wafer was capped in the same run as the portion from Sample A, resulting in a GaN cap of equal thickness. To obtain an estimate of the TD density of the template, a silane-treated highly resistive template (grown to the same specifications used in Sample B) was studied using AFM. The PITS program was used to find the TD density, which was approximately 6.8×10^9 cm^{-2}. Although the comparison is imperfect, Sample B clearly has a much higher TD density than Sample A. Dr. Clifford McAleese found the QW stack in Sample B to be comprised of GaN layers of thickness 7.7 ± 0.1 nm and In$_x$Ga$_{1-x}$N layers of thickness 2.6 ± 0.1 nm, with indium fraction $x = 0.179 \pm 0.007$ (using XRD).

4.4.2. STEM-HAADF

Z-contrast imaging was used to observe the MQW morphology, including the V-pits in the capped Sample B. The TEM sample was prepared with the standard mechanical polishing method, followed by ion milling, and etching with KOH, as described in section 2.3.1. STEM-HAADF was performed using an FEI Tecnai™ F20 G2 operating at 200 kV with a FEG and images were taken just off the $<11\bar{2}0>$ zone axis.

4.4.3. APT SAMPLE PREPARATION

APT samples used in this chapter were prepared using an FEI Company™ Helios Nanolab™ dual beam FIB/SEM equipped with an Omniprobe Autoprobe™ 200 micromanipulator. A number of samples in this chapter were prepared using the standard liftout and annular milling procedure, with both microtip and Cu/W sample mounts, as described in section 2.5.2. The capped Sample B was used for samples prepared on microtips, and Sample B without a cap was used for the sample on a Cu/W sample mount, which was examined in the TEM.

A new sample preparation technique was developed for the work presented in this chapter, in which the sample was turned and milled in a side-on orientation. Sample A and Sample B (both capped with GaN) were used for side-on APT samples. A description of the development of this sample preparation method is provided in section 4.5.1, where related SEM images illustrate the results of the method used.

4.4.4. TEM OF APT SAMPLES

TEM images of the APT sample on a Cu/W mount were taken with the assistance of Dr. Jonathan Barnard using an FEI Tecnai™ F20 G2 operating at 200 kV with a FEG. The Cu tube end of the sample holder was inserted into a Fischione Model 2050 on-axis rotation tomography holder using a standard 1 mm diameter cartridge.

The APT sample was imaged using STEM-HAADF. Images were taken near the $<11\bar{2}0>$ zone axis and then, after rotating the sample through approximately 30 degrees, near the $<1\bar{1}00>$ zone axis. The strain contrast around the TD was sufficient to determine its approximate location in the image.

4.4.5. APT

All APT samples in this chapter were run at the OPAL EPSRC National Atom Probe Facility at Oxford University, in collaboration with Prof. Alfred Cerezo and Prof. George Smith, and with the kind help and supervision of Dr. David Saxey. A LEAP 3000X HR was used, which was equipped with a reflectron and picosecond duration laser pulsing. Details of the LEAP conditions used for each run will be presented in section 4.5, with the associated APT data set. Once the data were collected, the APT reconstructions

were optimised to obtain flat wells and the correct well spacings, as indicated by TEM and XRD.

4.5. RESULTS AND DISCUSSION

4.5.1. SIDE-ON APT SAMPLE PREPARATION

The first aim of this chapter was to use APT to study a TD as it ran through MQWs. As Sample B was grown on a high TD density template, for which an approximate TD density of 6.8×10^9 cm^{-2} was obtained, it was possible to estimate the likelihood of capturing a TD in a standard orientation sample. Using a circular field of view of 100 nm in diameter, one TD could be expected to be captured in about every two samples, on average. To increase the chance that the APT sample would contain a dislocation, a side-on sample preparation method was used. A successful side-on sample contained the MQWs running down the long axis of the sample, and the TDs running across the APT sample. As depths of up to 1 μm can be analysed in APT samples, on average each sample could be expected to contain about seven TDs. In addition, with the MQWs running down the sample, the superior z-resolution of APT could be used to investigate in-plane In concentration variations (the question of 'In clustering'), which will be discussed in Chapter 6.

Side-on samples were prepared with the use of the recently developed Axial Rotational Manipulator (ARM) from Imago Scientific Instruments. First, a wedge of material was lifted out using the method described in section 2.5.2, ensuring that the width of the liftout wedge was sufficient to later form the long axis of the APT sample. Once freely attached to the micromanipulator needle in the FIB/SEM, the wedge was transported within the chamber to the ARM. Two schematic diagrams of the ARM can be seen in figure 4.7. An electropolished W needle is held under a plate with two screws, after which the needle bends through 90 degrees over the side of the aluminium base. To use the ARM, the end of the sample wedge not attached to the micromanipulator was glued to the ARM needle with FIB-Pt. Figure 4.8 shows this transfer taking place, with the micromanipulator on the left and the ARM needle on the right. Once the wedge was attached to the ARM needle, it was cut free from the micromanipulator. The ARM, with the sample attached, was taken out of the FIB/SEM chamber, and the W needle was rotated through 90 degrees to create a side-on wedge.
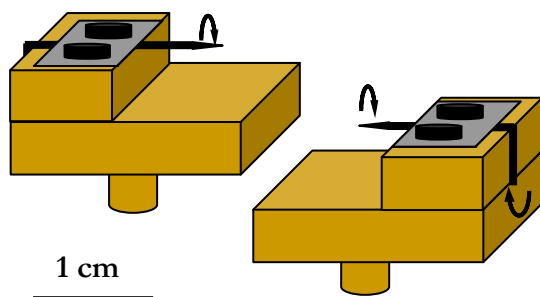
Figure 4.7. Schematic diagrams showing two views of the ARM. The arrows indicate that the W needle (black) can be rotated through 90 degrees once the wedge is attached to the needle, to turn the wedge on its side.
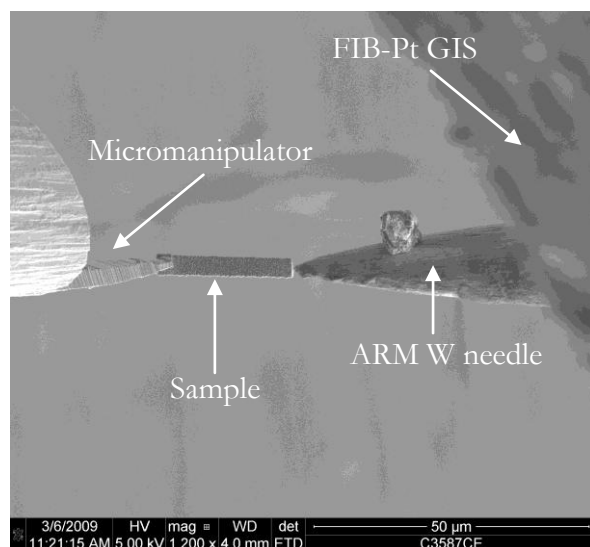
Figure 4.8. Electron beam image of the sample being transferred from the micromanipulator to the ARM needle. FIB-Pt is used to glue the sample to the ARM, after which the micromanipulator is cut away. Once the sample has been rotated through 90 degrees by the ARM, the sample is transferred back to the micromanipulator in the same way.

After returning the ARM with the sample to the FIB/SEM chamber, the side-on wedge was transferred back to the micromanipulator. The standard procedure for mounting samples on microtips was then followed, to create multiple side-on wedges that were ready to be sharpened. Figure 4.9 shows a side-on wedge mounted on a microtip. The MQWs were capped with approximately 260 nm of GaN, so that distance was measured in from the bright contrast of the sputter coated Pt layer that marked the position of the surface. Annular milling could then be centred on the MQWs, as indicated with dashed red lines in figure 4.9. The standard annular milling steps were carried out to sharpen the APT sample, producing a finished sample, as shown in figure 4.10.
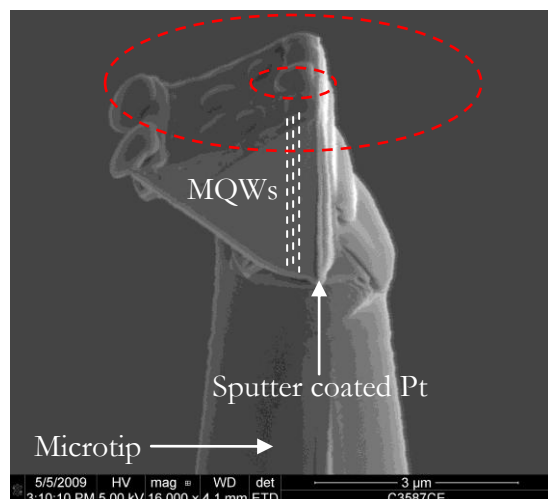
Figure 4.9. Electron beam image of a side-on wedge mounted onto a microtip. The bright contrast running down the right side of the wedge is the sputter coated Pt layer. The MQWs run down the length of the sample, illustrated by dashed white lines. The MQWs were centred in the annular milling patterns, as indicated by dashed red lines.
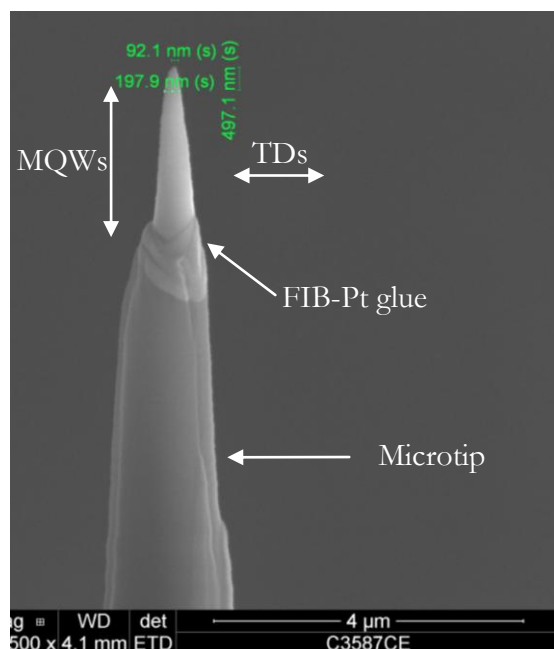
Figure 4.10. An electron beam image of a finished side-on sample, containing MQWs running down the length of the sample and TDs running across the sample. The tip diameter is less than 100 nm, gradually increasing in size to around 200 nm.

4.5.2. STEM-HAADF

Z-contrast imaging of thin foil TEM samples of Sample B was used to characterise the MQWs and to observe how the interaction with TDs affected their morphology. Figure 4.11a shows the MQW stack, with bright contrast corresponding to the InGaN wells. All ten wells appear to be flat and fairly uniform, although the top well appears somewhat thinner than the others, possibly due to material from the final GaN barrier and InGaN QW desorbing during the temperature ramp that was used during the first part of the growth run in which the additional GaN cap was deposited. This image is representative of areas without TDs, and the morphology seems consistent with previous observations of single temperature MQW growth[115].

V-pits were observed in the MQWs, associated with TDs. No V-pits were observed that began below the wells, as observed by Hangleiter *et al.*[104]. In all cases, the V-pits appeared to show InGaN layer sidewall decoration with thin InGaN QWs, consistent with the model of Wu *et al.*[99]. An image of such a V-pit can be seen in figure 4.11b, showing clear contrast of thin InGaN wells on the sidewalls. Although contrast associated with a TD cannot be seen at the apex of the V-pit in this image, many other V-pits were observed that showed contrast at a TD (as shown in figure 4.12). In this image, the V-pit appears to begin at the second well, although it is likely that the sample is too thin to contain the entire V-pit, and some of the defect and the associated TD have been milled away. The top well is missing, which suggests that the tenth well thickness may diminish in the vicinity of a V-pit. Of note, there does appear to be increased contrast at the apex of the defect, as described by Yang *et al.*[101], however the lower wells also appear brighter than those near the top of the stack, indicating that the brighter contrast could simply be due to a greater sample thickness near the bottom of the MQW stack.
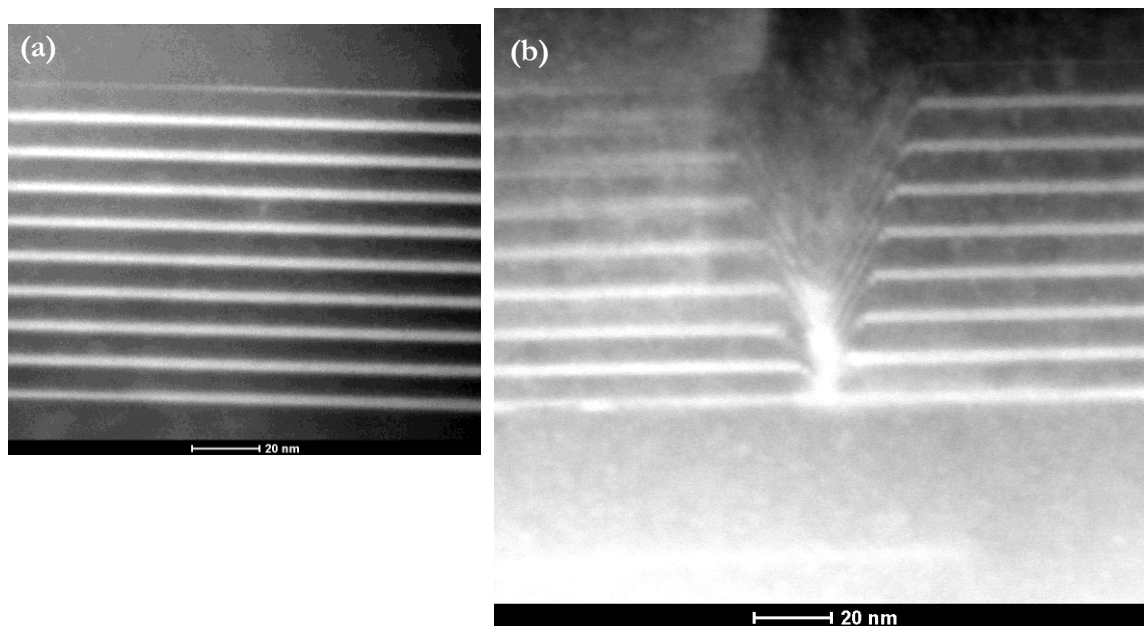
Figure 4.11. STEM-HAADF images of the MQW stack in the capped Sample B. (a) Region without any TDs visible, in which the QWs are flat and fairly uniform. (b) V-pit observed in the MQW stack, in which thin InGaN wells decorate the sidewalls of the defect.

A V-pit was observed that showed significant misalignment between wells on either side of the defect, as shown in figure 4.12. The degree of misalignment appeared to increase gradually during the sample growth, as indicated by the dashed white lines in the figure.
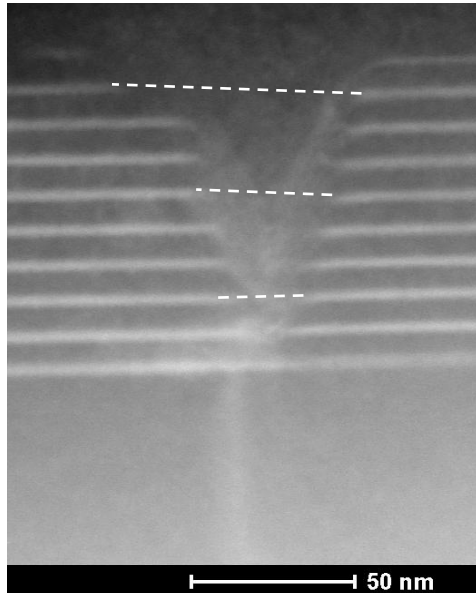
Figure 4.12. STEM-HAADF image of a V-pit in the MQW stack in the capped Sample B. Thin InGaN QWs are again observed on the sidewalls of the V-pit. The QWs are increasingly misaligned as growth is continued through the MQW stack, illustrated with dashed white lines connecting wells of equal number in the growth sequence.

4.5.3. APT OF TDS

Unfortunately, all eleven side-on samples that were made from Sample B fractured in the LEAP, with only one providing a small data set, in which some of the MQWs were observed, but no indication of a TD was seen. By contrast, the yield of standard orientation samples of the same material was three useful data sets out of five samples. In light of this difference, it was thought that perhaps in the side-on orientation, the high density of TDs increased the likelihood of fracture, which will be discussed further in section 4.5.5. In an attempt to reduce any problems arising due to the high dislocation density, side-on samples were prepared from capped Sample A, which had a lower TD density. It was estimated that one TD would be captured for every 1.2 side-on samples, on average. During attempts to run Sample A tips in the LEAP, base temperatures from 30 K up to 70 K were used, as very low temperatures can sometimes lead to sample fracture. Laser powers of up to 1 nJ were also used in an attempt to induce 'soft' turn-on at a low voltage. Finally, voltage pulsed mode was attempted. In all cases, a contamination-like spectrum was observed, quickly followed by sample fracture.

Atom probe data sets from Sample B were also obtained in the standard orientation. As previously mentioned, the likelihood of capturing a TD in standard orientation samples

was lower than for side-on samples, and so these samples were initially run simply to provide a reference for side-on data sets; however, the standard orientation data contained features consistent with V-pits in two data sets. In section 4.5.2, V-pits were shown to be associated with TDs in this material using STEM-HAADF.

The two APT data sets that contained a V-pit were collected using a LEAP base temperature of 30 K, and a laser pulse energy, or laser power, of 0.01 nJ. This laser power was the lowest value possible with the LEAP control software, and was used because this energy gives a Ga:N ratio near one. With higher laser powers, problems with the observed stoichiometry can arise, and the observed Ga:N ratio can be greater than one. Another run parameter that has an effect on the GaN stoichiometry is the evaporation rate: as the evaporation rate was increased, up to approximately 4 %, the GaN stoichiometry gradually improved, although the effect was smaller than that caused by varying the laser power. In this chapter, one sample was run at an evaporation rate of 2 %, and the other at 4 %.

In an attempt to prevent fracture of the APT samples, the final run conditions were approached slowly: the run was started with an evaporation rate of 0.5 %, and a laser energy of 0.2 nJ. These conditions were used to enable the APT sample to begin field evaporating, or 'turn on' at a low standing voltage. A layer of contaminants was usually adsorbed onto the APT sample, and a higher field was often necessary to evaporate this layer than the GaN material below. By using a high laser power (which results in a lower standing voltage), this contamination layer could be evaporated and the laser pulse energy could be lowered quickly in response to control the evaporation of GaN, and then lowered gradually to find the ideal evaporation conditions. The evaporation rate was gradually increased, both to optimise to the observed GaN stoichiometry and to accelerate data collection.

One of the data sets contained the full MQW stack with a small portion of a V-pit. An atom map of the reconstruction can be seen in figure 4.13a, with 0.5 % of Ga atoms shown in blue and 25 % of In atoms shown in orange, with all other atoms omitted for clarity. Figure 4.13b shows a slice parallel to the z-axis from the same data set (these slices are known as 'clippings', and can be defined parallel to the $x, y,$ or z axes), which allows the V-pit to be seen more clearly. Thin sidewall QWs are observed using APT,

similar to those seen with TEM. This result is in contrast to the assertion of Ding and Zeng[102] that sidewall QWs are a TEM artefact and do not actually exist. Unfortunately, the V-pit was not centred in the APT sample, and only the side of the defect was observed. The associated TD is likely to be just to the left of the data sets as they are shown in figure 4.13, meaning that the final stage of annular milling probably removed the dislocation.
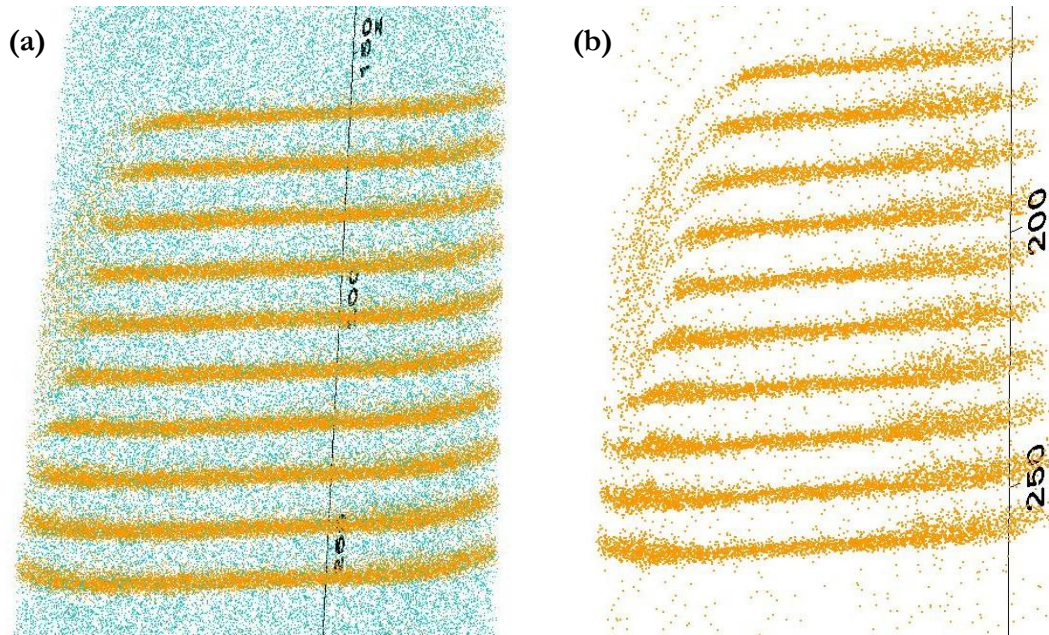
Figure 4.13. Reconstructed atom maps of Sample B, showing all ten QWs and the side of a V-pit. Indium atoms are shown as orange dots (25 % visible) and Ga atoms are shown as blue dots (0.5 % visible). (a) Entire MQW region of the data set shown, with 50 nm markers on the scale. (b) A clipping through the APT data set, showing 25 % of In atoms as dots of size 2, which highlights the V-pit and shows thin InGaN QWs decorating the sidewall of the defect.

In the second APT data set, the V-pit was located more centrally. Figure 4.14a is an atom map of the reconstructed data, with 2 % of Ga atoms and 100 % of In atoms shown. The top of the V-pit is very close to one edge of the APT sample, and the defect runs through five QWs in total before the point at which the sample fractured. Figure 4.14b is a clipping through the APT data set (with only In atoms visible) that shows the MQWs and the thin wells decorating the sidewalls of the V-pit. Figure 4.15a shows the clipping of the data set seen in figure 4.14b displayed with a 2.5 at.% In isoconcentration surface, which is a surface formed by joining up regions of 2.5 at.% In. The sidewall QWs can clearly be observed to be thinner than the MQWs at this

isoconcentration value, as was the case for all values used. Figure 4.15b is a top view of the data set, using 2.5 at.% In isoconcentration surfaces. The radius of the V-pit can be seen to decrease as the apex is approached.
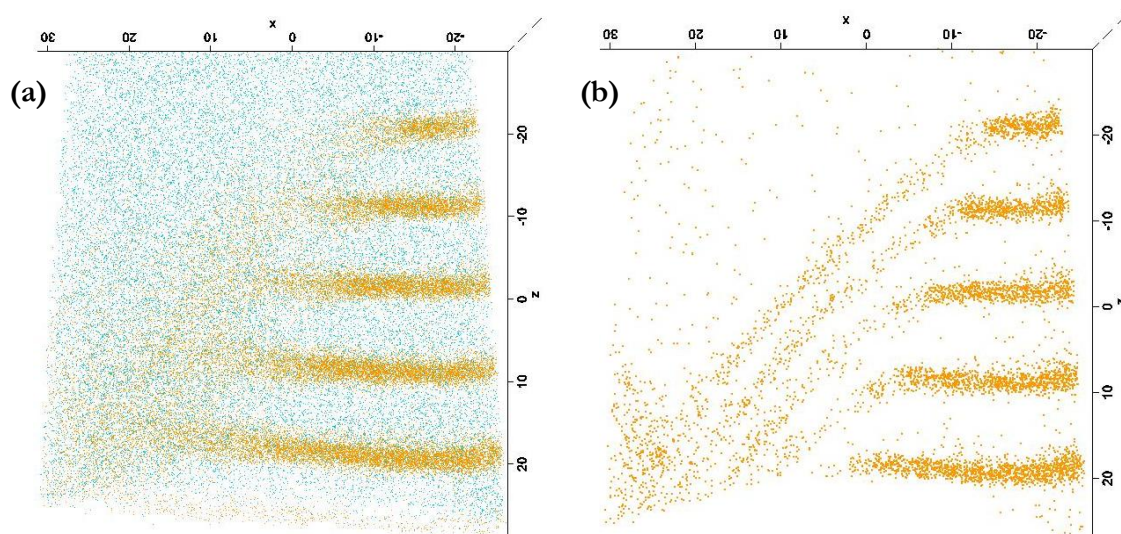
Figure 4.14. Reconstructed atom maps of the second data set of Sample B, showing five QWs and a large portion of a V-pit. Indium atoms are shown as orange dots (100 % visible) and Ga atoms are shown as blue dots (2 % visible). (a) Entire MQW region of the data set shown, with 10 nm markers on the scale. (b) A clipping through the data set, showing 100 % of In atoms as dots of size 2.
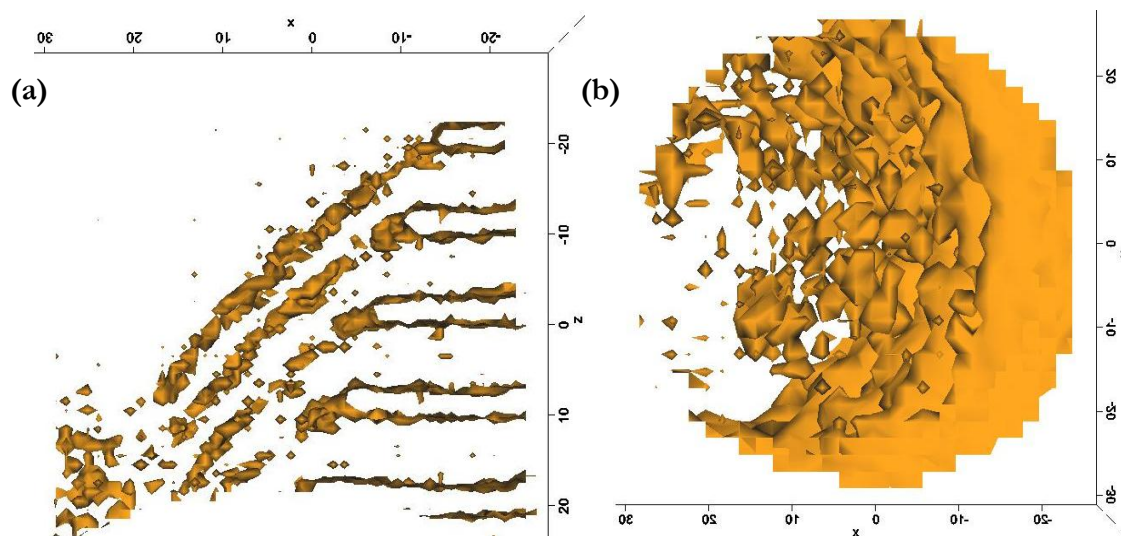
Figure 4.15. (a) Data set from figure 4.14b, with the QWs shown using a 2.5 at.% In isoconcentration surface. (b) Top view of the data set shown in figure 4.14a, using a 2.5 at.% In isoconcentration surface.

Given that the second data set fractured after just five QWs, it is interesting to estimate the position of the TD with respect to this fracture. It is important to understand, however, that the APT reconstruction may be more accurate in the z-direction than in x and y, because the reconstruction was optimised to ensure the correct z-spacings between the wells. To evaluate the APT reconstruction of the V-pit, the Z-contrast images were used to find the average V-pit structure: the width of the pit was measured (defined as the distance between the top edges of the V-pit), as well as the angle of the sidewall QWs from the vertical. The average V-pit had a width of 64 nm and sidewall QWs running at an angle of 29 °. The structural information gleaned from the Z-contrast images was then used to re-scale the APT data to ensure that the angle of the sidewall QWs was close to the average value for the V-pits. This need for re-scaling indicates imperfections in the lateral scale of the APT reconstruction. Figure 4.16 shows a schematic diagram overlaid on the re-scaled APT data set from figure 4.15a, estimating the shape of the V-pit. The QWs are shown as red dashed lines. The TD is assumed to run through the midline of the V-pit, which has been estimated from the TEM images to be 32 nm from the top edge. The TD is shown as a red dotted line. Assuming that this diagram comes close to the true shape of the V-pit, the APT sample appears to have fractured at or near the intersection of the sample with the dislocation.

As the data set may contain material at or near the core of a TD, it is worth investigating whether there are any compositional changes in the vicinity of the TD, such as might be caused by impurity or dopant segregation. The data set did contain an observable oxygen peak in the mass spectrum. As a number of studies have found TDs in GaN to be O-rich[107,106], the distribution of O was investigated. Figure 4.17 shows 100 % of the In atoms as orange dots, and 100 % of the O atoms as spheres of 0.3 nm diameter. A side view of the data set is shown in figure 4.17a, whereas figure 4.17b is a top view. In the vicinity of the V-pit, the O content is noticeably increased. To quantify this difference, a cylindrical region of interest of 10 nm in diameter and 40 nm in length was defined within the O-rich volume, parallel to the long axis of the data set, and centred at the estimated location of the V-pit apex. The O level in this region was found to be 0.023 at.%, or 2×10^{19} cm^{-3}. On the other side of the data set, a similar region of interest had a barely discernable O peak in the mass spectrum, yielding an O content of just 0.0065 at.%, or 0.6×10^{19} cm^{-3}. The O-rich region seems too large to be an O Cottrell atmosphere. It may instead be related to O surface contamination, which will be discussed further in section 7.4.1.1.
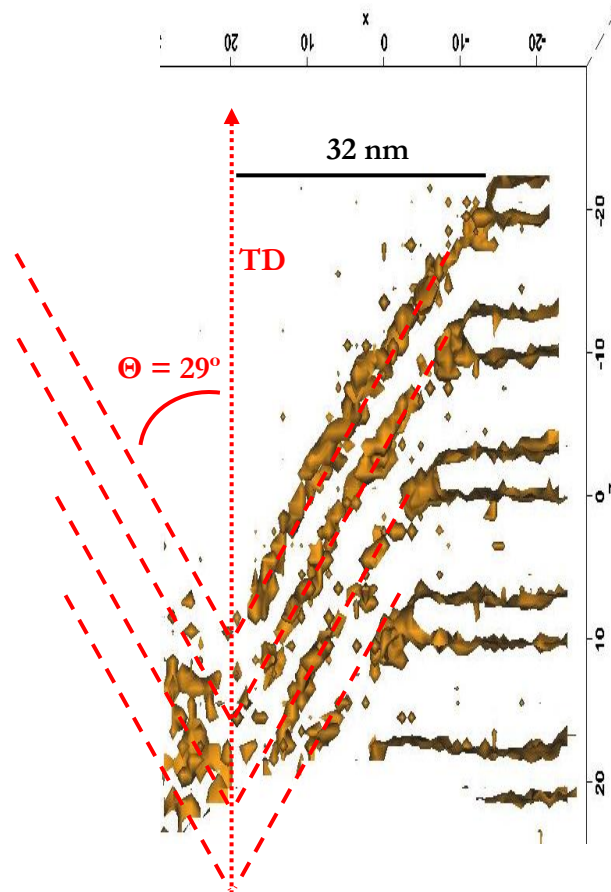
Figure 4.16. Schematic diagram of the shape of the V-pit, overlaid on the APT data shown in figure 4.15a, after lateral scaling. The average distance from the Vpit edge to its midpoint was found to be 32 nm (using Z-contrast images). The TD is shown as a red dotted line running through the apex of the V-pit.
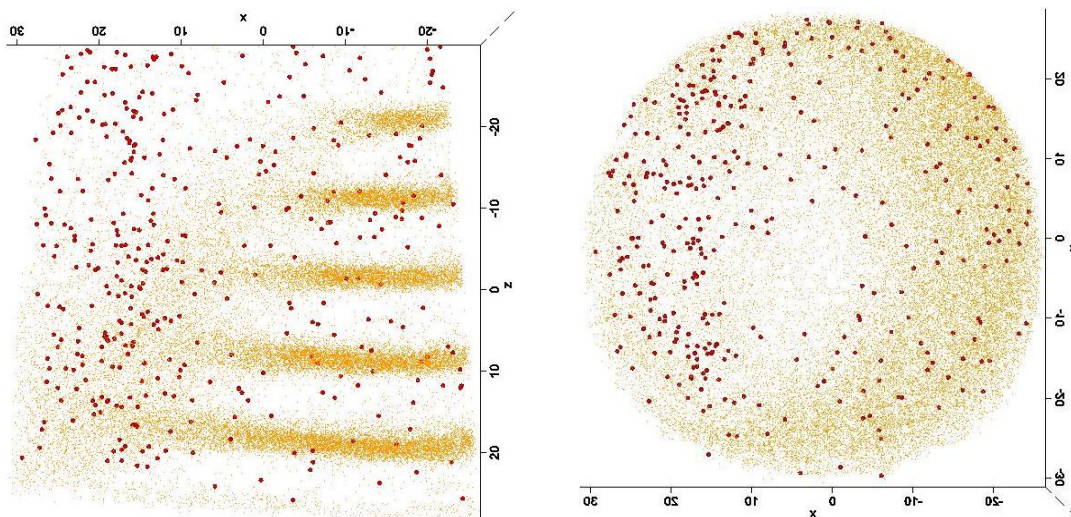
Figure 4.17. Data set from figure 4.14a, with 100 % of In atoms shown as orange dots, and 100 % of O atoms shown as red spheres of 0.3 nm diameter. (a) Side view. (b) Top view. Both (a) and (b) show more O in the vicinity of the V-pit.

4.5.4. TEM OF APT SAMPLES

The second aim of this chapter involved comparative microscopy: it was hoped that an APT sample containing a TD running through MQWs could be examined using both the TEM and the LEAP. As the sample was to be studied with two instruments, the sample mount geometry had to be suitable for both. Microtip coupons could not be studied in the TEM, so alternative Cu/W mounts were used, which were suitable for LEAP analysis. The Cu/W mounts were designed with Cu tubes of 1 mm outer diameter, specifically selected to fit into the Fischione on-axis rotation tomography holder.

A sample was prepared from the uncapped Sample B wafer using the standard lift-out and annular milling procedure in the FIB/SEM. Efforts were made to select an individual dislocation, to ensure that the sample contained a TD, and to attempt to centre this dislocation in the APT tip. The uncapped sample was used because the surface pits were visible in SEM images, as shown in figure 4.18. Unfortunately, the location of the selected TD pit proved difficult to track once the protective FIB-Pt layer was deposited and the wafer was lifted out. A sample was, however, made from an area with a relatively high density of TDs, to maximise the chance of capturing a dislocation.
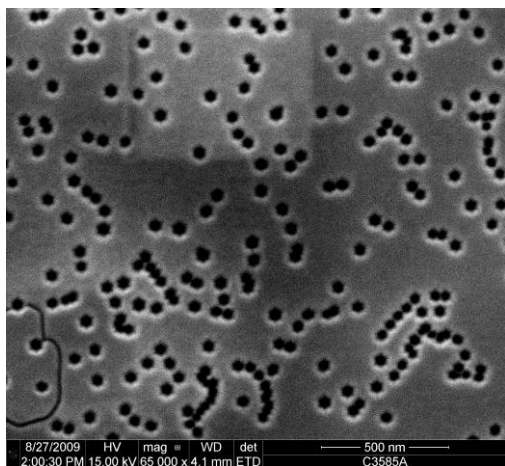
Figure 4.18. Electron beam image of the surface of uncapped Sample B, in which V-pits associated with TDs can be seen on the surface of the wafer.

The APT sample was then examined using STEM-HAADF. Unfortunately, the MQW stack was milled away in the sample preparation process. Using the uncapped sample, the MQWs were directly below the surface of the wafer. Despite efforts to minimise the amount of material removed from the sample apex, the MQWs were not successfully retained. The sample did, however, contain two TDs, as shown in figure 4.19a. One dislocation can be seen terminating at the edge of the sample, halfway up the tip, whereas the other can be seen sloping gradually from the bottom and terminating much nearer to

the end of the sample. Another image of the sample was taken after rotating through 30 degrees, as shown in figure 4.19b.
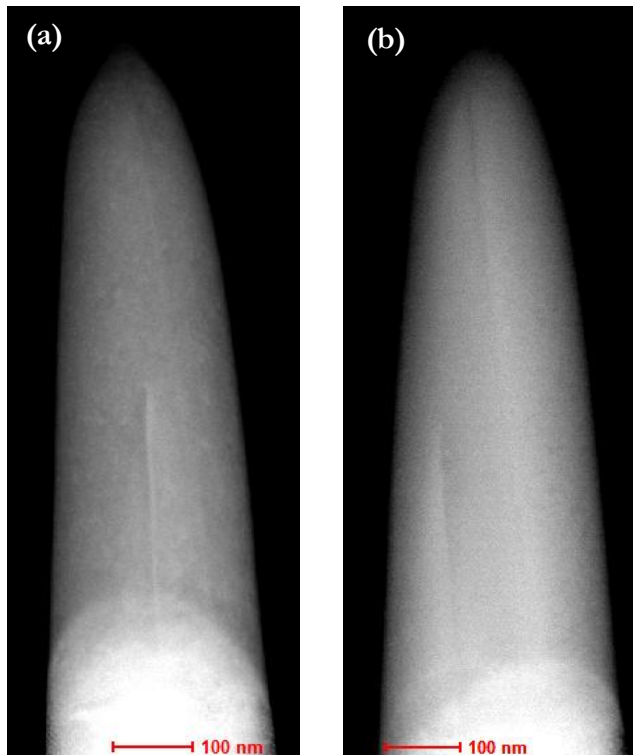
Figure 4.19. (a) STEM-HAADF image of the APT sample made from uncapped Sample B, taken near the <1̄100> zone axis. Two TDs are visible, one which exits the sample halfway up the side, and another that continues to the sample tip. (b) STEM-HAADF image of the same sample as in (a), after a 30 degree rotation to near the <112̄0> zone axis.

The location of the TD within the APT sample, which is assumed to be circular in cross-section, can be estimated using the relative change in position of the two TDs (referred to as the shorter and the longer TD) in the TEM images. Figure 4.20 illustrates the method used to estimate the TD position, which uses the exit of the shorter TD from the sample as the point of reference. In figure 4.20a, a red circle is overlaid on the image from figure 4.19a. The circle has the point of exit of the shorter TD on its edge, which is marked with a red 'x' (and a vertical line across the circle), and has a diameter defined by the sample width. The longer TD is highlighted using a red sloping line, and the point at which it intersects the circle is indicated by another 'x' (and a vertical line). In figure 4.20b, the same procedure is applied to the image from figure 4.19b, using a yellow circle.

The red and yellow circles are overlaid in figure 4.20c, after a 30 degree rotation of the red circle, corresponding to the rotation of the sample. The black 'x' where the shorter TD exited the sample was used as the point of alignment for the circles. Where the red and yellow lines on the right meet indicates the estimated location of the TD, as viewed from the above the sample. The estimated TD position is shown by a black star. The

diameter of the sample just above the point of TD exit was different in the two images (taken at equal magnification), indicating that the APT sample was actually slightly oval-shaped in cross section, which will lead to some errors in the analysis. As LEAP data are collected from the central region of the sample, two areas of 100 nm in diameter are indicated in figure 4.20c. The yellow dashed circle corresponds to the central region, as estimated from (b), and the red dashed circle similarly corresponds to the central region estimated using (a). With both estimates, the TD appears to be contained in the central region of the APT sample, making it suitable for APT analysis.
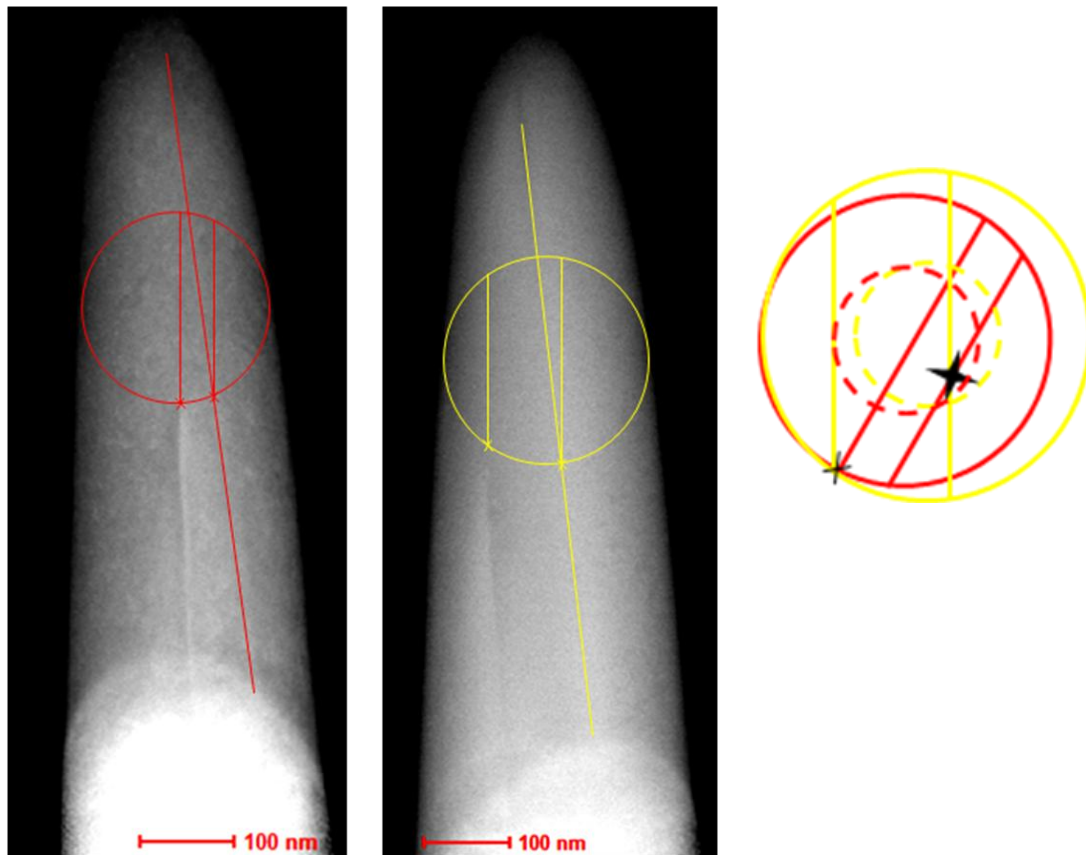
Figure 4.20. Method used to determine the location of the TD in the APT sample. (a) Overlay of the TD locations observed at this angle onto the image from figure 4.19a. (b) Similar overlay onto the image from figure 4.19b. (c) The TD positions recorded from the two images, rotated and overlaid to estimate of the TD position within the sample, as viewed from above. The dashed lines correspond to the estimates of the 100 nm diameter central regions of the sample (the red dashed line is the central region of the red circle). The TD, marked with a star, is thereby suggested to be within the central region of the APT sample.

The APT sample containing the TDs was then studied using the LEAP. Initially, the sample began to run with an evaporation pattern indicative of sample reshaping. A temperature of 26 K was used, as well as a relatively high laser power of 0.1 nJ, and an evaporation rate of 0.5 %, with a pulse repetition rate of 80 kHz (this was lower than the standard repetition rate, and was used to allow the heat to leave the tip between pulses, to achieve good mass resolution). As the sample appeared to have reshaped itself, the run was stopped and the pulse repetition rate was turned up to 200 kHz for faster data collection.

In this second run, all other run conditions were kept the same, and a mass spectrum indicative of GaN was observed. Unfortunately, the sample fractured after four million atoms were collected, which is a relatively small data set when compared with the 34 million atoms collected in the atom map shown in figure 4.13. Oxygen was present in the mass spectrum, and figure 4.21 shows an atom map of the 4 million ions collected from the APT sample, with 3 % of Ga atoms shown as blue dots, and an isoconcentration surface at 3 at.% O. The oxygen concentration appears to be substantially increased along a linear feature, however, this feature angles across the top of the data set, which suggests that it is not associated with the TD, which would be expected to have a large component in the z-direction, even if it were slightly inclined. The O-rich feature could possibly be an oxide layer on the GaN, or might be linked to surface contamination, but this is difficult to confirm.
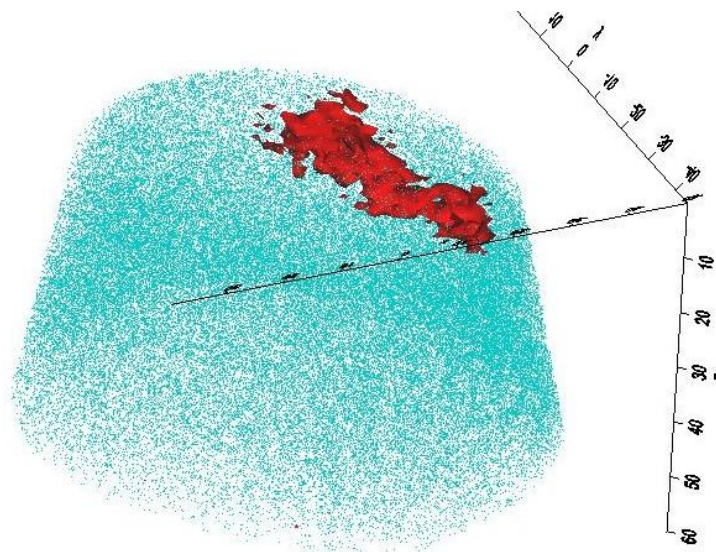
Figure 4.21. Reconstructed atom map of the APT sample shown to contain a TD using TEM. An isoconcentration surface of 3 at.% oxygen is shown in red, indicating an O-rich linear feature running across the top of the sample.

4.5.5 DISCUSSION

By examining the successes and failures of the various APT samples presented in this chapter, one could surmise that TDs may cause failure in APT samples. Sample fracture occurred in every one of the side-on samples, which were almost guaranteed to contain a TD due to their orientation. As GaN is a piezoelectric material, it is possible that that strain fields surrounding the TDs lead to electric fields that increase the stress on the sample when a voltage is applied, with the large number of dislocations found in the side-on orientation possibly exacerbating this effect.

In the standard orientation samples, several V-pits associated with TDs were observed. The dataset which contained a large portion of a V-pit only ran through five QWs, and an estimate of the possible TD position in the V-pit suggests that the sample may have fractured when the dislocation was reached.

Finally, the sample that was known to contain a TD failed after a relatively short run. In the TEM images, the TD was observed to slope gradually up to near the tip of the sample; however initial evaporation in the LEAP may have begun in an area without the TD. Sample fracture may then have occurred when evaporation of the sample revealed the TD. Before this theory can carry much weight, however, more efforts are needed to run samples known to contain a TD.

4.6. SUMMARY

In this chapter, a method of preparing side-on samples was used for the first time with GaN to make samples in which the MQWs ran down the long axis of the sample. Although these side-on samples were not productive, two data sets were collected from standard orientation samples, each containing a V-pit. STEM-HAADF images showed that such V-pits were associated with TDs, and that thin QWs decorated the sidewalls of the defects. The APT data also showed thin sidewall QWs in both data sets, refuting the recent claim made by Ding and Zeng[102] that sidewall QWs are an artefact of TEM imaging. In the APT data set that contained a large section of a V-pit, the position of the associated TD was estimated as near the point of fracture, indicating that TDs may cause sample failure. APT analysis showed an O-enriched region near the estimated position of the TD.

A TD was then captured in an APT sample on a Cu/W sample mount, and examined in the TEM. The position of the TD was estimated to be near the centre of the sample, making it appropriate for study in the LEAP. Unfortunately, although the sample began to run in the atom probe, it fractured after a small data set was collected. No feature clearly associated with the TD could be seen. Although an O-rich linear feature was observed, it ran across the top of the reconstructed data set, rather than along the axis of the sample, as would be expected for a TD.

5

APT AND TEM STUDIES OF P-TYPE SUPERLATTICES

5.1. AIMS

5.1.1. APT OF P-TYPE SUPERLATTICES

AlGaN/GaN superlattices (SLs) are often used to boost the carrier concentration in Mg-doped p-type GaN. In this chapter, we hoped to study a series of superlattices, grown with increasing Mg fluxes. Hall measurements conducted by Dr. Joy Sumner[116] indicated a drop in carrier concentration for increasing dopant concentrations, indicating that the additional Mg was not increasing the conductivity as desired. Additionally, SIMS characterisation suggested that the AlGaN layers contained more Mg than the GaN layers in all three SLs, although the two materials were nominally doped to the same level. In light of these findings, the first aim of this chapter was to use APT to investigate the 3D Mg distribution of all three superlattice samples. We hoped to use the APT data to identify any inhomogeneities in the Mg distribution, such as Mg-rich regions, in an effort to better understand the SIMS and Hall results.

5.1.2. TEM OF P-TYPE SUPERLATTICES

If Mg-rich regions were observed in the APT data of the superlattice samples, our second aim was to characterise their structure and composition using TEM, and to evaluate their similarity to literature reports of Mg-rich defects in p-type GaN.

5.1.3. COMPARISON BETWEEN APT AND TEM

Finally, if Mg-rich regions were characterised by both APT and TEM, the last aim of this chapter was to compare what could be learned about such regions using the two techniques. In this way, the strengths and weaknesses of APT and TEM as applied to this study could be compared.

5.2. BACKGROUND

5.2.1. P-TYPE DOPING OF GAN

Non-intentionally doped GaN usually shows n-type conductivity; however this residual doping level can be reduced sufficiently to allow controllable p-type doping[117]. After many groups struggled to realise p-type GaN, Amano *et al.*[118] succeeded in 1989, using controlled Mg doping with a bis-cyclopentadienyl magnesium (Cp_2Mg) source. As-grown Mg-doped GaN was found to be semi-insulating, yet Amano *et al.*[118] achieved p-type conductivity using a low-energy electron-beam irradiation (LEEBI) treatment after growth. In 1992, Nakamura *et al.*[34] showed that low conductive p-type GaN could be achieved using thermal annealing at temperatures around 700 °C in a hydrogen-free atmosphere. The authors concluded that hydrogen was responsible for passivation of the acceptors through the formation of neutral Mg-H acceptor complexes[34]. The LEEBI treatment and thermal annealing were suggested to provide the energy to break the Mg-H bond, activating Mg to be an acceptor[117,118]. The thermal annealing technique has become the standard method for dopant activation because it is straightforward, reliable, and can be implemented *in-situ,* within the MOVPE growth reactor.

Although thermal annealing can be used to activate hydrogenated Mg, p-type conductivity in GaN is intrinsically limited by the high ionisation energy of Mg (of approximately 200 meV)[119]. The deep nature of the Mg acceptor results in a low doping efficiency[119]: dopant concentrations at the 10^{19} cm^{-3} level are required to achieve hole densities on the order of 10^{17} cm^{-3}. Obloh *et al.*[119] used Hall measurements to study the

charge carrier density as a function of Mg concentration, as measured by SIMS. The authors found that the hole density reached a maximum at a Mg concentration of approximately $3 \times 10^{19}\,cm^{-3}$, thereafter decreasing with increasing dopant concentration, as shown in figure 5.1.
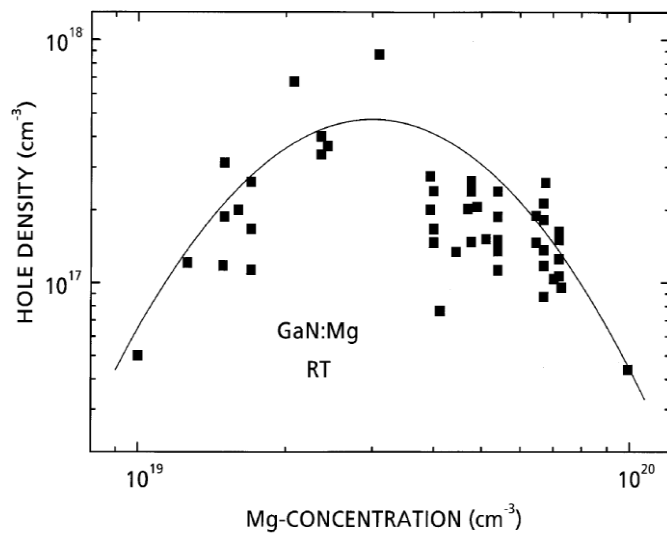
Figure 5.1. From Obloh *et al.*[119]**, Hall measurements of hole density plotted with respect to SIMS measurements of Mg dopant concentration (black squares). The line is a guide to the eye, showing that the hole density reaches a maximum at approximately $3 \times 10^{19}\,cm^{-3}$.**

5.2.2. DEFECTS OBSERVED IN P-TYPE GAN

In Mg-doped GaN with high Mg concentrations, such as those at which Obloh *et al.*[119] saw a decrease in conductivity, the Mg dopants have been observed to segregate to a variety of structural defects, such as rectangular and triangular pinholes[120], and pyramidal inversion domains (PIDs)[121,122]. Figure 5.2 shows an HRTEM image of a PID, with a schematic diagram in the inset, illustrating the proposed structure of the defect[121]. The orientation of the PIDs was found to depend on the polarity of the material, with the tip of the PID found to always point in the $[000\overline{1}]$ direction. In this study, Vennéguès *et al.*[121] found that the size of the defects (measured as the width of the side parallel to the basal plane) ranged between 2 and 20 nm. Benaissa *et al.*[122] used STEM-EELS to characterise similar PIDs, showing them to be Mg-rich[122]. Densities of these PIDs were observed to be very high (approximately $10^{18}\,cm^{-3}$), suggesting that the presence of these defects can exert a considerable influence on the properties of p-type GaN films. It is worth noting that such PIDs have not been observed in GaN without Mg dopants.

Figure 5.2. From Vennéguès et al.[121], a cross-sectional HRTEM image of a PID, with the tip of the defect pointing towards the [000$\bar{1}$] direction. The inset shows a schematic diagram of the defect structure proposed by the authors.

5.2.3. P-TYPE SUPERLATTICES

To increase the charge carrier density in Mg-doped GaN, an AlGaN/GaN superlattice can be used[123]. The alternating layers of GaN and AlGaN are strained, due to the mismatch of their lattice constants, resulting in piezoelectric fields. These fields induce a periodic oscillation of the valence band edge, as shown in the calculated band diagram in figure 5.3, where the circles represent the energy of the Mg acceptors. At the points where the valence band edge is above the Fermi energy (indicated with the dashed line), the acceptors are ionised. This occurs in the regions near the GaN/AlGaN interface, and the resulting holes accumulate close to the AlGaN/GaN interface. Although the SL structure leads to parallel sheets of confined carriers, the spatially averaged hole density can enhanced by up to ten times over bulk p-type GaN.

Figure 5.3. From Kozodoy et al.[123], a calculated valence band diagram for a Mg-doped AlGaN/GaN SL with piezoelectric fields taken into account. The dashed line indicates the Fermi energy. The circles represent the energy of the Mg acceptor, shown as filled when ionised.

5.3. EXPERIMENTAL

5.3.1. SAMPLE GROWTH

The three SL samples used in this chapter were grown by Dr. Rachel Oliver on *c*-plane sapphire substrates using a 6 × 2 inch Thomas Swan close-coupled showerhead MOVPE reactor. A high TD density template was used, as described in section 3.3.1. The SL was then grown at 1000 ºC, and was comprised of 24 repeat periods of approximately 10.5 nm $Al_{0.11}Ga_{0.89}N$ and approximately 10.5 nm GaN. The low, medium, and high Mg flux SLs were grown with Cp_2Mg fluxes of 0.243 µmol/minute, 0.364 µmol/minute, and 0.490 µmol/minute, respectively. To activate the Mg dopants, the sample was annealed at 780 ºC for 1200 s in N_2. In a separate run, the wafer was capped with 500 nm of non-intentionally doped GaN at 1005 ºC, to facilitate APT sample preparation.

5.3.2. SIMS

For preliminary characterisation of the Mg content of the SL layers, SIMS analysis was carried out at Loughborough Surface Analysis Ltd. by Dr. Alison Chew, using a Cameca IMS 3f. As standard samples for Mg in AlGaN were not available at the time of testing, the reliability of the SIMS data is limited. Figure 5.4 shows the SIMS data for the medium Mg flux SL, with the Mg trace in purple and the AlN trace in black. An oscillation in the Mg content is observed with the same period as the SL (which was also observed in the low and high Mg flux samples), indicating that the two materials in the SL have different Mg contents. Although the data appear to suggest that the GaN layers contain Al, this is almost certainly due to ion beam-induced intermixing between the thin SL layers that occurred during the SIMS measurement. This intermixing effect may also cause the observed decrease in oscillation of the Mg and AlN traces as data are collected from deeper into the sample, where intermixing becomes more significant. It appears that where there is more AlN, in the AlGaN layers, the level of Mg is correspondingly higher (illustrated with the dashed line), suggesting that the AlGaN layers contain more Mg than the GaN layers. The Mg level is observed to fall off with increasing distance into the sample. Dr. Joy Sumner measured the carrier concentration of these three SL samples using Hall probe[116]. Figure 5.5 shows that the carrier concentration (black squares) drops as the Mg flux is increased in the SL series, consistent with the findings of Obloh *et al.*[119]. The average Mg content of the SLs found by SIMS is also shown (blue squares).
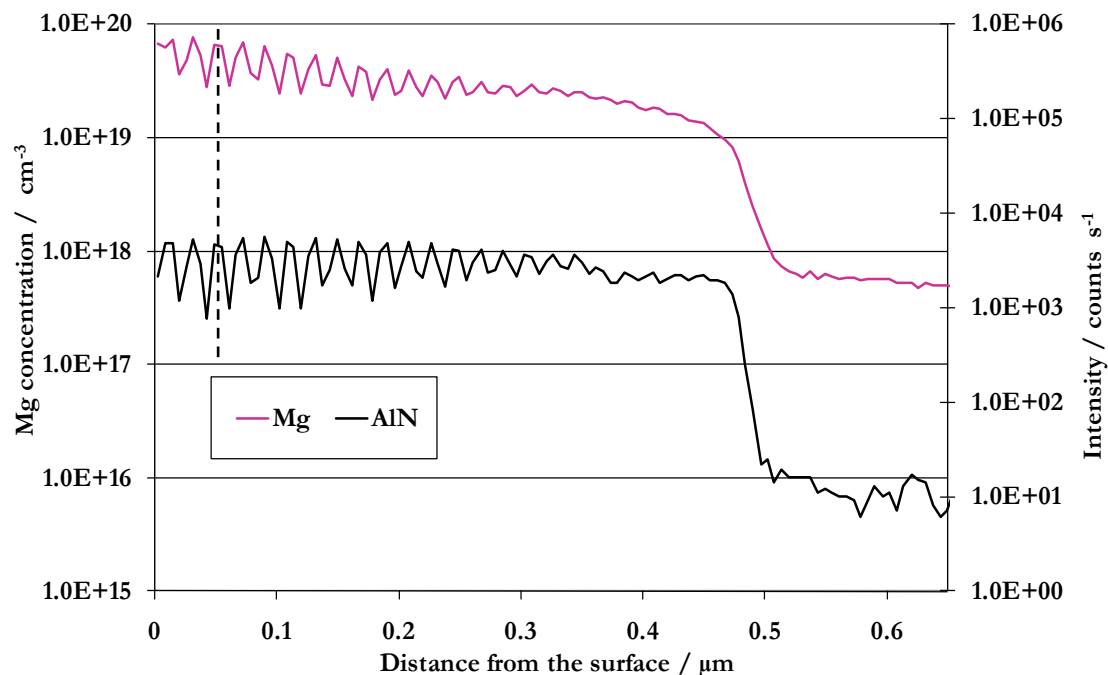
Figure 5.4. SIMS data for the medium Mg flux SL. Oscillations can be seen in the Mg concentration, which correspond to the SL layers. The period of one oscillation is approximately 21 nm, which is the same as one period of the SL. The dashed line serves to illustrate that peaks in the AlN trace, indicating the AlGaN layers, correspond to peaks in the Mg concentration.
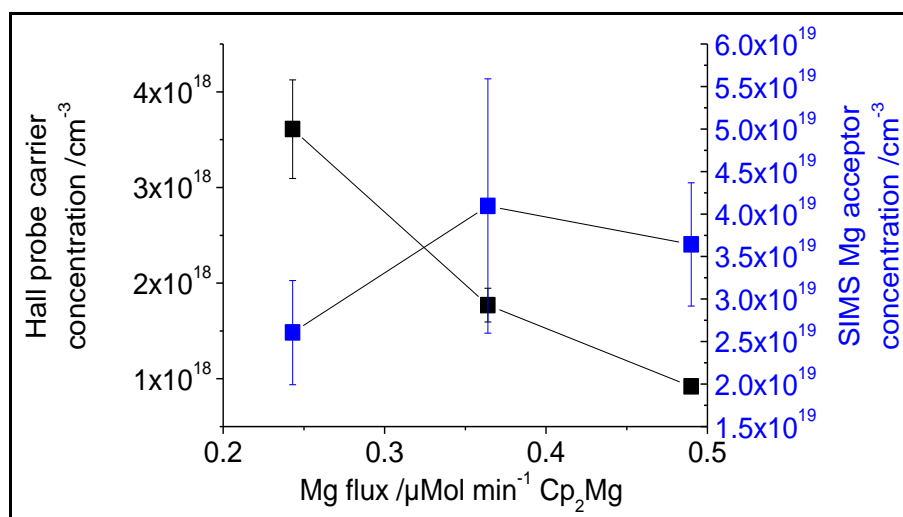
Figure 5.5. From Sumner[116], Hall probe data showing a drop in charge carrier concentration with increasing Mg flux (black squares). The blue squares show the average SL Mg concentration for the three SL samples, as found by SIMS.

5.3.3. APT SAMPLE PREPARATION

APT samples used in this chapter were prepared using the standard liftout and annular milling procedure, with microtip sample mounts, as described in section 2.5.2. For the medium Mg flux SL, the APT samples were prepared by Mr. David Olson of Imago Scientific Instruments, using an FEI Company™ Nova Nanolab™ dual beam FIB/SEM equipped with an Omniprobe Autoprobe™ 200 micromanipulator. APT samples of the low and high Mg flux SLs were prepared in Cambridge by the author, using an FEI Company™ Helios Nanolab™ dual beam FIB/SEM with an Omniprobe Autoprobe™ 200 micromanipulator.

5.3.4. APT

APT samples of the medium Mg flux sample were analysed at Imago Scientific Instruments with the assistance of Mr. Robert Ulfig, using a LEAP 3000X Si with picosecond duration laser pulsing. Although this instrument was not equipped with an energy compensating reflectron, the mass resolution was more than sufficient to identify the peaks in the mass spectrum. APT analysis of the low and high Mg flux SL samples was carried out at the OPAL EPSRC National Atom Probe Facility at Oxford University, as described in section 4.4.5. Details of the LEAP conditions used for each run will be presented in section 5.4.1, with the associated APT data set.

The APT data sets were reconstructed in IVAS by optimising the reconstruction parameters to ensure flat AlGaN layers (as observed by TEM) and the correct layer spacing, as far as was possible.

5.3.5. TEM

A TEM thin foil was prepared from the medium Mg flux SL, using the standard methods of mechanical polishing, ion milling with the PIPS™, and KOH etching, as described in section 2.3.1. Lattice fringe images with zero-loss energy filtering for improved contrast were taken on the $<11\bar{2}0>$ zone axis. Compositional measurements were attempted using both STEM-EELS and EFTEM mapping. Finally, WBDF imaging was used to investigate the existence of inversion domains. All TEM studies reported in this work of the SL sample were undertaken using an FEI Tecnai™ F20 G2 operating at 200 kV with a FEG, and with the kind supervision and extensive assistance of Dr. Jonathan Barnard.

5.4. RESULTS AND DISCUSSION

5.4.1. APT

Atom probe data sets were collected from all three Mg-doped AlGaN/GaN SL samples, permitting the 3D Mg distribution to be studied for the entire sample series.

5.4.1.1. Reconstructed Atom Maps of the SLs

The low Mg flux APT sample began evaporating in the SL layers, making it impossible to know the source location of the data set within the SL. The sample preparation was, however, tailored to aim for the top of the SL. This SL was analysed using a base temperature of 25 K, a laser power of 0.03 nJ, and an evaporation rate of 3 %. The final run conditions were approached slowly, to prevent sample fracture and to tune the conditions for optimal GaN stoichiometry. Although AlGaN and GaN will certainly have different evaporation fields, this difference was observed to be minimal, as the standing voltage did not change appreciably when the evaporation uncovered the next layer.

Figure 5.6a shows a reconstructed atom map of the low Mg flux sample, with 100 % of the Mg atoms shown as purple spheres of radius 0.2 nm, and 5 % of the Al atoms shown as light blue dots (all other atoms omitted for clarity). The alternating layer structure of the SL can be observed, with the Al atoms indicating the AlGaN layers, and the GaN layers indicated by a lack of Al atoms. The SL layers are tilted, indicating that the liftout wedge was tilted slightly during the sample preparation, probably when brought into contact with the microtip. Figure 5.6b shows the SL layers straight-on, by rotating the data set to a different angle. Although simply looking at an atom map is not a reliable way to judge the existence of Mg-rich regions, or 'clusters', the low Mg flux sample appears to show a fairly even distribution of Mg. In the following section, the observed Mg distributions in the three SLs will be compared to the distributions expected from a random alloy, to determine if any clustering of non-random origin is present.
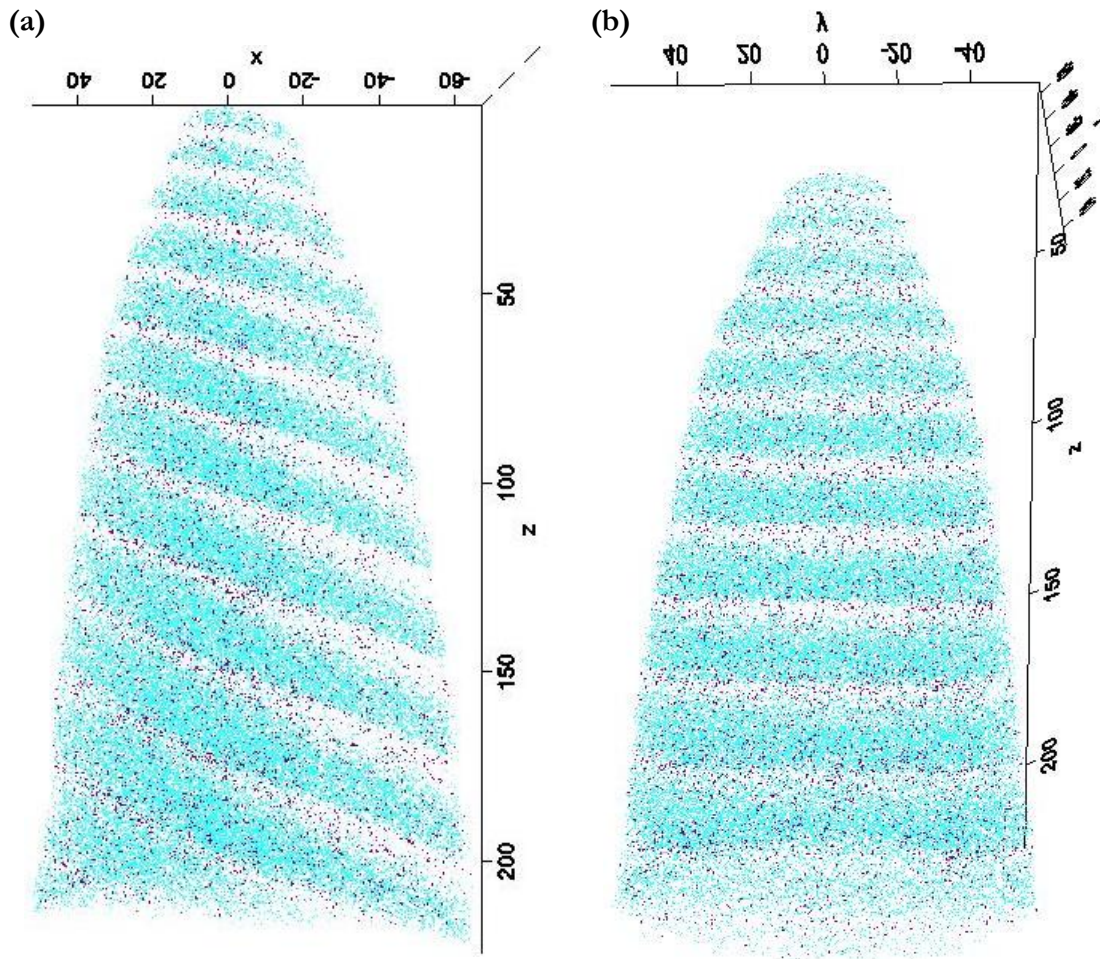
Figure 5.6. Reconstructed atom maps of the low Mg flux SL, with 100 % of Mg atoms shown as spheres of radius 0.2 nm, and 5 % of Al atoms shown as light blue dots (all other atoms omitted for clarity). The layers of AlGaN are characterised by a high density of Al atoms, alternating with the GaN layers, characterised by a lack of Al atoms. The Mg atoms appear to be fairly evenly distributed. (a) Orientation showing the SL layers are tilted relative to the long axis of the APT sample. (b) Orientation looking straight down the SL layers.

Both the medium and high Mg flux samples began evaporating in the GaN cap above the SL, so the data obtained are certainly from the top of the SL. APT data were collected from the medium Mg flux sample using a base temperature of 25 K, and a laser power of 0.02 nJ. The SL layers were uncovered after evaporating part of the GaN cap, resulting in the sample being relatively wide at the SL layers. To progress through the layers where the sample was wide, large numbers of atoms needed to be evaporated, which necessitated high evaporation rates due to limited available time. During evaporation of

the SL layers, the evaporation rate was gradually increased from 3 % to 5.5 %. The high Mg flux SL was also analysed using a base temperature of 25 K, but a higher laser power of 0.2 nJ was used to limit the stress on the sample, as the data set was collected from the last available tip. The first 40 million atoms of the 55 million atom data set were evaporated using a 2 % evaporation rate. To obtain the maximum amount of data in the time available, the final 15 million ions were collected at evaporation rates gradually increasing from 2 % to 4.5 %. Figure 5.7a and 5.7b show reconstructed atom maps of the SL layers from the medium and high Mg flux samples, respectively, with the same display specifications as in figure 5.6. It appears that Mg clusters exist in both data sets.
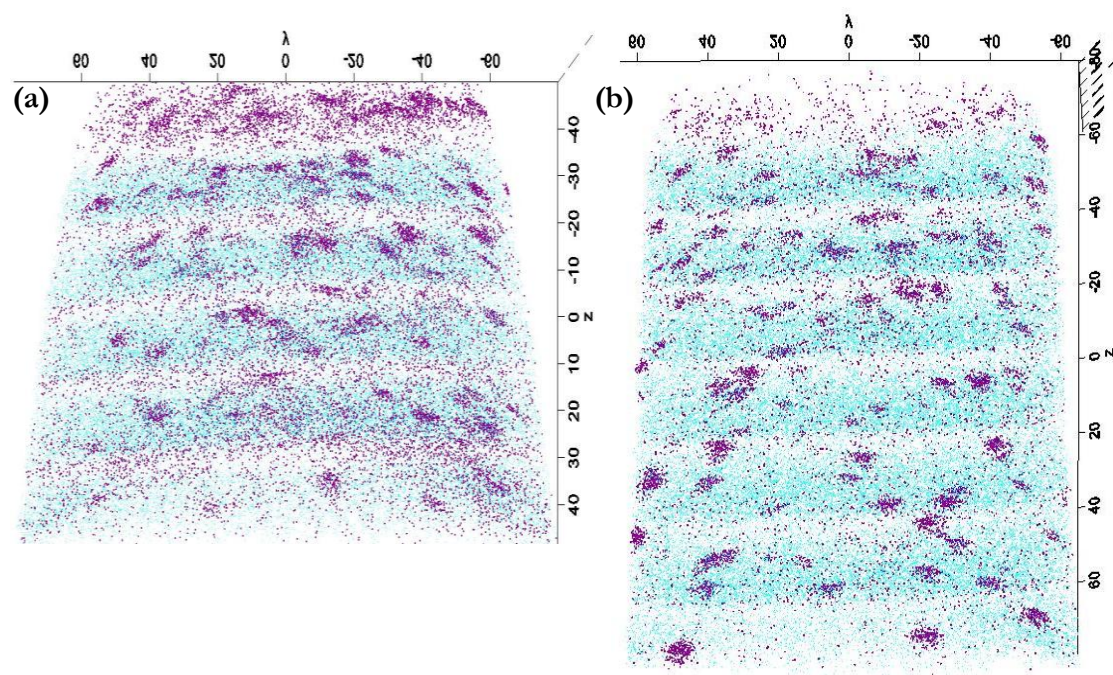
Figure 5.7. Reconstructed atom maps, with 100 % of Mg atoms shown as spheres of radius 0.2 nm, and 5 % of Al atoms shown as light blue dots (all other atoms omitted for clarity). Both atom maps appear to contain regions of increased Mg content. (a) Medium Mg flux sample. (b) High Mg flux sample.

Isoconcentration surfaces can also be used to represent the APT data. Figure 5.8 shows the medium Mg flux sample, with the top and bottom of the AlGaN layers shown using blue 5.5 at.% isoconcentration surfaces (corresponding to the nominal $Al_yGa_{1-y}N$ layer content of y = 0.11, assuming near stoichiometry in the GaN). The alternating AlGaN and GaN layers are labeled for clarity. Mg-rich clusters are highlighted using purple 1.5 at.% Mg isoconcentration surfaces. In this sample, the level of Mg is much lower on

average away from these clusters (approximately 0.02 at.%), so 1.5 at.% represents regions of significant Mg enrichment. It is important to note that the number and size of the Mg clusters depends on the isoconcentration surface used, as well as the level of smoothing. For layer isoconcentration surfaces, as shown in figure 5.8, a high level of smoothing is desirable; however the high level of smoothing also acts to 'spread out' the Mg content of the clusters, so a lower level of smoothing is used in quantitative studies of the Mg clusters. From the reconstructed data, it can be seen that there are more Mg clusters in the AlGaN layers than in the GaN layers (with approximately $(1.0 \pm 0.4) \times 10^{-4}$ clusters per nm^3 in the AlGaN and $(1.0 \pm 0.6) \times 10^{-5}$ clusters per nm^3 in the GaN, on average).
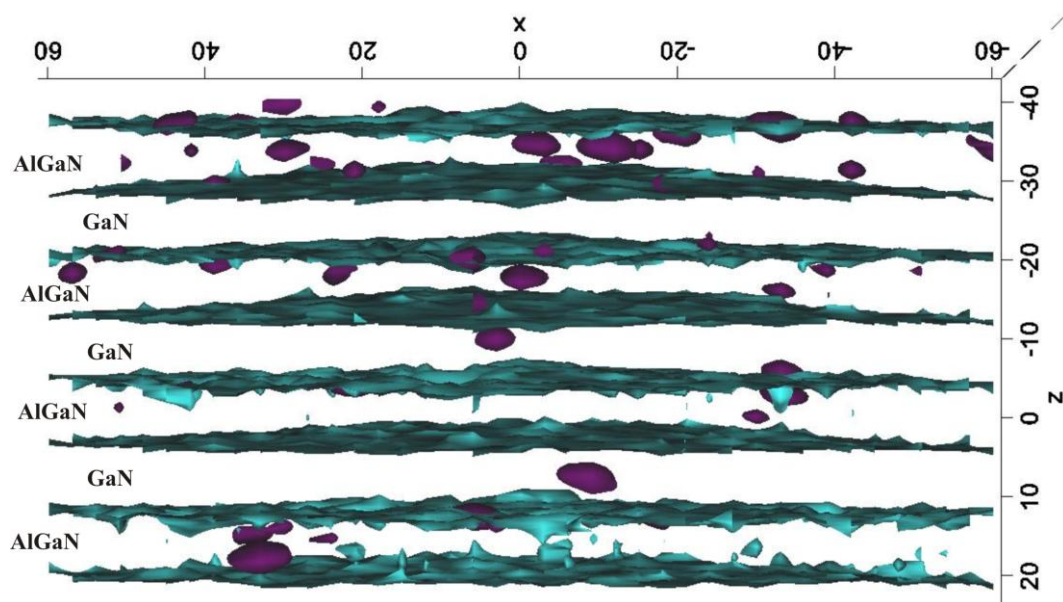
Figure 5.8. Reconstructed data set of the medium Mg flux SL, showing 5.5 at.% Al isoconcentration surfaces in blue at the top and bottom of each AlGaN layer (layers labeled for clarity), and 1.5 at.% Mg isoconcentration surfaces, showing the Mg-rich clusters.

5.4.1.2. Existence of Clustering

The atom maps in the preceding section appear to show that Mg clusters are present in the medium and high Mg flux samples, and that the low Mg flux sample does not exhibit such strong clustering. However, it is important to evaluate whether the observed distribution of Mg in fact deviates from that expected from a random alloy distribution. Thus, any observed clusters can be defined as having a random or non-random origin.

To assess whether the Mg distributions in our data sets would be expected to arise from random alloy fluctuations, the observed distribution was compared to a binomial distribution using a Pearson's χ^2 test[124]. This test is used in this chapter to determine the existence of Mg clusters, as well as in Chapters 6 and 7 to assess the In distribution in InGaN QWs and InAlN, respectively, therefore it is described in full here.

To conduct a χ^2 test, the volume of interest is first divided into blocks, or bins, each containing a certain number of atoms. The bin size selected is important, and should be chosen to contain a reasonable number of atoms of the species under investigation. If a material containing, say, five atomic percent Mg is divided into 100 atom bins, each bin would be expected to have five Mg atoms. A bin size of 10 atoms, however, would lead to only one Mg atom in every other bin, on average, indicating that the bin size is too small. Bin sizes corresponding to a volume much larger than the scale of the clustering investigated are also unsuitable, as Galtrey *et al.*[124] discussed in their investigation of possible In clustering in InGaN QWs. In this work, bin sizes were varied from 25 atoms up to more than 200 atoms, to ensure that the deviation from randomness was studied at multiple length scales. Once the data are divided into bins, the χ^2 statistic can be calculated as follows:

$$\chi^2 = \Sigma\ ((N_{obs} - N_{exp})^2\ /\ N_{exp})$$

where N_{obs} is the number of bins observed in the experimental data at a certain Mg content, and N_{exp} is the number of bins that would be expected from a random alloy, as modeled by a binomial distribution. Where necessary, several Mg contents were combined to ensure that all of the expected frequencies were greater than 5, as is generally advised for the χ^2 test. Finally, using the χ^2 value and the number of degrees of freedom (DOF) in the measurement, a χ^2 critical value, or p value, can be found. The p value indicates the probability that the observed distribution could have occurred by chance in a random alloy. A p value of less than or equal to 0.05 is generally interpreted as justification for rejecting the null hypothesis that the observed distribution is random.

When the χ^2 test was applied to the SL layers for the medium and high Mg flux SLs, the observed Mg distributions showed large deviations from the binomial distributions expected for a random alloy: for 100 atom bins, the p value for the medium and high Mg

flux samples was 0.000 for 8 and 10 DOF, respectively, indicating that the both SLs contained Mg clusters of a non-random origin. Figure 5.9a shows this deviation from randomness for the medium Mg flux SL, with a dashed line indicating the binomial distribution, and purple data points showing the observed Mg distribution. In section 5.4.1.4, the Mg-rich clusters will be examined in detail. χ^2 analysis of the low Mg flux sample resulted in a p value of 0.995, indicating that there were no clusters of a non-random origin; however, this analysis was based on just 2 DOF for 100 atom bins, due to the low level of Mg in the SL, which indicates that the statistical test has little relevance in this case. Varying the bin size from 25 to 500 atoms did not improve the statistical significance of the χ^2 analysis for the low Mg flux SL. A comparison between observed and expected Mg distributions for the low Mg flux SL is shown in figure 5.9b.
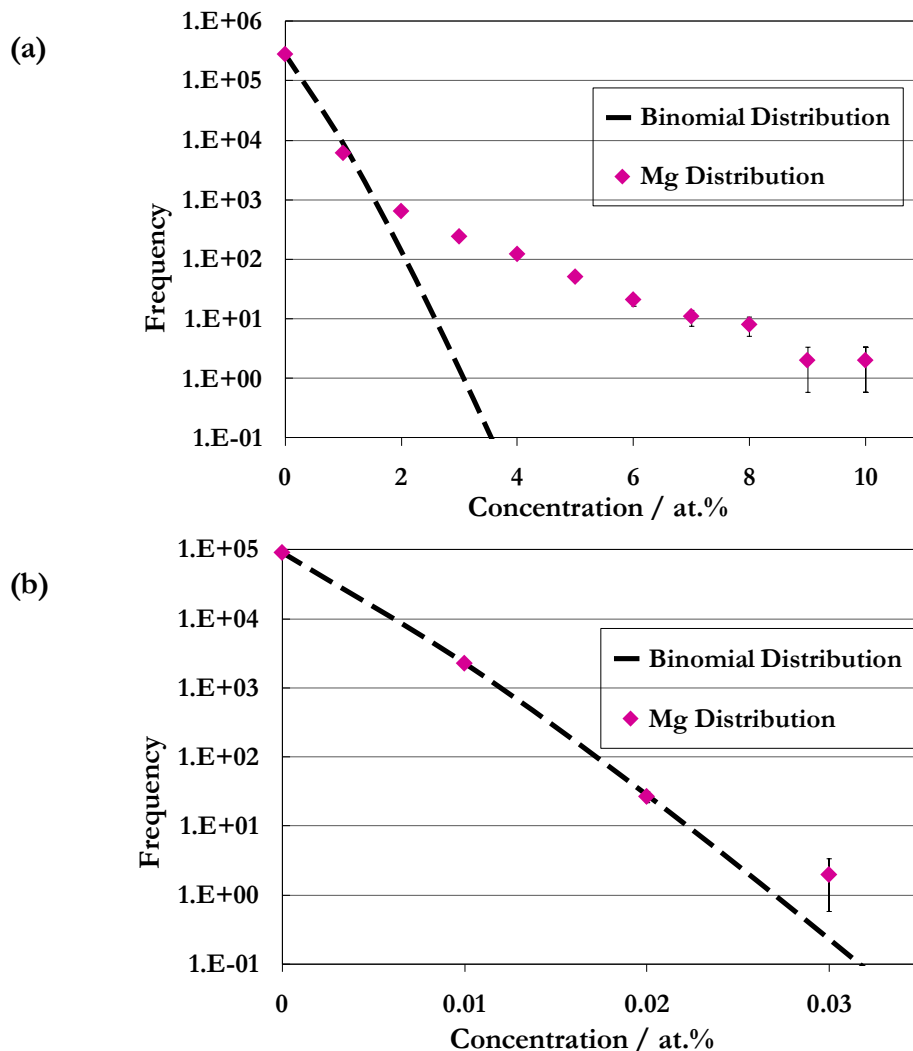
Figure 5.9. A comparison between the observed distribution of Mg (purple data points with error bars) and a binomial distribution. (a) For the medium Mg flux sample, showing the deviation of the Mg distribution from the binomial, which

indicates that the clusters have a non-random origin. (b) For the low Mg flux SL.

5.4.1.3. Mg Content of the SL

With both SIMS and APT data for all three of our SLs, it is possible to compare Mg concentration data found by each technique. It is worth noting, however, that APT is best used for relative, rather than absolute compositional information, as run conditions can affect the absolute composition observed, but are unlikely to alter the relative compositions within a data set. In this section, the Mg contents found by APT and SIMS for the SL as a whole, as well as the different types of layers will be compared. Additionally, using the APT data, the Mg content was measured away from the clusters in both types of layers, to investigate the Mg layer content without the influence of the Mg clusters. The compositions presented in this section, and throughout this work, were found using the bulk composition from the manual ranging of the mass spectrum.

The overall Mg concentration of the three SLs was measured using atom probe, and figure 5.10 shows the Mg contents measured for the three SLs, plotted against the Mg flux with which the samples were grown. The APT data indicate that the Mg content increases with increasing Mg flux, as would be expected. Corresponding SIMS measurements are shown in figure 5.5, however, this same trend was not clearly observed in the SIMS data.
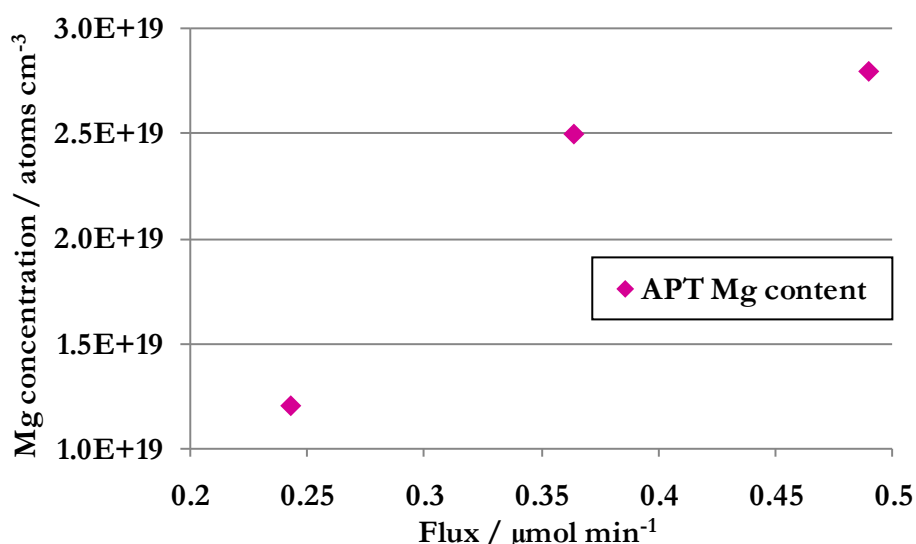
Figure 5.10. Mg contents measured using APT for the three SLs, plotted against the Mg flux with which each SL was grown. The Mg content is observed to increase with increasing Mg flux.

The SIMS measurements indicated that the AlGaN contained more Mg than the GaN, so the Mg contents of the two materials were found by APT, for comparison. The layers were isolated using 5.5 at.% Al isoconcentration surfaces, as shown in figure 5.8. For the medium and high Mg flux data sets, the Mg content of every layer was obtained. The low Mg flux data set contained many SL repeats, and as the layer isolation was highly time consuming with the current software, two SL repeats were measured each from the top, middle, and bottom of the data set. Table 5.1 summarises the difference in average Mg content in the AlGaN and GaN layers for the three SLs. In the low Mg flux sample, the APT data indicated that the two materials had similar Mg contents, although the AlGaN seemed to contain slightly more Mg. As the Mg flux was increased in the series, however, the average AlGaN layer Mg content was observed to rise much more than in the GaN. Additionally, within the AlGaN layers of the medium and high Mg flux samples, the standard deviation is notably higher, indicating a greater variation in the Mg contents of the individual AlGaN layers.

Table 5.1. Average Mg contents of the AlGaN and GaN layers, measured by APT.

SL type	Mg content of the AlGaN layers ($Mg\ cm^{-3}$)	Mg content of the GaN layers ($Mg\ cm^{-3}$)
Low Mg flux	$(1.5 \pm 0.1) \times 10^{19}$ (standard deviation of 0.2×10^{19})	$(1.3 \pm 0.1) \times 10^{19}$ (standard deviation of 0.2×10^{19})
Medium Mg flux	$(4.3 \pm 0.6) \times 10^{19}$ (standard deviation of 1.2×10^{19})	$(1.6 \pm 0.2) \times 10^{19}$ (standard deviation of 0.3×10^{19})
High Mg flux	$(4.5 \pm 0.5) \times 10^{19}$ (standard deviation of 1.1×10^{19})	$(1.9 \pm 0.1) \times 10^{19}$ (standard deviation of 0.3×10^{19})

As the Mg contents of the individual layers were measured by APT, it is possible to compare the SIMS and APT values for each layer. Figure 5.11 shows the Mg content of the layers from the top three SL repeats, as measured by APT, overlaid on the SIMS measurement for the medium Mg flux sample. The Mg content of the AlGaN layers is shown using purple circles, whereas the GaN layer Mg content is shown using purple diamonds. It should be noted that there were problems calibrating the SIMS data, as previously discussed, and so this comparison does not speak to the accuracy of the APT data. In fact, given the inaccuracies that may exist in both techniques, the results are

remarkably similar. The APT data appear to reinforce the SIMS observation that the Mg content decreased with distance into the sample.
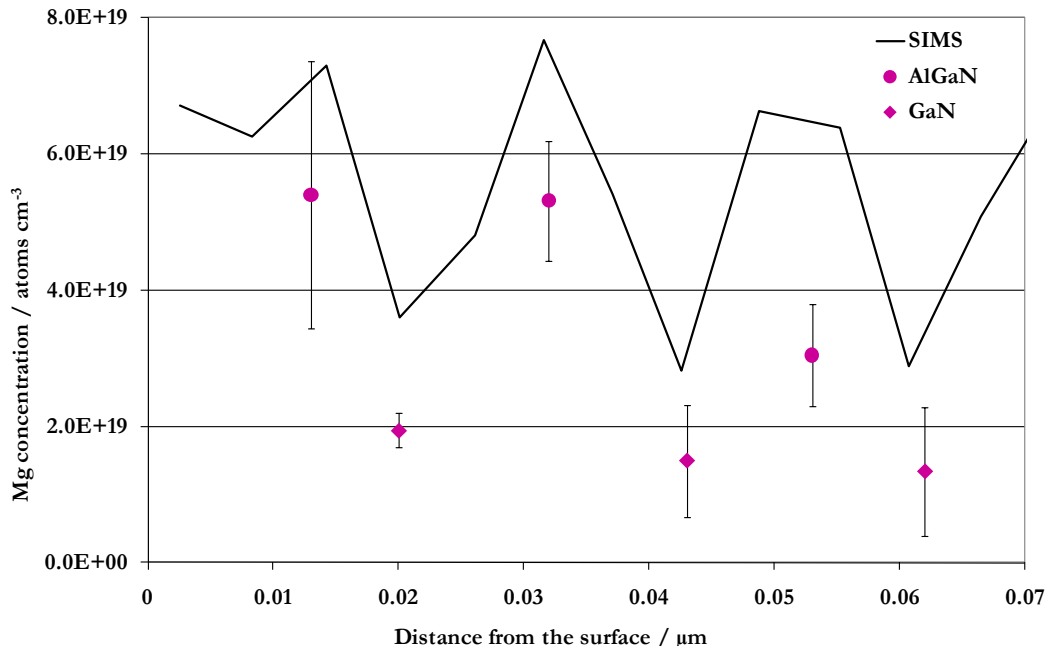
Figure 5.11. Comparison between SIMS and APT data for the medium Mg flux SL. The SIMS Mg trace is shown in black, and this is overlaid with the Mg contents of each layer, as measured by APT. The AlGaN layers correspond to the purple circles, and the GaN layers correspond to the purple diamonds.

To observe the difference in Mg contents of the two materials, without contribution from the clustered Mg, volumes away from the clusters were sampled. A region of interest (ROI) of 10 nm × 10 nm × 5 nm was used to sample a volume within one type of material. Samples were taken in both types of layers for the SLs that showed clustering. Table 5.2 summarises the average Mg contents for the volumes sampled within each material. Although there seems to be a higher Mg content in the AlGaN layers in both SL samples, an unpaired Student's t-test was applied, and suggested that there is not a genuine difference between the two means. Thus, these data suggest that the two materials incorporate similar amounts of Mg away from the clusters, with the excess Mg incorporation fueling the formation of clusters. The greater Mg content observed in the AlGaN layers seems to be mainly due to the presence of Mg-rich clusters, which are preferentially located in the AlGaN. It is also interesting to note that the Mg content away from the clusters is similar to the Mg content of the low Mg flux

SL, which may indicate that the low Mg flux SL contained a Mg content close to the limit, above which clusters begin to form under these growth conditions.

Table 5.2. Average Mg contents of the AlGaN and GaN layers away from the clusters, measured by sampling with ROIs of 10 nm × 10 nm × 5 nm wholly contained within one type of material.

SL type	Mg content of the AlGaN layers (Mg cm^{-3})	Mg content of the GaN layers (Mg cm^{-3})
Medium Mg flux	$(1.6 \pm 0.4) \times 10^{19}$	$(1.1 \pm 0.3) \times 10^{19}$
High Mg flux	$(2.5 \pm 0.9) \times 10^{19}$	$(1.2 \pm 0.5) \times 10^{19}$

5.4.1.4. Mg-Rich Clusters

As mentioned previously, the number of clusters and their size and shape are affected both by the isoconcentration value selected and the level of data smoothing used. To study the small clusters in our SLs, the smoothing was set to a low level (1 nm^3 volume pixel (voxel) size and 1 nm delocalisation in all directions), and a 4 at.% Mg isoconcentration value was chosen. With these values, it was possible to avoid selecting random background fluctuations in the Mg distribution. Additionally, the resulting surfaces visually appeared to provide a reasonable estimate for the boundary of the Mg-rich regions. In this section, the size and Mg content of the clusters is discussed.

The cluster size was defined as the greatest extent of the isoconcentration surface, and was measured for all clusters in the top three AlGaN/GaN repeats (which could be compared between the two SLs) of the medium and high Mg flux samples. The average size was remarkably similar in the two SLs, with the medium Mg flux sample having an average cluster size of 4.2 nm ± 0.2 nm, and the high Mg flux SL having an average cluster size of 4.0 nm ± 0.2 nm. (The systematic error present in this measurement is currently extremely difficult to determine. The errors given here are the "standard error", $\sigma/\sqrt{N}$, where σ is the standard deviation and N is the number of measurements.) To assess the hypothesis that these two means were different, an unpaired Student's *t*-test was applied to the size data from the two SLs, and suggested that there is not a genuine difference between the two means. Therefore, it appears that the even if the Mg flux is

different during SL growth, the resulting Mg clusters have a similar average size. The high Mg flux sample instead showed a greater cluster density: over the same volume in the top three repeats, the medium Mg flux sample contained 49 clusters, whereas the high Mg flux sample contained 57 clusters.

As the clusters have a lateral dimension that extends to just 4 nm on average, traditional microscopy techniques would struggle to ascertain their composition. With the APT data set, it was straightforward to obtain the average bulk Mg content within the clusters. Firstly, it is worth mentioning that the clusters do contain Ga, and those clusters in the AlGaN layers also contain Al, suggesting that they are not inclusions of an Mg_xN_y compound such as Mg_3N_2, as has been proposed in the literature[122], but rather they are volumes within the AlGaN or GaN matrix that show significant Mg enrichment.

To find the average cluster Mg content, an elliptical ROI (2 nm × 2 nm × 1 nm) was defined near the centre of each cluster in the top AlGaN layer, and the bulk composition within the ellipse was found. For the medium Mg flux sample, the average Mg content was 7.7 at.% (or 6.8×10^{21} Mg cm^{-3}), with a standard deviation of 1.8 at.%. The high Mg flux sample had a higher average cluster Mg content of 11.0 at.% (or 9.7×10^{21} Mg cm^{-3}), with a standard deviation of 3.1 at.%. Again, a Student's *t*-test was applied to assess the hypothesis that the two means were different, and suggested a confidence level greater than 99.95 % that the high Mg flux SL contained clusters with greater Mg content than the medium Mg flux SL. The considerably elevated Mg level within the clusters can be appreciated by comparing the average cluster Mg content with the Mg levels observed away from the clusters, summarised in table 5.2. There were too few clusters in the GaN layers to provide a meaningful average composition for comparison.

The suggestion in the literature that Mg segregates to the outside of Mg-rich inversion domains[122] motivated a study of the distribution of Mg within the clusters observed by APT. To observe how the Mg content changed through each cluster, a rectangular ROI of 1 nm × 1 nm × 10 nm was positioned through the middle of the cluster, as shown in figure 5.12a. To study compositional changes on such small length scales, the smoothing was set to a very low level (0.5 nm^3 voxel size and 0.5 nm delocalisation in all directions). A one dimensional (1D) concentration profile was calculated along the length of the ROI, and can be seen in figure 5.12b. By observing five separate clusters, it was found

that the Mg content increases substantially from the background level at the edges of the clusters; however, the Mg concentration is not then observed to drop off towards the cluster centre. Thus, there is no evidence from the APT data set that the Mg segregates to the outside of the Mg-rich regions. Yet it should be noted that the data shown in figure 5.12b are very noisy, due to the limited number of atoms per region used to calculate the 1D concentration profile. It may, therefore, be difficult to draw clear conclusions on this issue for such small clusters.
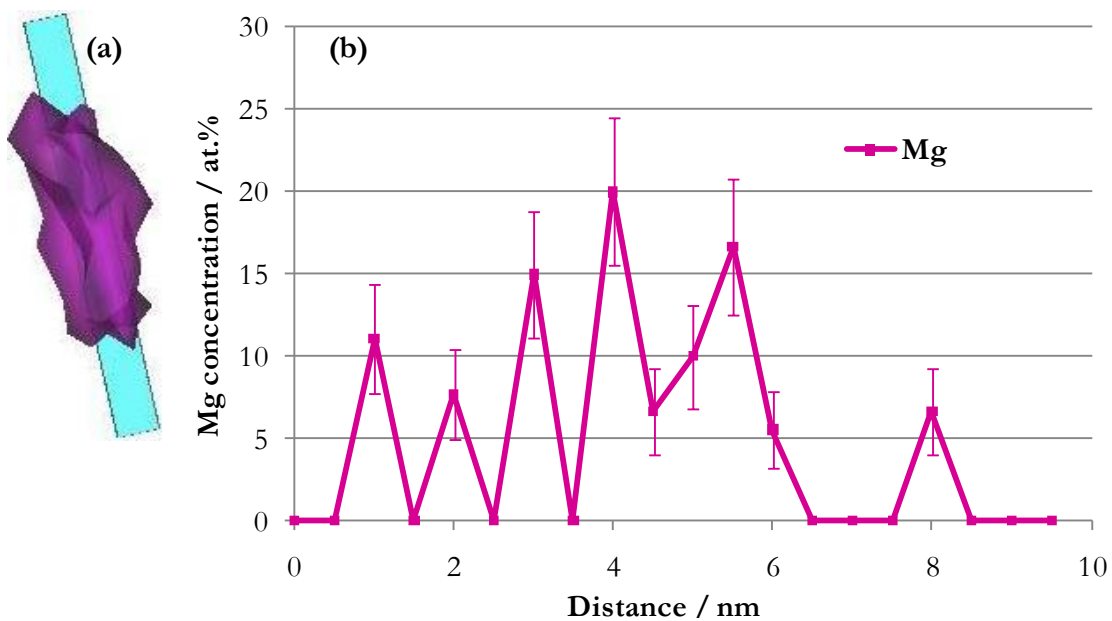
Figure 5.12. (a) Rectangular ROI of 1 nm × 1 nm × 10 nm running through a Mg cluster, used to measure the concentration profile across the cluster. (b) 1D concentration profile from the ROI pictured in (a), showing that the Mg level increases sharply at the edge of the cluster, but does not then drop off towards the middle of the cluster.

5.4.2. TEM

Having observed Mg-rich clusters in the APT, TEM was used to investigate their structure and composition, as well as to evaluate their similarity to defects reported in the literature[121,120,122]. Due to the time consuming nature of TEM sample preparation and analysis, only the medium Mg flux SL was selected for TEM analysis.

5.4.2.1. Energy Filtered Lattice Fringe Images

The small size of the Mg-rich regions makes it challenging to image them through the thickness of the TEM sample. As mentioned in section 5.3.5, a KOH treatment of the TEM sample was used to remove amorphous material, which helped in the imaging of the Mg-rich regions. Energy filtered HRTEM images were obtained of the clusters, and a cross-sectional image of the SL can be seen in figure 5.13a. The GaN and AlGaN layers are labeled, with the interfaces indicated by dotted lines. A small portion of the image, containing a defect (indicated by the white box in figure 5.13a), is shown in figure 5.13b. The defects were observed to be triangular in cross-section, with the tip of every defect pointing in the $[000\bar{1}]$ direction, consistent with Mg-rich PIDs reported in the literature[121,122]. The defects are seen in both types of layer, but not in the non-intentionally doped GaN cap, suggesting that the defects are related to the presence of Mg dopants.
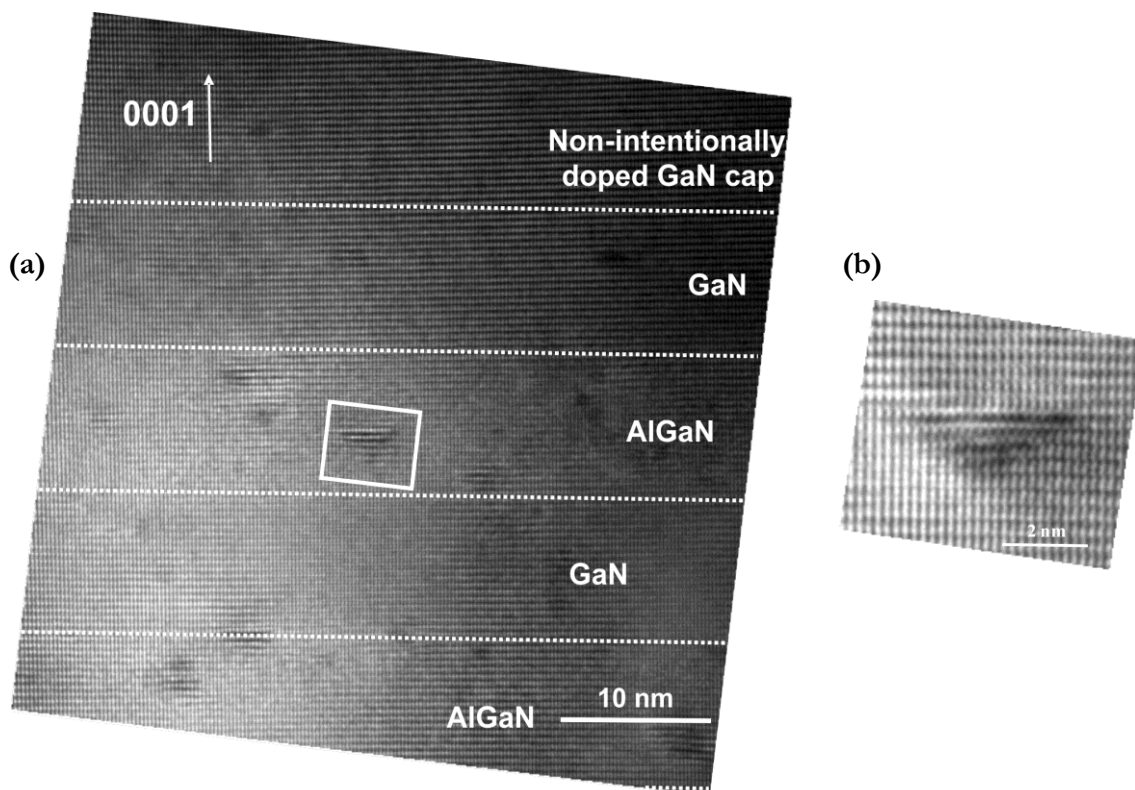
Figure 5.13. (a) Cross-sectional energy filtered HRTEM image of the top layers of the medium Mg flux SL and the non-intentionally doped GaN capping layer. Dotted lines provide a guide to the layer interfaces, and the layers are labeled. Pyramidal defects, triangular in cross-section, can be seen in the SL layers, but not in the GaN cap. (b) Detail from the white box in (a), containing a defect.

The average defect size was found from the TEM images by measuring the widest extent of the triangular base. The average size of the defects was found to be 5.1 nm ± 0.8 nm. A comparison between defect and cluster sizes measured by TEM and APT, respectively, will be discussed in section 5.4.3.

5.4.2.2. Compositional Measurements

Compositional measurements of the defects were attempted using both STEM-EELS and EFTEM mapping (with both jump ratio and three window technique background subtraction). Unfortunately, it was not possible to detect Mg in the defects or in the surrounding matrix using either method, making it impossible in this case to determine whether they were Mg-rich. The measurements made with these techniques are hampered by the relatively large sample thickness through which the small defects must be analysed, as well as by the projection of a 3D volume into a 2D image.

5.4.2.3. Inversion Domains

The structure of the defects observed in our SL sample was similar to those reported in the literature to be inversion domains. To confirm that our defects contained similar reversals of the crystal polarity, WBDF images of the same area were taken using the (0002) and $(000\bar{2})$ reflections. Contrast reversal was observed between the two images, as shown in figure 5.14, which is typical of inversion domains[121].
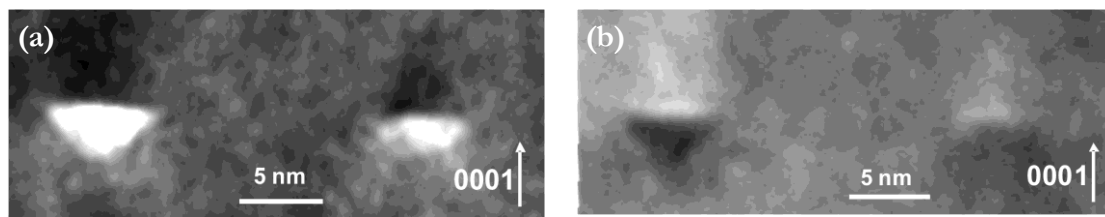
Figure 5.14. (a) (0002) WBDF TEM image of two defects, taken along the [10$\bar{1}$0] axis. (b) (000$\bar{2}$) WBDF TEM image of the same defects as in (a). Contrast reversal between the two images indicates that the defects are inversion domains.

5.4.3. COMPARISON OF INFORMATION GAINED BY APT AND TEM

The similarity in size and distribution of the clusters and defects measured by APT and TEM, respectively, suggests that the features observed by each technique are the same, and can best be described as Mg-rich PIDs. In addition, similar PIDs have been

observed in the literature[121], and reported to be Mg-rich[122], lending weight to the conclusion that the Mg-rich clusters observed by APT are the same as the PIDs observed by TEM. With information about the numerical density, size, shape, and Mg content of these PIDs, measured by one or both techniques, it is possible to compare the information obtained about the Mg-rich PIDs.

The numerical density of the clusters can be obtained easily in the APT data set, due to the 3D nature of the information. In the TEM study, on the other hand, this density is much more difficult to determine. Firstly, the thickness of the sample can be difficult to determine, and secondly, projection of the 3D sample information into the 2D image may obscure some defects entirely, or cause multiple PIDs to appear as one. Thus, numerical density is much more easily characterised using APT, for our SL data. It should be noted that 3D TEM techniques, such as electron tomography, may provide greater insight into the numerical density, but these methods have not yet been attempted with this sample.

When considering the size of the clusters measured by APT, it is important to consider whether the Mg-rich regions had a sufficiently different evaporation field to the surrounding matrix to cause trajectory aberrations, resulting in magnification errors within the reconstructed data set[125]. The similarity in average feature size measured by both APT and TEM suggests that local magnification effects did not substantially influence the size of the features observed by APT. This indicates, therefore, that the Mg-rich regions are unlikely to have had a significantly different evaporation field to the surrounding matrix. Although the sizes of the regions were similarly measured between APT and TEM, the information gained about the features is fundamentally different: in TEM, the size of the inversion domain is measured. APT instead measures the extent of the Mg-rich region, which could, like a Cottrell atmosphere around a TD, extend beyond the boundaries of the structural defect. With TEM measurement of the structural defect, it is also important to note that the feature size could be underestimated if the defect were to intersect the TEM sample surface.

A similar comment can be made about the shape measured by the two methods: the shape of the PID is measured by TEM, whereas the shape of the Mg-rich region is measured by APT. In APT, the isoconcentration value and smoothing selected further

complicates the definition of feature shape, as the observed shape can change depending on the values chosen. Additionally, even if the Mg were to lie exactly within the PID, the random fluctuations in the Mg distribution could blur the isoconcentration surface. Therefore, the fact that the APT does not show a pyramidal cluster shape does not provide conclusive information about whether the Mg-rich region is enclosed within the PID. TEM and APT of the *same* defect could provide insight into this question.

The composition of the PIDs was only found using APT, as both TEM-based methods were unsuccessful at studying the composition of such small defects. The APT data set permitted the average Mg content of the clusters to be obtained, and allowed an attempt to be made to study the Mg content variation within the clusters.

The preceding discussion, comparing the information gained by APT and TEM about the medium Mg flux sample, is summarised in table 5.3. It is evident that a wealth of information can be obtained about even tiny features such as the PIDs observed in our SLs, by making use of the combination of APT and TEM techniques.

Table 5.3. Comparison between information gained about the Mg-rich regions by APT and TEM for the medium Mg flux sample.

Defect/ Cluster Property	APT	TEM
Density	More clusters in AlGaN than GaN AlGaN $(1 \pm 0.4) \times 10^{-4}$ clusters/nm^3 GaN $(1 \pm 0.6) \times 10^{-5}$ clusters/nm^3 (on average)	More defects in AlGaN than GaN (numerical density difficult to obtain due to unknown thickness of TEM sample)
Size	4.2 nm $\pm$ 0.2 nm (estimates size of Mg-rich region)	5.1 $\pm$ 0.8 nm (at widest extent of the defect)
Shape	Difficult to determine (Mg-rich regions do not appear to have a pyramidal shape)	Triangular in cross-section, all pointing in the [000$\bar{1}$] direction
Mg content	7.7 at.% average Mg content, with a standard deviation of 1.8 at.%	STEM-EELS and EFTEM mapping both unsuccessful

5.5. SUMMARY

In this chapter, a series of three Mg-doped SLs grown with different Mg fluxes was characterised using APT and TEM. Atom maps were reconstructed for all three samples, and the APT data suggested that the medium and high Mg flux SLs contained Mg-rich clusters, and that the low Mg flux SL was devoid of such clustering. Statistical methods were used to confirm this observation, by comparing the observed Mg distributions with those expected from a random alloy. In this way, the clusters in the medium and high Mg flux SLs were shown to have a non-random origin.

The Mg content of the SL as a whole was measured by APT, which indicated that as the Mg flux was increased, the SL Mg incorporation also increased. As the SIMS measurements indicated that the AlGaN contained more Mg than the GaN, the different layer Mg contents were studied using the APT data, both with and without the influence of the Mg-rich clusters. The APT data confirmed that the AlGaN contained more Mg, and suggested that much of the excess Mg was due to the increased density of clusters in the AlGaN layers. Away from the clusters, the three SL samples were found to have similar Mg contents. From this result, one might expect that the SL samples would show similar carrier concentrations. The observed decrease in carrier concentration as the Mg flux was increased through the SL series suggests that the Mg clusters have an additional detrimental effect on the conductivity. This effect may be caused by local electrical charge or carrier trapping at the clusters; however further investigations are needed to determine the cause of any detrimental effect of the Mg-rich clusters on the electrical properties of the SL.

The size of the Mg clusters was measured by APT, along with their average Mg content. The clusters were found to have an average size of approximately 4 nm, and to contain Mg levels two orders of magnitude higher than the background level. The Mg content was not observed to fall off at the centre of the clusters, and so the APT data did not provide any evidence that the Mg segregates to the outside of the Mg-rich regions.

Finally, a TEM sample of the medium Mg flux sample was examined using energy filtered HRTEM and WBDF. PIDs were observed in the Mg-doped SL layers, similar to those reported in the literature. As the size and distribution of these defects was

comparable to the clusters observed in the APT, it was concluded that the two techniques were measuring the same feature, allowing a comparison to be made between the information gained about the Mg-rich PIDs by both techniques. The two techniques are highly complementary, in this case providing a large amount of information about our Mg-rich PIDs.

6

APT STUDIES OF THE MICROSTRUCTURAL ORIGIN OF LOCALISATION IN InGaN

6.1. AIMS

Chapter 3 introduced the remarkable capacity of GaN-based devices to emit light, despite their high threading dislocation density. The reason for this behaviour has been a subject of intense debate, and many mechanisms have been suggested for localisation of charge carriers away from defects in the InGaN QWs that make up the active region of such devices. In this chapter, we will discuss the microstructural origin of localisation in InGaN, and attempt to improve our understanding of the possible localisation mechanisms by using APT to study InGaN/GaN MQWs.

6.1.1. APT OF BLUE QWs

Recently, APT has been used to study InGaN/GaN MQWs in an attempt to answer the questions surrounding the existence of indium 'clusters', which have been suggested to localise the charge carriers[126]. Building on this work, our first aim was to study a blue-

emitting InGaN/GaN MQW structure with APT, using both standard orientation and side-on samples. It was hoped that with the side-on samples, as described in section 4.5.1, it would be possible to collect a large amount of data from the MQWs running down the length of the APT sample. Additionally, with the side-on samples, we aimed to use the superior z-resolution of the LEAP to investigate the In distribution in the plane of the wells in more detail than has previously been possible. If the standard orientation and side-on APT data sets could be obtained, we hoped to compare the observed In distributions from the InGaN MQWs to those expected from a random alloy.

6.1.2. APT OF ELECTRON BEAM IRRADIATED BLUE QWS

It has been proposed that electron beam exposure during TEM-based characterisation damages InGaN, causing strain contrast that has previously been attributed to In clustering[127]. The next aim of this chapter was to prepare APT samples containing blue-emitting InGaN/GaN MQWs, and to irradiate a number of these samples with a known electron beam dose in the TEM. We then aimed to run both irradiated samples and non-irradiated reference samples in the LEAP. If data sets from both types of sample were collected, we aimed to assess any changes in the In distribution, as well as any other changes in the sample microstructure, between the reference and irradiated samples.

6.1.3. APT OF GREEN QWS WITH GROSS WELL-WIDTH FLUCTUATIONS

Broader scale microstructures have been observed in InGaN MQWs, which may function to keep carriers away from dislocations[104,128,129,130]. One such microstructure, in which gross fluctuations in QW width were observed, resulted in particularly efficient green emission[129]. The next aim of this chapter was to use APT to study green-emitting MQWs with these gross well-width fluctuations, to investigate the morphology and composition of the wells, in an effort to study how these properties might affect the charge carrier recombination.

6.1.4. APT OF MBE-GROWN QWS

The previous aims of this chapter have focused on the characterisation of MOVPE-grown InGaN MQWs. Our final aim was to use APT to study a QW that was grown by MBE. If a data set containing an MBE-grown InGaN QW was obtained, we hoped to again compare the In distribution observed with that expected from a random alloy. In this way, we could compare the MBE and MOVPE-grown samples, and thereby extend our understanding of InGaN/GaN QW microstructure to include MBE-grown material.

6.2. BACKGROUND

In this section, some of the proposed mechanisms for localisation of carriers in InGaN will be introduced, with the discussion focusing on those mechanisms investigated in the experimental work in this chapter. Particular attention will be paid to the model that postulates carrier localisation at non-random variations in the In distribution on the 3 to 5 nm scale, usually termed 'indium clustering', as well as experiments that seem to refute this model. A number of other localisation mechanisms will then be discussed in brief. The final section focuses on QWs that show gross well-width fluctuations, as broader scale microstructure (on the 100 nm scale) has also been shown to affect the luminescence from QWs.

6.2.1. LOCALISATION IN InGAN QWs

6.2.1.1. Light Output and Carrier Recombination

As introduced in Chapter 1, GaN-based LEDs and LDs often employ InGaN QWs in the active region of the device, from which light emission is achieved. However, TDs have been suggested to act as non-radiative recombination centres, limiting the efficiency of such devices[131]. To explain the seeming paradox of bright light output from high TD density material, it has long been suggested that some feature of the micro- or nano-structure prevents carriers from diffusing to TDs, hence preventing non-radiative recombination. The next section will focus on the model of In clustering.

6.2.1.2. Indium Clustering Model

The existence of In clusters within InGaN QWs was proposed by Narukawa et al.[132]. Cross-sectional TEM imaging was used to examine the microstructure of the QWs, which were found to contain small dark regions of strain contrast, with diameters of between 2 and 5 nm. Figure 6.1 shows a cross sectional image that exhibited this contrast, which was presented by Narukawa et al.[132]. The authors interpreted these regions to be self-formed quantum dots, which energy dispersive X-ray spectroscopy (EDX) analysis suggested were rich in In, compared to the surrounding well. It should be noted, however, that the error on these EDX measurements may have been large, as the authors mention that there was significant spreading of the incident electron beam

used for analysis, and do not specify the size of the incident probe. Such clusters would be expected to localise carriers, due to the reduced bandgap of the In-rich material[133].
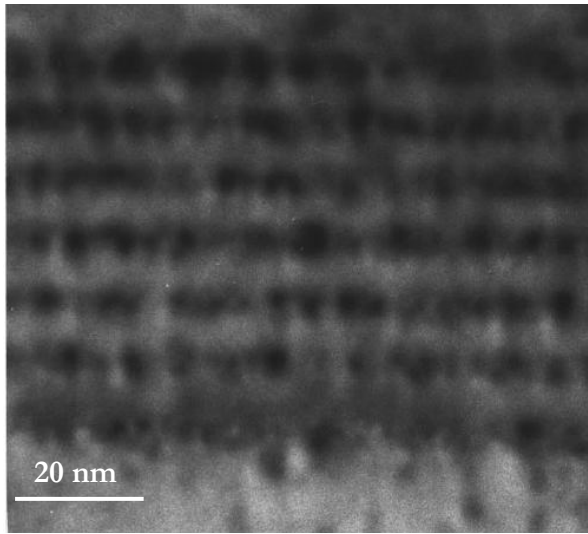
Figure 6.1. From Narukawa et al.[132], a cross-sectional TEM image of InGaN MQWs, in which blotchy contrast can be observed within the wells. This strain contrast was interpreted as self-formed quantum dot-like regions, which EDX analysis suggested were In-rich.

In support of the In clustering model, Gerthsen et al.[134] used lattice fringe spacing analysis of HRTEM images to suggest that the In enrichment of the clusters could be in excess of 0.8 (here quoted as the value of x in $In_xGa_{1-x}N$). Figure 6.2 shows a colour map of the local In content of the QW, which contains a small region with In content greater than x = 0.73.
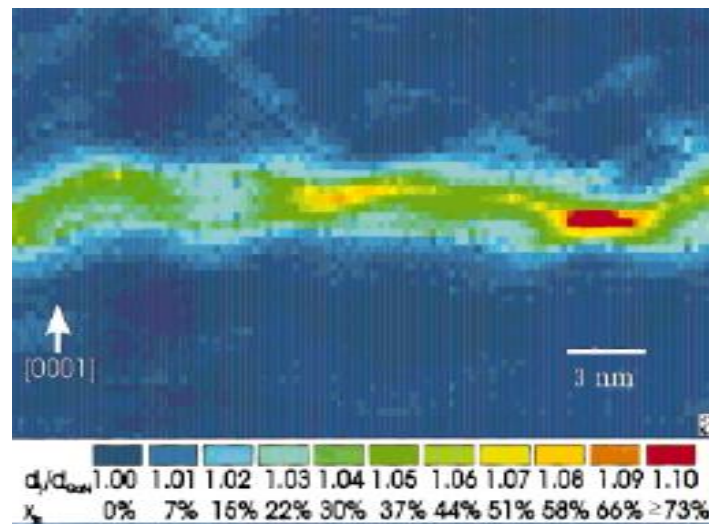
Figure 6.2. From Gerthsen et al.[134], a map of local In concentration within an InGaN QW, produced using lattice fringe spacing analysis of HRTEM images. A small region can be observed that was suggested to have more than x = 0.73 In.

The observed regions of high In content were proposed to have formed by spinodal decomposition, a barrier-less phase separation mechanism[132]. This conclusion was based

on the theoretical phase diagram of bulk, relaxed InGaN proposed by Ho and Stringfellow[135], as shown in figure 6.3. At typical InGaN growth temperatures of between 700 and 800 °C, their calculations suggested that for blue and green-emitting QWs (containing around x =0.2 In), decomposition would occur, leading to regions of high and low In content. With experimental evidence for In clustering, alongside the theoretical basis for cluster formation, it seemed that the enigma of GaN-based LEDs had been explained.
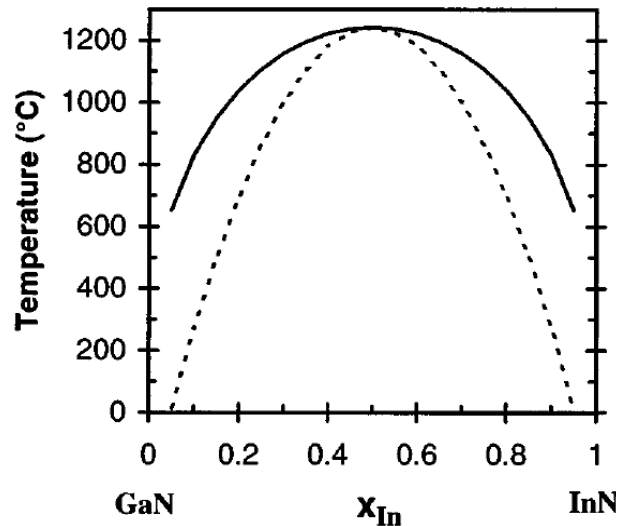
Figure 6.3. From Ho and Stringfellow[135], a theoretical phase diagram calculated for bulk InGaN, suggesting that spinodal decomposition would occur in the InGaN QW regions of blue and green-emitting QWs, which contain about x = 0.2.

6.2.1.3. Challenges to the Indium Clustering Model

It is important to note that the phase diagram calculated by Ho and Stringfellow[135] did not take into account coherency strains, which would occur between the In-rich clusters and the In-depleted matrix if decomposition were to occur. Such coherency strains could provide an energetic barrier to decomposition. Further problems with the In clustering model also began to surface: Karpov[136] recognised that the phase diagram shown above was for bulk-like relaxed GaN, and did not accurately model InGaN QWs that are biaxially strained, due to lattice mismatch with GaN. Karpov[136] calculated the phase diagram of biaxially strained InGaN, which can be seen in figure 6.4. The spinode was dramatically shifted to higher indium contents and lower temperatures, implying that phase separation would not occur in blue and green-emitting QWs. Indeed, the author calculated that InGaN should be a random alloy in blue, green and UV-emitting QWs. In support of these findings, recent phase equilibria calculations by Chan *et al.*[133] also suggest that the spinode is suppressed by biaxial strain.
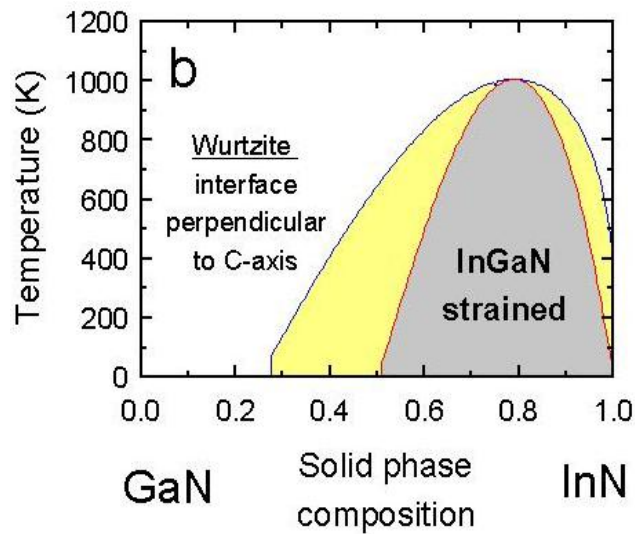
Figure 6.4. From Karpov[136], a theoretical phase diagram calculated for InGaN, taking into account the effect of biaxial strains. Compared to bulk InGaN, phase separation is suppressed at low In contents, suggesting that phase separation would not occur in blue, green and UV-emitting QWs.

Doubt was cast onto the TEM-based evidence for indium clustering by Smeeton et al.[127] and O'Neill et al.[137], who both observed that the high electron current density incident on TEM specimens during their examination appeared to be damaging the QWs. Both reports found that InGaN QWs that had not been exposed to the electron beam prior to the image being taken showed little to none of the strain contrast previously associated with clustering. Upon further exposure to the electron beam, however, these rather uniform QWs were observed to develop definite fluctuations in strain contrast. Figure 6.5a-d shows the evolution of strain contrast observed by Smeeton et al.[127], using HRTEM lattice fringe images with increasing exposure times to a 200 kV electron beam flux of approximately 35 A cm^{-2}.
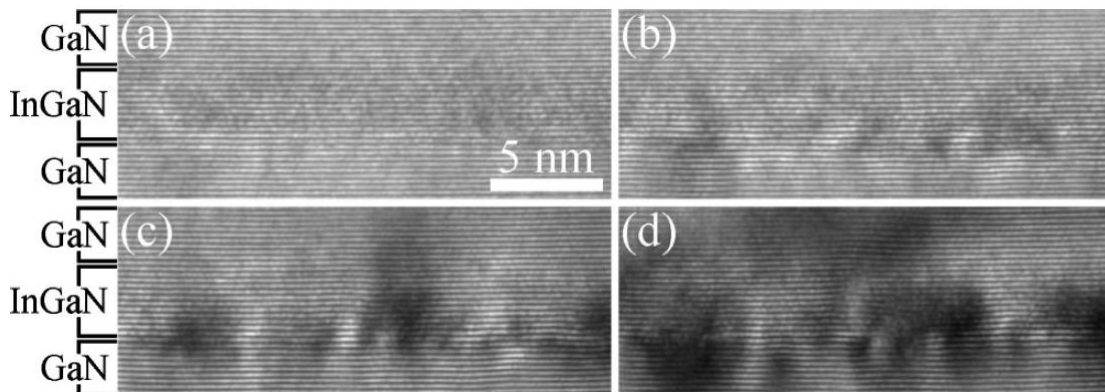
Figure 6.5. From Smeeton et al.[127], HRTEM lattice fringe images, showing the effect of increasing exposure time of the InGaN QW to a 200 kV electron beam flux of approximately 35 A cm^{-2}. (a) 20 s exposure, (b) 220 s exposure, (c) 420 s exposure, (d) 620 s exposure.

Smeeton *et al.*[127] noted that the strain contrast shown in figure 6.5d was typical of QW images obtained when particular care was not paid to minimising the electron beam exposure, and that the image shows contrast similar to what might be expected from genuine clustering. Both sets of authors concluded that the potential certainly existed for false cluster detection in TEM experiments, which cast significant doubt onto the validity of the In clustering model. In a further study, Smeeton *et al.*[138] showed that this electron beam-induced strain contrast was present even in a TEM sample that was prepared without thinning in the PIPS™, which could cause ion beam damage to the sample.

To circumvent the problem of electron beam damage, APT was used to study the In distribution in InGaN QWs[126,115]. Galtrey *et al.*[115] used the LEAP to study both blue and green-emitting QWs. In the resulting APT data sets, regions were selected from within the QW layers, and the data were divided into blocks of, for instance, 50 atoms. The indium content of these blocks was measured and the observed distribution of In contents was compared with a random alloy, which would be expected to follow a binomial distribution. Figure 6.6a shows a reconstructed atom map of three green-emitting InGaN/GaN QWs, with the In atoms shown as black and the Ga atoms shown as gray. All other ions are omitted for clarity. The results of the statistical analysis can be seen in figure 6.6b, where the observed In distribution is shown with crosses, and the binomial distribution with a black line.
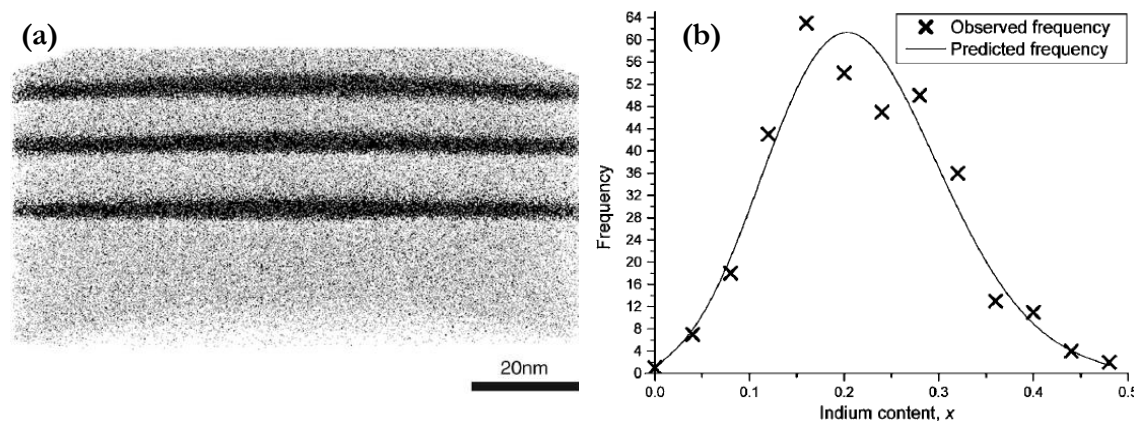
Figure 6.6. From Galtrey *et al.*[115], (a) Reconstructed atom map of green-emitting InGaN/GaN QWs, with In atoms shown in black, Ga atoms shown in gray, and all other atoms omitted. (b) Comparison between the observed In distribution from (a) (black crosses) and the distribution expected from a random alloy.

Galtrey et al.[115] conducted a χ^2 test to compare the observed and predicted distributions, as described in section 5.4.1.2, and found no statistically significant deviation from randomness. Thus, it was concluded that the APT data provided no evidence for clustering in either sample, implying that In clusters cannot be necessary for bright light emission from InGaN QWs. Yet in their APT analysis, the authors could have achieved better spatial resolution: the QW material was located in the *x-y* plane of the data set, and the spatial resolution of the technique is better in the *z*-direction than in the *x* and *y* directions. Further weight could therefore be lent to the authors' conclusions if the clustering analysis were performed on QW material that ran down the length of the APT sample, to take advantage of the superior *z*-resolution. It is also important to note that the APT data presented by Galtrey et al.[115] do not imply that In clusters are never present in InGaN QWs.

6.2.1.4. Alternative Localisation Mechanisms

In addition to In clustering, a number of other charge carrier localisation mechanisms have been suggested, and may be of great importance, due to the doubts cast upon the existence of In clusters. Firstly, a number of theoretical studies have predicted that charge carriers may be localised at a near-atomic level, even in an entirely random alloy of InN and GaN[139,140,133]. Wang[140] modelled wurtzite InGaN, predicting hole localisation at chains of atoms containing just two adjacent In atoms. These -In-N-In- chains would be expected to exist even in a random alloy. Experimental work in support of these theoretical conclusions was provided by Chichibu et al.[141], who used positron annihilation spectroscopy to provide evidence for hole localisation on a short length scale, which the authors suggested was due to localisation at these -In-N-In- chains. However, a recent theoretical work by Chan et al.[133] found no obvious correlation between -In-N-In- chains and charge carrier localisation. However, the authors reported that in a random alloy the compositional fluctuations do act to strongly localise the holes. It should be noted that such atomic scale localisation may be present in InGaN QWs, regardless of other nanoscale or broader scale localisation mechanisms.

Nanoscale fluctuations in QW width, of the order of one or two monolayers, have also been suggested to be highly effective as a mechanism for carrier localisation[142]. In InGaN QWs, slight changes in well thickness would be expected to decrease the confinement energy as the QW width increases; in addition, the high piezoelectric

constants of this material also lead to band-bending in the strained QWs, an effect that increases with the well thickness[143]. In fact, Graham et al.[142] calculated that for a 3.3 nm thick QW with 25 % In, a one monolayer increase in thickness would shift the transition energy by 58 meV, which could localise charge carriers at room temperature. In support of this model, APT[115] and TEM[144] studies of InGaN QWs have demonstrated the existence of monolayer and bilayer fluctuations in well-width through investigation of upper and lower QW interface roughness. Recently, Watson-Parris et al.[145] calculated the localisation lengths of the electrons and holes in InGaN QWs using numerical solutions of the effective mass Schrödinger equation. The authors' model took into account the results of APT studies of InGaN QWs[115]: the distribution of In atoms was modelled as random, and the effect of well width fluctuations was also considered. The well width fluctuations were found to decrease the electron localisation length, although this effect was negligible for the holes. In agreement with the work of Chan et al.[133], the authors reported that the holes were localised around regions of high indium fraction within the random InGaN alloy.

Finally, broader scale microstructures have also been proposed to prevent carriers from reaching TDs and non-radiatively recombining. This effect differs slightly from the previously discussed localisation mechanisms, in which carriers are localised in a small region: these broad scale microstructures are suggested to provide a barrier to carrier diffusion to the TD, whilst allowing the charge carriers to otherwise move freely within the QW. As discussed in Chapter 4, Hangleiter et al.[104] observed V-pits in InGaN QWs. The sidewalls of these V-pits were decorated with thinner QWs, which would result in a higher potential in the region surrounding the TD, preventing the carriers from reaching the dislocation. Additionally, Grandjean et al.[130] found that pinning of surface steps by TDs during InGaN growth led to thinning of the QWs. Such broad scale screening of dislocations may indeed function alongside nanoscale and atomic scale charge carrier localisation.

Another broad scale microstructure that has been shown to affect the luminescence properties of InGaN QWs has been termed 'QW network structures'[129,146]. These structures are particularly relevant to the experiments that will be described in section 6.4.3, and are therefore discussed in more detail below.

6.2.2. QW NETWORK STRUCTURES

Van der Laak *et al.*[129] used TEM to observe gross thickness fluctuations in MOVPE-grown InGaN QWs. In this case, the term gross refers to fluctuations of between several monolayers and the full width of the well, in which case a gap is observed in the QW, filled with GaN. The authors postulated that the 'gappy' QW morphology was a result of the two-temperature MOVPE growth method used, in which the InGaN QW growth temperature was lower than that used for GaN barrier growth, and the QW was left exposed during the temperature ramp required for GaN growth.

Van der Laak *et al.*[129] then used AFM to study thin InGaN epilayers grown to have a surface representative of the gappy QW morphology: the epilayers were subjected to a temperature ramp similar to that used for GaN barrier growth, and then immediately cooled. The AFM images showed a network of interlinking InGaN strips, aligned roughly parallel to the [11$\bar{2}$0] direction, and separated by GaN-filled troughs, as shown in figure 6.7a. TEM was used to further characterise these network structures, and figure 6.7b shows a STEM-HAADF image of a cross-section through one of these strips, with crosses indicating the probe positions for EDX analyses of the In:Ga ratio. The EDX data are shown in figure 6.7c, suggesting that the centre of the strip is In rich, and the In content falls off towards the edges. The authors suggested that this composition profile would localise excitons at the centres of these strips.

As InGaN QWs grown by this two-temperature method have been shown to have high internal quantum efficiencies[147], van der Laak *et al.*[129] studied the relationship between the InGaN strips and the position of TDs. Using a bright field multi-beam imaging technique that revealed all types of TDs[93], the authors showed that $90 \pm 10\,\%$ of the TDs pass through the QW either in the gaps between strips, or in the very edges of the strips, where the In content is lower. This observation has more recently been confirmed by CL data[143]. The QW morphology thus results in screening effect, due to the higher potential around the dislocations.
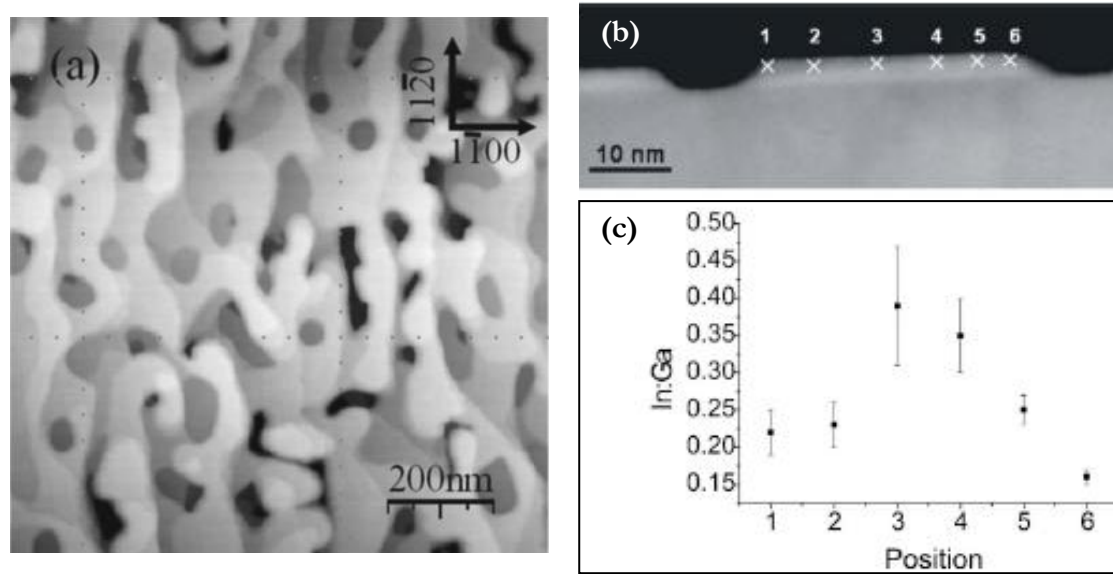
Figure 6.7. From van der Laak *et al.*[129], (a) an AFM image of an InGaN epilayer, grown to have a morphology similar to an InGaN QW grown by a two-temperature method. A network of interlinking InGaN strips can be observed, aligned roughly parallel to the [11$\bar{2}$0] direction. (b) STEM-HAADF cross-sectional image looking down an InGaN strip from a network structure. The crosses indicate the positions of the probe for EDX analysis. (c) EDX results, showing that the centre of the strip is In-rich, and the In content decreases towards the edges of the strip.

6.3. EXPERIMENTAL

6.3.1. SAMPLE GROWTH

The blue-emitting MQW samples studied in this chapter have been described in section 4.4.1, as Sample A and Sample B, both capped with GaN to facilitate APT sample preparation.

The green-emitting sample with gross well-width fluctuations was grown on a low TD density template using a 3D to 2D method, as described in section 4.4.1. On this template, an $In_{0.2}Ga_{0.8}N$/GaN 10 QW structure was grown with a two temperature method, in which the InGaN wells were grown at 680 °C and the GaN barriers were grown at 860 °C. No growth took place during the temperature ramp between the well

and barrier growth. This green-emitting sample was previously characterised by Dr. Pedro Costa, who used cross-sectional STEM-HAADF imaging to study the gross fluctuations in well-width, as shown in figure 6.8. Gaps can be observed in the QWs, as labeled in the figure. Additionally, the photoluminescence from this sample was analysed, and for the 552 nm emission wavelength, it exhibited a high internal quantum efficiency of 12 %[147].
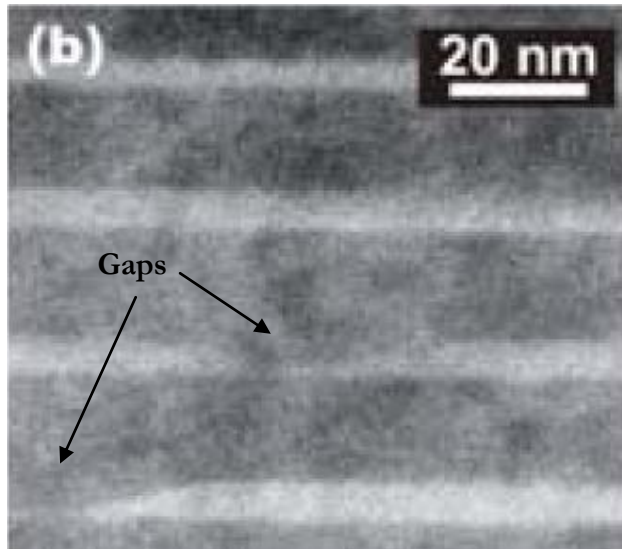
Figure 6.8. From Costa *et al.*[147], a cross-sectional STEM-HAADF image of the green-emitting sample studied in this chapter. The wells were observed to exhibit gross fluctuations in width, even appearing to be absent in some regions, leaving a gap in the QW.

Finally, the MBE-grown InGaN QW was grown at Sharp Laboratories of Europe, as discussed in section 2.1.2. The QW was part of a full sequence of layers used in a green-emitting laser diode. Figure 6.9 shows the nominal layer structure, including the Si or Mg dopants used in each layer to produce either n-type or p-type material, respectively. The 10 µm MOVPE-grown GaN template was supplied by Lumilog. On this template, the layers up to the InGaN QW were grown by reactive MBE. Both the QW and the AlGaN layer immediately above it were then grown by RF-PAMBE. The subsequent layers were then grown by reactive MBE. The Mg dopant level in the p-type layers was measured with SIMS at Sharp Laboratories of Europe, and found to be in the range of $3 - 5 \times 10^{19}$ cm^{-3}.

Electroluminescence (EL) measurements on the MBE-grown sample were provided by Sharp Laboratories of Europe, and showed that an area near the centre of the wafer had an emission wavelength of approximately 540 nm, whereas an area nearer the edge had an emission wavelength nearer to 490 nm. This difference was believed to be due to the substrate mounting during MBE growth, which caused the wafer temperature to increase slightly from the centre to the edge of the sample. Although only data from the QW will

be examined in this chapter, further characterisation of the laser diode structure will be the subject of Chapter 8.

Nominal Layer Structure	Dopant
10 nm GaN	Mg
595 nm $Al_{0.045}Ga_{0.955}N$	Mg
235 nm GaN	Mg
5 nm $Al_{0.2}Ga_{0.8}N$	
3.5 nm $In_{0.18}Ga_{0.82}N$ QW	
20 nm GaN	
100 nm $In_{0.02}Ga_{0.98}N$	Si
55 nm GaN	Si
480 x (1.6 nm $Al_{0.1}Ga_{0.9}N$ + 1.6 nm GaN) superlattice	Si
220 nm GaN	Si
10 um GaN	Si
Al_2O_3 substrate	

Figure 6.9. Nominal layer structure of the green-emitting laser diode structure, grown by MBE at Sharp Laboratories of Europe. The InGaN QW studied in this chapter was grown to be 3.5 nm thick, with x = 0.18 In. Mg and Si were used to dope the material p- and n-type, respectively. The dopant used is indicated to the right of each layer.

6.3.2. APT SAMPLE PREPARATION

The APT samples used in this chapter were prepared using the standard liftout and annular milling method, as described in section 2.5.2. All samples were prepared in Cambridge, using an FEI Company™ Helios Nanolab™ dual beam FIB/SEM with an Omniprobe Autoprobe™ 200 micromanipulator. The samples were mounted onto microtips, with the exception of the APT sample that was exposed to the electron beam in the TEM, which used a Cu/W needle mount. The side-on orientation samples were prepared using the method described in section 4.5.1.

6.3.3. TEM

The blue QW sample on a Cu/W mount was imaged and electron beam irradiated with the TEM, using instrumentation as described in section 4.4.4, and with the help of Dr. Jonathan Barnard. The QWs were imaged prior to TEM-mode irradiation using STEM-HAADF, with effort taken to limit the electron dose to the InGaN in order to take 'pre-damage' images. The STEM-HAADF images were taken near the $<11\bar{2}0>$ zone axis. The QWs were then exposed to the 200 kV electron beam in TEM-mode for a total of 64 minutes. Although this irradiation time was longer than the exposure times

shown to damage InGaN QWs by Smeeton *et al.*[127], the APT sample was significantly thicker (greater than 150 nm in diameter at the QWs) than the TEM thin foils presented by the authors, and this experiment aimed to ensure that damage to the QWs had occurred. The current entering the CCD camera was measured with a picoammeter and the current density incident on the sample was found by dividing this value by the irradiated area. The current density during electron beam exposure was approximately 1.1 A cm^{-2}. STEM-HAADF images were taken after irradiation, to obtain 'post-damage' images of the InGaN QWs, again near the $<11\bar{2}0>$ zone axis.

6.3.4. APT

All APT experiments described in this chapter were carried out at the OPAL EPSRC National Atom Probe Facility at Oxford University, as described in section 4.4.5. Details of the LEAP conditions used for each run will be presented in section 6.4, with the associated APT data set. Once the data were collected, the APT reconstructions were optimised as far as possible to obtain flat layers and correct layer spacings, as indicated by TEM.

6.4. RESULTS AND DISCUSSION

6.4.1. BLUE QWs

6.4.1.1. Standard Orientation QWs

In an attempt to reproduce the work of Galtrey *et al.*[115], and to thereby determine whether the results obtained were consistent with those previously reported, standard orientation APT samples of the blue-emitting InGaN QWs were run in the LEAP. One data set was collected from Sample A and one from Sample B, although a second data set from Sample A was collected as a reference for the electron beam irradiated QWs, and will be discussed in section 6.4.2. It should be noted that Sample A and Sample B were grown with the same InGaN QW growth recipe, just on different TD density templates. No V-pits associated with TDs were observed in the data used for In distribution analysis.

The data set from Sample A was collected using a base temperature of 30 K, a laser pulse energy of 0.1 nJ and an evaporation rate of 2.5 %. All ten QWs were observed, as shown

in figure 6.10a, with 100 % of In atoms shown as orange dots, and 2.5 % of Ga atoms shown as blue dots. The reconstruction shows the QWs increasingly bowing near the bottom of the QW stack, indicating that the field changed slightly during the run (only a global field value can be used in the reconstruction). To minimise pole-related density fluctuations, and to obtain flat layers throughout, a central cylinder of 20 nm × 110 nm running perpendicular to the QWs was selected, as shown in figure 6.10b. Within this cylinder, each QW was isolated using an isoconcentration surface set at half the maximum In content of the well. The volumes enclosed were divided into 100 atom bins, and the data from all ten QWs was combined for χ^2 analysis.
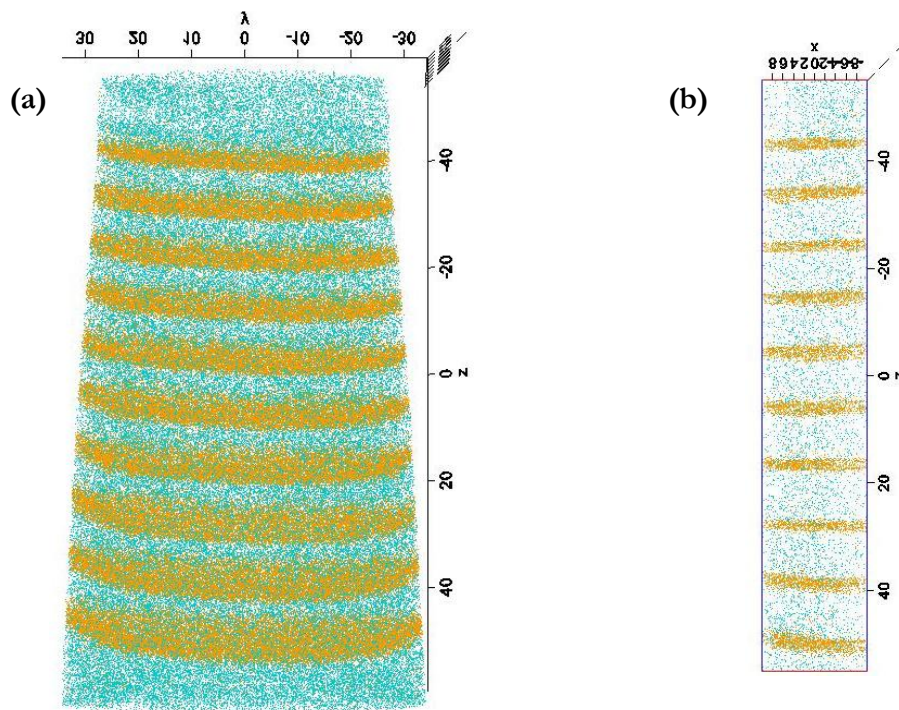
Figure 6.10. (a) Side view of the entire reconstructed atom map of the standard orientation data set from Sample A. 2.5 % of Ga atoms are shown as blue dots, with 100 % of In atoms shown as orange dots. The QWs near the top are flatter than the ones towards the bottom of the stack, due to changes in the evaporation field during the run. (b) A central cylinder of 20 nm × 110 nm, selected from (a) to minimise the effect of QW bowing and pole-related density fluctuations.

The χ^2 analysis of Sample A suggested no statistically significant deviation from randomness for the In distribution within the QWs. Bin sizes were varied between 25 and 200 atoms, with similar results achieved for all bin sizes. For 100 ion bins, the p value was found to be 0.96 for 14 DOF, which strongly suggests that there were not any

non-random In clusters present in our MQW sample. Figure 6.11 shows the observed In frequency distribution, compared with the binomial. To check that the combined χ^2 analysis was representative of the individual QWs, the p value of each well was computed, and no well showed evidence of non-random In clustering.
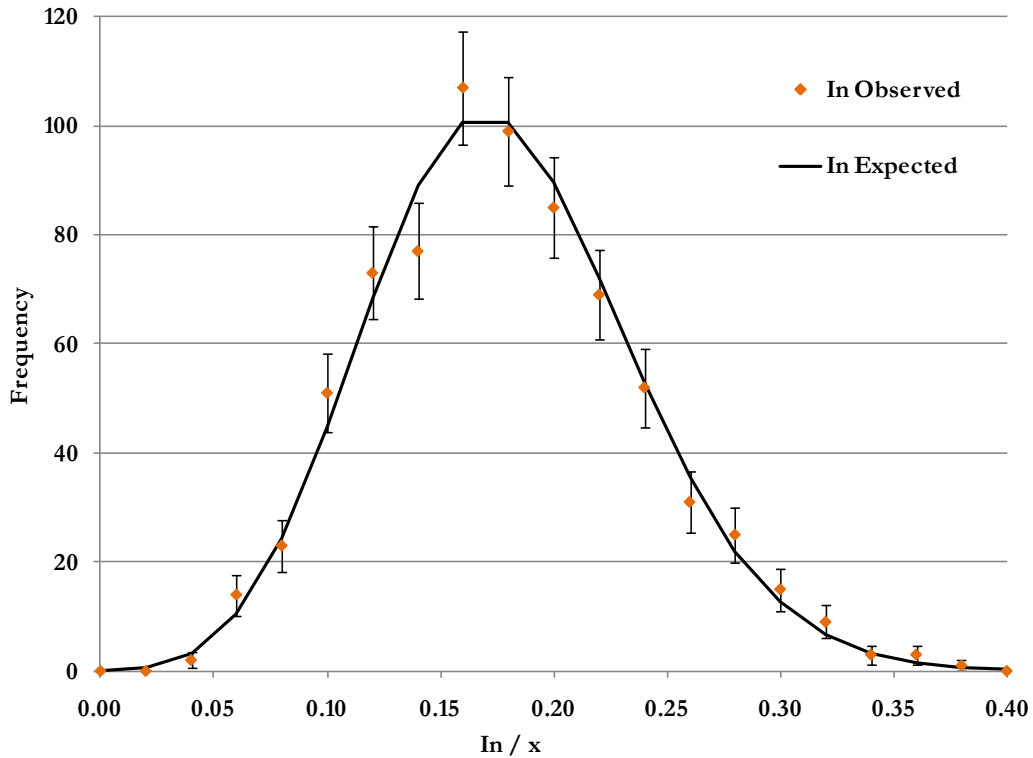
Figure 6.11. A comparison between the observed distribution of In within all ten QWs of Sample A, and that expected from a random alloy. The volume within the QWs was split into 100 atom blocks and the In content of each block was calculated. χ^2 analysis shows no significant deviation from randomness.

The data set from Sample B was discussed in section 4.5.3, as it contained all ten QWs and a small portion of a V-pit. A reconstructed atom map of the data set can be seen in figure 4.13. A central cylinder, away from the V-pit, was selected for analysis of the In distribution. As the data set was wider than that of Sample A (shown in figure 6.10a), a slightly wider cylinder of 35 nm × 110 nm was selected. The InGaN QWs were again isolated using isoconcentration surfaces with values corresponding to half of the maximum In content of each well. The combined χ^2 analysis for all ten QWs with 100 ion bins resulted in a p value of 0.24 for 17 DOF. These results and those for Sample A support the conclusion that non-random In clusters were not present in our InGaN MQWs, in agreement with the work of Galtrey *et al.*[115].

6.4.1.2. Side-on Orientation QWs

As previously mentioned, the spatial resolution of APT in the z-direction is better than that in the x-y plane. To take advantage of the improved z-resolution, side-on APT samples were prepared from capped Sample A and Sample B, as described in section 4.5.1. It was hoped that these side-on samples would serve to both to capture a TD and to collect data from the MQWs as they ran down the length of the sample. As discussed in section 4.5.3, all of the side-on samples fractured in the LEAP, although one small data set of Sample B, with approximately 350,000 atoms, was obtained that contained the InGaN MQWs. This data set was collected using a base temperature of 30 K, a laser pulse energy of 0.1 nJ and low evaporation rates of between 0.2 % and 0.5 %. The mass spectrum collected during the run was noisier than typically observed for standard orientation samples, and so the run was stopped prior to specimen fracture to test the suitability of the local electrode: the local electrode is a consumable part of the LEAP, and if dirty or damaged, can cause noise in the mass spectrum. The local electrode was found to be suitable, but unfortunately, when evaporation was restarted under the same run conditions, the specimen fractured.

The side-on data set was collected during the initial stages of evaporation, when the tip was likely to still have been reshaping. This effect is evident from the inhomogeneous distribution of atoms on the detector, which can be seen as a large decrease in atomic density from one side of the data set to the other. Figure 6.12a shows a top view of the entire data set, with 100 % of In atoms shown as orange spheres of 0.1 nm diameter, and 25 % of Ga atoms shown as blue dots, with all other atoms omitted. The density on the right of the data set drops to almost nothing, which suggests that the tip was initially flatter on that side, resulting in a local electric field well below the threshold for field evaporation. An oxygen peak was detected in the mass spectrum, and the distribution of O was investigated. Figure 6.12b shows 100 % of the O atoms as red spheres of diameter 0.2 nm, in addition to the In and Ga, shown as in figure 6.10a. The O atoms are clearly observed at the edge of the low density region, suggesting that they originate from O-rich surface contamination, which was in the process of being removed as the tip reshaped itself during turn on. It should be noted that the reconstruction parameters could not be optimised in this case to provide completely flat layers, however this should not significantly affect the In distribution within the wells.

Figure 6.12. (a) Top view showing the reconstructed atom map of the small side-on data set from Sample B. 25 % of Ga atoms are shown as blue dots, with 100 % of In atoms shown as orange spheres of 0.1 nm diameter. The density of atoms falls to almost nothing on the right of the data set, indicating that the tip was still reshaping, with the right side being flatter. Portions of four InGaN QWs can be observed, with two complete wells collected. (b) 100 % of O atoms are shown as red circles of diameter 0.2 nm, overlaid on the atom map from (a).

Figure 6.13 shows a side view of the reconstructed data set, with the same image specifications as in figure 6.12a. On the left side of the data set, where the tip shape was already conducive to evaporation, two InGaN QWs can be seen that run down the length of the sample. These QWs were used to study the In distribution, taking advantage of the improved z-resolution to determine whether there was any indication of nanoscale In clustering. Only the regions inside the QWs were used, and these were isolated using isoconcentration surfaces at half the maximum In content of each QW. For the QW shown on the left in figure 6.13, or 'QW 1', the isoconcentration surface used was 4.5 at.% In, while the QW on the right, or 'QW 2', was isolated using a 4.8 at.% In isoconcentration surface.
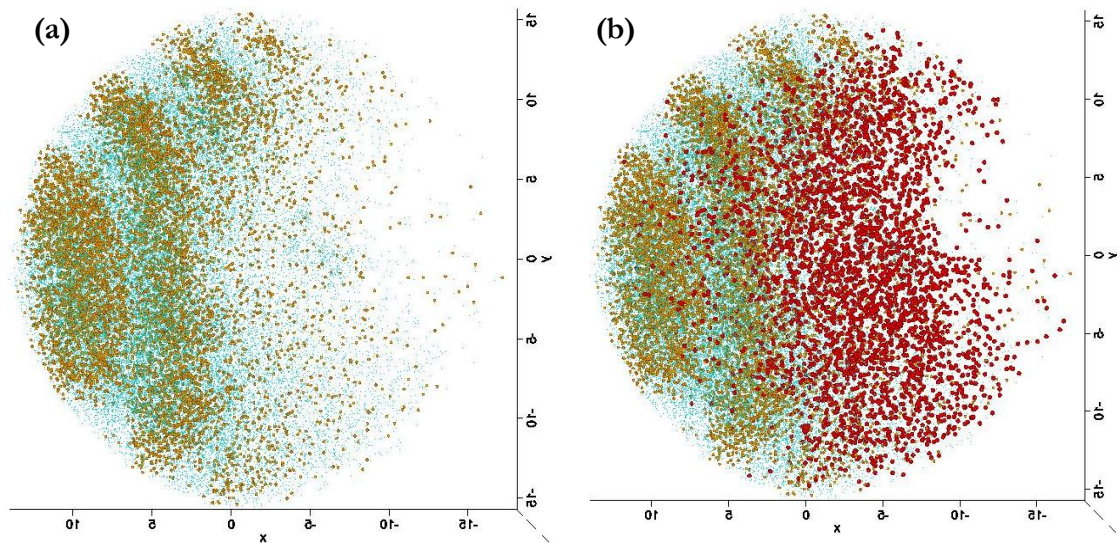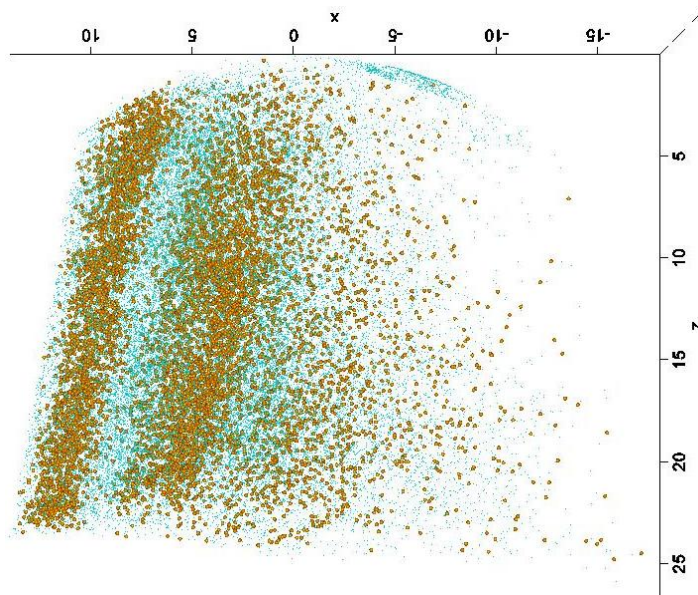
Figure 6.13. Side view of the reconstructed atom map of the small side-on data set from Sample B. 25 % of Ga atoms are shown as blue dots, with 100 % of In atoms shown as orange spheres of 0.1 nm diameter. Two InGaN QWs are observed on the high density side of the data set.

The distribution of In was studied by dividing the volume within the QWs into 100 atom bins and using a χ^2 test to compare the observed distributions with those expected from a random alloy, as described in section 5.4.1.2. For QW 1, the p value was 0.11 for 12 DOF, which implies that it is not possible to reject the null hypothesis that the InGaN is a random alloy. For QW 2, which was closer to the low density region, the p value was 0.06, which is just above the threshold below which a deviation from randomness would be indicated. Thus, the results from analysis of the In distribution in the side-on data set are in agreement with the results from the standard orientation data sets and the previous observation by Galtrey *et al.*[115].

The distributions of Ga and N_2 were also analysed in the side-on dataset. Although the N_2 distribution showed no deviation from randomness, as would be expected, the Ga surprisingly showed a clear non-random distribution within the QW regions (in the barriers there was no indication of a deviation from randomness in the Ga distribution). At 100 atom bins, QW 1 and QW 2 both showed Ga distributions with p values of 0.00, for 24 and 27 DOF, respectively. This non-random Ga distribution casts doubt onto the validity of the In distribution analysis, since a random distribution of In would be expected to be associated with a random Ga distribution, given that In sits on Ga sites. It should be noted, however, that this region of the sample was liable to have been damaged by implanted Ga atoms from the Ga^+ ion beam during FIB/SEM sample preparation, which may have altered the distribution of Ga. FIB damage of APT samples will be investigated further in Chapter 7.

As the side-on data set was extremely small, likely to have been obtained during tip reshaping, and contained a non-random distribution of Ga in the QW regions, these data are not particularly reliable. Yet, even with these issues, the In distribution was still not observed to deviate significantly from randomness. Although firm conclusions cannot be drawn from this data set, it certainly does not provide any evidence *for* indium clustering.

On the weight of evidence, both from the work in this chapter, and from the evidence presented by Galtrey *et al.*[115], it seems apparent that the blue-emitting InGaN QWs studied do not show any evidence for In clustering, implying that these clusters cannot be necessary for bright light emission. Although this negative result has now been repeatedly observed, those critical of such APT studies have suggested that nanoscale In-rich clustering might not be detected by APT, even if it were present. Therefore, it would be highly interesting to examine a sample with known clustering in the LEAP, to determine whether these clusters could be observed. Such an investigation is the subject of the next section.

6.4.2. ELECTRON BEAM IRRADIATED BLUE QWs

Both Smeeton *et al.*[127] and O'Neill *et al.*[137] challenged the TEM-based evidence for the In clustering model by suggesting that the observed contrast was a result of electron beam induced damage. In light of this controversy, the next aim of this chapter was to irradiate an APT sample containing InGaN QWs in the TEM, in an effort to induce this damage, and then to study both the irradiated sample and a reference non-irradiated sample in the LEAP. APT data were successfully collected from both irradiated and non-irradiated blue-emitting QWs from Sample B, making it possible to study any changes induced.

6.4.2.1. TEM of the APT Sample

An APT sample was made from Sample B on a Cu/W mount, as described in section 4.5.4. In this case, the sample was prepared from the capped Sample B, to reduce the likelihood that the MQWs would be milled away during APT sample preparation. An image of the MQWs was taken using STEM-HAADF prior to significant damage by electron beam irradiation in TEM-mode, with every effort taken to minimise the exposure time. This image can be seen in figure 6.14a, and shows that all ten QWs were

captured in the APT sample, below approximately 100 nm of GaN cap. A layer was observed surrounding the end of the tip, and this was found to be amorphous, although slight QW contrast could still be seen. An EDX line profile showed that the layer contained mostly Ga and O. The sample was then exposed to 64 minutes of approximately 1.1 A cm^{-2} current density in TEM-mode, after which a post-damage STEM-HAADF image was taken, as seen in figure 6.14b. The post-damage image showed blotchy strain contrast both in the MQW stack and in the GaN cap.
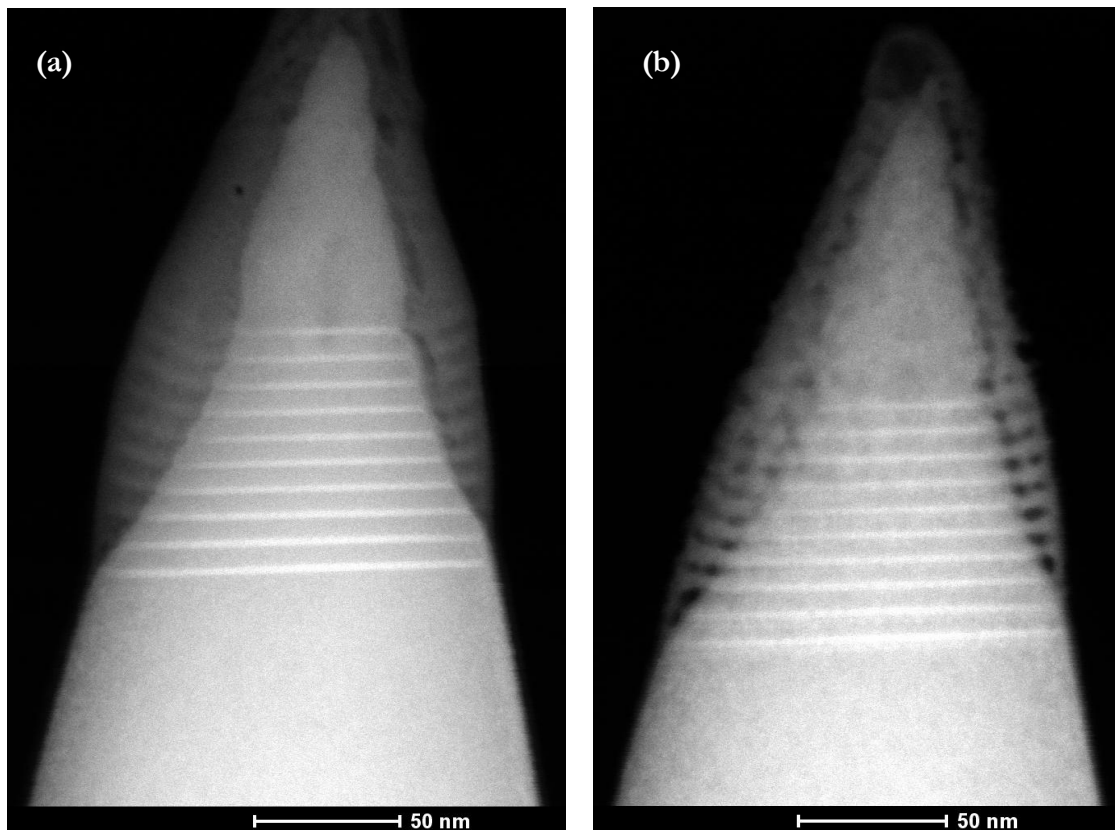
Figure 6.14. STEM-HAADF images of the InGaN/GaN blue-emitting MQWs in capped Sample B, in which InGaN QWs show brighter contrast. (a) Pre-damage image taken prior to irradiation in TEM-mode, in which the wells appear uniform. An amorphous layer can be seen surrounding part of the tip, which was shown to be Ga and O-rich. (b) Post-damage image taken after 64 minutes of TEM-mode electron beam irradiation with a current density of approximately 1.1 A cm^{-2}. Blotchy strain contrast can be observed throughout the MQW stack and in the GaN capping layer.

The O-rich amorphous layer surrounding the APT sample was observed by TEM for the first time here, although the side-on sample showed what appeared to be an O-rich contamination layer in the APT data. The cause of this amorphous region is not yet understood. Interestingly, in the similarly-prepared APT sample with a TD shown in figure 4.19, no amorphous region was observed, nor was such a layer observed by Galtrey[65] in similar TEM studies of APT samples. The amorphous layer observed here clearly showed blotchy strain contrast after irradiation. As the TEM image is a projection through the entire sample, it is difficult to say whether the MQWs themselves showed significant strain contrast, or if projection through the amorphous region made the QWs, barriers, and GaN cap simply appear to show such contrast. By the very nature of the technique, however, the electron beam penetrated the entire sample. Additionally, the exposure time was long, which would suggest that any damage typically observed in TEM studies of In clustering would have been induced in these MQWs.

6.4.2.2. APT

The APT data set from the irradiated MQW sample was collected using a base temperature of 26 K. In an effort to evaporate through the amorphous layer, without fracturing the sample, a high laser power of 0.8 nJ was initially used, with an evaporation rate of 0.2 %. Oxygen peaks were observed in the mass spectrum during this initial evaporation. A burst of evaporation was observed, which indicated that the amorphous layer, and perhaps some of the GaN cap, may have popped off the end of the sample. The laser power was then lowered to 0.3 nJ, and the evaporation rate raised to 0.8 %, under which conditions data from the first four QWs were collected. For the next three QWs, the laser power was lowered again to 0.1 nJ, while the evaporation rate was raised to 1.5 %. Data from the final three QWs was collected with an evaporation rate of 2 %. As the evaporation rate and laser power can have some effect on the data observed, the data from QWs with the same evaporation rate were combined in the analysis.

A non-irradiated reference of Sample B was run immediately after the irradiated sample, to ensure consistent LEAP performance. As discussed in the last section, both standard and side-on orientation data sets from Sample B had already been collected, with neither showing evidence for In clustering. The reference sample was run at a base temperature of 26 K. Again, a burst of evaporation was observed during sample turn-on, indicating that perhaps an amorphous layer was also present on the reference sample. After this

burst, the MQWs were observed. The laser power was held constant at 0.1 nJ during data collection. The evaporation rate was again increased gradually: the first QW was evaporated at 1 %, the next five QWs were evaporated at 1.5 %, and the final four QWs were evaporated at 2 %. Although the evaporation rate has never been observed to have an effect on the evidence suggesting a lack of In clustering, an effort was made to run the damage reference sample at comparable evaporation rates to the irradiated sample.

The atom maps collected from both samples did not show a visually perceptible difference in the QW In distribution. Figures 6.15a and 6.15b show a 35 nm central cylinder from the irradiated and reference sample, respectively, with 100 % of In atoms shown as orange dots and all other atoms omitted for clarity. As mentioned in section 5.4.1.1, however, visual examination is not an effective technique to determine the existence of nanoscale clustering. Statistical evaluation of both samples was undertaken using χ^2 analysis. Again, the central cylinder was used for analysis, and the QWs were isolated using In isoconcentration surfaces set at half the maximum QW concentration.
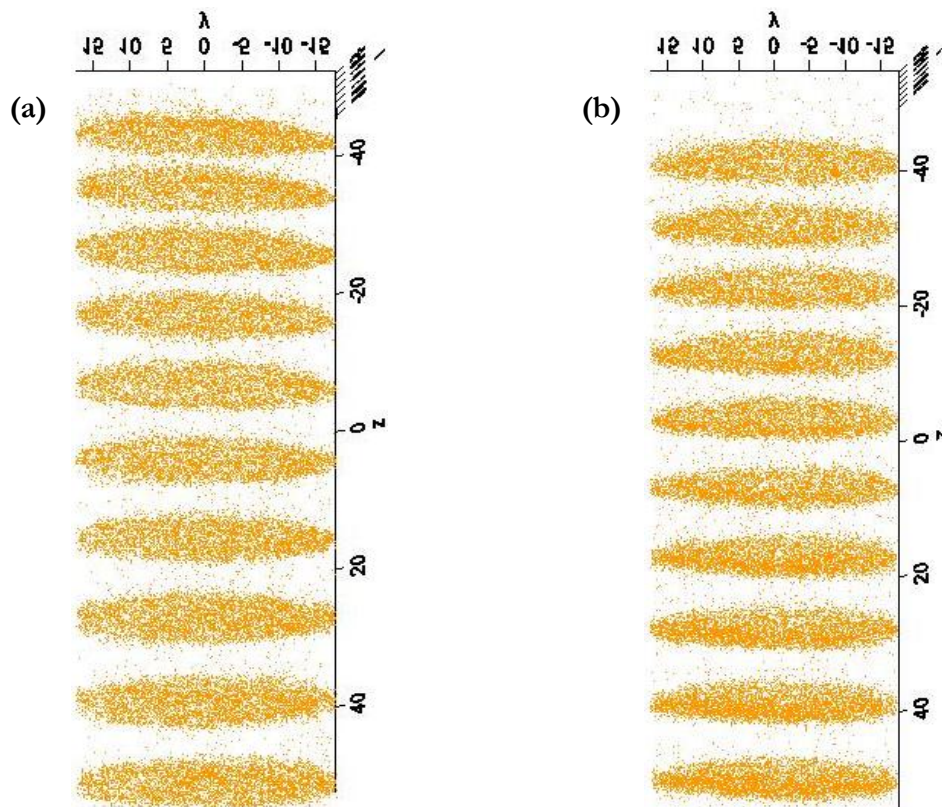
Figure 6.15. Reconstructed atom maps of 35 nm diameter central cylinders from the APT data sets of Sample B, with 100 % of the In atoms shown as orange dots. (a) After electron beam irradiation in the TEM. (b) Without irradiation.

The QWs in the reference sample were divided into 100 atom blocks for χ^2 analysis. The QWs collected at the three evaporation rates of 1 %, 1.5 %, and 2 % showed p values of 0.94 for 14 DOF, 0.28 for 19 DOF, and 0.17 for 18 DOF, respectively. These results indicate that the In distribution within the reference sample was consistent with that observed for the standard orientation Sample B data set in the previous section, showing no indication of In clustering. The irradiated sample, on the other hand, showed a statistically significant deviation from randomness: within the top four QWs, with 100 atom bins, the In p value was 0.00 for 19 DOF. Figure 6.16 compares the observed In distribution with that expected from a random alloy. A lower frequency than expected was observed at intermediate In contents, whereas greater than expected numbers of bins were observed containing either low or high amounts of In. These data suggest that electron beam irradiation leads to clustering of the In within the InGaN QWs.
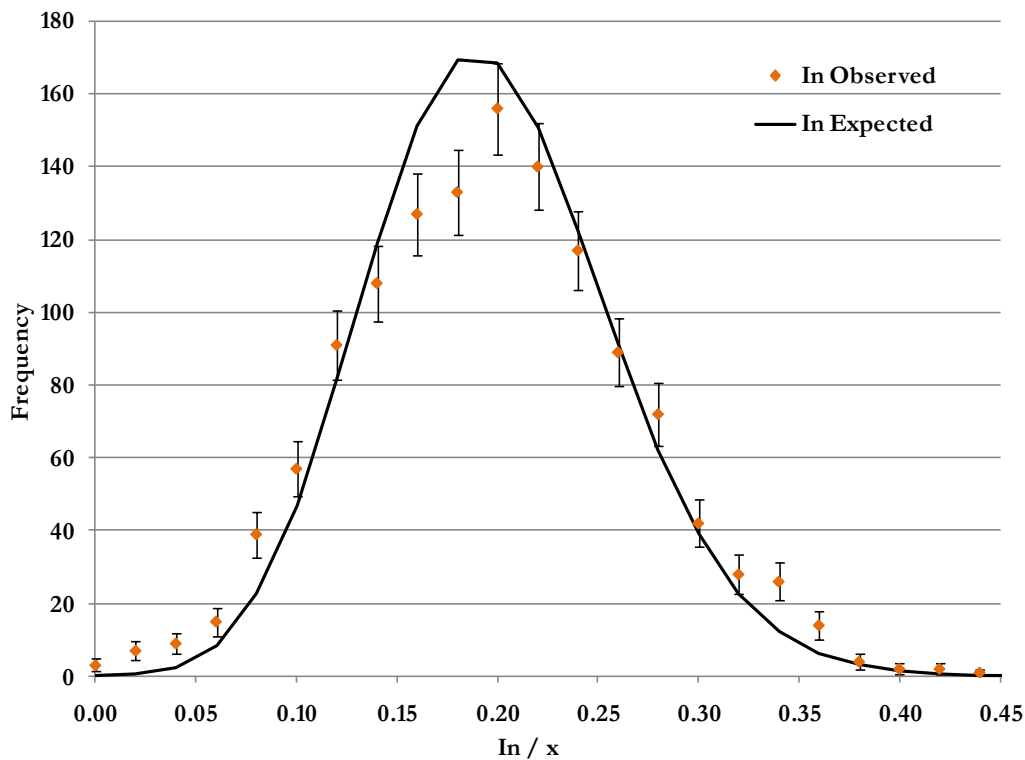
Figure 6.16. A comparison between the observed distribution of In within the top four QWs of electron beam irradiated Sample B, and that expected from a random alloy. χ^2 analysis with 100 atom blocks shows a statistically significant deviation from randomness.

After data was collected from the first four QWs in the irradiated sample, the laser power was lowered to 0.1 nJ, and evaporation rates of 1.5 % and 2 % were used. For the data

collected at an evaporation rate of 1.5 %, χ^2 analysis with 100 atom bins indicated that the In distribution was right on the edge of a deviation from randomness: the p value was 0.059 for 17 DOF, just above the threshold of 0.05. The In distribution within the lowest three QWs again showed a deviation from randomness: with 100 atom bins, the p value was 0.00 for 19 DOF. These results suggest that the statistical deviation from randomness observed in the top four wells was not simply related to the higher laser power used, as the bottom three wells also showed such a deviation.

Many questions remain regarding the cause and extent of electron beam damage to InGaN QWs. Although the APT results presented in this section indicate that irradiation causes In clustering, the level of clustering observed here does not extend to the level observed by Gerthsen et al.[134], who identified clusters that the authors believed contained more than x = 0.73 In. However, the results reported by Gerthsen et al.[134] appear unconvincing under further scrutiny: for the lattice fringe analysis to yield such high In content clusters, the TEM sample would be required to have a thickness similar to the size of the clusters, which only extend to a few nanometres, or the clusters would need to be rod-like, running through the entire sample. In fact, it would be impossible to achieve the reported results given a reasonable sample thickness if the clusters were roughly spherical, with projection effects taken into account. It is worth noting as well that the results reported by Gerthsen et al.[134] are based upon relating the local lattice parameter to the In content, yet In content variations may not be the sole cause of local changes in lattice parameter, which could be affected by other damage mechanisms.

More recent HRTEM studies have suggested that In fluctuations are smaller by an order of magnitude than the structures previously reported by Gerthsen et al.[134], although they are suggested to be greater than random alloy fluctuations[148]. In this section, we have observed that electron beam irradiation led to In fluctuations greater than would be expected from a random alloy, and that without this irradiation, no deviation from a random alloy distribution was observed.

The Ga and N_2 distributions were also compared between the irradiated and reference samples, using a volume in the middle of the GaN barrier, just below the first QW. The volume was selected in each data set using a 35 nm × 5 nm region of interest, placed roughly equidistant from 5 % In isoconcentration surfaces, which were used to visualise

the top and bottom of the GaN barrier layer. The volumes were divided into 100 ion bins, and the reference sample showed no deviation from randomness for either distribution: the p value for the Ga distribution was 0.08 for 25 DOF, and the p value for the N_2 distribution was 0.47 for 19 DOF. In the irradiated sample, however, both the Ga and N_2 distributions had p values of 0.00, for 28 and 24 DOF, respectively. Thus, it appears that electron beam irradiation also causes damage to the GaN layers.

Finally, the effect of APT sample thickness on the amount of damage induced in the GaN was briefly investigated. Volumes for study were selected in the irradiated data set using 35 nm × 3 nm regions of interest, placed just above and below the QWs. Above the MQW stack, both the Ga and the N_2 distributions were observed to have p values of 0.00, for 27 and 23 DOF, respectively. Below the QWs, neither distribution showed a deviation from randomness: the p value for the Ga distribution was 0.23 for 22 DOF, and the p value for the N_2 distribution was 0.43 for 18 DOF. These results suggest that the level of damage was greatest at the top of the MQW stack, decreasing as the APT sample thickness increased.

6.4.3. GREEN-EMITTING QW NETWORK STRUCTURES

The next aim of this chapter was to use APT to examine the brightly-emitting green QWs with gross well-width fluctuations characteristic of the network structures observed by van der Laak *et al.*[129]. Five APT data sets were obtained that each contained the entire MQW stack. Although the field of view in the LEAP was fairly small compared to the width of the InGaN strips, a number of gaps in the QWs were observed, consistent with the previous TEM observations[147]. Figure 6.17 shows one of the APT data sets, collected using a base temperature of 30 K, a laser power of 0.01 nJ and an evaporation rate of 3 %. 100 % of the indium atoms are shown as orange dots, with 2.5 % of Ga atoms shown as blue dots. This side-on view of the atom map resembles the cross-sectional TEM images presented by Costa *et al.*[147], in which the well width was observed to vary significantly, in some places even leaving gaps.
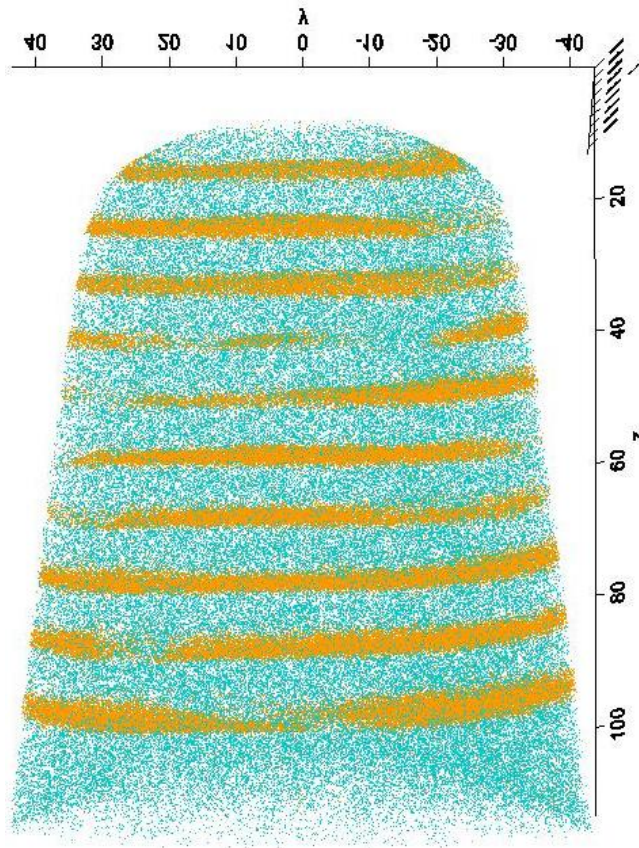
Figure 6.17. Reconstructed atom map of the green-emitting MQW sample with gross well-width fluctuations. All ten InGaN QWs can be observed, with 100 % of In atoms shown as orange dots. Just 2.5 % of Ga atoms are shown as blue dots, with all other atoms omitted for clarity. From the side, the APT data appears similar to the TEM images presented by Costa *et al.*[147], in which the QWs were observed to vary in width, in places dropping to nothing.

The 3D nature of the APT data set allows each well in the MQW stack to be examined from any angle, and top-view images clearly show elongated gaps in the QW layers. Four QWs from the data set in figure 6.17 are shown in figure 6.18a-d, using 3.5 at.% In isoconcentration surfaces. Although the shape of the gaps depends on the isoconcentration surface used, the APT data do show that the In content drops to near zero in some of the gaps. For instance, the gap shown in figure 6.18a persists in the data set even with a 0.5 at.% In isoconcentration surface. Despite the small field of view available in the atom probe, the observed microstructure appeared to be similar to the network structures seen by van der Laak *et al.*[129].
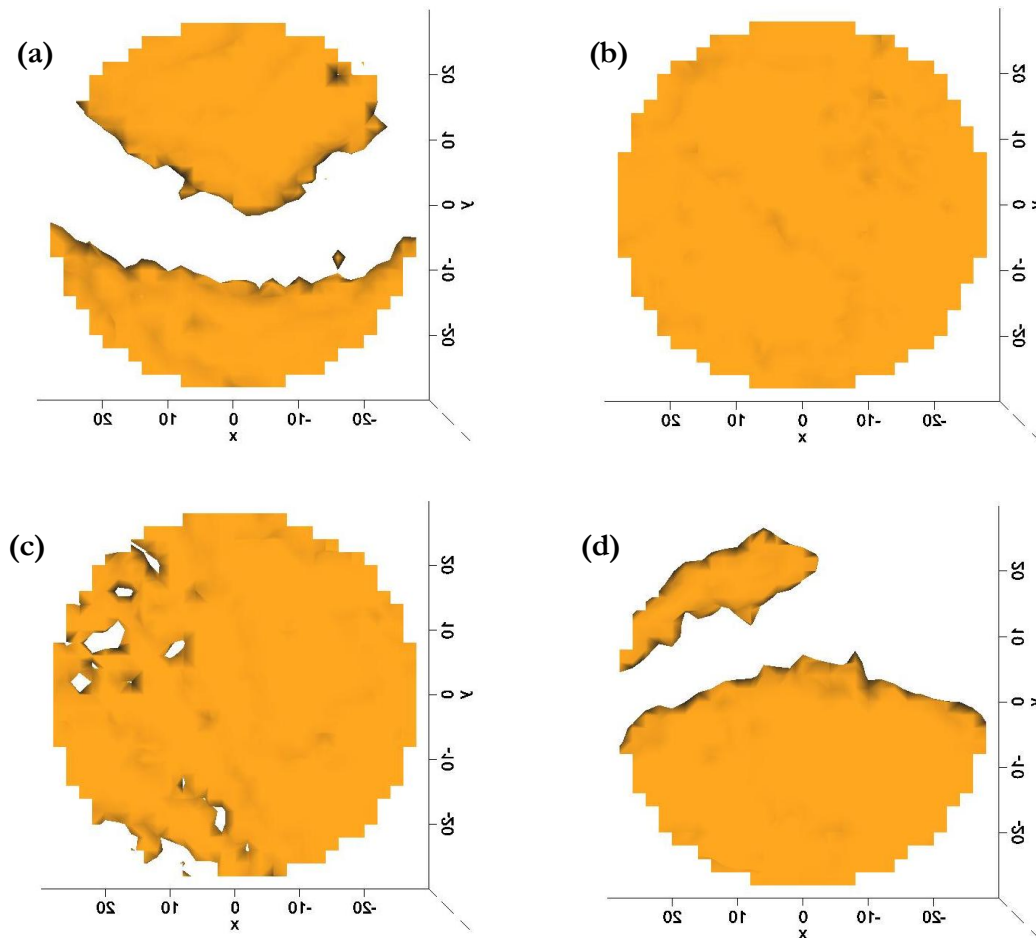
Figure 6.18. Individual layers from the data set in figure 6.17, shown with 3.5 at.% In isoconcentration surfaces. (a) and (d) show gaps in the wells, whereas (b) and (c) appear more uniform.

In the network structures observed by van der Laak *et al.*[129], the authors found that the In content of the InGaN strips decreased towards the edges. This variation was proposed to localise carriers in the middle of the strips, and away from TDs. To study how the In content varied from the body of the InGaN strip towards its edge in our APT data, a region of interest of 15 nm × 5 nm × 1 nm was defined within the QW, running from the centre of the strip towards the gap. A 1D concentration profile was obtained along the long axis of this volume, and figure 6.19 shows that the In content falls as the edge of the InGaN strip is approached. Comparable analysis across several QWs from different data sets revealed similar results, showing that the edges of the strips are less In-rich than the centres.
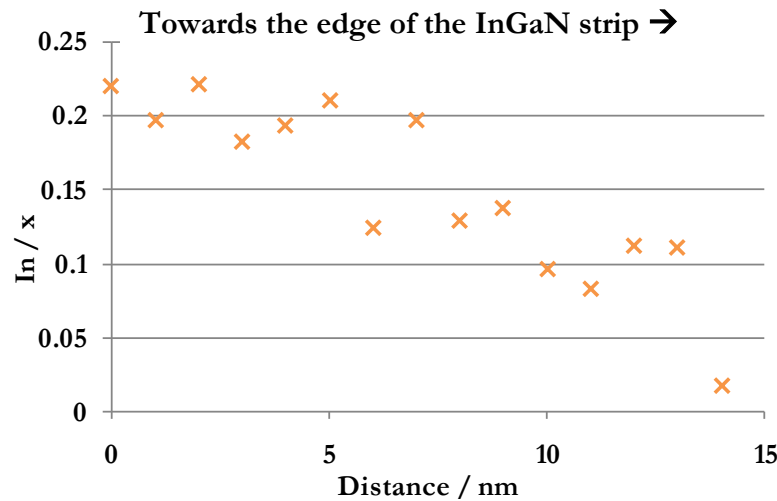
Figure 6.19. Indium 1D concentration profile, from the centre of the InGaN strip, towards the edge. The In content was observed to fall as the gap was approached.

The network structures observed by van der Laak *et al.*[129] showed gaps between the InGaN strips that were aligned roughly parallel to the [11$\bar{2}$0] direction. The APT data sets were therefore analysed to determine whether the gaps in the QWs showed a preferential orientation. The angles of the gaps were approximated using the isoconcentration surfaces, as shown in figure 6.20a. On either side of a gap, lines were drawn between the points where the isoconcentration surface entered and exited the field of view. The midline between these lines was drawn, with the use of an overlaid grid, and the angle between the midline and the *y* axis was found. The orientations of the gaps are shown in the histogram in figure 6.20b, and there appears to be a peak at around 30 – 45 °, although clear conclusions are difficult to draw, as the data set is very small. The observed distribution suggests that the gaps may be aligned along a certain crystallographic direction, in support of the work by van der Laak *et al.*[129].

The APT studies of green-emitting InGaN QWs with gross well-width fluctuations have confirmed observations of the morphology and composition of the wells made by van der Laak *et al.*[129]. The APT data showed that the InGaN strips are indeed In-rich at their centres, compared to their edges, which could provide a mechanism for excitonic localisation away from TDs. In addition, analysis of the gap orientations suggested that the InGaN strips may show a preferential orientation, similar to previous observations of network structures[129]. Future APT experiments might endeavour to determine the crystallographic direction of such orientation. Optimisation of this type of broad scale QW morphology could play an important part in improving the efficiency of green-emitting devices.
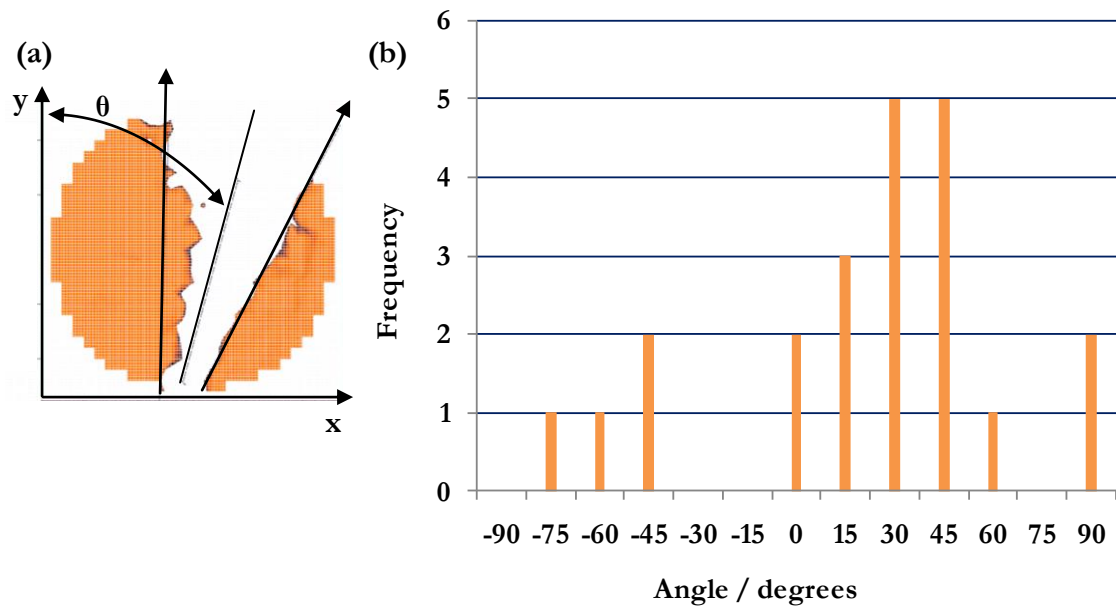
Figure 6.20. (a) Illustration of the method used to estimate the angle of the gaps, θ, relative to the *y* axis in the data set.   (b) Plot of the gap orientations observed, showing what appears to be a peak at around 30 − 45 °, which suggests that the gaps may be aligned along a certain crystallographic direction.

6.4.4. MBE-GROWN QWS

The final aim of this chapter was to extend the analysis of In distributions to an MBE-grown QW. The QW formed part of a full laser diode structure, described in section 6.3.1, which will be discussed in more detail in Chapter 8 of this work. As previously mentioned, a 540 nm emission wavelength was measured using EL at an area near the centre of the wafer, or 'Region A', whereas an area nearer to the edge, or 'Region B', grown at a higher temperature, showed a 490 nm emission wavelength. APT samples were prepared from material lifted out of both Region A and Region B, and two data sets were collected from each area.

All four data sets were collected with a base temperature of 30 K and a laser power of 0.01 nJ, with evaporation rates that were gradually increased to 3 %. One of the Region A data sets contained the full GaN layer above the QW, grown with a nominal thickness of 235 nm, which was helpful for reconstruction optimisation. The same reconstruction parameters were applied to the other Region A and the two Region B data sets, resulting in layer thicknesses that compared reasonably well with the growth recipe.

A reconstructed atom map of one of the Region A data sets is shown in figure 6.21, with 25 % of In atoms visible as orange dots and 25 % of Al atoms visible as light blue dots, with all other atoms omitted for clarity. The InGaN QW and the 235 nm GaN layer are both labeled.
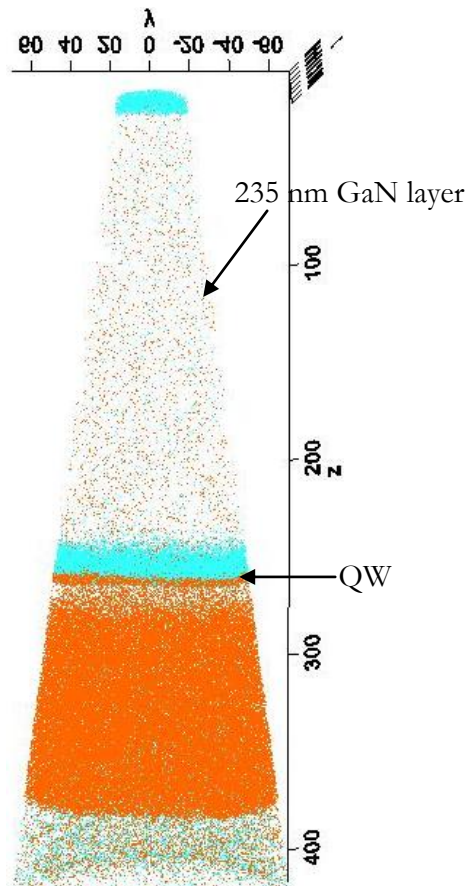
Figure 6.21. Reconstructed atom map of the MBE-grown laser diode structure grown at Sharp Laboratories of Europe. The sample is from the centre of the wafer, or Region A, which showed green wavelength emission. 25 % of In atoms are shown as orange dots and 25 % of the Al atoms are shown as light blue dots, with all other atoms omitted for clarity. The InGaN QW is near the middle of the data set, as indicated, and the 235 nm GaN layer used for reconstruction optimisation is also labeled.

As before, to minimise the impact of pole-related density fluctuations, a central cylinder of 35 nm diameter was selected for analysis in each of the four data sets. Layer interfaces were aligned approximately perpendicular to the long axis of the cylinder. Within this cylinder, the QW was again isolated using an In isoconcentration surface with a value equal to half the maximum In content of the well. The QWs from the Region A data sets were found to have a maximum In content of $x = 0.22$ on average, whereas the maximum In content of the QWs from the Region B data sets was found to be just $x = 0.16$ on average. The higher In content of the QW in Region A serves to explain the longer emission wavelength, compared to Region B.

Once the QW was isolated in each data set, the volumes were divided into bins for χ^2 analysis, comparing the observed In distribution with that expected from a random alloy. On the whole, the observed In distributions from all four QWs were similar to those

observed for MOVPE-grown material, in that no bins were found with significantly enriched In contents. Yet the results of the χ^2 analysis were somewhat inconclusive. The p value for one of the Region A QWs was 0.10 for 14 DOF (with 100 atom bins), indicating no significant deviation from randomness. The observed and expected distributions for this data set are shown in figure 6.22a. The other Region A QW, however, had a p value of 0.00 for 17 DOF, indicating a statistically significant departure from a random alloy distribution. In addition, the two Region B QWs also showed p values of 0.00 for 14 and 15 DOF. A comparison between the observed and expected In distributions for a Region B QW can be seen in figure 6.22b.
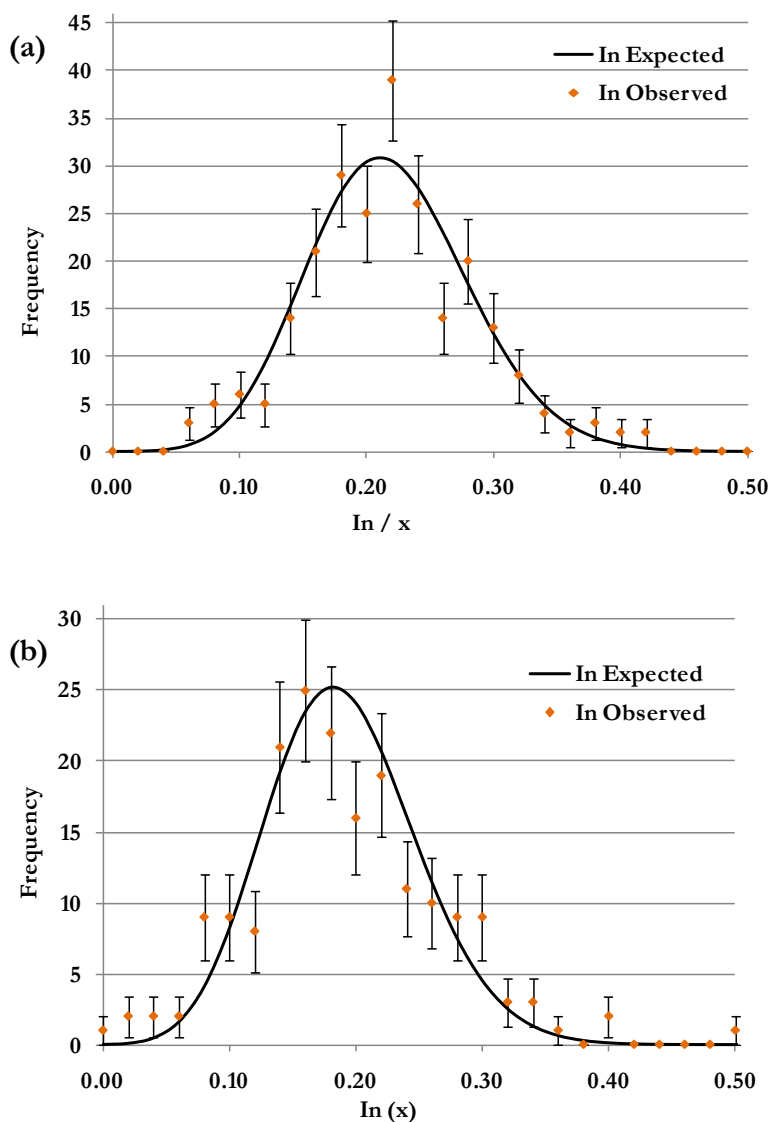
Figure 6.22. A comparison between the observed distribution of In within the QW (isolated using an isoconcentration surface at half the maximum In content of the well) and that expected from a random alloy, with 100 atom bins. (a) QW from the central region, which showed no statistical deviation from a random distribution. (b) QW from the edge region, which did show a deviation from a random alloy.

In the data set shown in figure 6.22b, as well as the other distributions that showed a statistical deviation from randomness, a large contribution to the χ^2 value came from bins with very low In contents, whereas the contribution was much less from bins with high In contents. This observation was in contrast to the electron beam irradiated QWs,

which showed excess In-rich bins, as well as bins with low In contents. In light of this finding, the QWs were further characterised to determine whether the observed deviation from randomness related to an inhomogeneous distribution within the plane of the well, as would be expected in the presence of In clusters, or whether it arose from the variation in composition through the thickness of the well in the growth direction.

To eliminate this uncertainty, it was necessary to understand the collection method for the bins containing the requisite number of atoms. The software creates bins of size 1 nm by 1 nm in y/z, with the x direction of variable length to include the selected number of atoms. A region of interest with a depth of 1 nm in the z-direction was therefore defined near the centre of each QW, ensuring that only in-plane variations in the In content would be observed. Within these regions, no significant deviation from randomness was observed for any of the data sets. With 50 atom bins, the Region A QWs had p values of 0.98 for 9 DOF and 0.78 for 9 DOF. The Region B QWs had p values of 0.43 for 8 DOF and 0.42 for 6 DOF. Figure 6.23 shows the observed and expected distributions for the Region A data set that had a p value of 0.98. It appears, therefore, that the through-thickness variations were the cause of the deviation from randomness observed in the MBE-grown QWs isolated with isoconcentration surfaces.
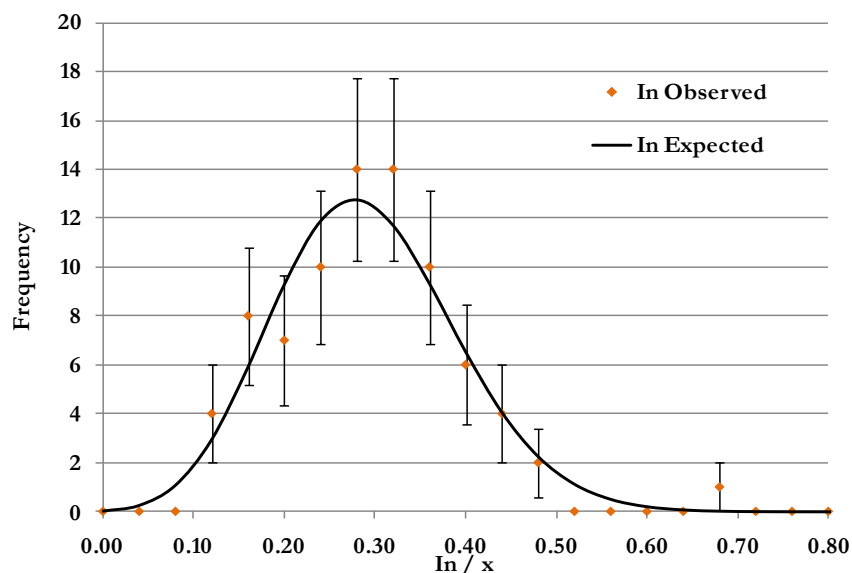
Figure 6.23. A comparison between the observed distribution of In within a QW from the central region (isolated using a region of interest near the centre of the well, with a depth of 1 nm) and that expected from a random alloy, with 50 atom bins. No statistical deviation from randomness was observed.

It can be concluded that the MBE-grown InGaN QWs investigated in this section showed no indication of in-plane In variations that deviated from those expected from a random alloy. These data strongly suggest that InGaN QWs grown by MBE show a microstructure similar to MOVPE-grown wells, in which In clusters are not necessary for bright light emission.

6.5. SUMMARY

In this chapter, several APT investigations of InGaN QWs were reported. First, blue-emitting MQWs were studied using both standard and side-on orientation APT samples. In support of the work by Galtrey *et al.*[115], standard orientation APT samples grown on both high and low TD density templates showed no indication of non-random In clustering. Although the side-on data set was small, and had a number of other issues, χ^2 analysis showed that the observed In distribution did not show a statistically significant deviation from that expected for a random alloy. The weight of evidence strongly suggests that In clusters cannot be a microstructure necessary for devices with an InGaN active region.

To study whether electron beam irradiation caused In clustering in the InGaN MQWs, both irradiated and non-irradiated reference samples were studied by APT. Visual inspection of the atom maps did not reveal a difference between the two samples. However, χ^2 analysis of the irradiated and reference data sets showed that the irradiated sample exhibited a deviation from randomness in the In distribution, in contrast to the reference sample, in which no such deviation was observed. Additionally, irradiation caused damage to the GaN, with both the Ga and N_2 distributions exhibiting non-random clustering. Thus, it has been shown that the APT technique is capable of identifying non-randomness in InGaN QWs, a result which suggests that if as-grown QWs were to show a deviation from randomness, this clustering could be observed by APT.

The next investigation reported was an APT study of high efficiency green-emitting MQWs that had been observed by TEM to show gross well-width fluctuations. Consistent with these previous studies, gaps were observed between InGaN strips in the

APT data. These InGaN strips were found to be In-rich at their centres, and to show a preferential orientation.

The final investigation reported in this chapter extended the analysis of In distribution to MBE-grown InGaN QWs. Four data sets were obtained of a green-emitting laser diode structure, in which an InGaN QW formed the active region. Although the χ^2 analysis of the In distribution was at first inconclusive, further studies were undertaken in which just the in-plane variations in the In content were taken into account. These studies showed no indication of in-plane In variations that would suggest the presence of statistically non-random In clustering.

7

APT STUDIES OF InAlN

7.1. AIMS

In Chapter 6, APT was used to study the alloy InGaN, which has been employed extensively in the active region of light-emitting devices. In this chapter, we continue to investigate binary nitride alloys, turning now to APT studies of the less commonly used alloy InAlN.

7.1.1. APT OF MOVPE-GROWN InAlN

The initial aim of this chapter was to carry out the first APT studies of thick InAlN layers by studying an MOVPE-grown InAlN/GaN distributed Bragg reflector. If data sets could be obtained, the In distribution within the InAlN would be assessed, to investigate whether there was evidence of phase separation in the material. If possible, the structure of the InAlN/GaN interfaces would also be investigated.

7.1.2. APT OF MBE-GROWN InAlN

The next aim of this chapter was to use APT to study MBE-grown InAlN, which would again represent the first investigation of its kind. If APT data were obtained, the In distribution would be studied to determine whether there was any indication of phase separation in MBE-grown InAlN, and thereby observe any difference in microstructure

between MOVPE and MBE-grown material. MBE-grown InAlN samples have been reported to show columnar domains, with In-rich domain boundaries[149,150]. Such a structure would be expected to show an observed In distribution that deviated from a random alloy distribution.

7.1.3. FIB GALLIUM IMPLANTATION DAMAGE

Although the dual beam FIB/SEM is an invaluable tool for the fabrication of APT samples from semiconductor materials, and has therefore been used to prepare all samples used in this work, the Ga ion beam does cause ion implantation damage. In previous chapters, the materials under investigation contained native Ga, making it difficult to study the ion beam Ga (or 'FIB-Ga') implantation damage. The final aim of this chapter was to use the thick InAlN layers in both the MOVPE and MBE-grown samples to assess the implantation of FIB-Ga.

7.2. BACKGROUND

As its growth has proved challenging, InAlN is the least characterised and employed of the binary nitride alloys: much less is known about its properties, compared to AlGaN and InGaN. In this section, the microstructure of InAlN will be discussed, with particular attention paid to the possibility of phase separation in the alloy studied in this chapter. The damage caused by the ion beam in the FIB will also be discussed, as the implantation of Ga ions is applicable to all FIB-prepared APT samples in this thesis.

7.2.1. INALN

The basic properties of InAlN are far from well understood, as discussed in section 1.1. It is known, however, that InAlN can be grown lattice-matched to GaN by using an In fraction of around $x = 0.18$[151]. Such material was grown at approximately 800 °C to produce strain-free layers for application in distributed Bragg reflectors (DBRs)[151]. DBRs are multilayer mirrors, made from alternating layers of two different materials with different refractive indices. These structures exhibit a high reflectivity around a desired wavelength, with a lower reflectivity at other wavelengths, due to interference of light reflected from the DBR interfaces. The growth of lattice-matched DBRs can prevent cracking within the structure, which is highly advantageous, as cracks can lead to poor DBR performance because the reflectivity is dependent on the uniformity of the layer thicknesses. DBRs are mainly used to create microcavities in semiconductor devices,

such as vertical cavity surface emitting lasers (VCSELs), as well as being used as reflectors at the back of LEDs to increase the total light output[14]. In this chapter, both the MOVPE-grown DBR and the MBE-grown InAlN samples were produced near lattice-matched to GaN.

A solid phase miscibility gap has been suggested to exist for the InAlN system, raising the issue of phase separation, as was discussed in some depth with regard to InGaN in section 6.2. Teles et $al.$[152] used first principles calculations to calculate the phase diagram for cubic $In_xAl_{1-x}N$ (plotting temperature against In composition, x). Although the InAlN studied in this chapter is of the wurtzite crystal structure, it has been proposed that the thermodynamic properties should not vary greatly between the cubic and hexagonal structures[153]. Figure 7.1 shows the calculated phase diagram. At 800 °C, the temperature at which InAlN lattice matched to GaN can be grown by MOVPE[14], spinodal decomposition is predicted for In contents between approximately 0.10 and 0.85. MBE-grown InAlN lattice matched to GaN can be grown at 600 °C, at which temperature spinodal decomposition is predicted for alloys with In contents between 0.05 and 0.90. This result predicts phase separation for the alloys studied in this chapter.
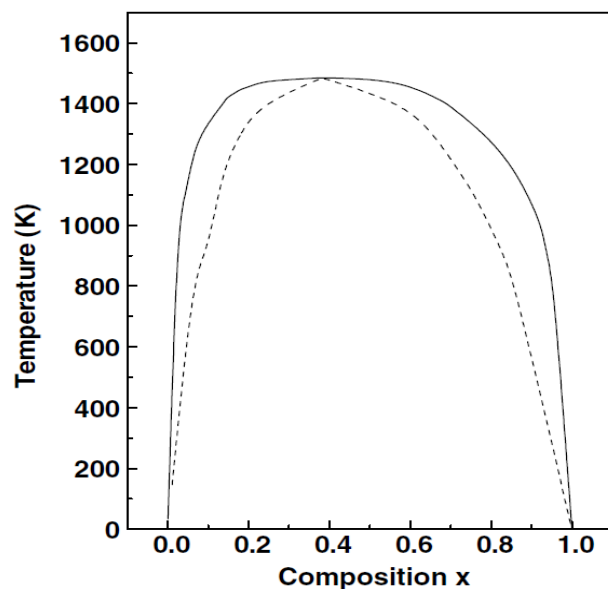
Figure 7.1. From Teles et $al.$[152], a calculated phase diagram for unstrained cubic $In_xAl_{1-x}N$ alloys. The solid line indicates the binodal curve, and the dashed line indicates the spinodal curve.

The preceding phase diagram was calculated for unstrained InAlN, ignoring the possible effects caused by biaxial epitaxial strain of the InAlN layers, as was shown to have a significant effect on the phase diagram for InGaN[136]. With lattice-matching of the InAlN to the GaN substrate, no biaxial strain would be anticipated. However, coherency strain between the pseudomorphic phase separated regions could have an effect on the phase diagram, and Elyukhin et $al.$[153] attempted to study this effect using a modified valence

force field calculation. The results predicted stabilisation of InAlN due to coherency strain, with the miscibility gap moved to lower temperatures. The authors suggested that phase separation would not be expected for lattice-matched InAlN grown by MOVPE at 800 °C, although the MBE-grown InAlN at 600 °C was suggested to be near the decomposition threshold. Thus, coherency strains could act to shift the miscibility gap in such a way as to produce different microstructures in the MOVPE and MBE-grown InAlN alloys studied in this chapter. As these and other theoretical studies do not agree on whether lattice-matched InAlN will undergo spinodal decomposition, the opportunity exists for experimental studies of InAlN microstructure to clarify this question.

7.2.2. MICROSTRUCTURAL CHARACTERISATION OF INALN

Although both MOVPE and MBE have been used to grow InAlN, few studies have focused on the microstructure of the material or the effect of growth conditions on this microstructure. As the structure of InAlN lattice matched to GaN is of particular interest, this section will first discuss studies of the surface morphology of such layers, as their morphology is relevant to investigations of the interface structure in the lattice-matched DBR structure studied here. TEM studies of microstructure of InAlN layers will then be presented, as such investigations are relevant to studies of the In distribution.

Sadler et al.[154] used light microscopy and AFM to assess the surface morphology of MOVPE-grown InAlN layers that were lattice-matched to GaN. The growth temperature and ammonia flux were varied to study the effect on the surface roughness. The authors found that a growth temperature of 790 °C and an ammonia flux of 4 slm led to a lattice matched relationship between the InAlN and the GaN, with reasonable fine-scale roughness. These growth conditions were found to produce an InAlN surface microstructure with dislocation-related pits, as well as hillocks, where the hillocks were reported to be 50 to 200 nm in diameter and 2 - 3 nm in height, as shown in the AFM image in figure 7.2[155]. Hillocks of diameter closer to 50 nm could be captured in the field of view accessible in the LEAP, similar to the gaps in the QWs observed in section 6.4.3.

Figure 7.2. From Sadler *et al.*[155], an AFM image of an InAlN surface, grown at 790 ºC with an ammonia flux of 4 slm. Hillocks can be observed, as well as dislocation-related surface pits, which are indicated with arrows.
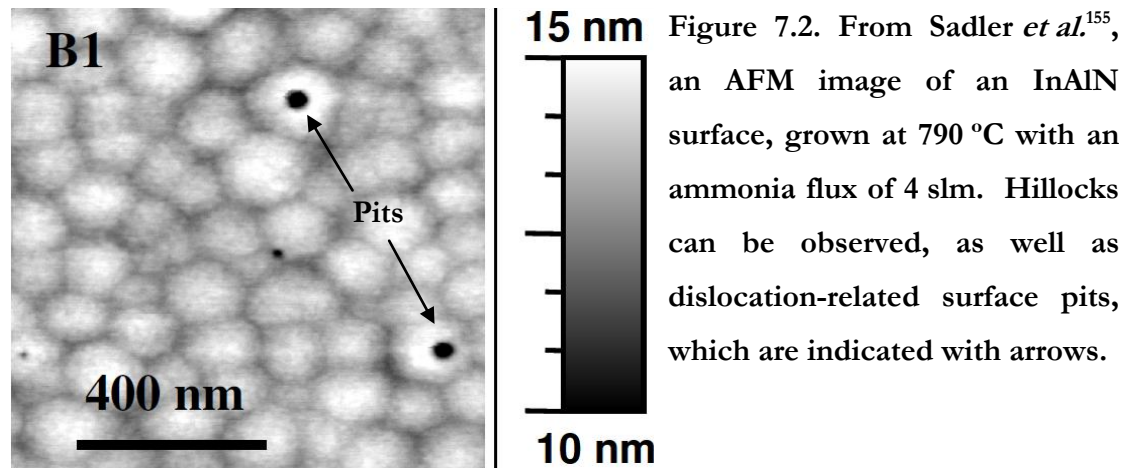
The microstructure of MOVPE-grown InAlN lattice-matched to GaN was studied by Carlin *et al.*[156] at École Polytechnique Fédérale de Lausanne (EPFL), where much of the work on InAlN has taken place. The authors grew a 20 period InAlN/GaN DBR on a GaN buffer layer, and used cross-sectional TEM to study the microstructure. A high magnification image of the DBR can be seen in figure 7.3a, with the GaN layers having brighter contrast. The layer interfaces are observed to be sharp and flat. A lower magnification image of the full DBR structure can be seen in Figure 7.3b, showing TDs as lines of dark contrast, which originate at the GaN/sapphire interface, with no noticeable increase in TD density within the DBR. No evidence for phase separation was observed in these MOVPE-grown InAlN layers.

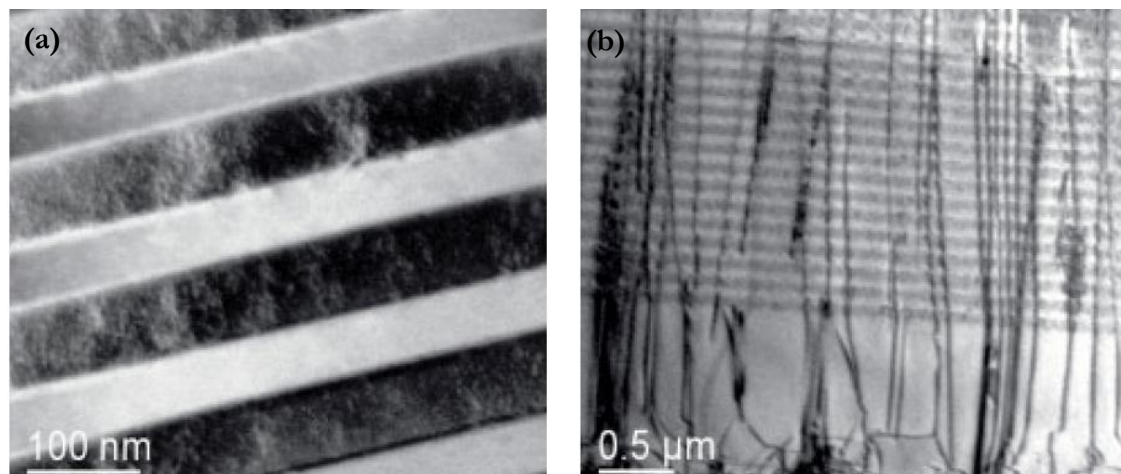Figure 7.3. From Carlin *et al.*[156], TEM images of a 20 period InAlN/GaN DBR, grown with the InAlN lattice matched to the GaN. The GaN layers show brighter contrast. (a) High magnification image, showing sharp and flat interfaces. (b) Lower magnification image, which highlights TDs as lines of dark contrast running parallel to the growth direction. Additional TDs do not appear to be generated by the DBR.

TEM studies of MBE-grown InAlN lattice matched to GaN have revealed a microstructure indicative of phase separation. Zhou *et al.*[150] observed lateral non-uniformities in composition in InAlN epilayers with In compositions between x = 0.13 and 0.19. A hexagonal honeycomb structure was revealed using TEM, with cells of 5 to 10 nm in diameter, oriented parallel to the (0001) growth direction. STEM-HAADF was then used to show that the cell walls were In-rich. The authors claimed that this structure did not arise by spinodal decomposition. Instead, they proposed a mechanism in which compositional non-uniformities developed in the early stages of growth, leading to the hexagonal honeycomb structure. The mechanism that the authors proposed is not very clear, however, and little evidence was provided in support of their assertions.

In a later study of similar MBE-grown material, Sahonta *et al.*[149] observed similar honeycomb-like structures. Figure 7.4a shows a plan-view TEM image of a 100 nm thick InAlN film grown near lattice-matched to GaN, which shows evidence of a honeycomb structure. A STEM-HAADF image of the same area is shown in figure 7.4b, which shows bright contrast at the cell walls, due to increased In content. The authors disagreed with the formation mechanism proposed by Zhou *et al.*[150], instead suggesting that the In composition modulations could be attributed to the initial formation of Al-rich platelets, due to the high sticking coefficient of Al on GaN at the low growth temperatures. Incorporation of In is increased at platelet boundaries, leading to the honeycomb structure. It is not yet known whether this honeycomb structure is found in all MBE-grown InAlN films, or if it occurs only under specific growth conditions.
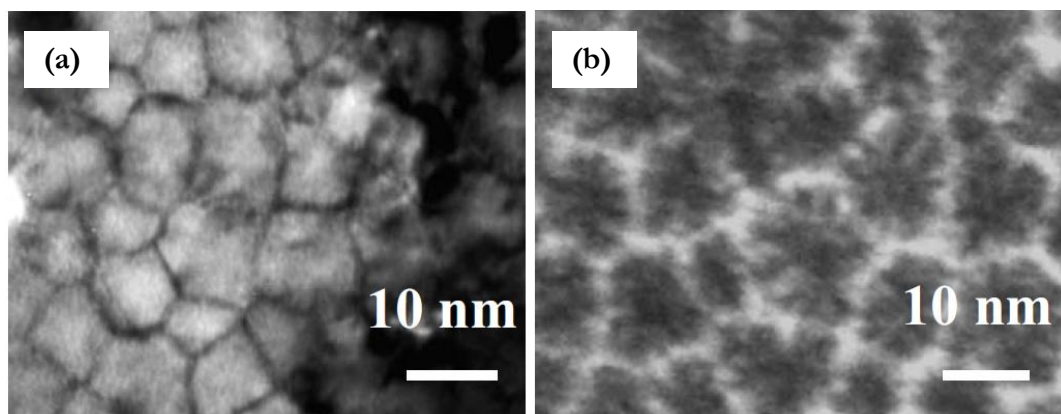
Figure 7.4. From Sahonta *et al.*[149], a plan-view TEM image of a 100 nm thick InAlN layer grown near lattice matched to the GaN template. (a) TEM image. (b) STEM-HAADF image of the same area as in (a), showing bright contrast at the cell walls, due to elevated In content.

7.2.3. FIB GALLIUM IMPLANTATION

As discussed in section 2.4.2, FIB-based APT sample preparation results in implantation of Ga ions, which can produce damaged regions and amorphise crystalline materials. In addition to these detrimental effects, the implanted Ga can also lead to APT sample fracture, due to the stress resulting from the large size of the Ga atoms. The extent of Ga implantation into the sample can be directly measured by APT in some materials, making it possible to evaluate the damage, as well as the effectiveness of steps taken to minimise the ion implantation[157]. Figure 7.5 shows a reconstructed atom map of FIB-Ga implantation into a Si APT sample, with only Ga atoms shown in red. The sample was prepared using annular milling with a 30 keV ion beam, and Ga implantation has clearly occurred at the apex of the APT sample and down the sidewalls[64]. The central region, marked with dashed lines, corresponds to a typical field of view formerly attainable in a narrower field of view atom probe instrument. This accessible volume has now been significantly increased, and data from such damaged sidewall regions are now being collected using the LEAP.
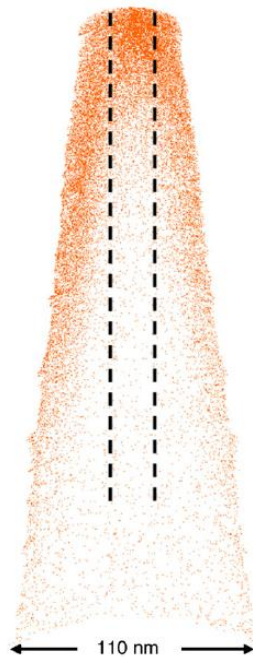
Figure 7.5. From Thompson et al.[64], a reconstructed atom map of implanted Ga ions in a Si APT sample. Ga ions are shown as red dots, with all other ions omitted for clarity. The APT sample was prepared by annular milling with a 30 keV ion beam. Ga implantation is evident at the sample apex and down the sidewalls. The dashed lines correspond to the field of view formerly attainable on narrower field of view APT instruments.

The level of Ga implantation can be minimised with the use of a protective layer deposited on the wafer surface in the region desired for liftout. FIB-Pt is often used for this protective layer, and Thompson et al.[64] used the "Stopping and Range of Ions in Matter" (SRIM) software to estimate the thickness required to prevent Ga ion penetration into the sample below. The authors' SRIM calculations suggest that at 30 keV, 10 nm of Pt is required to prevent Ga implantation into the APT sample. As the

FIB-Pt is approximately 50 % Pt, and this material was surmised to be less effective at stopping the Ga ions, the authors suggested that a 200 nm thick FIB-Pt layer should be more than sufficient to protect the underlying sample[64].

Thompson *et al.*[58] showed that a clean-up step can be employed to remove FIB-Ga implanted material after the final stage of annular milling. Using low energy (2 to 5 keV) ion beam milling, the quantity and penetration depth of the FIB-Ga can be dramatically reduced. The authors prepared Si APT samples at 30 keV, and subsequently used a clean-up step on a number of these at either 2 keV or 5 keV. Data sets containing one million Si atoms were collected from each type of sample. By overlaying the resulting mass spectra in the region of the Ga peaks, the damage reduction can be observed: figure 7.6 shows the Ga mass-to-charge region for the Si APT sample prepared with a 30 keV ion beam (red), overlaid with the spectrum from a sample initially prepared at 30 keV and subsequently cleaned with a 5 keV ion beam (pink), or a 2 keV ion beam (blue). The observed Ga concentration is reduced almost to zero following the 2 keV cleaning step. A 5 keV low energy clean-up step was used for all APT samples prepared in this thesis. It has been shown that low energy milling also causes samples to sharpen slightly[65], which is beneficial, as the sample is likely to turn on at a lower standing voltage.
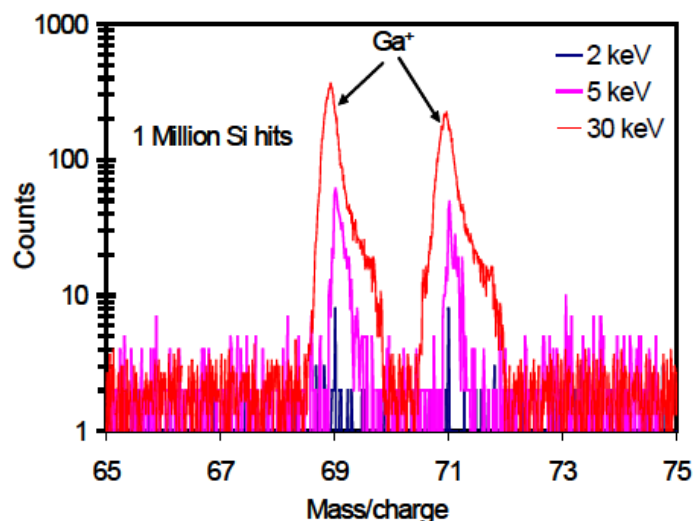
Figure 7.6. From Thompson *et al.*[58], the mass spectrum from Si APT samples, in the region of the Ga peaks. The red spectrum corresponds to a sample that was prepared by annular milling with a 30 keV Ga ion beam. The pink and blue spectra correspond to samples initially prepared with a 30 keV ion beam, which then underwent a low energy clean-up step at 5 keV or 2 keV, respectively. The extent of Ga implantation is significantly reduced with the low energy clean-up.

7.3. EXPERIMENTAL

7.3.1. SAMPLE GROWTH

The InAlN/GaN DBR sample used in this chapter was grown by Dr. Rachel Oliver on a *c*-plane sapphire substrate using a 6 × 2 inch Thomas Swan close-coupled showerhead MOVPE reactor. A low TD density template was used, as described in section 4.4.1. On this template, the 30 period DBR was grown, with each period nominally made up of 48.3 nm of InAlN and 45.5 nm of GaN. Dr. Tom Sadler found the approximate composition of the InAlN layers in the DBR by examining calibration layers grown before and after the DBR growth run[14]. As the composition was found by XRD to be 18.4 ± 0.8 % In before the growth run, and 18.6 ± 0.8 % In after, it was assumed that the InAlN layers in the DBR all had the same composition, of approximately 18.5 %.

The InAlN layers in the DBR were grown at 790 °C, with an ammonia flux of 4 slm (178.4 mmol min^{-1}), a TMI flux of 16.1 μmol min^{-1}, a TMA flux of 15.8 μmol min^{-1}, and a nitrogen carrier gas flow rate of 16 slm, at a pressure of 50 Torr. The GaN layers were grown using a two temperature method[158], which began with growth of 10 nm of GaN at the same temperature as the InAlN, with an ammonia flux of 446 mmol min^{-1}, and a TMG flux of 82 μmol min^{-1}. The carrier gas was then switched to hydrogen, and the temperature was ramped to 1000 °C, whilst the pressure was increased to 100 Torr. The remainder of the GaN layer was then grown under these conditions, with a TMG flux of 340 μmol min^{-1}.

The DBR sample was previously characterised by Dr. Tom Sadler, using STEM-HAADF[14]. Figure 7.7a shows a cross-sectional Z-contrast image of the 30 period DBR, with the GaN layers showing brighter contrast than the InAlN layers. The layers appear remarkably uniform in thickness, with flat interfaces. High resolution STEM-HAADF images can be seen in figure 7.7b and 7.7c, which show the GaN on InAlN interface and the InAlN on GaN interface, respectively. The GaN on InAlN interface appears to have a rougher interface morphology. The high resolution Z-contrast images show no obvious evidence of phase separation.
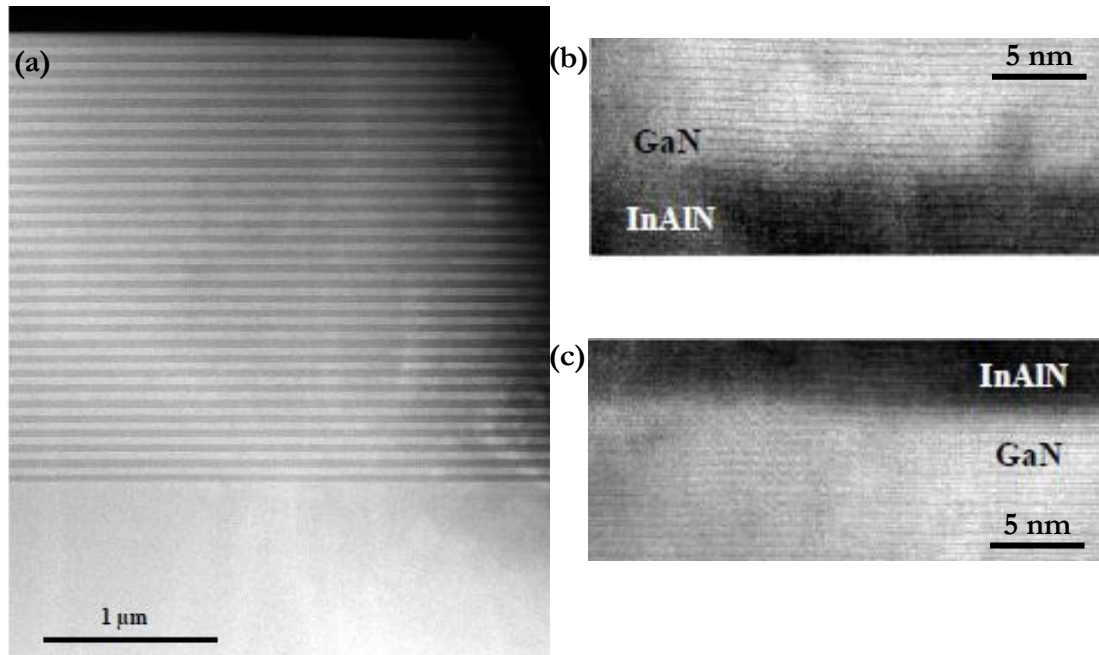
Figure 7.7. From Sadler[14], cross-sectional STEM-HAADF images. The GaN layers show brighter contrast than the InAlN layers. (a) The 30 period InAlN/GaN DBR studied in this chapter. (b) and (c) show high resolution images of the GaN on InAlN interface and the InAlN on GaN interface, respectively. The GaN on InAlN interface shown in (b) appears to be rougher.

The MBE-grown InAlN sample was grown at Sharp Laboratories of Europe, as discussed in section 2.1.2. A 10 μm MOVPE-grown GaN template, supplied by Lumilog, was used. On this template, a Si-doped 250 nm GaN layer was grown by reactive MBE at 900 °C, followed by InAlN growth by RF-PAMBE at 600 °C. The composition was found by Sharp Laboratories of Europe to be 20 % In using XRD, although the systematic error in this measurement was reported to be unknown. The InAlN layer had a nominal thickness of 100 nm. Cross-sectional BF TEM images were provided by Sharp Laboratories of Europe, and one such image can be seen in figure 7.8. The InAlN layer is labeled for clarity. Striations in contrast can be observed within the layer, running parallel to the growth direction. These striations could be consistent with the honeycomb structure previously observed in MBE-grown InAlN[149,150].
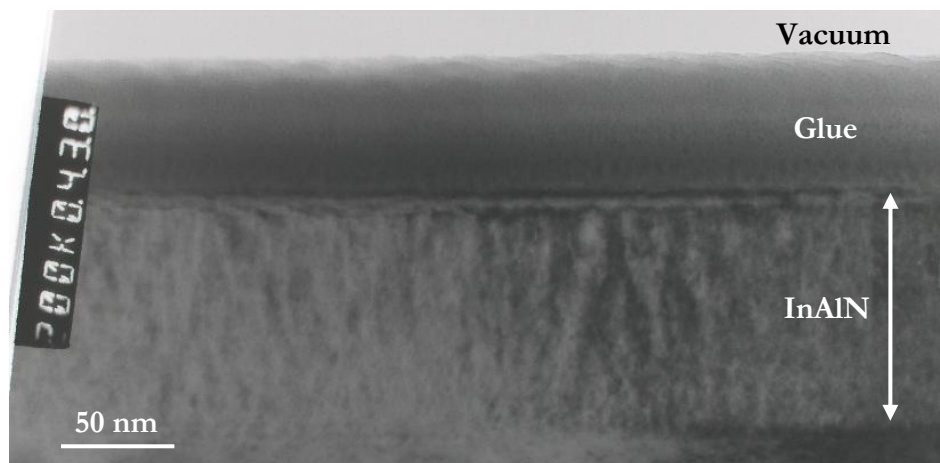
Figure 7.8. Cross-sectional BF TEM image of the MBE-grown InAlN, taken at Sharp Laboratories of Europe. The InAlN layer is labeled for clarity. Striations in contrast are observed along the growth direction of the InAlN, which could be consistent with a honeycomb structure[149,150].

7.3.2. APT SAMPLE PREPARATION

APT samples used in this chapter were prepared using the standard liftout and annular milling procedure, with microtip sample mounts, as described in section 2.5.2. It should be noted that the FEI Company™ Helios Nanolab™ dual beam FIB/SEM employed for sample preparation was equipped with a monoisotopic ^{69}Ga ion beam source.

7.3.3. APT

All APT experiments reported in this chapter were carried out at the OPAL EPSRC National Atom Probe Facility at Oxford University, as described in section 4.4.5. Details of the LEAP conditions used for each run will be presented in section 7.4, with the associated APT data set. The reconstructions of the data sets were optimised, where possible, to obtain flat layers and correct layer spacings, as indicated by TEM, although further comments on data reconstruction will also be provided in the next section.

7.4. RESULTS AND DISCUSSION

7.4.1. APT OF MOVPE-GROWN InAlN

7.4.1.1. *Reconstructed Atom Maps of the DBR*

Two APT data sets were obtained from the MOVPE-grown InAlN/GaN DBR. A base temperature of 30 K was used for both runs. The first data set, or 'DBR 1', was collected

using a laser pulse energy of 0.03 nJ and an evaporation rate of 1 %. The data set contained the end of a GaN layer, followed by a full period of InAlN and GaN, ending just as the next InAlN layer began to evaporate.

The InAlN and GaN were observed to have very different evaporation fields: the standing voltage, adjusted to maintain a constant detection rate, changed dramatically at the interface between the two materials. Figure 7.9a shows the variation in standing voltage on the DBR 1 APT sample that occurred during the run. At the point in the evaporation sequence labeled 1, the end of the GaN layer was observed, and the InAlN layer was just beginning to evaporate. The point labeled 2 corresponds to the end of the InAlN layer, at which point the next GaN layer had begun evaporating. Although the standing voltage would be expected to increase gradually as the tip blunts, the standing voltage was observed to increase sharply into point 1, upon initial evaporation of InAlN, and to decrease significantly into point 2, as the GaN evaporation commenced. This behaviour suggests that InAlN has a significantly higher evaporation field than GaN. For comparison, figure 7.9b shows a similar voltage record during evaporation of the medium Mg flux AlGaN/GaN SL, in which it can be observed that the standing voltage increases gradually, without sharp increases or decreases. This result indicates that AlGaN and GaN have similar evaporation fields.
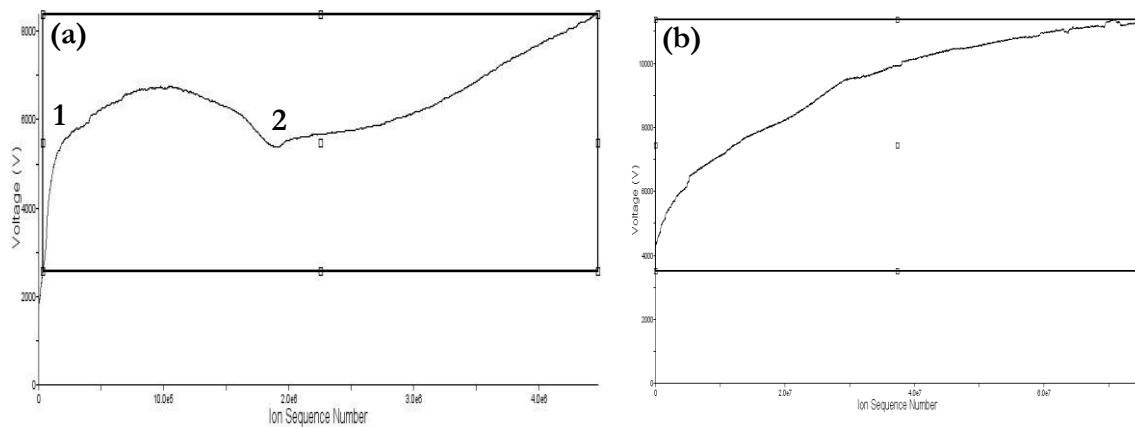
Figure 7.9. Record of the standing voltage required to maintain a constant detection rate during collection. (a) The DBR 1 data set. At the point in the ion sequence labeled 1, the InAlN layer is just beginning to evaporate. At the point labeled 2, the InAlN layer is complete, and the GaN layer has begun to evaporate. (b) For comparison, the medium Mg flux AlGaN/GaN SL data set, which showed a gradual increase in voltage during evaporation of both AlGaN and GaN.

The difference in evaporation fields between InAlN and GaN led to difficulties with data reconstruction. In a 'voltage' reconstruction, which is used for all reconstructions in this work unless otherwise stated, the radius of the reconstructed tip is defined according to the equation shown in section 2.5.2, in which the radius is inversely proportional to the evaporation field at the sample. A global evaporation field parameter must be used for the reconstruction, which leads to inaccuracies in reconstructed data sets of materials with very different evaporation fields. Although such problems could be mitigated with the use of layer-specific evaporation field values, this feature is not yet available in the commercial IVAS software used for data reconstruction.

A voltage reconstruction of the DBR 1 data set is shown in figure 7.10a, with 50 % of In atoms shown as orange dots, and 10 % of Ga atoms shown as blue dots. Although the GaN layer has been reconstructed with a layer thickness that is approximately correct, it is apparent that the global evaporation field value applied to the InAlN layer has caused it to be reconstructed with a reduced thickness and an unrealistically bulging shape. In order to reconstruct that data with a realistic tip shape, a 'shank angle' reconstruction was employed. With this method, a constant shank angle is used to constrain the reconstructed tip, assuming a hemispherical end shape. Although the shank angle of the APT sample can be estimated from FIB/SEM images taken during sample preparation, in practice, the value for shank angle is optimised to most accurately reproduce the layer thicknesses determined by TEM.

For the DBR 1 data set, a 15 ° shank angle was used. The resulting shank angle reconstruction is shown in figure 7.10b, with 50 % of In atoms shown as orange dots, and 10 % of Ga atoms shown as blue dots. Both the InAlN and GaN layers have layer thicknesses close to those observed by TEM. Unfortunately, due to the large difference in evaporation field of the two materials, it is likely that the interfaces were not very accurately reconstructed. Thus, it was not possible to study the structure of the DBR interfaces, as had been hoped.

Figure 7.10. Reconstructed atom maps of the DBR 1 data set, with 50 % of In atoms shown as orange dots, and 10 % of Ga atoms shown as blue dots. (a) Voltage reconstruction, in which the InAlN is inaccurately reconstructed. (b) Shank angle reconstruction with a 15 ° angle, which yields layer thicknesses close to those observed by TEM.

The In content of the InAlN layer was found to be 21.9 % (using a central cylinder for analysis), which is higher than the value of 18.5 % found by XRD. It is worth noting, however, that InAlN has a higher evaporation field than GaN, which may cause more nitrogen atoms to be evaporated as N_2^{++}, as opposed to N^+. It is difficult to differentiate between the two species, however, as both peaks are found at a mass-to-charge ratio of 14. If the observed peak in the DBR 1 data set was ranged as N_2^{++}, then the resulting In content was 18.7 %, closer to the XRD value, although this also resulted in poor stoichiometry, with a nitrogen content of greater than 50 %. As previously discussed, the run conditions can also affect the observed stoichiometry, and the run conditions may not have been completely optimised for the InAlN layers. In light of these issues, it is difficult to determine the precise In content of the layer using the APT data.

The second DBR data set, or 'DBR 2', was collected using a laser pulse energy of 0.06 nJ and a lower evaporation rate of 0.2 %. The data set also began at the end of a GaN layer, and contained a full period of InAlN and GaN, ending slightly further into the next

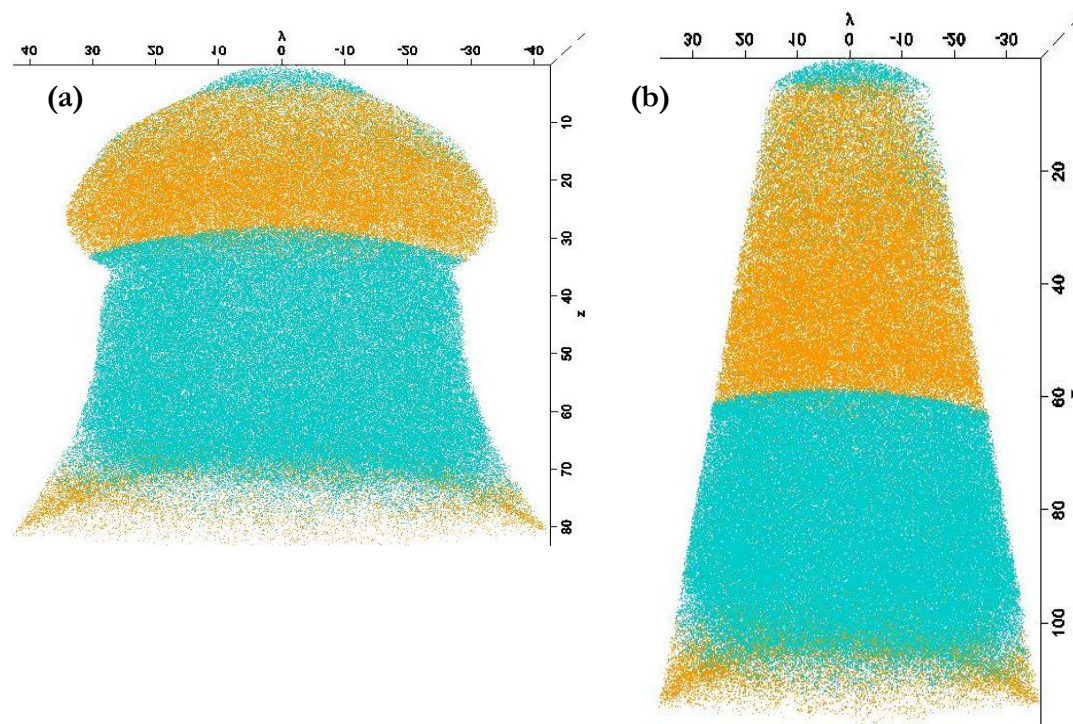InAlN layer than DBR 1. Figure 7.11a shows a 15 ° shank angle reconstruction of the DBR 2 data set, with 50 % of In atoms shown as orange dots, and 10 % of Ga atoms shown as blue dots. Within the top InAlN layer, a large area on the right hand side of the image was observed that was depleted of In. The composition within this area was investigated, and found to be O-rich. Figure 7.11b highlights this region within the top InAlN layer with a 5 at.% In isoconcentration surface, with O atoms shown as red spheres of 0.3 nm diameter and 10 % of Al atoms shown as green dots. To quantify the level of O enrichment, a cylindrical region of interest of 5 nm diameter and 20 nm length was defined to the right of the In isoconcentration surface. The O level was found to be 7.5 at.% within this cylinder. Away from the O-rich region, the In content of the InAlN layer was found to be 22.3 % (with the peak at 14 ranged as N^+), which was again higher than that observed by XRD, yet similar to that found for the InAlN layer in DBR 1.
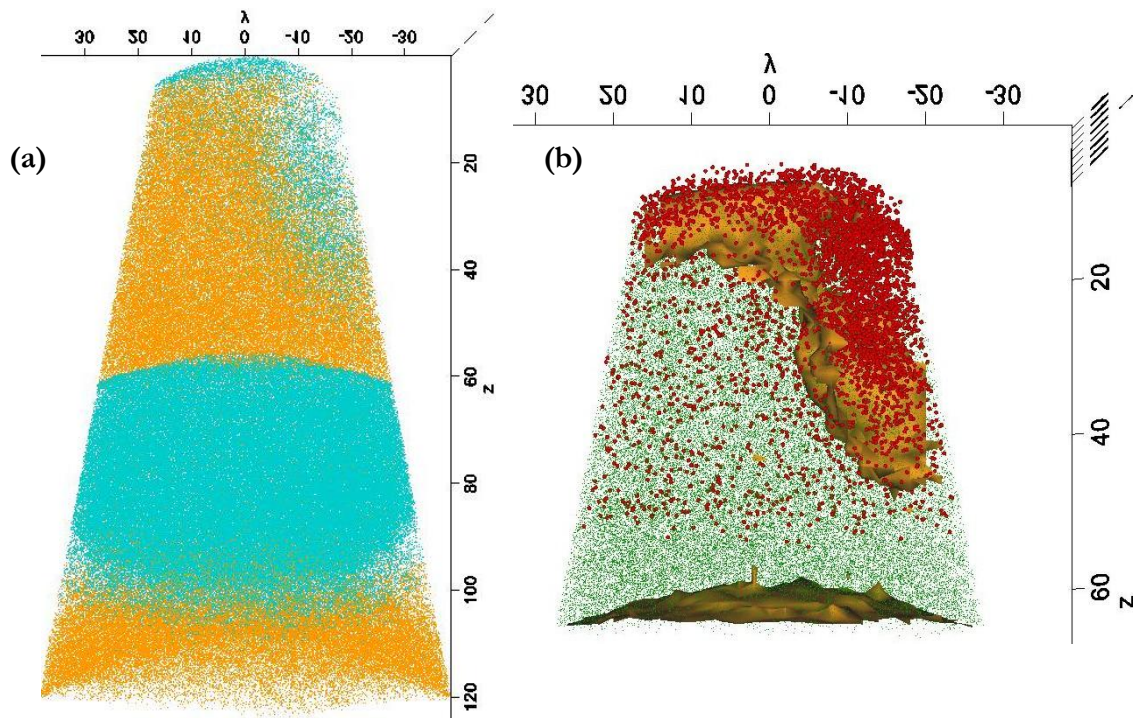
Figure 7.11. (a) Atom map of the DBR 2 data set, using a 15 ° shank angle reconstruction, with 50 % of In atoms shown as orange dots, and 10 % of Ga atoms shown as blue dots. (b) The top InAlN layer from the data set in (a), shown with an orange In isoconcentration surface at 5 at.%. O atoms are shown as red spheres of 0.3 nm diameter and 10 % of Al atoms are shown as green dots. An In-depleted region is observed at the top right of the layer, in which the O level is significantly enriched.

The reason for the O enrichment in the DBR 2 data set is not completely clear. It may be that the O-rich region corresponds to a dislocation-related pit[155], like those shown in figure 7.2, which has been filled in with GaN. In section 4.5.3, O enrichment was observed near the estimated location of a TD within a V-pit, but in too large a region to be consistent with a Cottrell atmosphere, so O-rich surface contamination was suspected. Again, in section 6.4.1, O enrichment was proposed to be associated with contamination on the surface of the APT sample because evidence of tip reshaping was observed. In the present case, the O may again be from surface contamination. Yet in the DBR 2 data set, no significant difference in overall atomic density was observed that might indicate tip reshaping.

To investigate the composition of the material near the O-enriched region in DBR 2, a cylindrical region of interest of 5 nm in diameter and 35 nm in length was defined across the top of the data set, running into the O-rich region, as shown with a top view image in figure 7.12a. A 1D concentration profile, calculated down the long axis of the cylinder, is shown in figure 7.12b. As the In-depleted and O-rich region is approached, the Ga content is observed to rise. Although the mass spectrum contained both isotopes of Ga, the $^{69}Ga/^{71}Ga$ ratio in this region was higher than predicted by the natural occurrence of the isotopes, suggesting that the region contained excess ^{69}Ga implanted by the FIB.
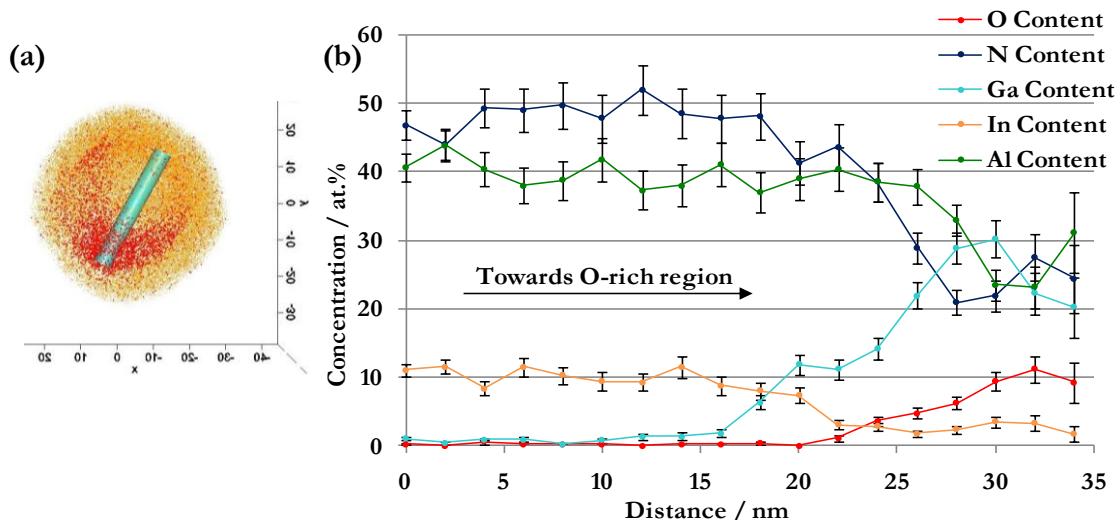
Figure 7.12. (a) Top view of the atom map of DBR 2, with 100 % of O atoms shown as red dots and 50 % of In atoms shown as orange dots. A cylindrical region of interest of 5 nm in diameter and 35 nm in length was defined across the top of the data set, into the O-rich region. (b) 1D concentration profile through the long axis of the cylinder from (a).

As the O-rich material may show evidence of ion beam damage, it is quite likely that the O-rich region is associated with surface contamination. The difference in atomic density within the O-rich region between this data set and that shown in section 6.4.1 may be related to the very different evaporation fields of the materials in the DBR.

7.4.1.2. Indium Distribution Studies

With APT data from thick MOVPE-grown InAlN layers, it was possible to study the In distribution in order to investigate if there was any evidence of phase separation. Regions for analysis were selected within the top InAlN layers of both data sets. The region selected from DBR 1 was a cylinder of 20 nm in diameter, and 30 nm in length, positioned near the centre of the data set, and away from visible Ga implantation damage. χ^2 analysis was carried out on this volume to compare the observed In distribution to that expected from a random alloy. This comparison is shown in figure 7.13. With 100 atom bins, the analysis indicated that the In distribution deviated from randomness: the p value was 0.000 for 16 DOF. Greater than expected numbers of bins were observed containing both low and high amounts of In, suggesting that the InAlN had phase separated to some extent in this region. Bin sizes of between 25 and 200 atoms were examined, with all analyses suggesting a deviation from randomness.

Figure 7.13. A comparison between the observed distribution of In within the top InAlN layer of DBR 1, and that expected from a random alloy. χ^2 analysis with 100 atom blocks showed a statistically significant deviation from randomness.

To determine whether the result for the In distribution within DBR 1 was in fact associated with through-thickness variations of the In content, the same analysis was undertaken on material from a shorter cylinder of 20 nm in length and 20 nm in diameter, positioned in the middle of the layer. This material also showed a deviation from randomness, suggesting that the previous result was not associated with through-thickness In variations. It is also worth noting that no deviation from randomness was observed in the Al or N_2 distributions, despite the fact that Al would be expected to show such a deviation in a material with a non-random distribution of In, as InAlN is assumed to be a substitutional alloy.

A smaller cylinder of 20 nm in diameter, and 10 nm in length was positioned away from the In-depleted region in the DBR 2 data set, in an area away from visible Ga implantation damage. χ^2 analysis was again carried out to determine if this data set also suggested some level of phase separation within the InAlN. The plot of the expected and observed In distributions is shown in figure 7.14. With 100 atom bins, the analysis indicated that there was no statistically significant deviation from randomness, although the p value of 0.058 for 16 DOF was close to the threshold of 0.05. Bin sizes of between 25 and 200 atoms were examined, with all analyses suggesting no statistically significant deviation from randomness. As in the DBR 1 data set, no deviation from randomness was observed in the Al or N_2 distributions. With the In distributions from DBR 1 and DBR 2 showing seemingly conflicting results, it seems that further study is needed to determine whether phase separation occurs in MOVPE-grown InAlN that is lattice matched to GaN. From the two data sets, it is impossible to tell whether the InAlN layers studied originate from the same part of the DBR. It is possible, for instance, that data set DBR 1 contains a layer that was grown early in the DBR run, and that the other data set (DBR 2) is from a layer grown much later in the run. If that were the case, then the layer grown first would have spent a much longer time at an elevated temperature and hence, phase separation might have occurred in this layer, but not in the other layer.
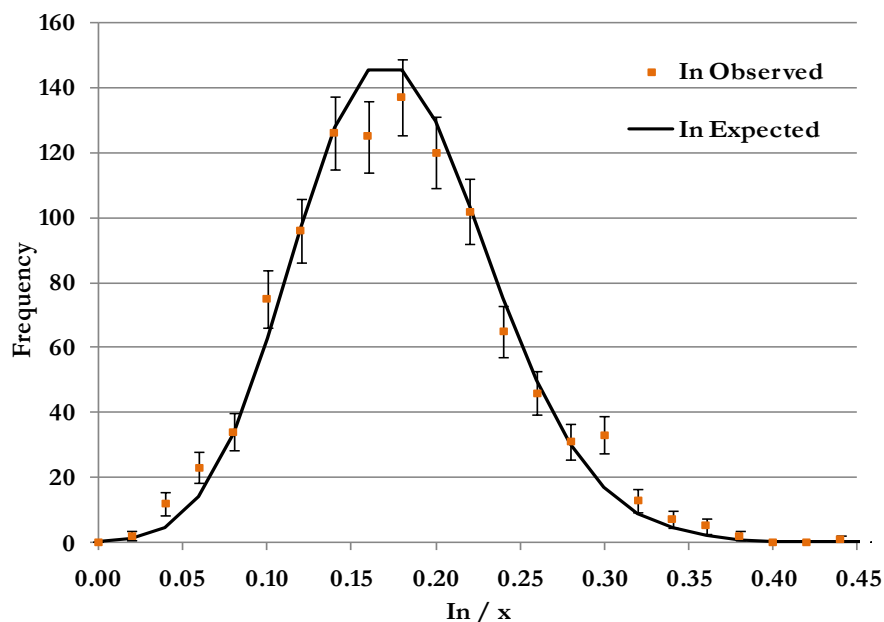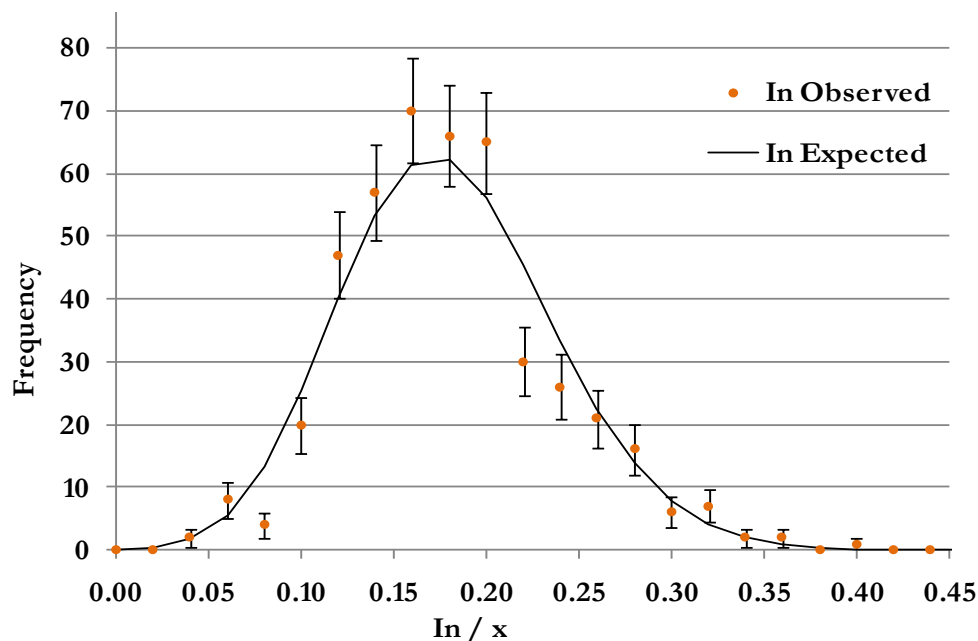
Figure 7.14. A comparison between the observed distribution of In within the top InAlN layer of DBR 2, and that expected from a random alloy. χ^2 analysis with 100 atom bins showed no statistically significant deviation from randomness, although the *p* value observed was just above the threshold of 0.05.

7.4.2. APT OF MBE-GROWN INALN

7.4.2.1. Reconstructed Atom Maps of the InAlN Layer

Three APT data sets were obtained from two samples of MBE-grown InAlN. A base temperature of 25 K was used for all runs. The samples proved fragile, so a higher laser power was used, in an effort to prevent fracture. The first data set, or 'MBE 1', was collected using a laser pulse energy of 0.4 nJ and an evaporation rate of 1.5 %. There were no known features within the InAlN layer on which to base the reconstruction, as the sample fractured prior to reaching the interface with the underlying GaN. Therefore, all three InAlN data sets were reconstructed using a 15 ° shank angle reconstruction, as was used for the MOVPE-grown InAlN/GaN DBR data. Figure 7.15 shows a reconstructed atom map of MBE 1, the largest of the three data sets collected, with 100 % of In atoms shown as orange dots, and 100 % of Ga atoms shown as blue dots. FIB-Ga implantation is evident at the top of the data set, and will be discussed in the next section. Using a central analysis cylinder, the In content of the InAlN layer in MBE 1 was found to be 25.5 % (with the peak at 14 ranged as N^+), which was higher than the 20 % observed by XRD.
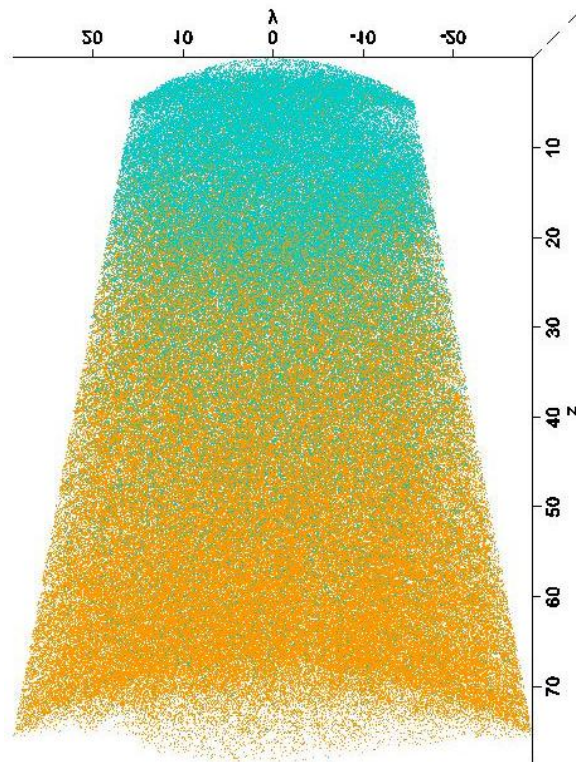
Figure 7.15. Reconstructed atom map of the MBE 1 data set, using a 15 ° shank angle reconstruction, with 100 % of In atoms shown as orange dots, and 100 % of Ga atoms shown as blue dots.

The second and third data sets were collected from the same tip, and as such will be referred to as 'MBE 2A' and 'MBE 2B', where MBE 2A contains data from the tip of the APT sample, and MBE 2B contains data from material below. Figure 7.16a shows an atom map of MBE 2A and figure 7.16b shows an atom map of MBE 2B, with the same image specifications as in figure 7.15. The small data set MBE 2A contains little or no useful data from the InAlN layer, due to the large amount of FIB-Ga implantation damage. The data from MBE 2B, however, originated from below the highly damaged region, and the central region of the data set appears to contain relatively undamaged InAlN material that is suitable for In distribution analysis. Using a central analysis cylinder, the In content of the InAlN layer in MBE 2B was found to be 25.9 % (with the peak at 14 ranged as N^+), which was again higher than the 20 % observed by XRD, but similar to that observed for MBE 1.
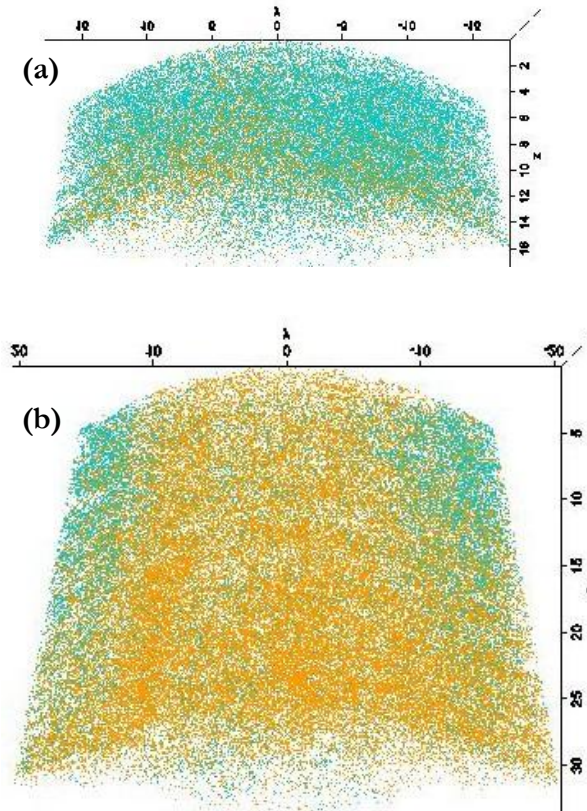
Figure 7.16. Reconstructed atom maps of the MBE-grown InAlN data sets, using a 15 º shank angle reconstruction, with 100 % of In atoms shown as orange dots, and 100 % of Ga atoms shown as blue dots. (a) Data set MBE 2A, showing data from the tip of the APT sample. Little useful data was collected in this data set, due to the extent of FIB-Ga implantation. (b) Data set MBE 2B, showing data collected from the region of the sample below that shown in (a). The central region appears to contain material useful for analysis.

7.4.2.2. Indium Distribution Studies

It was possible to study the In distribution in the MBE-grown InAlN by selecting regions for analysis away from the visibly FIB-Ga damaged regions in both the MBE 1 and MBE 2B data sets. A central cylinder of 30 nm in diameter, and 10 nm in length was defined in the MBE 1 data set, and χ^2 analysis was carried out on this volume to investigate the existence of phase separation. The comparison between observed and expected In distributions is shown in figure 7.17. With 150 atom bins, the observed p value was 0.000 for 21 DOF, indicating a non-random In distribution, and suggesting that the material may have undergone phase separation. In the MBE 2B data set, a central cylinder of 20 nm in diameter and 10 nm in length was defined, and χ^2 analysis yielded similar results: for 19 DOF, the p value was 0.00. Comparable results for both data sets were obtained when the bin size was varied between 25 and 200 atoms, and no other species were found to have distributions that deviated from randomness. Again, it is worth noting that if the In distribution is observed to deviate from randomness, the Al distribution should be expected to show such a deviation as well.
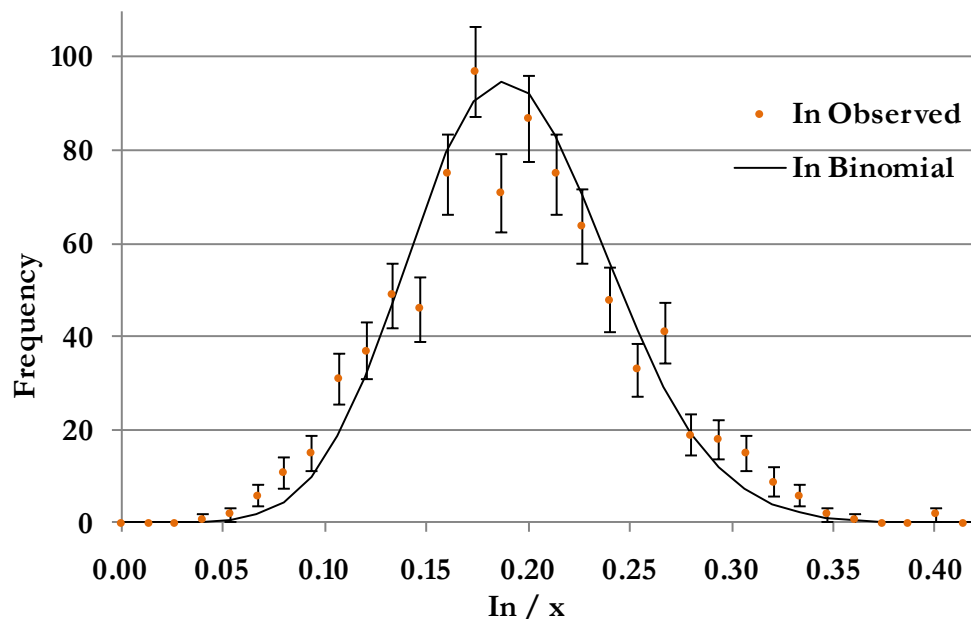
**Figure 7.17. A comparison between the observed In distribution for MBE 1 and a binomial distribution, as would be expected for a random alloy. χ^2 analysis with 150 atom bins showed a statistically significant deviation from randomness.**

Unlike the MOVPE-grown InAlN discussed in the previous section, the MBE-grown InAlN showed visible inhomogeneities in the In distribution within the atom maps. Figure 7.18 shows the MBE 2B data set, as shown in figure 7.16b, but with Ga atoms omitted and isoconcentration surfaces of 16.5 at.% In added. The isoconcentration surfaces highlight columns of In rich material, running roughly parallel to the growth direction, which could be consistent with the honeycomb structures previously observed by TEM in MBE-grown InAlN[149,150].
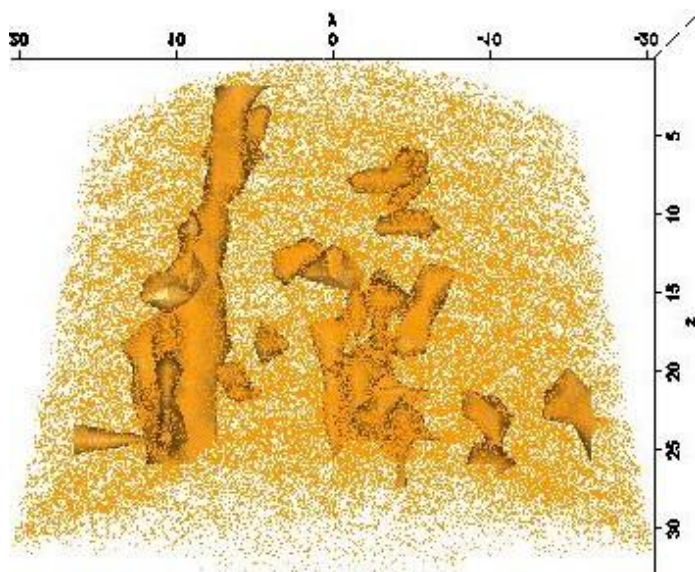
Figure 7.18. Data set MBE 2B, shown as in figure 7.16b, with Ga atoms omitted and In isoconcentration surfaces of 16.5 at.% added. Columns of In-rich material are seen running roughly parallel to the InAlN growth direction.

7.4.3. FIB GALLIUM IMPLANTATION DAMAGE

The APT data sets presented in the previous sections contained evident FIB-Ga implantation. In this section, the extent of the FIB-induced damage is examined. First, an estimate of the implantation of Ga into InAlN at different accelerating voltages is found using the SRIM software package. The Ga implantation is then studied in both the MBE-grown InAlN layer and also the MOVPE-grown DBR, in which the FIB-Ga must be differentiated from the native Ga from the GaN layers.

7.4.3.1. Modeling of Ga Implantation into InAlN

The SRIM software package was used to estimate the implantation depth and profile of FIB-Ga into InAlN lattice matched to GaN. As these simulations model a stationary beam held over a planar surface, which is not milled away by the beam, they will not accurately represent the annular milling of a needle-shaped APT sample. Yet the calculations give some insight into the maximum implantation depth of the FIB Ga beam at the energies used during sample preparation. To perform the simulations, the density of the InAlN layer was estimated using a weighted average of the densities of InN and AlN. Although the lattice parameters for InAlN are thought to deviate from Vegard's Law, as discussed in section 1.1.1, a weighted average was thought to provide a reasonable first approximation for the density of the lattice matched InAlN. Figure 7.19a shows the calculated range of 30 keV Ga ions into a 100 nm InAlN layer, and figure 7.19b shows this range using 5 keV ions. The y-axis corresponds to the sample surface. As discussed in section 7.2.3, the 5 keV ion beam used for clean-up implants Ga to a much lower depth, of approximately 10 nm, compared to the 30 keV ion beam, which implants Ga up to 50 nm into the sample.
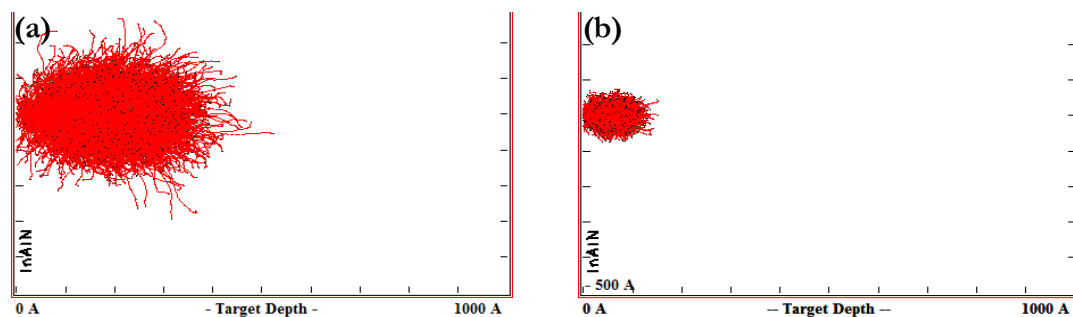
Figure 7.19. SRIM-calculated ranges for Ga ions into InAlN that is lattice matched to GaN. The y-axis corresponds to the sample surface. (a) Range for 30 keV ions. (b) Range for 5 keV ions.

7.4.3.2. Ga Implantation into MBE-Grown InAlN

The APT data sets of the MBE-grown InAlN layers offer a unique opportunity to study FIB-Ga implantation into III-Nitride materials, due to the absence of native Ga. Figure 7.15 showed the FIB-Ga atoms implanted into MBE 1. To quantify the level of implantation, a cylinder of 15 nm in diameter and 65 nm in length was defined in the centre of the data set, running parallel to the growth direction. Figure 7.20 shows a 1D concentration profile running down the long axis of this cylinder. The FIB-Ga can be observed at a considerably high level in the first 20 nm of the collected data, persisting at a level greater than 5 at.% up to 35 nm into the data set. After that point, the In content is observed to stabilise at a level near the nominal value. In light of the SRIM predictions, this result suggests that the 5 keV clean-up step was not completely successful at removing the Ga implantation due to the annular milling at 30 keV. It should be noted, however, that the InAlN layer was not capped with GaN, as was the case for other samples studied in this work. As such, the low keV clean-up step was kept shorter than with capped samples, in an effort preserve the InAlN layer within the APT sample. These observations do, however, reinforce the importance of analysing material from central regions, positioned away from the significant FIB-Ga implantation often found at the top and sides of the data set, as has been attempted throughout this work.
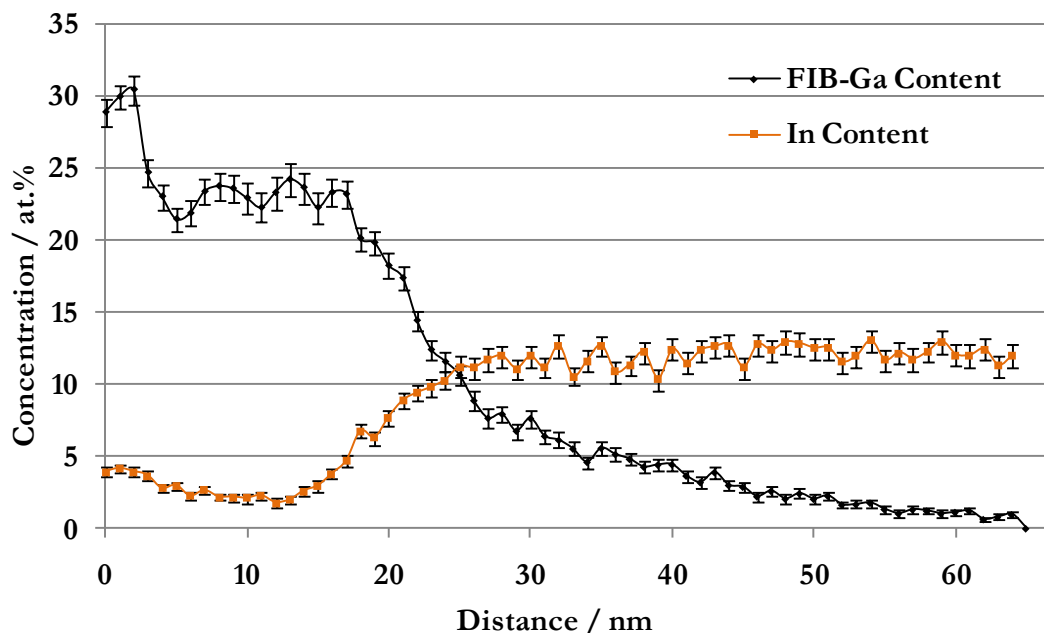
Figure 7.20. 1D concentration profile through a cylinder of 15 nm in diameter and 65 nm in length, defined parallel to the growth direction in the MBE 1 data set. The FIB-Ga level remains above 5 at.% up to 35 nm into the data set.

As the MBE 2B data set was collected below the damaged tip region, it is possible to visualise the implantation into the sidewalls of the APT sample. Figure 7.21a shows a top view of the atom map of MBE 2B, with 100 % of the In atoms shown as orange dots, and 100 % of the Ga atoms shown as blue dots. FIB-Ga can be observed from the sidewalls of the APT sample, extending between 5 and 10 nm in from the edge of the data set. The Ga observed in the MBE-grown InAlN was monoisotopic, as seen in the Ga mass-to-charge region of the mass spectrum from MBE 2B, shown in figure 7.21b. The ^{69}Ga peak is evident, but only a very small ^{71}Ga peak can be observed above the background signal.
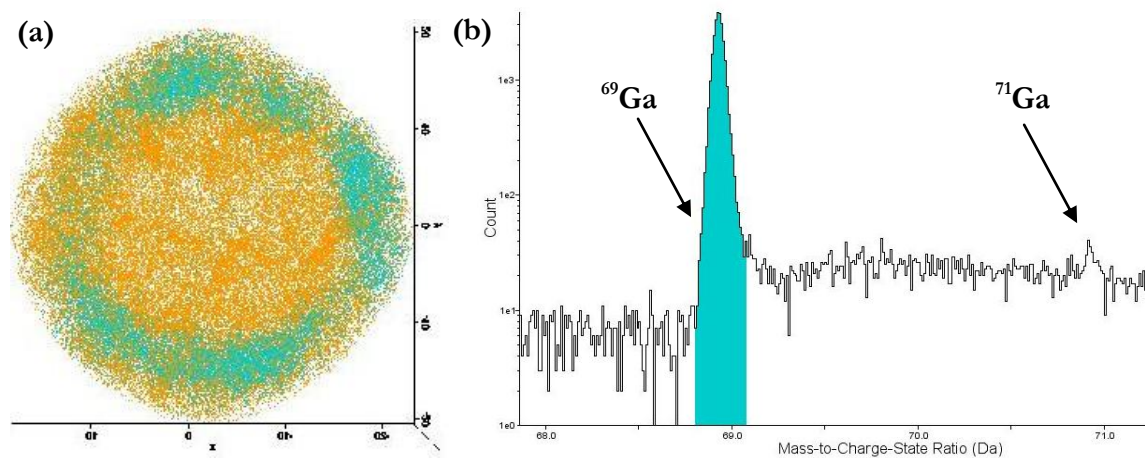
Figure 7.21. (a) Top view of the atom map of MBE 2B, with 100 % of the In atoms shown as orange dots, and 100 % of the Ga atoms shown as blue dots. FIB-Ga implantation is evident around the edge of the data set, indicating damage to the sidewalls of the APT sample. (b) The mass spectrum from the data set in (a), showing the Ga mass-to-charge region. The peak at ^{69}Ga, from the monoisotopic FIB-Ga source, is clearly observed. Only a very small ^{71}Ga peak can be identified above the background signal.

7.4.3.3. Ga Implantation into MOVPE-Grown InAlN

The MOVPE-grown DBR samples contain native Ga, in addition to Ga arising from FIB implantation. It is possible to qualitatively separate these two effects by observing the distribution of the two isotopes of Ga: where there is only ^{69}Ga, and little to no ^{71}Ga, the region shows evidence of FIB-Ga damage. In order to visualise the two isotopes of Ga, they were assigned different colours. Figure 7.22 shows an atom map of the DBR 1 data set, with 20 % of ^{69}Ga atoms shown as black dots, and 20 % of ^{71}Ga atoms shown as red dots, with all other atoms omitted. The GaN and InAlN layers are labeled for clarity.

The GaN layers contain both isotopes, whereas the InAlN layer shows just [69]Ga, indicating FIB implantation damage by the monoisotopic source.
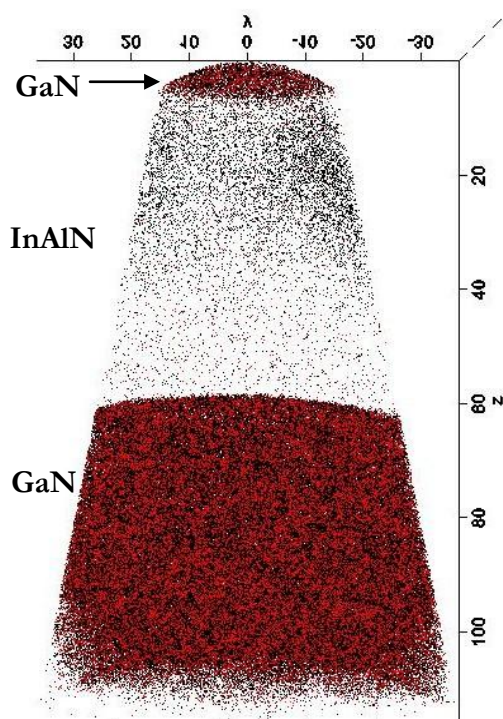
Figure 7.22. Atom map of the DBR 1 data set, showing 20 % of [69]Ga atoms as black dots, and 20 % of [71]Ga atoms as red dots. The GaN and InAlN layers are labeled for clarity. The GaN layers contain both isotopes, whereas the InAlN layer contains just [69]Ga atoms, due to FIB implantation damage.

As in the MBE 2B data set, the FIB-Ga damage to the InAlN layer of DBR 1 was mainly restricted to the sample sidewalls. Within a central cylinder of 15 nm in diameter and 100 nm in length, the InAlN layer did not contain a measurable amount of either Ga isotope, as shown in a 1D concentration profile in figure 7.23. The DBR layers are labeled for clarity. This result illustrates that it can be possible to use central cylinders to access undamaged regions for analysis.
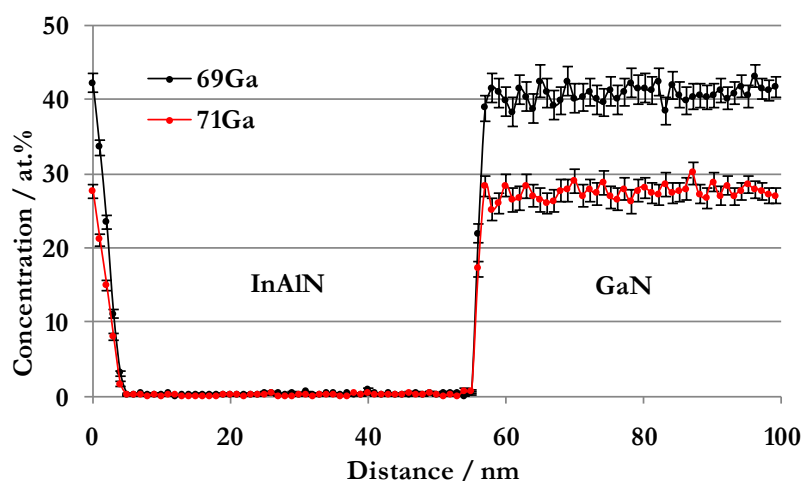
Figure 7.23. Central cylinder of 15 nm in diameter and 100 nm in length, running through the data set shown in figure 7.22. Damage, associated with the [69]Ga isotope, is not observed in the InAlN layer.

7.5. SUMMARY

Both MOVPE-grown InAlN/GaN DBR samples and MBE-grown InAlN samples were successfully run in the LEAP. Examination of the resulting data sets using χ^2 analysis yielded dissimilar results for the materials grown by the two different methods. The analysis of the In distribution in MOVPE-grown InAlN was inconclusive, with one data set suggesting a deviation from randomness in the observed In distribution, and a second showing no such deviation. These results suggest that further investigation is needed to determine whether phase separation occurs in MOVPE-grown InAlN lattice matched to GaN. The MBE-grown InAlN, on the other hand, showed both a statistically significant deviation from randomness, as well as visually identifiable regions of increased In content, although no deviation from randomness was observed in the Al distribution, as would be expected for a substitutional alloy. Highlighted with In isoconcentration surfaces, the In-rich regions were observed to run roughly parallel to the growth direction of the InAlN, a result that could be consistent with the honeycomb structures previously observed by TEM in MBE-grown InAlN[149,150].

As InAlN does not contain native Ga, the extent of FIB-Ga implantation could be investigated. The MBE-grown InAlN showed clear implantation to approximately 35 nm at the tip of the APT sample, as well as damaged regions of between 5 and 10 nm down the sidewalls of the data set. By examining the implantation of the [69]Ga isotope, which is the only isotope found in the ion source for the FIB used in this work, the damage to the InAlN layer in the DBR data set could also be investigated, despite the fact that the sample contained native Ga. Damage to the sidewall regions was found in the InAlN layer, however, a central cylinder was found to be without detectable FIB-Ga, implying that this material was not damaged, and could be used for analysis. The results of the FIB implantation studies presented in this chapter reinforce the need to select central regions for analysis, away from the top of the data set, which is likely to contain more FIB-implanted Ga.

8

APT STUDIES OF AN MBE-GROWN LASER DIODE STRUCTURE

8.1. AIMS

The aim of this chapter was to perform the first APT studies of an MBE-grown full laser diode (LD) structure. The APT study of such a structure had a number of challenges, including the possibility of sample fracture caused by biaxial strain at the layer interfaces, and data reconstruction difficulties posed by the different evaporation fields of each layer. As the LD contained a number of thick layers, obtaining an overall picture of the structure required the analysis of a significant volume of material, much more than could formerly be studied by APT with older instrumentation. If data could be collected from multiple layers within the LD structure, it was hoped that questions could be answered about individual layers, regarding properties such as In distribution, bulk composition, and dopant level. It should be noted that the In distribution studies reported for an MBE-grown InGaN QW in section 6.4.4 were in fact from the active region of the LD structure discussed here. As such, the QW will not be addressed further in this chapter.

8.2. BACKGROUND

8.2.1. MBE-GROWN LASER DIODES

The basic properties of LDs were introduced in section 1.3.2. Throughout the development and commercialisation of GaN-based LDs, epitaxial growth of these structures has been dominated by the MOVPE technique. Although proponents of the alternative growth technique of MBE claim that it could provide advantages over MOVPE growth, such as reduced consumption of source materials[159], until recently MBE had not been successfully used to produce high quality GaN-based LDs. A breakthrough in this effort was announced in 2004, when the first MBE-grown LD was reported by Hooper *et al.*[159]. The authors overcame difficulties with growing high quality InGaN to produce an InGaN MQW LD, with a structure as shown in figure 8.1. The lower diode layers were doped with Si to produce n-type material, and the upper layers were doped with Mg to produce p-type material. The p-type layers did not require an annealing step for activation of the Mg dopants. The LD active region was formed of three InGaN QWs, separated by GaN barriers. This type of LD is known as a separate confinement heterostructure (SCH), because the light produced in the MQW region is confined by outer barrier layers of AlGaN, which have a lower refractive index. Lasing was observed from this structure at room temperature using pulsed current injection, demonstrating the potential of MBE for LD growth.
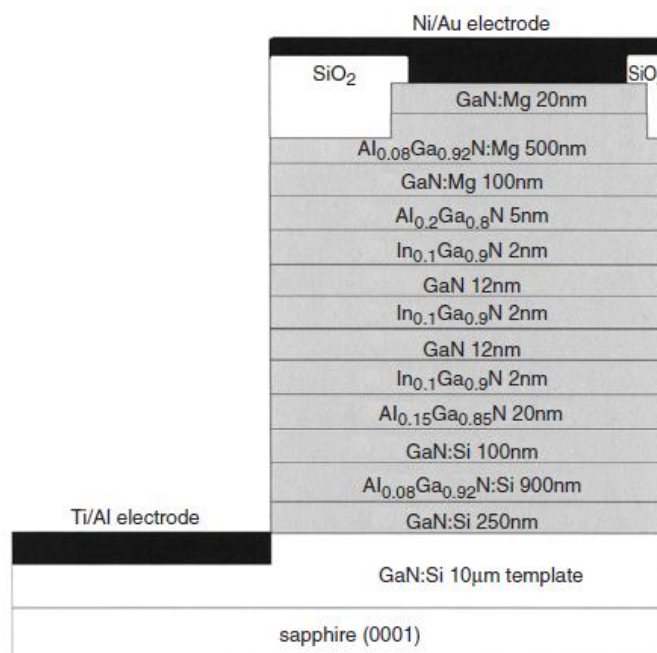
Figure 8.1. From Hooper *et al.*[159], schematic diagram of the structure of the InGaN MQW LD grown by MBE. The layers below the InGaN MQWs are doped n-type with Si, and the layers above the MQW active region are doped p-type with Mg. The undoped AlGaN layers act as outer barriers, confining the light emitted from the MQW active region.

8.3. EXPERIMENTAL

8.3.1. SAMPLE GROWTH

The growth details and layer structure for the MBE-grown LD were provided in section 6.3.1. The nominal layer structure is reproduced here, with the layers contained in some or all of the four APT data sets shaded in green. The results from the QW material were presented in section 6.4.4. The individual layers that will be discussed in section 8.4 have colour coded text: indium distribution results from the 100 nm InGaN layer (orange text) will be presented in section 8.4.2.2. Next, the actual composition of the layer that is nominally 20 nm of GaN (red text) will be discussed in section 8.4.2.3, followed by the Al content of the 5 nm AlGaN layer (blue text) in section 8.4.2.4. Finally, the measured Mg dopant level in the nominally 235 nm GaN and 595 nm AlGaN layers (purple text) will be reported in section 8.4.2.5. It is worth restating that the Mg dopant level in the p-type layers was measured with SIMS to be in the range of $3 - 5 \times 10^{19}$ cm^{-3}.

Nominal Layer Structure	Dopant
10 nm GaN	Mg
595 nm Al$_{0.045}$Ga$_{0.955}$N	Mg
235 nm GaN	Mg
5 nm Al$_{0.2}$Ga$_{0.8}$N	
3.5 nm In$_{0.18}$Ga$_{0.82}$N QW	
20 nm GaN	
100 nm In$_{0.02}$Ga$_{0.98}$N	Si
55 nm GaN	Si
480 x (1.6 nm Al$_{0.1}$Ga$_{0.9}$N + 1.6 nm GaN superlattice)	Si
220 nm GaN	Si
10 um GaN	Si
Al$_2$O$_3$ substrate	

Figure 8.2. Nominal layer structure of the green-emitting LD, grown by MBE at Sharp Laboratories of Europe. The layers contained within some or all of the APT data sets are shaded green. The colour coded text serves to identify individual layers that will be discussed in section 8.4.

8.3.2. TEM

A TEM thin foil of the LD structure was prepared using the standard methods of mechanical polishing and ion milling with the PIPS™, as described in section 2.3.1. BF TEM images were taken along the [10$\bar{1}$0] zone axis using a Philips CM30 300 kV analytical TEM equipped with a LaB$_6$ source.

8.3.3. APT SAMPLE PREPARATION

The APT samples used in this chapter were previously described in section 6.3.2.

8.3.4. APT

The APT data sets reported in this chapter were collected at the OPAL EPSRC National Atom Probe Facility at Oxford University, as described in section 4.4.5. Details of the LEAP conditions used for the runs were presented in section 6.4.4. The data sets were reconstructed using shank angle reconstructions, as discussed in section 7.4.1.1, and optimised to obtain flat layers and correct layer spacings, as indicated by TEM and the nominal layer structure.

8.4. RESULTS AND DISCUSSION

8.4.1. TEM

A thin film prepared from the LD structure was examined in the TEM. Figure 8.3 shows a BF image, taken at 21,000 times magnification. The MOVPE-grown GaN template is labeled, as are the QW and the GaN layer above (with a nominal layer thickness of 235 nm). The dark lines running in the growth direction are TDs, and are indicated using arrows. In addition to those initiated at the template, some TDs were observed to arise at the QW or at the top of the GaN layer. The overall TD density is low, however, which suggests that the APT samples were unlikely to have contained a dislocation. The QW layer was observed to be flat, and this information was used to optimise the data reconstruction. Finally, the nominally 235 nm thick GaN layer was measured by TEM to be closer to 350 nm in thickness. Although this disparity may be due to inaccuracies in the magnification from the TEM, it suggests that a degree of caution should be exercised when considering the accuracy of the nominal layer structure of the LD.
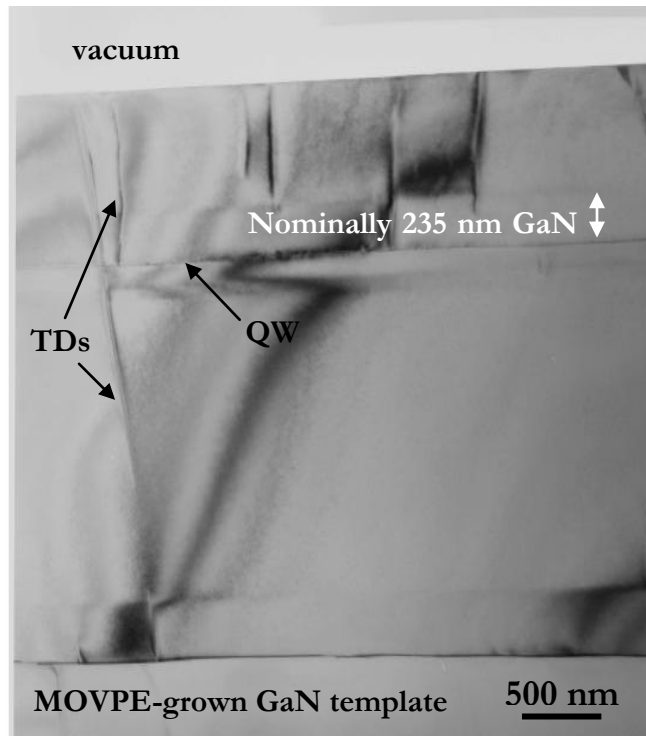
Figure 8.3. BF TEM image of the MBE-grown LD structure. The MOVPE-grown template is labeled for clarity, as are the QW and the GaN layer above, nominally grown with a thickness of 235 nm. The TDs are labeled, and can be observed to run in the growth direction, being initiated both at the template and at the QW and layers above.

8.4.2. APT

8.4.2.1. Atom Maps

Four data sets were collected from the LD structure, as discussed in section 6.4.4: two from Region A and two from Region B, where Region A had a slightly lower growth temperature. Although the LD structure contained many layers, which may each have had different evaporation fields, little difference was observed between the voltage and shank angle reconstructions, indicating that the evaporation fields were not significantly different between the layers. In the end, a shank angle reconstruction was used to avoid a slight bowing of the data set around the QW and the 5 nm AlGaN layer. A reconstructed atom map of one Region A data set was shown in figure 6.21. A second reconstructed atom map of the LD structure can be seen in figure 8.4. This data set originated from Region B. 25 % of In atoms are visible as orange dots and 25 % of Al atoms are visible as light blue dots, with all other atoms omitted for clarity. It is worth noting that the atoms visible in the nominally 235 nm GaN layer correspond to the background level, not due to identifiable In and Al peaks in the mass spectrum in that region. The individual layers that will be discussed in the following sections are labeled and colour coded, using the same colour scheme as in figure 8.2. As described in section 6.4.4, a central cylinder of 35 nm diameter was used for all analysis.
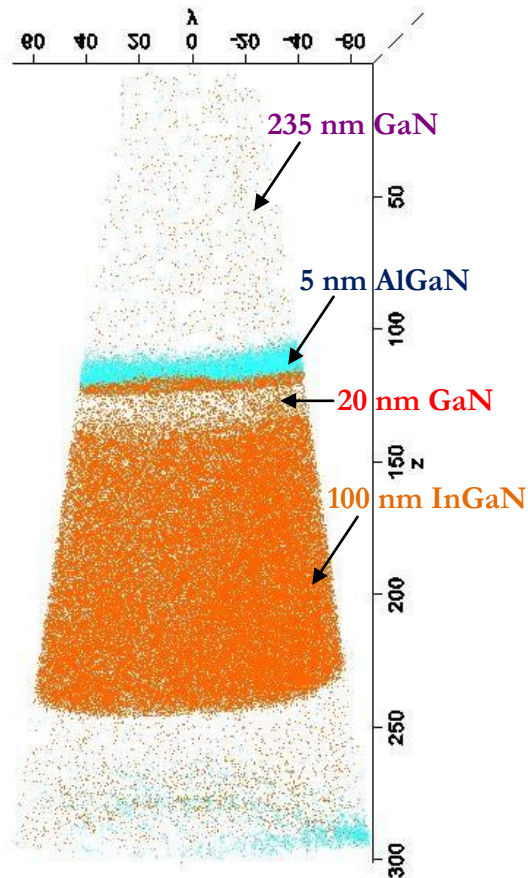
Figure 8.4. Reconstructed atom map of the MBE-grown LD structure grown at Sharp Laboratories of Europe. The sample is from the edge of the wafer, or Region B, which showed blue-green wavelength emission. 25 % of In atoms are shown as orange dots and 25 % of the Al atoms are shown as light blue dots, with all other atoms omitted for clarity. The individual layers that will be discussed in sections 8.4.2.2 through 8.4.2.5 are labeled and colour coded, with the same colour scheme as used in figure 8.2.

8.4.2.2. Indium Distribution Study: 100 nm InGaN Layer

The APT data from the 100 nm $In_{0.02}Ga_{0.98}N$ layer were used to measure the In content of the layer, which was found to be x = 2.6 ± 0.1, close to the nominal value. The InGaN layer was then studied to determine if there was any evidence of phase separation, indicated by a deviation from a random alloy distribution. Kachkanov *et al.*[160] used an extended X-ray absorption fine structure (EXAFS) study to suggest that a non-random indium distribution was more likely to be found in low indium content layers than in those with high indium contents. The authors reported that the EXAFS data showed weak phase separation in the form of InN-rich and GaN-rich InGaN regions, which increased as the In content fell, down to the lowest In composition studied[160], of x = 0.1. Yet the authors' suggestion that the phase separation increases as the amount of In falls is the opposite of what would be expected from a model of phase separation based on a phase diagram showing a spinode. The authors propose no alternative model, however, which would support their assertions. To determine if there

was any evidence of such phase separation in the low In content layer of the LD, χ^2 analysis was used.

In all four data sets, cylindrical regions of interest of 20 nm in diameter and 50 nm in length were defined within the 100 nm InGaN layer. The cylinders were positioned in the centre of the data sets and in the middle of the 100 nm layer (as some of the data sets did not contain the full 100 nm InGaN layer). χ^2 analysis with 100 atom bins yielded clear results with regard to the possibility of phase separation: there was no indication of a deviation from randomness for the In distribution for any of the data sets. The two Region A data sets had p values of 0.131 and 0.217 for 5 and 6 DOF, respectively. For the two Region B data sets, the p values were 0.446 and 0.156 for 6 DOF in each case. Figure 8.5 shows the comparison between observed and expected In distribution for the 100 nm InGaN layer from a Region B data set with 100 atom bins, which resulted in a p value of 0.446 for 6 DOF. Bin sizes of between 50 and 200 atoms yielded similar results for the In distribution, indicating that there is no evidence for phase separation in this very low In content material, as predicted by phase diagrams of the InGaN alloy.
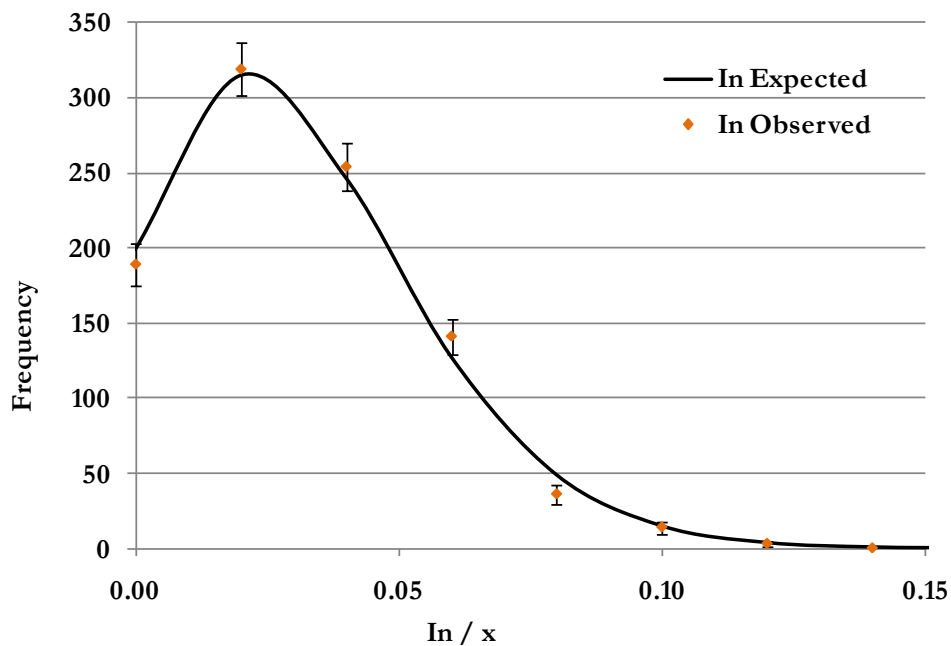
Figure 8.5. A comparison between the observed distribution of In within the 100 nm InGaN layer of a Region B data set, and that expected from a random alloy, using 100 atom bins. χ^2 analysis indicated no deviation from randomness.

8.4.2.3. Composition of the Nominally 20 nm GaN Layer

Although the 20 nm GaN layer was not intended to have any appreciable In content, a 1D concentration profile through a data set from Region A indicates that the In level does not drop to zero within the 20 nm layer, as shown in figure 8.6a. The InGaN QW, nominally 20 nm GaN layer, and 100 nm InGaN layer are labeled, for clarity. The dashed line box in figure 8.6a indicates the region of the 1D concentration profile shown in figure 8.6b, in which it can be seen that the In level within the 20 nm layer is non-zero.
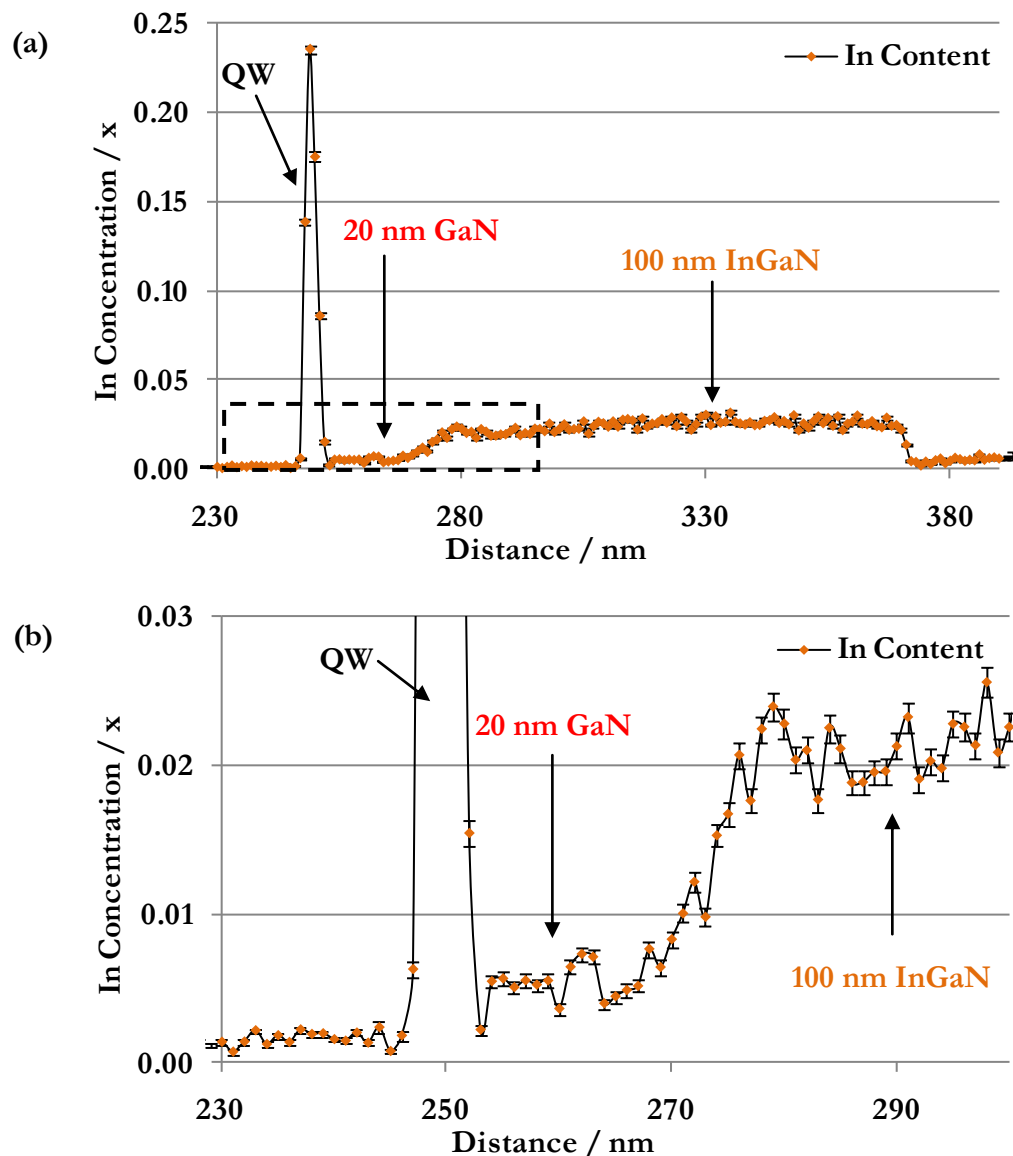
Figure 8.6. (a) 1D concentration profile showing the In content of a Region A data set. The InGaN QW and 100 nm InGaN region are labeled, as is the nominally 20 nm GaN layer. (b) Portion of the 1D concentration profile indicated in (a) with a dashed line box. The In content of the nominally 20 nm GaN layer is non-zero.

Figure 8.6b shows that the In level of the nominally 20 nm GaN layer (below the QW) is greater than the background level of In observed above the QW. The In unintentionally present within this nominally In-free region may originate from the growth reactor, as some In may have been deposited on system components during the growth of the 100 nm InGaN layer, and then migrated to the sample during the growth of the nominally 20 nm GaN layer. Alternatively, the In may have accumulated on the surface of the thick InGaN layer below the nominally GaN layer during the InGaN growth and may have then been incorporated into the growing GaN. To quantify the In content within this 20 nm layer, a cylindrical region of interest of 35 nm diameter and 15 nm length was defined within the central analysis cylinder, roughly in the middle of the layer. Table 8.1 shows the In content of the 20 nm layer in all four data sets. This low, yet non-zero level of In would be difficult to detect within the structure with other techniques. Such information can inform future LD growth, helping to optimise the nominal structure, which can potentially lead to improved device performance.

Table 8.1. Indium content within the layer nominally grown to be 20 nm of GaN, in all four data sets of the green-emitting LD.

	Region A data sets		Region B data sets	
In content / x	0.004	0.007	0.006	0.007

8.4.2.4. Al Content of the 5 nm AlGaN Layer

Above the InGaN QW, a 5 nm AlGaN layer was grown with a nominal Al content of $x = 0.2$ (estimated with XRD studies of calibration layers). The APT data were used to find the bulk level of Al within this layer, for comparison with the nominal value. In all four data sets, the AlGaN layer was isolated using an isoconcentration surface set at half the maximum Al content of the layer. Table 8.2 shows the Al content found within the 5 nm AlGaN layer for all four data sets. The measured Al content was observed to be close to, but slightly higher than the nominal value. Both Region A and Region B showed similar AlGaN contents, which indicates that the difference in growth temperature had a lesser effect on the composition of the AlGaN layer, compared with the InGaN QW, as might be expected.

Table 8.2. Al content within the 5 nm AlGaN layer in all four data sets of the green-emitting LD.

	Region A data sets		Region B data sets	
Al content / x	0.22 ± 0.01	0.21 ± 0.01	0.21 ± 0.01	0.21 ± 0.01

8.4.2.5. Mg Dopant Levels

The final aim of this chapter was to use APT to study the dopant levels present in the LD structure. Unfortunately, due to peak overlap between $^{28}Si^+$ and N_2^+, the level of Si dopants in the n-type layers cannot be revealed in this data set, or in any APT studies of III-Nitride materials. In the p-type layers, however, it was possible to observe a peak in the mass spectrum associated with Mg, allowing the dopant level to be investigated.

All four data sets contained material from the Mg-doped 235 nm GaN layer. To find the Mg content of the GaN layer, cylindrical regions of interest of 35 nm diameter and 225 nm in length were defined at the centre of each of the four data sets. The Region A data set shown in figure 6.21 also contained a portion of the Mg-doped 595 nm AlGaN layer above the 235 nm GaN layer. To study the Mg dopants within this AlGaN layer, a cylindrical region of interest of 35 nm in diameter and 7 nm in length was defined in the centre of the data set. The Mg dopant levels found for the p-type layers of the LD data sets are shown in table 8.3.

Table 8.3. Mg dopant level within the p-type layers in all four data sets of the green-emitting LD.

Mg dopant level / cm^{-3}	Region A data sets		Region B data sets	
595 nm AlGaN layer	2.1×10^{19}	-	-	-
235 nm GaN layer	1.1×10^{19}	9.7×10^{18}	1.1×10^{19}	1.8×10^{19}

The APT values for the Mg dopant level were found to be slightly lower than the SIMS measurements, which reported the Mg dopant level to be in the range of $3 - 5 \times 10^{19}$ cm^{-3}. It is worth noting, however, that the error bounds on the Mg level measured by SIMS were reported by Sharp Laboratories of Europe to be large. Reviewing the Mg levels measured by APT, both in this chapter and for the p-type superlattices studied in Chapter 5, it is found that in all cases the APT measurements were lower than the SIMS measurements. Whether these results indicate a systematic

underestimate by APT, a systematic overestimate by SIMS, or pure coincidence is unknown.

8.5. SUMMARY

In this chapter, a full MBE-grown LD structure was examined in the LEAP. Four data sets were obtained, two from Region A, and two from Region B. These data sets are very large, containing in excess of 60 million atoms, which allowed for the analysis of much more material in a single run than could be collected on older atom probe instruments. The data sets of the LD structure contained volumes of up to 400 nm in depth and 120 nm in width, including the active region, as well as the n and p-type layers. Although a larger volume of material was observed in the TEM image, the APT data set was significantly more informative.

The four APT data sets collected enabled the detailed study of individual layers within the structure. The question of phase separation in the InGaN layers was addressed using statistical analysis of both the InGaN QW and the 100 nm InGaN layer. The results from the QW analysis were presented in Chapter 6. Analysis of the In distribution within the 100 nm InGaN layer showed no indication of a deviation from randomness, a result which is consistent with what would be predicted by InGaN phase diagrams for strained layers. The APT data also revealed that the layer intended to be 20 nm of GaN in fact contained a non-zero amount of In, perhaps due to residual In found in the reactor after growth of a thick layer of InGaN. Next, the measured Al content of the 5 nm AlGaN layer was reported, and found to be near the nominal value. In fact, for all layers studied, the measured compositions were similar to the nominal compositions, with the notable exception of the non-zero In level found within the GaN layer. Finally, the Mg dopant level was quantified in the p-type layers and compared with SIMS values. The APT data again provided a lower estimate of the Mg content than SIMS, consistent with the data reported in Chapter 5. The reasons for this consistent difference are not yet clear. Combining the information reported in this chapter with the QW studies presented in Chapter 6, APT has enabled a very thorough analysis of the MBE-grown LD structure.

9

CONCLUDING REMARKS

The use of APT and complementary microscopy techniques to study defects, alloys, and a full device structure made it possible to achieve the main aim of this work, set out in Chapter 1: evaluating the capabilities of APT, as applied to III-nitride research.

With regard to defects, it was found that, unfortunately, TDs may cause fracture in III-nitride APT samples. Yet one notable APT data set did contain a significant portion of a V-pit, associated with a TD, with the position of sample fracture estimated to be at the intersection with the TD core. With that data set, the existence of sidewall QWs within the V-pit was confirmed, and O-enrichment near the TD was observed. In general, however, it was not possible to obtain APT data revealing the composition at the TDs, for correlation with KPFM observations showing that TDs were electrically active. On the other hand, the application of APT to study Mg-rich defects in p-type AlGaN/GaN superlattices proved altogether successful, and the 3D compositional characterisation supplemented the structural information gained by TEM.

This work presented the first APT studies of AlGaN and InAlN. It was found that AlGaN has a similar evaporation field to GaN, making it straightforward to collect data

from samples containing both materials. InAlN, in contrast, was found to have a much higher evaporation field than GaN (and hence presumably than other III-nitrides), which can cause difficulties in data collection and reconstruction when a sample contains InAlN, as well as other III-nitride materials. Yet despite these problems, it has proved possible to use APT to study a number of InAlN samples. APT was also used to investigate the microstructural origin of localisation in InGaN QWs. Not only was the absence of a deviation from randomness in the In distribution observed, consistent with previous reports, but the presence of such a deviation was also revealed, after the InGaN QWs were exposed to the electron beam.

Finally, a full MBE-grown LD device structure was analysed using APT. The resulting data sets contained a large volume of material, starting in the n-type layers, and running through the active region into the p-type layers. From one data set of the LD structure, it was possible to study a number of features of interest, including the In distribution within the QW, the p-type dopant level, and the bulk composition of individual layers. It is interesting to surmise that such APT characterisation could be an invaluable tool in any attempts to reverse engineer these types of device structures.

Overall, the work presented in this thesis demonstrates that APT is a highly valuable tool for III-nitrides research. The technique has largely lived up to its promise to provide 3D compositional information at the nanoscale, revealing the composition of 5 nm Mg-rich features, and enabling binary nitride alloy homogeneity to be successfully characterised. In addition, the 3D nature of the technique made it possible to study the morphology and composition of InGaN QW network structures, as well as sidewall QWs decorating V-pits. APT does not provide a definite answer to all questions, however, and there are certainly limitations to its applicability to III-nitride research. The experiments reported in this thesis have shown that APT struggles to successfully analyse material containing TDs, perhaps because strain associated with the crystal defect leads to fracture of the APT sample. Even when a data set has been successfully obtained, peak overlap in the mass spectrum obscures the answers to some important questions. For instance, the peak overlap between the Si^+ n-type dopants and N_2^+ prevents characterisation of Si dopants in nitride materials. Despite these issues, APT studies of III-nitrides can be highly informative, providing unique information. The technique certainly has the potential to become an important tool in the characterisation of nitride materials.

The studies reported in this thesis represent just the start of the possible APT investigations into III-nitride materials. To begin with, a number of other experiments can be recommended which could lead to a deeper understanding of the topics discussed in this work. For instance, it would be useful to prepare more APT samples containing TDs, ensuring that the MQWs remain to serve as a marker for the TD position. When examining the samples in the TEM, the type of TD should be determined, in addition to noting its position within the sample. By running further samples with TDs in the LEAP, it should be possible either to collect an APT data set containing a dislocation, or to determine whether the position of fracture is consistently associated with the intersection with a TD, or a certain type of TD. In addition to capturing a TD running through MQWs, it would be very interesting to observe a TD in p-type GaN, to investigate if the Mg dopants segregate to the dislocation.

It would also be worthwhile to repeat the investigation of electron beam damage to InGaN MQWs. Further APT samples of blue-emitting single-temperature InGaN QWs should be prepared, with an attempt made to capture the MQWs at the tip of the APT sample, as the amount of damage was seen to decrease with depth. If a method could be found to avoid or eliminate the O-rich amorphous region that surrounded the APT sample reported in this work, that would make the information gained from the TEM images more easily interpretable.

As all side-on APT samples that were prepared in this work fractured in the LEAP, it would be interesting to separate the role of TDs from that of crystal orientation in causing sample fracture. This investigation would require the preparation of a side-on sample that did not contain a TD, a fact which could be confirmed by TEM. A very low TD density template would be needed for material growth, and this could be provided either by growth on a free-standing GaN substrate, or on a wing region of an ELOG sample.

Beyond investigations pertaining to the work reported in this thesis, APT can be applied to any avenue of III-nitride research that requires insight into the 3D nanoscale composition. One notable opportunity pertains to the study of III-nitrides grown in other orientations, such as non- and semi-polar. Such III-nitride materials have yet to be

studied with APT, and the question remains as to whether it will be possible to do so, as the effect of orientation is further complicated by the high density of crystal defects often found in such materials. If these orientations can be investigated with APT, many of the questions already addressed for c-plane material will require examination anew.

Although APT data sets can be highly informative, it is important to emphasise the utility of comparative microscopy in gaining a complete understanding of the material system. It is of great value to study the structure and composition of a material by two different methods, such as APT and TEM. In future studies, however, emphasis should be placed on attempting to correlate the material's structure or composition with its properties. For instance, it should be possible to use CL to examine the luminescence from an area surrounding a TD, which may then be characterised by TEM and then APT. In this way, a complete understanding of the structure – property link could be obtained.

Lastly, it is hoped that the work contained in this thesis has demonstrated the ability of APT to characterise III-nitride materials, thereby providing unique and valuable 3D information.

'Nothing tends so much to the advancement of knowledge as the application of a new instrument.'
-- Sir Humphry Davy

APPENDIX 1

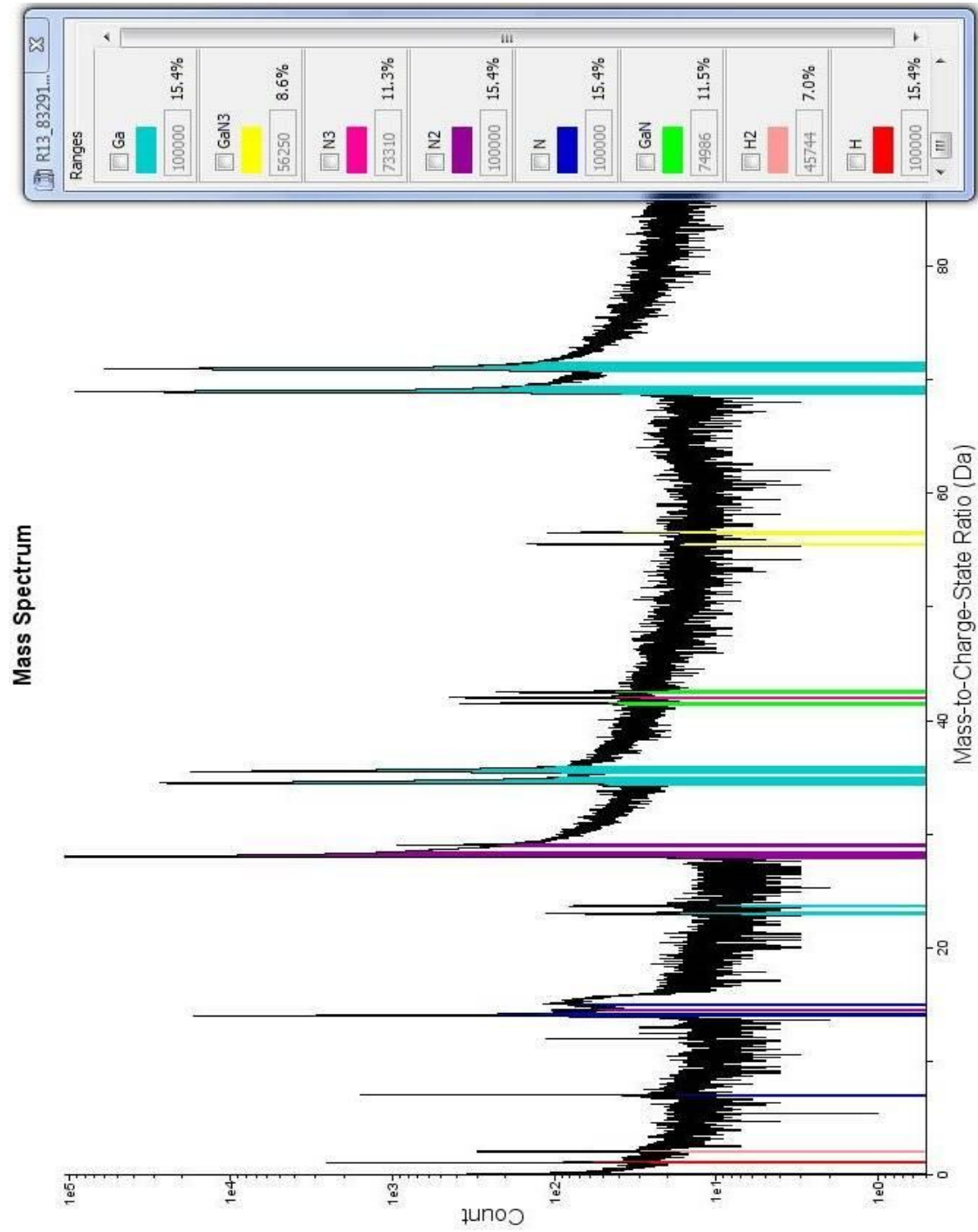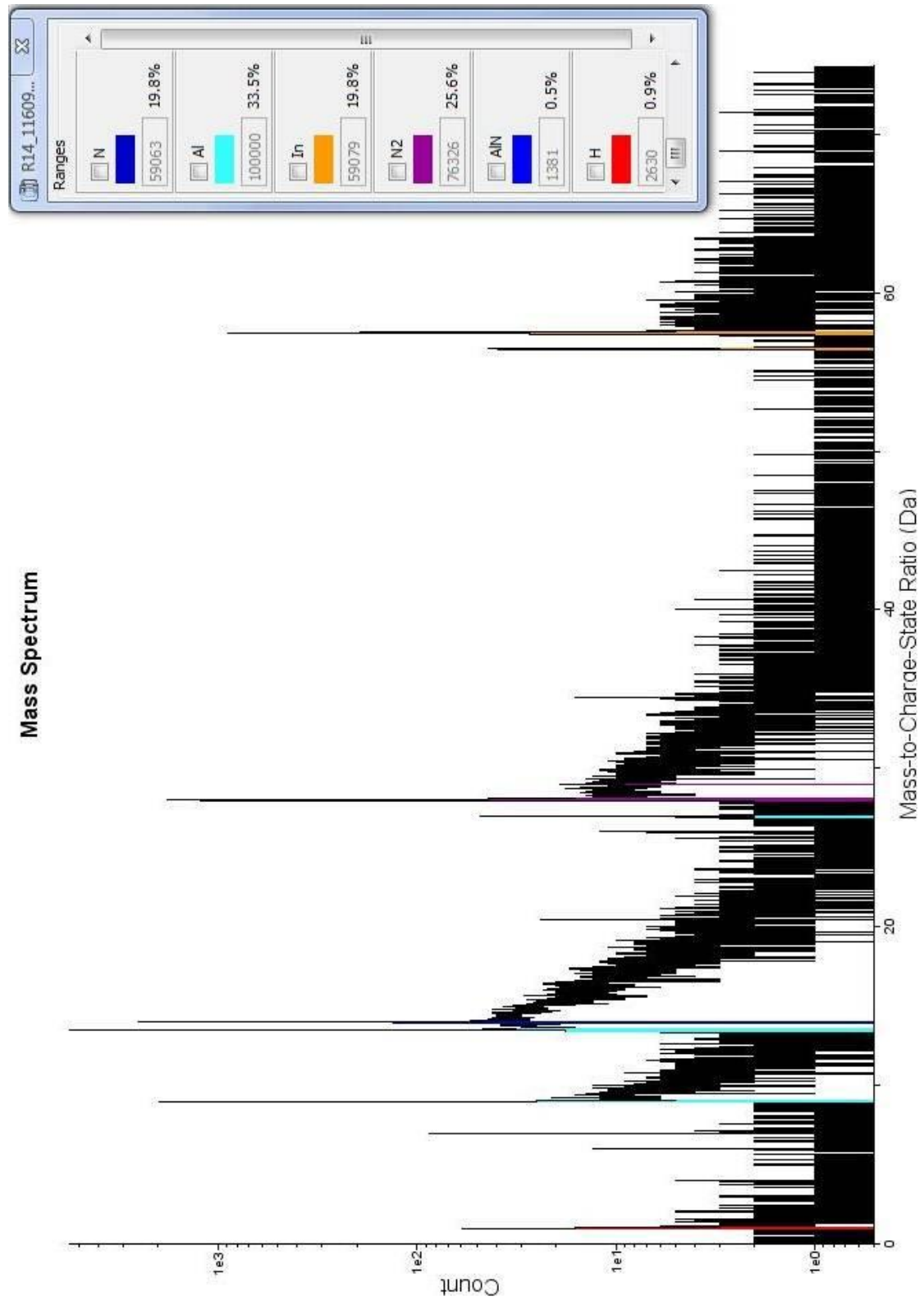**Fig. 1. Example mass spectrum of GaN.**

Fig. 2. Example mass spectrum of InAlN.

REFERENCES

1.   Nakamura, S., *Introduction to Nitride Semiconductor Blue Lasers and Light Emitting Diodes*. Taylor and Francis: London and New York, 2000.

2.   Tsao, J. Y., Light emitting diodes (LEDs) for general illumination: An OIDA technology roadmap. Optoelectronics Industry Development Association: Washington, DC, 2002.

3.   Lester, S. D.; Ponce, F. A.; Craford, M.; Steigerwald, D. A., High dislocation densities in high-efficiency GaN-based light-emitting-diodes. *Applied Physics Letters* **1995,** *66* (10), 1249-1251.

4.   Orton, J. W.; Foxon, C. T., Group III nitride semiconductors for short wavelength light-emitting devices. *Reports on Progress in Physics* **1998,** *61* (1-75).

5.   Cherns, P. D. A transmission electron microscopy study of AlGaN/GaN heterostructures. University of Cambridge, 2007.

6.   Wagner, J.-M.; Bechstedt, F., Properties of strained wurtzite GaN and AlN: *Ab initio* studies. *Physcial Review B* **2002,** *66*, 115202-1 - 115202-20.

7.   Vurgaftman, I.; Meyer, J. R., Band parameters for nitrogen-containing semiconductors. *Journal of Applied Physics* **2003,** *94*, 3675.

8.   Moram, M. A.; Vickers, M. E., X-ray diffraction of III-nitrides. *Reports on Progress in Physics* **2009,** *72*, 036502-1 - 036502-40.

9.   Dridi, Z.; Bouhafs, B.; Ruterana, P., First-principles investigation of lattice constants and bowing parameters in wurtzite $Al_xGa_{1-x}N$, $In_xGa_{1-x}N$ and $In_xAl_{1-x}N$ alloys. *Semiconductor Science and Technology* **2003,** *18*, 850-856.

10.   Darakchieva, V.; Xie, M.-Y.; Tasnadi, F.; Abrikosov, I. A.; Hultman, L.; Monemar, B.; Kamimura, J.; Kishino, K., Lattice parameters, deviations from Vegard's rule, and E_2 phonons in InAlN. *Applied Physics Letters* **2008,** *93*, 261908-1 - 261908-3.

11.   Bernardini, F.; Fiorentini, V.; Vanderbilt, D., Spontaneous polarization and piezoelectric constants of III-V nitrides. *Physical Review B* **1997,** *56* (16), R10024-R10027.

12.   Wu, J., When group-III nitrides go infrared: new properties and perspectives. *Journal of Applied Physics* **2009,** *106*, 011101-1 - 011101-28.

13.   Safta, N.; Mejri, H.; Belmabrouk, H.; Zaidi, M. A., Effects of high doping on the bandgap bowing for $Al_xGa_{1-x}N$. *Microelectronics Journal* **2006,** *37*, 1289-1292.

14.   Sadler, T. Nitride distributed Bragg reflectors for single photon source applications. University of Cambridge, 2009.

15.   Gibart, P., Metal organic vapour phase epitaxy of GaN and lateral overgrowth. *Reports on Progress in Physics* **2004,** *67*, 667-715.

16.   Grzegory, I.; Krukowski, S.; Leszczynski, M.; Perlin, P.; Suski, T.; Porowski, S., The application of high pressure in physics and technology of III-V nitrides. *Acta Physica Polonica A* **2001,** *100*, 57-109.

17.   Ruterana, P.; Nouet, G., Atomic structure of extended defects in wurtzite GaN epitaxial layers. *Physica Status Solidi B* **2001,** *227* (1), 177-228.

18.   Akasaki, I., Key inventions in the history of nitride-based blue LED and LD. *Journal of Crystal Growth* **2007,** *300*, 2-10.

19.   Schubert, E. F., *Light emitting diodes*. Cambridge University Press: Cambridge, 2003.

20.   Zhu, D. MOVPE growth and characterisation of near-UV emitters based on III-nitrides. University of Cambridge, 2007.

21.   Nakamura, S.; Senoh, M.; Nagahama, S.; Iwasa, N.; Yamada, T.; Matsushita, T.; Kiyoku, H.; Sugimoto, Y., InGaN-based multi-quantum-well-structure laser diodes. *Japanese Journal of Applied Physics* **1996,** *35* (2), L74-L76.

22.   Miller, M. K., *Atom probe tomography: analysis at the atomic level*. Kluwer Academic/Plenum Publishers: New York, 2000.

23.   Muller, E. W., *Zhurnal Tekhnicheskoi Fiziki* **1936,** *17*, 412.

24.   Kelly, T. F.; Miller, M. K., Invited reveiw article: atom probe tomography. *Review of Scientific Instruments* **2007,** *78*, 031101-1 - 031101-20.

25.   Cerezo, A.; Godfrey, T. J.; Smith, G. D. W., Application of a position-sensitive detector to atom probe microanalysis. *Review of Scientific Instruments* **1988,** *59* (6), 862-866.

26.   Kelly, T. F.; Camus, P. P.; Larson, D. J.; Holzman, L. M.; Bajikar, S. S., On the many advantages of local-electrode atom probes. *Ultramicroscopy* **1996,** *62*, 29-42.

27.   DenBaars, S. P., Basic Physics and Materials Technology of GaN LEDs and LDs. In *Introduction to Nitride Semiconductor Blue Lasers and Light Emitting Diodes*, Nakamura, S.; Chichibu, S. F., Eds. Taylor and Francis: London, 2000.

28.   Thrush, E. J., Presentation: Monitoring MOVPE growth of GaN. University of Cambridge, 2008.

29.   Kim, S.; Oh, J.; Kang, J.; Kim, D.; Won, J.; Kim, J. W.; Cho, H.-K., Two-step growth of high quality GaN using V/III ratio variation in the initial growth stage. *Journal of Crystal Growth* **2004,** *262*, 7-13.

30.   Oliver, R. A.; Kappers, M. J.; McAleese, C.; Datta, R.; Sumner, J.; Humphreys, C. J., The origin and reduction of dislocations in gallium nitride. *Journal of Materials Science: Materials in Electronics* **2008,** *19*, S208 - S214.

31.   Ou, J.; Chen, W.-K.; Lin, H.-C.; Pan, Y.-C.; Lee, M.-C., An elucidation of solid incorporation of InGaN grown by metalorganic vapor phase epitaxy. *Japanese Journal of Applied Physics* **1998,** *37* (2), L633 - L636.

32.   Matsuoka, T.; Yoshimoto, N.; Sasaki, T.; Katsui, A., Wide-gap semiconductor InGaN and InGaAlN grown by MOVPE. *Journal of Electronic Materials* **1992,** *21* (2), 157-163.

33.   Koukitu, A.; Taki, T.; Takahashi, N.; Seki, H., Thermodynamic study on the role of hydrogen during the MOVPE growth of group III nitrides. *Journal of Crystal Growth* **1999,** *197*, 99-105.

34.   Nakamura, S.; Mukai, T.; Senoh, M.; Iwasa, N., Thermal annealing effects on p-type Mg-doped GaN films. *Japanese Journal of Applied Physics* **1992,** *31* (2B), L139 - L142.

35.   Pankove, J. I., *Gallium nitride (GaN) II*. Academic Press: San Diego, 1999.

36.   Strite, S.; Ruan, J.; Li, Z.; Salvador, A.; Chen, H.; Smith, D. J.; Choyke, W. J.; Morkoc, H., An investigation of the properties of cubic GaN grown on GaAs by plasma-assisted molecular-beam epitaxy. *Journal of Vacuum Science and Technology* **1991,** *9* (4), 1924-1929.

37.   Lei, T.; Fanciulli, M.; Molnar, R. J.; Moustakas, T. D.; Graham, R. J.; Scanlon, J., Epitaxial growth of zinc blende and wurtzitic gallium nitride thin films on (001) silicon. *Applied Physics Letters* **1991,** *59* (8), 944-946.

38.   Hoke, W. E.; Lemonias, P. J.; Weir, D. G., Evaluation of a new plasma source for molecular beam epitaxial growth of InN and GaN films. *Journal of Crystal Growth* **1991,** *111*, 1024-1028.

39.   Oliver, R. A., Advances in AFM for the electrical characterization of semiconductors. *Reports on Progress in Physics* **2008,** *71*, 076501-1 - 076501-37.

40.   Martin, Y.; Williams, C. C.; Wickramasinghe, H. K., Atomic force microscope force mapping and profiling on a sub 100-A scale. *Journal of Applied Physics* **1987,** *61*, 4723-4729.

41.   Oliver, R. A., AFM lecture 1. University of Cambridge, 2007.

42. Williams, D. B.; Carter, C. B., *Transmission electron microscopy - a textbook for materials science*. 2nd ed.; Springer: New York, 2009.

43. Smeeton, T. M. The nanostructures of InGaN quantum wells. University of Cambridge, 2005.

44. Barnard, J. S.; Bennett, S. E.; Oliver, R. A.; Kappers, M. J.; Humphreys, C. J., The role of rough surfaces in quantitative ADF imaging of gallium nitride-based materials. *Journal of Physics: Conference Series* **2010,** *209*, 012019-1 - 012019-4.

45. Cockayne, D. J. H.; Ray, I. L. F.; Whelan, M. J., Investigations of dislocation strain fields using weak beam. *Philosophical Magazine* **1969,** *20* (168), 1265-1270.

46. Wu, X. H.; Brown, L. M.; Kapolnek, D.; Keller, S.; Keller, B.; DenBaars, S. P.; Speck, J. S., Defect structure of metal-organic chemical vapor deposition-grown epitaxial (0001) GaN/Al$_2$O$_3$. *Journal of Applied Physics* **1996,** *80* (6), 3228-3237.

47. Smith, D. J., High resolution transmission electron microscopy. In *Handbook of Microscopy for Nanotechnology*, Yao, N.; Wang, Z. L., Eds. Springer US: New York, 2005.

48. Wang, Z. L.; van Heerden, D.; Josell, D.; Shapiro, A. J., Energy-filtered high-resolution electron microscopy for quantitative solid state structure determination. *Journal of Research of the National Institute of Standards and Technology* **1997,** *102* (1), 1-13.

49. Nellist, P. D., Scanning transmission electron microscopy. In *Science of microscopy*, Hawkes, P. W.; Spence, J. C. H., Eds. Springer: New York, 2007.

50. Howie, A., Image-contrast and localized signal selection techniques. *Journal of Microscopy - Oxford* **1979,** *117* (SEP), 11-23.

51. Crewe, A. V., The physics of the high-resolution scanning microscope. *Reports on Progress in Physics* **1980,** *43*, 621-639.

52. Jeanguillaume, C.; Trebbia, P.; Colliex, C., About the use of electron energy-loss spectroscopy for chemical mapping of thin foils with high spatial resolution. *Ultramicroscopy* **1978,** *3*, 237-242.

53. Liu, J., High-resolution scanning electon microscopy. In *Handbook of Microscopy for Nanotechnology*, Yao, N.; Wang, Z. L., Eds. Springer US: New York, 2005.

54. Reichelt, R., Scanning electron microscopy. In *Science of microscopy*, Hawkes, P. W.; Spence, J. C. H., Eds. Springer: New York, 2007.

55. Everhart, T. E.; Thornley, R. F. M., Wide-band detector for micro-microampere low-energy electron currents. *Journal of Scientific Instruments* **1960,** *37* (7), 246-248.

56. Reimer, L., *Scanning electron microscopy - physics of image formation and microanalysis*. 2nd ed.; Springer: New York, 1998.

57. Yao, N., Focused ion beam system - a multifunctional tool for nanotechnology. In *Handbook of Microscopy for Nanotechnology*, Yao, N.; Wang, Z. L., Eds. Springer US: New York, 2005.

58. Thompson, K.; Gorman, B.; Larson, D. J.; van Leer, B.; Hong, L., Minimization of Ga induced FIB damage using low energy clean-up. *Microscopy and Microanalysis* **2006,** *12* (S2), 1736-1737.

59. Kelly, T. F.; Larson, D. J.; Thompson, K.; Alvis, R. L.; Bunton, J. H.; Olson, J. D.; Gorman, B. P., Atom probe tomography of electronic materials. *Annual Review of Materials Research* **2007,** *37*, 681-727.

60. Seidman, D. N., Three-dimensional atom-probe tomography: advances and applications. *Annual Review of Materials Research* **2007,** *37*, 127-158.

61. Cerezo, A.; Clifton, P. H.; Galtrey, M. J.; Humphreys, C. J.; Kelly, T. F.; Larson, D. J.; Lozano-Perez, S.; Marquis, E. A.; Oliver, R. A.; Sha, G.; Thompson, K.; Zandbergen, M.; Alvis, R. L., Atom probe tomography today. *Materials Today* **2007,** *10* (12), 36-42.

62. Kellogg, G. L.; Tsong, T. T., Pulsed-laser atom-probe field-ion microscopy. *Journal of Applied Physics* **1980,** *51* (2), 1184-1193.

63. Miller, M. K.; Russell, K. F.; Thompson, G. B., Strategies for fabricating atom probe specimens with a dual beam FIB. *Ultramicroscopy* **2005,** *102*, 287-298.

64. Thompson, K.; Lawrence, D.; Larson, D. J.; Olson, J. D.; Kelly, T. F.; Gorman, B., In situ site-specific specimen preparation for atom probe tomography. *Ultramicroscopy* **2007,** *107*, 131-139.

65. Galtrey, M. J. The mechanism of luminescence in III-Nitrides. University of Cambridge, 2009.

66. Birdseye, P. J.; Smith, D. A., The electric field and the stress on a field-ion specimen. *Surface Science* **1970,** *23*, 198-210.

67. Miller, M. K.; Cerezo, A.; Hetherington, M. G.; Smith, G. D. W., *Atom probe field ion microscopy*. Oxford University Press: Oxford, 1996.

68. Muller, E. W.; Krishnaswamy, S. V., Energy deficits in pulsed field evaporation and deficit compensated atom-probe designs. *Review of Scientific Instruments* **1974,** *45* (9), 1053-1059.

69. Gault, B.; Moody, M. P.; De Geuser, F.; La Fontaine, A.; Stephenson, L. T.; Haley, D.; Ringer, S. P., Spatial Resolution in Atom Probe Tomography. *Microscopy and Microanalysis* **2010,** *16*, 99-110.

70.   Nakamura, S., The roles of structural imperfections in InGaN-based blue light-emitting diodes and laser diodes. *Science* **1998,** *281*, 956-961.

71.   Ferdous, M. S.; Wang, X.; Fairchild, M. N.; Hersee, S. D., Effect of threading defects on InGaN/GaN multiple quantum well light emitting diodes. *Applied Physics Letters* **2007,** *91*, 231107-1 - 231107-3.

72.   Ning, X. J.; Chien, F. R.; Pirouz, P., Growth defects in GaN films on sapphire: The probable origin of threading dislocations. *Journal of Materials Research* **1995,** *11* (3), 580-592.

73.   Wu, X. H.; Fini, P.; Tarsa, E. J.; Heying, B.; Keller, S.; Mishra, U. K.; DenBaars, S. P.; Speck, J. S., Dislocation generation in GaN heteroepitaxy. *Journal of Crystal Growth* **1998,** *189/190*, 231-243.

74.   Fini, P.; Wu, X.; Tarsa, E. J.; Golan, Y.; Srikant, V.; Keller, S.; DenBaars, S. P.; Speck, J. S., The effect of growth environment on the morphological and extended defect evolution in GaN grown by metalorganic chemical vapor deposition. *Japanese Journal of Applied Physics* **1998,** *37*, 4460-4466.

75.   Narayanan, V.; Lorenz, K.; Kim, W.; Mahajan, S., Origins of threading dislocations in GaN epitaxial layers grown on sapphire by metalorganic chemical vapor deposition. *Applied Physics Letters* **2001,** *78* (11), 1544-1546.

76.   Narayanan, V.; Lorenz, K.; Kim, W.; Mahajan, S., Gallium nitride epitaxy on (0001) sapphire. *Philosophical Magazine A* **2002,** *82* (5), 885-912.

77.   Moram, M. A.; Oliver, R. A.; Kappers, M. J.; Humphreys, C. J., The spatial distribution of threading dislocations in gallium nitride films. *Advanced Materials* **2009,** *21*, 3941-3944.

78.   Oliver, R. A.; Kappers, M. J.; Humphreys, C. J., Insights into the origin of threading dislocations in GaN/Al$_2$O$_3$ from atomic force microscopy. *Applied Physics Letters* **2006,** *89*, 011914-1 - 011914-3.

79.   Oliver, R. A.; Kappers, M. J.; Sumner, J.; Datta, R.; Humphreys, C. J., Highlighting threading dislocations in MOVPE-grown GaN using an in situ treatment with SiH4 and NH3. *Journal of Crystal Growth* **2006,** *289*, 506-514.

80.   Gmeinwieser, N.; Schwarz, U. T., Pattern formation and directional and spatial ordering of edge dislocations in bulk GaN: microphotoluminescence spectra and continuum elastic calculations. *Physical Review B* **2007,** *75*, 245213-1 - 245213-7.

81.   Herzog, A. H.; Keune, D. L.; Craford, M. G., High-efficiency Zn-diffused GaAs electroluminescent diodes. *Journal of Applied Physics* **1972,** *43* (2), 600-608.

82.   Brantley, W. A.; Lorimor, O. G.; Dapkus, P. D.; Haszko, S. E.; Saul, R. H., Effect of dislocations on green electroluminescence efficiency in GaP grown by liquid phase epitaxy. *Journal of Applied Physics* **1975,** *46* (6), 2629-2637.

83.   Kamiyama, S.; Iwaya, M.; Takanami, S.; Terao, S.; Miyazaki, A.; Amano, H.; Akasaki, I., UV light-emitting diode fabricated on hetero-ELO-grown Al$_{0.22}$Ga$_{0.78}$N with low dislocation density. *Physica Status Solidi A* **2002,** *192* (2), 296-300.

84.   Bougrioua, Z.; Azize, M.; Lorenzini, P.; Laugt, M.; Haas, H., Some benefits of Fe doped less dislocated GaN templates for AlGaN/GaN HEMTs grown by MOVPE. *Physica Status Solidi A* **2005,** *202* (4), 536-544.

85.   Sugahara, T.; Hao, M.; Wang, T.; Nakagawa, D.; Naoi, Y.; Nishino, K.; Sakai, S., Role of dislocation in InGaN phase separation. *Japanese Journal of Applied Physics* **1998,** *37*, L1195-L1198.

86.   Rosner, S. J.; Carr, E. C.; Ludowise, M. J.; Girolami, G.; Erikson, H. I., Correlation of cathodoluminescence inhomogeneity with microstructural defects in epitaxial GaN grown by metalorganic chemical-vapor deposition. *Applied Physics Letters* **1997,** *70* (4), 420-422.

87.   Knott, J. F., Lecture notes on semi-conductors: dislocations. 2009.

88.   Cherns, D.; Jiao, C. G.; Mokhtari, H.; Cai, J.; Ponce, F. A., Electron holography studies of the charge on dislocations in GaN. *Physica Status Solidi B* **2002,** *234* (3), 924-930.

89.   Cherns, D.; Jiao, C. G., Electron holography studies of the charge on dislocations in GaN. *Physical Review Letters* **2001,** *87* (20), 205504-1 - 205504-4.

90.   Cai, J.; Ponce, F. A., Determination by electron holography of the electronic charge distribution at threading dislocations in epitaxial GaN. *Physica Status Solidi A - Applied Research* **2002,** *192* (2), 407-411.

91.   Simpkins, B. S.; Yu, E. T.; Waltereit, P.; Speck, J. S., Correlated scanning Kelvin probe and conductive atomic force microscopy studies of dislocations in gallium nitride. *Journal of Applied Physics* **2003,** *94* (3), 1448-1453.

92.   Fox, M., *Optical properties of solids*. Oxford University Press: 2007.

93.   Datta, R.; Kappers, M. J.; Barnard, J. S.; Humphreys, C. J., Revealing all types of threading dislocations in GaN with improved contrast in a single plan view image. *Applied Physics Letters* **2004,** *85* (16), 3411-3413.

94.   Hemmingsson, C.; Boota, M.; Rahmatalla, R. O.; Junaid, M.; Pozina, G.; Birch, J.; Monemar, B., Growth and characterization of thick GaN layers grown by halide vapour

phase epitaxy on lattice-matched AlInN templates. *Journal of Crystal Growth* **2009,** *311*, 292-297.

95.   Youtsey, C.; Romano, L. T.; Molnar, R. J.; Adesida, I., Rapid evaluation of dislocation densities in n-type GaN films using photoenhanced wet etching. *Applied Physics Letters* **1999,** *74* (23), 3537-3539.

96.   Weyher, J. L.; Brown, P. D.; Rouviere, J. L.; Wosinski, T.; Zauner, A. R. A.; Grzegory, I., Recent advances in defect-selective etching of GaN. *Journal of Crystal Growth* **2000,** *210*, 151-156.

97.   Kuwano, N.; Tajima, R.; Bohyama, S.; Miyake, H.; Hiramatsu, K.; Shibata, T., Influence of etching condition on surface morphology of AlN and GaN layers. *Physica Status Solidi A* **2004,** *201* (12), 2755-2759.

98.   Marchand, H.; Ibbetson, J. P.; Fini, P. T.; Wu, X. H.; Keller, S.; DenBaars, S. P.; Speck, J. S.; Mishra, U. K., Fast lateral epitaxial overgrowth of gallium nitride by metalorganic chemical vapor deposition using a two-step process. *MRS Internet Journal of Nitride Semiconductor Research* **1999,** *4*.

99.   Wu, X. H.; Elsass, C. R.; Abare, A.; Mack, M.; Keller, S.; Petroff, P. M.; DenBaars, S. P.; Speck, J. S., Structural origin of V-defects and correlation with localized excitonic centers in InGaN/GaN multiple quantum wells. *Applied Physics Letters* **1998,** *72* (6), 692-694.

100.   Shiojiri, M.; Chuo, C. C.; Hsu, J. T.; Yang, J. R.; Saijo, H., Structure and formation mechanism of V defects in multiple InGaN/GaN quantum well layers. *Journal of Applied Physics* **2006,** *99*, 073505-1 - 073505-6.

101.   Yang, J. R.; Li, W. C.; Tsai, H. L.; Hsu, J. T.; Shiojiri, M., Electron microscopy investigations of V defects in multiple InGaN/GaN quantum wells and InGaN quantum dots. *Journal of Microscopy - Oxford* **2010,** *237* (3), 275-281.

102.   Ding, K.; Zeng, Y., Do sidewall quantum wells exist in GaInN-based light-emitting diodes? *Japanese Journal of Applied Physics* **2010,** *49*, 028001-1 - 028001-2.

103.   Kim, I.-H.; Park, H.-S.; Park, Y.-J.; Kim, T., Formation of V-shaped pits in InGaN/GaN multiquantum wells and bulk InGaN films. *Applied Physics Letters* **1998,** *73* (12), 1634-1636.

104.   Hangleiter, A.; Hitzel, F.; Netzel, C.; Fuhrmann, D.; Rossow, U.; Ade, G.; Hinze, P., Suppression of nonradiative recombination by V-shaped pits in GaInN/GaN quantum wells produces a large increase in the light emission efficiency. *Physical Review Letters* **2005,** *95*, 127402-1 - 127402-4.

105.   Xu, X.; Beckman, S. P.; Weber, E. R.; Chrzan, D. C.; Erni, R. P.; Arslan, I.; Browning, N.; Bleloch, A.; Kisielowski, C., Distortion and segregation in a dislocation core region at atomic resolution. *Physical Review Letters* **2005,** *95*, 145501-1 - 145501-4.

106.   Arslan, I.; Bleloch, A.; Stach, E. A.; Ogut, S.; Browning, N. D., Using EELS to observe composition and electronic structure variations at dislocation cores in GaN. *Philosophical Magazine* **2006,** *86* (29), 4727-4746.

107.   Hawkridge, M.; Cherns, D., Oxygen segregation to nanopipes in gallium nitride. In *Microscopy of Semiconducting Materials*, Cullis, A. G.; Hutchison, J. L., Eds. Springer: Berlin, 2005; Vol. 107, pp 45-50.

108.   Cherns, D.; Young, W. T.; Steeds, J. W.; Ponce, F. A.; Nakamura, S., Observation of coreless dislocations in alpha-GaN. *Journal of Crystal Growth* **1997,** *178*, 201-206.

109.   Thompson, K.; Flaitz, P. L.; Ronsheim, P.; Larson, D. J.; Kelly, T. F., Imaging of arsenic cottrell atmospheres around silicon defects by three-dimensional atom probe tomography. *Science* **2007,** *317*, 1370-1373.

110.   Cerezo, A.; Gibuoin, D.; Godfrey, T. J.; Hyde, J. M.; Kim, S.; Setna, R. P.; Sijbrandij, S. J.; Venker, F. M.; Wilde, J.; Smith, G. D. W., Three-dimensional atom probe microanalysis. In *Proceedings of the International Conference on Microstructures and Functions of Materials*, Igata, N.; Hiki, Y.; Yoshida, I.; Sato, S., Eds. University of Tokyo Press: Tokyo, 1996; pp 281-291.

111.   Wilde, J.; Cerezo, A.; Smith, G. D. W., Three-dimensional atomic-scale mapping of a Cottrell atmosphere around a dislocation in iron. *Scripta Materialia* **2000,** *43*, 39-48.

112.   Cottrell, A. H.; Bilby, B. A., Dislocation theory of yielding and strain ageing of iron. *Proceedings of the Physical Society of London Section A* **1947,** *62* (349), 49-62.

113.   Blavette, D.; Cadel, E.; Fraczkiewicz, A.; Menand, A., Three-dimensional atomic-scale imaging of impurity segregation to line defects. *Science* **1999,** *286*, 2317-2319.

114.   Miller, M. K., Characterization of dislocations with a local electrode atom probe: practical considerations and limitations. *Microscopy and Microanalysis* **2006,** *12* (S2), 60-61.

115.   Galtrey, M. J.; Oliver, R. A.; Kappers, M. J.; Humphreys, C. J.; Clifton, P. H.; Larson, D.; Saxey, D. W.; Cerezo, A., Three-dimensional atom probe analysis of green- and blue-emitting $In_xGa_{1-x}N$/GaN multiple quantum well structures. *Journal of Applied Physics* **2008,** *104*, 013524-1 - 013524-7.

116.   Sumner, J. Scanning probe microscopy studies on gallium nitride. University of Cambridge, 2007.

117.   Sheu, J. K.; Chi, G. C., The doping process and dopant characteristics of GaN. *Journal of Physics: Condensed Matter* **2002,** *14*, R657 - R702.

118.   Amano, H.; Kito, M.; Hiramatsu, K.; Akasaki, I., P-type conduction in Mg-doped GaN treated with low-energy electron beam irradiation (LEEBI). *Japanese Journal of Applied Physics* **1989,** *28* (12), L2112 - L2114.

119.   Obloh, H.; Bachem, K. H.; Kaufmann, U.; Kunzer, M.; Maier, M.; Ramakrishnan, A.; Schlotter, P., Self-compensation in Mg doped p-type GaN grown by MOCVD. *Journal of Crystal Growth* **1998,** *195*, 270-273.

120.   Liliental-Weber, Z.; Benamara, M.; Swider, W.; Washburn, J.; Grzegory, I.; Porowski, S.; Lambert, D. J. H.; Eiting, C. J.; Dupuis, R. D., Mg-doped GaN: Similar defects in bulk crystals and layers grown on Al_2O_3 by metal-organic chemical-vapor deposition. *Applied Physics Letters* **1999,** *75* (26), 4159-4161.

121.   Vennegues, P.; Benaissa, M.; Beaumont, B.; Feltin, E.; De Mierry, P.; Dalmasso, S.; Leroux, M.; Gibart, P., Pyramidal defects in metalorganic vapor phase epitaxial Mg doped GaN. *Applied Physics Letters* **2000,** *77* (6), 880-882.

122.   Benaissa, M.; Vennegues, P.; Beaumont, B.; Gibart, P.; Saikaly, W.; Charai, A., Electron energy-loss spectroscopy characterization of pyramidal defects in metalorganic vapor-phase epitaxy Mg-doped GaN thin films. *Applied Physics Letters* **2000,** *77* (14), 2115-2117.

123.   Kozodoy, P.; Smorchkova, Y. P.; Hansen, M.; Xing, H.; DenBaars, S. P.; Mishra, U. K.; Saxler, A. W.; Mitchel, W. C., Polarization-enhanced Mg doping of AlGaN/GaN superlattices. *Applied Physics Letters* **1999,** *75* (16), 2444-2446.

124.   Galtrey, M. J.; Oliver, R. A.; Kappers, M. J.; Humphreys, C. J., Response to "Comment on 'Three-dimensional atom probe studies of an $In_xGa_{1-x}N$/GaN multiple quantum well structure: assessment of possible indium clustering'" [Appl. Phys. Lett. 91, 176101 (2007)]. *Applied Physics Letters* **2007,** *91*, 176102-1 - 176102-2.

125.   De Geuser, F.; Lefebvre, W.; Danoix, F.; Vurpillot, F.; Forbord, B.; Blavette, D., An improved reconstruction procedure for the correction of local magnification effects in three-dimensional atom-probe. *Surface and Interface Analysis* **2007,** *39*, 268-272.

126.   Galtrey, M. J.; Oliver, R. A.; Kappers, M. J.; Humphreys, C. J.; Stokes, D. J.; Clifton, P. H.; Cerezo, A., Three-dimensional atom probe studies of an $In_xGa_{1-x}N$/GaN multiple quantum well structure: Assessment of possible indium clustering. *Applied Physics Letters* **2007,** *90*, 061903-1 - 061903-3.

127.   Smeeton, T. M.; Kappers, M. J.; Barnard, J. S.; Vickers, M. E.; Humphreys, C. J., Electron-beam-induced strain within InGaN quantum wells: False indium   "cluster" detection in the transmission electron microscope. *Applied Physics Letters* **2003,** *83* (26), 5419-5421.

128.   Narayan, J.; Wang, H.; Ye, J.; Hon, S.-J.; Fox, K.; Chen, J. C.; Choi, H. K.; Fan, J. C. C., Effect of thickness variation in high-efficiency InGaN/GaN light-emitting diodes. *Applied Physics Letters* **2002,** *81* (5), 841-843.

129.   van der Laak, N. K.; Oliver, R. A.; Kappers, M. J.; Humphreys, C. J., Role of gross well-width fluctuations in bright, green-emitting single InGaN/GaN quantum well structures. *Applied Physics Letters* **2007,** *90*, 121911-1 - 121911-3.

130.   Grandjean, N.; Feltin, E.; Butte, R.; Carlin, J.-F.; Sonderegger, S.; Deveaud, B.; Ganiere, J.-D., Growth mode induced carrier localization in InGaN/GaN quantum wells. *Philosophical Magazine* **2007,** *87* (13), 2067-2075.

131.   Sugahara, T.; Sato, H.; Hao, M.; Naoi, Y.; Kurai, S.; Tottori, S.; Yamashita, K.; Nishino, K.; Romano, L. T.; Sakai, S., Direct evidence that dislocations are non-radiative recombination centers in GaN. *Japanese Journal of Applied Physics* **1998,** *37*, L 398 - L 400.

132.   Narukawa, Y.; Kawakami, Y.; Funato, M.; Fujita, S.; Fujita, S.; Nakamura, S., Role of self-formed InGaN quantum dots for exciton localization in the purple laser diode emitting at 420 nm. *Applied Physics Letters* **1997,** *70* (8), 981-983.

133.   Chan, J. A.; Liu, J. Z.; Zunger, A., Bridging the gap between atomic microstructure and electronic properties of alloys: The case of (In,Ga)N. *Physical Review B* **2010,** *82*, 045112-1 - 045112-11.

134.   Gerthsen, D.; Hahn, E.; Neubauer, B.; Rosenauer, A.; Schon, O.; Heuken, M.; Rizzi, A., Composition fluctuations in InGaN analyzed by transmission electron microscopy. *Physica Status Solidi A* **2000,** *177*, 145-155.

135.   Ho, I.-h.; Stringfellow, G. B., Solid phase immiscibility in GaInN. *Applied Physics Letters* **1996,** *69* (18), 2701-2703.

136.   Karpov, S. Y., Suppression of phase separation in InGaN due to elastic strain. *MRS Internet Journal of Nitride Semiconductor Research* **1998,** *3*, 16.

137.   O'Neill, J. P.; Ross, I. M.; Cullis, A. G.; Wang, T.; Parbrook, P. J., Electron-beam-induced segregation in InGaN/GaN multiple-quantum wells. *Applied Physics Letters* **2003,** *83* (10), 1965-1967.

138.   Smeeton, T. M.; Humphreys, C. J.; Barnard, J. S.; Kappers, M. J., The impact of electron beam damage on the detection of indium-rich localisation centres in InGaN

quantum wells using transmission electron microscopy. *Journal of Materials Science* **2006,** *41* (9), 2729-2737.

139.   Bellaiche, L.; Mattila, T.; Wang, L.-W.; Wei, S.-H.; Zunger, A., Resonant hole localization and anomalous optical bowing in InGaN alloys. *Applied Physics Letters* **1999,** *74* (13), 1842-1844.

140.   Wang, L.-W., Calculations of carrier localization in $In_x Ga_{1-x}N$. *Physical Review B* **2001,** *63*, 245107-1 - 245107-7.

141.   Chichibu, S. F.; Uedono, A.; Onuma, T.; Haskell, B. A.; Chakraborty, A.; Koyama, T.; Fini, P. T.; Keller, S.; DenBaars, S. P.; Speck, J. S.; Mishra, U. K.; Nakamura, S.; Yamaguchi, S.; Kamiyama, S.; Amano, H.; Akasaki, I.; Han, J.; Sota, T., Origin of defect-insensitive emission probability in In-containing (Al,In,Ga)N alloy semiconductors. *Nature Materials* **2006,** *5*, 810-816.

142.   Graham, D. M.; Soltani-Vala, A.; Dawson, P.; Godfrey, M. J.; Smeeton, T. M.; Barnard, J. S.; Kappers, M. J.; Humphreys, C. J.; Thrush, E. J., Optical and microstructural studies of InGaN/GaN single-quantum-well structures. *Journal of Applied Physics* **2005,** *97*, 103508-1 - 103508-5.

143.   Oliver, R. A.; Bennett, S. E.; Zhu, T.; Beesley, D. J.; Kappers, M. J.; Saxey, D. W.; Cerezo, A.; Humphreys, C. J., Microstructural origins of localisation in InGaN quantum wells (Invited article). *Journal of Physics D* **2010,** *43*, 354003-1 - 354003-8.

144.   Smeeton, T. M.; Kappers, M. J.; Barnard, J. S.; Humphreys, C. J., Analysis of InGaN-GaN quantum well chemistry and interfaces by transmission electron microscopy and X-ray scattering. In *MRS Symposia Proceedings No. 798*, 2003; pp 787-792.

145.   Watson-Parris, D.; Godfrey, M. J.; Oliver, R. A.; Dawson, P.; Galtrey, M. J.; Kappers, M. J.; Humphreys, C. J., Energy landscape and carrier wave-functions in InGaN/GaN quantum wells. *Physica Status Solidi C* **2010,** *7* (7-8), 2255-2258.

146.   van der Laak, N. K.; Oliver, R. A.; Kappers, M. J.; Humphreys, C. J., Characterization of InGaN quantum wells with gross fluctuations in width. *Journal of Applied Physics* **2007,** *102*, 013513-1 - 013513-8.

147.   Costa, P. M. F. J.; Datta, R.; Kappers, M. J.; Vickers, M. E.; Humphreys, C. J.; Graham, D. M.; Dawson, P.; Godfrey, M. J.; Thrush, E. J.; Mullins, J. T., Misfit dislocations in In-rich InGaN/GaN quantum well structures. *Physica Status Solidi A* **2006,** *203* (7), 1729-1732.

148.   Kisielowski, C.; Bartel, T. P., Comment on "Three-dimensional atom probe studies of an $In_x Ga_{1-x}N$/GaN multiple quantum well structure: Assessment of possible

indium clustering" [Appl. Phys. Lett. 90, 061903 (2007)]. *Applied Physics Letters* **2007,** *91*, 176101-1 - 176101-2.

149.   Sahonta, S.-L.; Dimitrakopulos, G. P.; Kehagias, T.; Kioseoglou, J.; Adikemenakis, A.; Iliopoulos, E.; Georgakilas, A.; Kirmse, H.; Neumann, W.; Komninou, P., Mechanism of compositional modulations in epitaxial InAlN films grown by molecular beam epitaxy. *Applied Physics Letters* **2009,** *95*, 021913-1 - 021913-3.

150.   Zhou, L.; Smith, D. J.; McCartney, M. R.; Katzer, D. S.; Storm, D. F., Observation of vertical honeycomb structure in InAlN/GaN heterostructures due to lateral phase separation. *Applied Physics Letters* **2007,** *90*, 081917-1 - 081917-3.

151.   Carlin, J.-F.; Ilegems, M., High-quality AlInN for high index contrast Bragg mirrors lattice matched to GaN. *Applied Physics Letters* **2003,** *83* (4), 668-670.

152.   Teles, L. K.; Scolfaro, L. M. R.; Furthmuller, J.; Bechstedt, F.; Leite, J. R., Phase separation, gap bowing, and structural properties of cubic In$_x$Al$_{1-x}$N. *Physica Status Solidi B* **2002,** *234* (3), 956-960.

153.   Elyukhin, V. A.; Avrutin, E. A.; Marsh, J. H.; Portnoi, E. L., Decomposition and stability of group-III nitride ternary cubic spontaneously ordered alloys. *IEEE Journal of Selected Topics in Quantum Electronics* **1998,** *4* (3), 531-536.

154.   Sadler, T. C.; Kappers, M. J.; Oliver, R. A., The effect of temperature and ammonia flux on the surface morphology and composition of In$_x$Al$_{1-x}$N epitaxial layers. *Journal of Crystal Growth* **2009,** *31*, 3380-3385.

155.   Sadler, T. C.; Kappers, M. J.; Oliver, R. A., Investigation of optimum growth conditions of InAlN for application in distributed Bragg reflectors. *Journal of Physics: Conference Series* **2010,** *209*, 012015-1 - 012015-4.

156.   Carlin, J.-F.; Zellweger, C.; Dorsaz, J.; Nicolay, S.; Christmann, G.; Feltin, E.; Butte, R.; Grandjean, N., Progresses in III-nitride distributed Bragg reflectors and microcavities using AlInN/GaN materials. *Physica Status Solidi B* **2005,** *242* (11), 2326-2344.

157.   Miller, M. K.; Russell, K. F.; Thompson, K.; Alvis, R.; Larson, D. J., Review of atom probe FIB-based specimen preparation methods. *Microscopy and Microanalysis* **2007,** *13*, 428-436.

158.   Sadler, T. C.; Kappers, M. J.; Oliver, R. A., Optimisation of GaN overgrowth of InAlN for DBRs. *Physica Status Solidi C* **2009,** *6* (S2), S666-S670.

159.	Hooper, S. E.; Kauer, M.; Bousquet, V.; Johnson, K.; Barnes, J. M.; Heffernan, J., InGaN multiple quantum well laser diodes grown by molecular beam epitaxy. *Electronics Letters* **2004,** *40* (1), 33-34.

160.	Kachkanov, V.; O'Donnell, K. P.; Pereira, S.; Martin, R. W., Localization of excitation in InGaN epilayers. *Philosophical Magazine* **2007,** *87* (13), 1999-2017.